

# **Cu/Ce<sub>x</sub>Zr<sub>1-x</sub>O<sub>2</sub> CATALYSTS FOR SOLID OXIDE FUEL CELL ANODES**

**Jonathan Kearney**

**A Thesis Submitted for the Degree of PhD  
at the  
University of St Andrews**



**2010**

**Full metadata for this item is available in  
St Andrews Research Repository  
at:**

**<http://research-repository.st-andrews.ac.uk/>**

**Please use this identifier to cite or link to this item:**

**<http://hdl.handle.net/10023/1845>**

**This item is protected by original copyright**

**This item is licensed under a  
Creative Commons Licence**

**Cu/Ce<sub>x</sub>Zr<sub>1-x</sub>O<sub>2</sub> Catalysts for Solid Oxide Fuel Cell  
Anodes**

**Jonathan Kearney**

**Submitted for the Degree of Doctor of Philosophy**

**University of St Andrews**

## Declaration

I, Jonathan Kearney, hereby certify that this thesis, which is approximately 42540 words in length, has been written by me, that it is the record of work carried out by me and that it has not been submitted in any previous application for a higher degree.

I was admitted as a research student in September 2005 and as a candidate for the degree of PhD in September 2005; the higher study for which this is a record was carried out in the University of St Andrews between 2005 and 2008.  
date.....

I hereby certify that the candidate has fulfilled the conditions of the Resolution and Regulations appropriate for the degree of PhD in the University of St Andrews and that the candidate is qualified to submit this thesis in application for that degree.  
date.....

In submitting this thesis to the University of St Andrews we understand that we are giving permission for it to be made available for use in accordance with the regulations of the University Library for the time being in force, subject to any copyright vested in the work not being affected thereby. We also understand that the title and the abstract will be published, and that a copy of the work may be made and supplied to any bona fide library or research worker, that my thesis will be electronically accessible for personal or research use unless exempt by award of an embargo as requested below, and that the library has the right to migrate my thesis into new electronic forms as required to ensure continued access to the thesis. We have obtained any third-party copyright permissions that may be required in order to allow such access and migration, or have requested the appropriate embargo below.

The following is an agreed request by candidate and supervisor regarding the electronic publication of this thesis:

Embargo on both all and any part of printed copy and electronic copy for the same fixed period of two years (maximum five) on the following ground:

publication would be commercially damaging to the researcher, or to the supervisor, or the University;

publication would preclude future publication;

date..... ..signature of candidate .....

signature of supervisor.....

## **Acknowledgements**

I am grateful to the Supergen Fuel Cells consortium for providing the funding for this work and St Andrews University for hosting me during my studies.

I would like to thank my supervisor Dr Richard Baker, for all his help, support and input throughout my time at St Andrews. I wish to thank Sylvia Williamson, for collecting the BET data and Robert Cathcart for his help in building and establishing the TP rig.

On a personal note I wish to thank Helen Shelton for her unerring support throughout my studies, without which I could not have completed this work. I wish to thank Lynzi Robb for convincing me to continue my studies at St Andrews and who has remained a close friend throughout my studies. There are a number of people who have made my time in St Andrews so memorable and so I wish to thank Stuart Millar, David Aldous, Lindsey Richie, Charlotte Jones, Lynn Power Ben Parnham and Sneh Jain for their friendship and support. I would finally wish to thank Troy Dogherty for the numerous discussions and conversations we have had.

## Abstract

$\text{Ce}_x\text{Zr}_{1-x}\text{O}_2$  mixed oxides of varying compositions were prepared by a sol-gel citrate complexation technique. In order to improve the catalytic activity of the oxides they were impregnated with copper using two different impregnation techniques. The bare oxides and copper impregnated samples were investigated using a range of Temperature Programmed (TP) techniques, in an attempt to establish their effectiveness as anode materials for solid oxide fuel cells (SOFCs) run on hydrocarbon fuels. In order to conduct the TP experiments a novel system was designed and constructed.

The high Ce containing mixed oxides were shown to be reduced at lower temperature than high Zr content samples. TPR experiments were employed to investigate which of the oxides was most prone to carbon deposition when reacted in methane, with the high ceria sample displaying the lowest level of carbon deposition. Lightoff experiments were undertaken to establish which oxide composition was the most active for methane oxidation. The activity of the oxides increased with ceria content up to 75 mole% (ZCe75), before decreasing for ZCe90. All the mixed oxides were shown to be more active for methane oxidation than  $\text{CeO}_2$ .

The Ce/Zr mixed oxides were impregnated with copper using two different impregnation techniques in order to form catalysts. The wet-impregnated technique was shown to produce samples with copper agglomerations at relatively low loadings (5 wt%). Samples impregnated with copper during preparation were found to have high copper dispersion and distribution even at elevated loadings (10 wt%). The TPR results of the copper impregnated samples contained up to four reduction peaks which have been attributed to reduction of both the copper and the oxide support. Samples prepared using the single step preparation technique was found to be more active for all oxide compositions and copper loadings examined.

## Abbreviations

AFC	Alkaline Fuel Cell
CHP	Combined Heat and Power
CO-PROX	Preferential Oxidation of CO
DMFC	Direct Methanol Fuel Cell
EDX	Energy Dispersive X-ray
GC	Gas Chromatograph
LGSM	Strontium and Magnesium doped Lanthanum Gallate
LSM	Strontium-doped Lanthanum Manganite
MFC	Mass Flow Controller
OSC	Oxygen Storage Capacity
PAFC	Phosphoric Acid Fuel Cells
PEMFC	Proton Exchange Membrane Fuel Cell
QMS	Quadrupole Mass Spectrometer
SEM	Scanning Electron Microscope
SEM	Secondary Electron Multiplier
SOFC	Solid Oxide Fuel Cell
SSA	Specific Surface Area
TPD	Temperature Programmed Desorption
TPO	Temperature Programmed Oxidation
TPR	Temperature Programmed Reduction
TPRx	Temperature Programmed Reaction
TCD	Thermal Conductivity Detector
TWC	Three-Way Automotive Catalysts
WGS	Water Gas Shift (Reaction)
XRD	X-Ray Diffraction
YSZ	Yttria Stabilised Zirconia

## Contents

<b>Declaration</b> .....	II
<b>Acknowledgements</b> .....	III
<b>Abstract</b> .....	IV
<b>Abbreviations</b> .....	V
<b>Contents</b> .....	VI
<b>Chapter 1. Introduction to Fuel Cell Technology</b> .....	1
<b>1.1 Fuel Cells</b> .....	2
<b>1.2 Solid Oxide Fuel Cells</b> .....	5
<b>1.2.1 Cell Configurations</b> .....	5
<b>1.3 SOFC Components</b> .....	7
<b>1.3.1 Electrolyte</b> .....	8
<b>1.3.2 Anode</b> .....	10
<b>1.3.3 Cathode</b> .....	11
<b>1.3.4 Interconnect Materials</b> .....	11
<b>1.4 Anode Development</b> .....	12
<b>1.4.1 Operation of SOFCs Using Hydrocarbon Fuels</b> .....	12
<b>1.4.2 SOFC with Ni-Based Anodes</b> .....	13
<b>1.4.3 Ceramic Anodes</b> .....	14
<b>1.5 Summary</b> .....	14
<b>1.6 References</b> .....	15
<b>Chapter 2. Temperature Programmed Studies and Catalysis Background</b> .....	17
<b>2.1 Introduction</b> .....	18
<b>2.2 Temperature Programmed Techniques</b> .....	18
<b>2.2.1 Introduction</b> .....	18
<b>2.2.2 Temperature Programmed Desorption (TPD)</b> .....	18
<b>2.2.2.1 Experimental Procedure</b> .....	18
<b>2.2.2.2 Theory</b> .....	19
<b>2.2.3 Temperature Programmed Reduction (TPR)</b> .....	22
<b>2.2.4 Temperature Programmed Reaction (TPRx)</b> .....	23
<b>2.2.5 Temperature Programmed Oxidation (TPO)</b> .....	23
<b>2.3 Experimental Considerations</b> .....	23
<b>2.4 Light-off Experiments</b> .....	24
<b>2.5 Theory of Scanning Electron Microscopy (SEM) and Energy-dispersive X-ray Spectroscopy (EDX)</b> .....	25
<b>2.6 XRD Theory</b> .....	26
<b>2.7 Ceria-Zirconia Mixed Oxides</b> .....	27
<b>2.7.1 Introduction</b> .....	27
<b>2.7.2 Three-Way Catalysis (TWC)</b> .....	28
<b>2.7.3 Preferential CO Oxidation in Excess Hydrogen</b> .....	29
<b>2.7.4 Direct Oxidation of Hydrocarbons Leading to SOFC Anode Development</b> .....	31
<b>2.8 Summary</b> .....	34
<b>2.9 Aims</b> .....	36
<b>2.10 References</b> .....	37

<b>Chapter 3. Experimental Details</b> .....	41
<b>3.1 Introduction</b> .....	42
<b>3.2 Material Preparation</b> .....	42
<b>3.2.1 Oxide Preparation</b> .....	42
<b>3.2.2 Copper Impregnation</b> .....	43
<b>3.2.2.1 Incipient Wetness</b> .....	43
<b>3.2.2.2 Impregnation During Preparation</b> .....	44
<b>3.3 Scanning Electron Microscopy (SEM)</b> .....	45
<b>3.4 X-ray Diffraction (XRD)</b> .....	45
<b>3.5 BET Surface Area Analysis</b> .....	45
<b>3.6 Temperature Programmed Apparatus</b> .....	46
<b>3.7 Temperature Programmed Experiments</b> .....	50
<b>3.7.1 Temperature Programmed Desorption (TPD)</b> .....	51
<b>3.7.2 Temperature Programmed Reduction (TPR)</b> .....	51
<b>3.7.3 Temperature Programmed Reaction (TPRx)</b> .....	52
<b>3.7.4 Temperature Programmed Oxidation (TPO)</b> .....	52
<b>3.7.5 Lightoff Experiments</b> .....	52
<b>3.8 Detector Settings</b> .....	53
<b>3.8.1 Mass Spectrometry</b> .....	54
<b>3.8.2 Detector Calibration</b> .....	54
<b>3.8.3 Data Manipulation</b> .....	55
<b>3.8.4 Thermocouple Adjustments</b> .....	56
<b>3.8.5 Lightoff Modifications</b> .....	57
<b>3.8.6 Further Modifications</b> .....	58
<b>3.9 References</b> .....	58
<b>Chapter 4. Ceria-Zirconia Oxides as Catalyst Supports</b> .....	59
<b>4.1 Introduction</b> .....	60
<b>4.2 Characterisation</b> .....	60
<b>4.2.1 Scanning Electron Microscopy</b> .....	60
<b>4.3 BET Surface Area Analysis</b> .....	63
<b>4.4 Temperature Programmed Studies</b> .....	63
<b>4.4.1 Temperature Programmed Desorption</b> .....	64
<b>4.4.2 Temperature Programmed Reduction</b> .....	69
<b>4.4.2.1 The Effect of TPDs prior to TPRs</b> .....	69
<b>4.4.2.2 The Effect of Mixed Oxide Composition on TPRs</b> .....	72
<b>4.4.3 Temperature Programmed Reaction</b> .....	82
<b>4.4.4 Temperature Programmed Oxidation</b> .....	85
<b>4.4.5 Lightoff Experiments</b> .....	88
<b>4.5 Summary</b> .....	97
<b>4.6 References</b> .....	98
<b>Chapter 5. Copper Impregnated Ceria-Zirconia Oxides</b> .....	99
<b>5.1 Introduction</b> .....	100
<b>5.2 SEM images and Elemental Maps</b> .....	100
<b>5.3 XRD</b> .....	105
<b>5.4 BET Surface Area Analysis</b> .....	107
<b>5.5 Temperature Programmed Studies</b> .....	108
<b>5.5.1 Temperature Programmed Desorption</b> .....	108
<b>5.5.1.1 Effect of Calcination Temperature</b> .....	108

5.5.1.2	Effect of Mixed Oxide Composition.....	111
5.5.2	Temperature Programmed Reduction .....	116
5.5.2.1	Effect of the Copper Impregnation Technique.....	116
5.5.2.2	Effect of Oxide Composition.....	120
5.5.2.3	Effect of Copper Loading.....	124
5.5.3	Temperature Programmed Reaction.....	134
5.5.4	Temperature Programmed Oxidation.....	138
5.5.5	Lightoff Experiments .....	140
5.5.5.1	Effect of Catalyst Reduction Temperature .....	141
5.5.5.2	Effect of Catalyst Composition and Impregnation Technique.....	143
5.6	Summary .....	155
5.7	References.....	157
<b>Chapter 6.</b>	<b>Discussion .....</b>	<b>158</b>
6.1	Oxygen Evolution During TPDs.....	159
6.1.1	Low Temperature (<200°C) Oxygen Species .....	159
6.1.2	High Temperature Oxygen Species.....	159
6.2	TPR Results.....	163
6.2.1	Assignment of TPR Peaks.....	163
6.2.2	Effect of Impregnation Technique .....	166
6.2.3	Increased Copper Loading .....	167
6.3	Effect of TPD on TPR Results .....	168
6.4	Lightoff Mechanisms.....	169
6.5	Catalyst Performance.....	169
6.6	References.....	171
<b>Chapter 7.</b>	<b>Conclusions.....</b>	<b>173</b>
7.1	Ce/Zr Mixed Oxides .....	174
7.2	Copper - Containing Ce/Zr Mixed Oxides .....	175
7.3	References.....	177
<b>Chapter 8.</b>	<b>Further Work.....</b>	<b>178</b>
8.1	Further Work.....	179
<b>Appendix 1.</b>	<b>TPD/Rs of Ce/Zr Mixed Oxides .....</b>	<b>Error! Bookmark not defined.</b>
<b>Appendix 2.</b>	<b>Lightoffs of Ce/Zr Mixed Oxides .....</b>	<b>Error! Bookmark not defined.</b>
<b>Appendix 3.</b>	<b>TPDs of Copper Impregnated Mixed Oxides.....</b>	<b>Error! Bookmark not defined.</b>
<b>Appendix 4.</b>	<b>TPR and TPD/R of Copper Impregnated Mixed Oxides.....</b>	<b>Error! Bookmark not defined.</b>
<b>Appendix 5.</b>	<b>Lightoffs of Copper Impregnated Mixed Oxides.....</b>	<b>Error! Bookmark not defined.</b>

## List of Tables

<b>Table 2.1</b>	Reduction peaks from TPRs of a range of Ce-Zr oxides.	34
<b>Table 3.1</b>	Masses of nitrates used in preparation of the Ce/Zr mixed oxides.	43
<b>Table 4.1</b>	Peak positions and water production data for TPR and TPD/R experiments on Ce/Zr mixed oxides.	81
<b>Table 4.2</b>	Lightoff temperatures obtained from O <sub>2</sub> and CH <sub>4</sub> consumption, and H <sub>2</sub> O and CO <sub>2</sub> production traces for mixed oxides and CeO <sub>2</sub> in a 2:1 mixture of O <sub>2</sub> and CH <sub>4</sub> .	95
<b>Table 5.1</b>	Water and O <sub>2</sub> released during the course of TPD, TPD/R and TPR experiments for I impregnated samples.	133
<b>Table 5.2</b>	Water and O <sub>2</sub> released during the course of TPD, TPD/R and TPR experiments for D impregnated samples.	133
<b>Table 6.1</b>	O <sub>2</sub> desorption during TPD's of 5 % (wt) Cu samples.	160

## List of Figures

<b>Figure 1.1</b>	A Solid Oxide Fuel Cell.	3
<b>Figure 1.2</b>	Tubular Solid Oxide Fuel Cell.	6
<b>Figure 1.3</b>	Planar Solid Oxide Fuel Cell.	7
<b>Figure 1.4</b>	The three-phase boundary regions in an electronically and an electronic/ionically conducting material.	10
<b>Figure 2.1</b>	Dependence of surface coverage, desorption rate and temperature on time during a TPD experiment.	20
<b>Figure 2.2</b>	A block diagram of a typical SEM system.	25
<b>Figure 2.3</b>	Bragg reflections that result from a set of crystal planes with the spacing $d_{hkl}$ .	27
<b>Figure 3.1</b>	Apparatus for temperature programmed experiments.	48
<b>Figure 3.2</b>	Furnace and reactor arrangement.	49
<b>Figure 3.3</b>	Quartz micro-reactor.	50
<b>Figure 3.4</b>	QMS response depending on accelerator voltage.	54
<b>Figure 3.5</b>	Carbon species evolved during a TPO following a TPRx.	56
<b>Figure 3.6</b>	Comparison of temperature readings from two different thermocouple arrangements.	57

<b>Figure 3.7</b>	Modifications to gas lines for lightoff experiments.	58
<b>Figure 4.1</b>	SEM images of mixed oxides.	61
<b>Figure 4.2</b>	SEM image and elemental maps for ZCe10.	62
<b>Figure 4.3</b>	SEM image and elemental maps for ZCe90.	62
<b>Figure 4.4</b>	BET SSAs for mixed oxides.	63
<b>Figure 4.5</b>	TPD traces for as prepared mixed oxide samples.	64
<b>Figure 4.6</b>	CO <sub>2</sub> traces from TPD experiments on as-prepared mixed oxide samples.	68
<b>Figure 4.7</b>	H <sub>2</sub> O traces from the TPDs of as-prepared mixed oxide samples.	69
<b>Figure 4.8</b>	(a) TPR of ZCe50 sample as prepared, b) TPD/R of ZCe50.	70
<b>Figure 4.9</b>	Water and hydrogen traces from TPR of as-prepared ZCe50.	71
<b>Figure 4.10</b>	TPR traces for as-prepared mixed oxide samples.	72
<b>Figure 4.11</b>	Water traces from TPD, TPD/R and TPR experiments of mixed oxides.	75
<b>Figure 4.12</b>	Water traces from TPRs conducted on as-prepared mixed oxides.	77
<b>Figure 4.13</b>	Water traces from TPD/Rs for mixed oxide samples.	78
<b>Figure 4.14</b>	Reduction peak positions from the TPR and TPD/R of mixed oxide samples.	79
<b>Figure 4.15</b>	Moles of water produced during TPR and TPD/R of ZCe mixed oxides. Maximum theoretical water evolution is also plotted for comparison.	80
<b>Figure 4.16</b>	Water produced during the TPR and TPD/Rs for all ZCe mixed oxide compositions as a percentage of the maximum theoretical yield.	82
<b>Figure 4.17</b>	Log TPRx traces for as-prepared a) ZCe50 b) ZCe90.	83
<b>Figure 4.18</b>	Linear TPRx traces for as-prepared a) ZCe50 b) ZCe90.	84
<b>Figure 4.19</b>	Log TPO traces for (a) ZCe50 and (b) ZCe90, after TPRx experiments.	86
<b>Figure 4.20</b>	Linear TPO traces for (a) ZCe50 and (b) ZCe90 after TPRx experiments.	87
<b>Figure 4.21</b>	Lightoff plot of ZCe50 sample pre-reduced at 500°C.	88
<b>Figure 4.22</b>	Lightoff plot for experiment run using an empty reactor.	89
<b>Figure 4.23</b>	O <sub>2</sub> traces from lightoffs of ZCe mixed oxides and CeO <sub>2</sub> .	91
<b>Figure 4.24</b>	CH <sub>4</sub> traces from lightoffs of ZCe mixed oxides and CeO <sub>2</sub> .	91
<b>Figure 4.25</b>	CO <sub>2</sub> traces from lightoffs of ZCe mixed oxides and CeO <sub>2</sub> .	92
<b>Figure 4.26</b>	H <sub>2</sub> O traces from lightoffs of ZCe mixed oxides and CeO <sub>2</sub> .	92

<b>Figure 4.27</b>	CO traces from lightoffs of ZCe mixed oxides and CeO <sub>2</sub> .	93
<b>Figure 4.28</b>	H <sub>2</sub> traces from lightoffs of ZCe mixed oxides and CeO <sub>2</sub> .	93
<b>Figure 4.29</b>	Lightoff temperatures obtained from O <sub>2</sub> consumption trace for mixed oxides and CeO <sub>2</sub> in a 2:1 mixture of O <sub>2</sub> and CH <sub>4</sub> .	94
<b>Figure 4.30</b>	Lightoff temperatures obtained from O <sub>2</sub> and CH <sub>4</sub> consumption, H <sub>2</sub> O and CO <sub>2</sub> production traces for mixed oxides and CeO <sub>2</sub> .	95
<b>Figure 4.31</b>	Schematic representation of the catalytic cycle of methane combustion.	96
<b>Figure 5.1</b>	SEM image and elemental maps for 5-50-D.	100
<b>Figure 5.2</b>	SEM image and elemental maps for 5-50-I (II).	101
<b>Figure 5.3</b>	SEM image and elemental maps for 5-10-I (II).	102
<b>Figure 5.4</b>	SEM image and elemental maps for 7-50-I (II).	103
<b>Figure 5.5</b>	SEM image and elemental maps for 10-50-I (II).	104
<b>Figure 5.6</b>	SEM image and elemental maps for 10-50-D.	104
<b>Figure 5.7</b>	XRD patterns for 5-I and 5-D and Bare oxides.	106
<b>Figure 5.8</b>	BET SSA values for bare oxides, 5-I and 5-D samples.	107
<b>Figure 5.9</b>	TPD traces for (a) 5-50-I (I), (b) 5-50-I (II), (c) 5-50-D.	110
<b>Figure 5.10</b>	CO <sub>2</sub> traces (m/q = 44) from TPDs of as-prepared 5-D samples.	112
<b>Figure 5.11</b>	O <sub>2</sub> traces (m/q = 32) from TPDs of as-prepared 5-D samples.	113
<b>Figure 5.12</b>	H <sub>2</sub> O traces (m/q = 18) from TPDs of as-prepared 5-D samples.	114
<b>Figure 5.13</b>	Moles of O <sub>2</sub> desorbed during TPD of 5-I and 5-D samples.	115
<b>Figure 5.14</b>	O <sub>2</sub> traces from the TPDs of as-prepared 50-I (II) samples of varying copper loadings.	115
<b>Figure 5.15</b>	TPR traces of (a) CuO nano-powder (b) CuO prepared from Cu(NO <sub>3</sub> ) <sub>2</sub> ·3H <sub>2</sub> O.	117
<b>Figure 5.16</b>	TPR traces of as-prepared (a) 5-50-I (II) and (b) 5-50-D.	119
<b>Figure 5.17</b>	TPR water traces for as-prepared 5-I (II) samples.	121
<b>Figure 5.18</b>	TPR water traces for as-prepared 5-D samples.	122
<b>Figure 5.19</b>	Moles of water from TPRs and TPD/Rs for 5-I and 5-D samples.	123
<b>Figure 5.20</b>	TPR water traces for as-prepared 2-I (II) samples.	126
<b>Figure 5.21</b>	TPR water traces for as-prepared 5-I (II) samples.	126
<b>Figure 5.22</b>	TPR water traces for as-prepared 7-I (II) samples.	126
<b>Figure 5.23</b>	TPR reduction peak positions for as-prepared I samples for varying oxide compositions.	127

<b>Figure 5.24</b>	TPR reduction peak positions for as-prepared 50-I (II) samples as a function of copper loading.	128
<b>Figure 5.25</b>	Water traces from TPD/R of 5-I (II) samples.	129
<b>Figure 5.26</b>	Water traces from TPD/R of 5-D samples.	129
<b>Figure 5.27</b>	The amount of water evolved during TPR and TPD/R experiments for all copper wt% and oxide composition samples.	130
<b>Figure 5.28</b>	TPR and TPD/R reduction peak temperatures for 5 wt% copper impregnated samples.	132
<b>Figure 5.29</b>	Log TPRx traces for as-prepared a) 5-50-I (II), b) 5-50-D, c) 10-50-I (II).	136
<b>Figure 5.30</b>	Linear TPRx traces for as-prepared a) 5-50-I (II), b) 5-50-D, c) 10-50-I (II).	137
<b>Figure 5.31</b>	Log TPO traces post TPRx for a) 5-50-I (II), b) 5-50-D, c) 10-50-I (II).	139
<b>Figure 5.32</b>	CO <sub>2</sub> traces from the TPOs post TPRx for a) 5-50-D, b) 10-50-I (II), c) 5-50-I (II).	140
<b>Figure 5.33</b>	Lightoff plot of 5-50-I (II) sample pre-reduced at 500°C.	141
<b>Figure 5.34</b>	Reactants and products from lightoff experiments for 5-50-I (II) samples pre-reduced at a range of temperatures.	142
<b>Figure 5.35</b>	CH <sub>4</sub> traces from lightoff experiments for I and D samples.	144
<b>Figure 5.36</b>	O <sub>2</sub> traces from lightoff experiments for I and D samples.	146
<b>Figure 5.37</b>	CO <sub>2</sub> traces from lightoff experiments for I and D samples.	147
<b>Figure 5.38</b>	H <sub>2</sub> O traces from lightoff experiments for I and D samples.	148
<b>Figure 5.39</b>	CO traces from lightoff experiments for I and D samples.	149
<b>Figure 5.40</b>	H <sub>2</sub> traces from lightoff experiments for I and D samples.	150
<b>Figure 5.41</b>	O <sub>2</sub> traces from lightoff experiments on bare oxides and copper impregnated samples for all oxide compositions.	151
<b>Figure 5.42</b>	Lightoff temperatures from O <sub>2</sub> consumption for copper impregnated samples, bare Ce/Zr oxides and CeO <sub>2</sub> .	152
<b>Figure 5.43</b>	Lightoff temperatures from O <sub>2</sub> and CH <sub>4</sub> consumption, as well as CO <sub>2</sub> and H <sub>2</sub> O production for 5 wt% copper impregnated samples.	154
<b>Figure 6.1</b>	a) SSA and b) percentage theoretical reduction due to O <sub>2</sub> evolution during TPD experiments for 5-I and 5-D samples.	161
<b>Figure 6.2</b>	Moles of O <sub>2</sub> desorbed during TPD experiments for all 5	162

wt% Cu impregnated samples.

**Figure 6.3** Moles of O<sub>2</sub> desorbed during TPD experiments for ZCe50-I samples of a range of copper loadings. 163

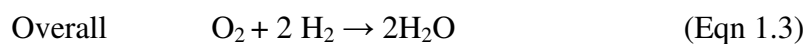
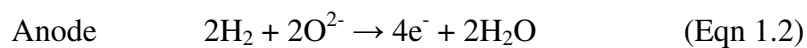
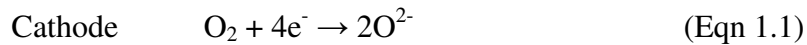
**Figure 6.4** TPR water trace for as-prepared 2-90-I (II) sample. 165

**Figure 6.5** Water (and O<sub>2</sub> where applicable) evolved as a percentage of total theoretical reduction of samples copper content. 166

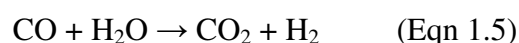
# **Chapter 1. Introduction to Fuel Cell Technology**

## 1.1 Fuel Cells

A fuel cell is an electrochemical reactor in which electrical energy is obtained from chemical energy, similar to the operation principles of batteries. Fuel cells differ from batteries in that they utilise a continuously supplied fuel. [1] Fuel cells have a number of potential advantages, such as high efficiency, simplicity (with few if any moving parts) and low emissions (with the general product of the reaction from a fuel cell operating on H<sub>2</sub> being H<sub>2</sub>O). [2] Fuel cell systems consist of four components; an anode, cathode, electrolyte and an interconnect which connects the anode and cathode of neighbouring cells. The cathode is the oxygen or air electrode, where oxygen is reduced to O<sup>2-</sup> (Eqn 1.1). The electrolyte is an ionic conductor that typically conducts H<sup>+</sup> or O<sup>2-</sup> ions. The anode is the fuel electrode. Most fuel cell systems currently operate using high purity hydrogen and in theory the systems can operate using a range of hydrocarbons such as CH<sub>4</sub>. The operation of a Solid Oxide Fuel Cell (SOFC) based on O<sup>2-</sup> conduction is shown in Figure 1.1. In this system, the O<sup>2-</sup> ions react with the hydrogen source leading to the formation of H<sub>2</sub>O and a flow of electrons (Eqn 1.2) which pass along the external circuit to the cathode.



The overall reaction as shown in Eqn 1.3 shows that water is the only product from a fuel cell operating using hydrogen. Currently around 90% of the world's H<sub>2</sub> is obtained from the steam reforming of methane, Eqn 1.4. [3] Steam reforming is often followed by the water-gas shift reaction (WGS), (Eqn 1.5) in which the CO from the steam reforming is reacted with steam over a catalyst to produce CO<sub>2</sub> and more H<sub>2</sub>. If hydrogen is to be used extensively for fuel cells then there is the need for new infrastructure for the production and storage of hydrogen. One of the major problems with the use of hydrogen as an energy source is that despite having a high energy density on a gravimetric basis it has a low volumetric energy density. [3] The problems associated with H<sub>2</sub> distribution and storage led to an emphasis on research into fuel-cell systems that can operate directly using hydrocarbons. [4]



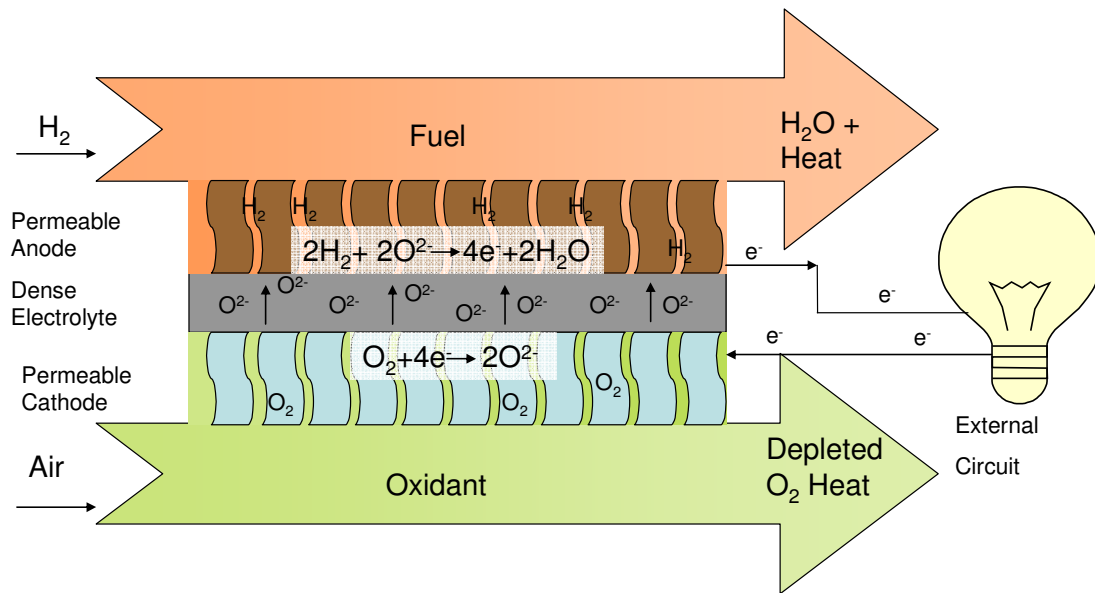


**Figure 1.1** A diagram showing the operation of a SOFC based on an oxygen ion conducting electrolyte. The light bulb is shown to demonstrate the utilization of the current produced for electrical power.

There are a range of fuel cell systems currently being investigated. These systems are distinguished by the material they employ as the electrolyte. The different electrolytes employ a range of mobile ions, such as  $\text{OH}^-$  in Alkaline Fuel Cells (AFCs),  $\text{H}^+$  in Proton Exchange Membrane (PEMFC), Direct Methanol (DMFC) and Phosphoric Acid Fuel Cells (PAFC). A brief introduction to the range of fuel cell technologies will now be given.

AFCs were the first fuel cell technology to be practically employed. [5] The electrolyte is an aqueous potassium hydroxide solution. [6] The electrodes consist of an active catalyst layer and a hydrophobic layer. The hydrophobic layer prevents the electrolyte from leaking into the reactant gas streams. The presence of carbon dioxide in the oxidant stream leads to the formation of carbonates which precipitate out. These carbonates may then block the electrode pores and the electrolyte pathways. [6] As a result, if air is to be used as the oxidant for these cells, it is necessary to employ gas scrubbers to remove  $\text{CO}_2$ . [7]

PEMFCs were employed as early as the 1960s on the Gemini space craft, as auxiliary power units. Further development then largely stagnated until the late 1980s, when there was significant reconfiguration of the fundamental system design. [8] A PEM cell contains a proton exchange membrane electrolyte and two electrodes which both contain catalyst

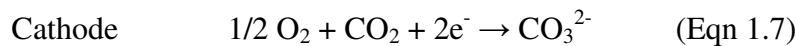
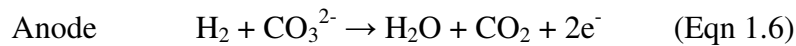
layers and gas diffusion layers. PEMFCs are low temperature systems generally operating between 80°C and 120°C. This is owing to the membrane being hydrated, so higher temperatures would result in steam management issues and possible membrane decomposition. The established membrane material is “Nafion” a perfluorosulfonic acid developed by Du Pont. [9] Nafion was a revolutionary material that provided a two-fold increase in membrane conductivity and increased the membrane life time by four orders of magnitude. [9] There are also however drawbacks to the use of Nafion. It is a very expensive material (around US \$700 per m<sup>2</sup>) and evolves toxic and corrosive gases if operated above 150°C. [9] The low operating temperature of PEMFCs means that highly active Pt catalysts are required. Extensive research has led to a large decrease in the amount of Pt required for the catalysts (reduced from 4 mg/cm<sup>2</sup> to as low as 0.014 mg/cm<sup>2</sup> reported). [8] PEMFCs generally operate on very high grade H<sub>2</sub>, as the Pt catalysts have very low tolerance for CO. [10]

In order to overcome the need for high grade hydrogen DMFCs have been developed which employ methanol as a fuel. These DMFCs have much higher power densities than currently employed rechargeable batteries. As a result they are being researched by a number of companies such as Toshiba, Hitachi and Fujitsu for a range of mobile electronic devices. [11]

PAFCs as the name suggests employ an electrolyte composed of primarily phosphoric acid. The electrodes make use of platinum catalysts, with the operating temperature for PAFC systems typically between 150°C and 200°C. [12] As with PEMFCs, PAFCs employ protons as charge carriers. The protons are generated by the reduction of hydrogen or hydrogen rich gas at the anode. The protons then pass through the phosphoric based electrolyte to the cathode. At the cathode the protons react with oxygen and electrons to release water. [12] These systems have been shown to be very efficient, with electrical efficiency of 40% [13] and total efficiency of up to 87%, when used in Combined Heat and Power (CHP) systems. [12] The major PAFC developers are UTC Fuel Cells, Toshiba and Fuji Electric. [12]

Molten carbonate fuel cells (MCFC) employ as an electrolyte a molten mixture of lithium, potassium and sodium carbonates. In order to maintain the electrolyte in the liquid state the temperature in the cell must be maintained above 500°C with the typical operating

temperature round 650°C. [14] A sophisticated auxiliary system with a precise temperature controller is required in order to maintain the electrolyte. The auxiliary system, low current densities and a comparatively thick electrode-electrolyte assembly mean that MCFCs are primarily envisaged for static power generation. [14] The high operating temperature used in MCFC means that it is possible to use Ni based catalysts for both electrodes (NiCo for the anode, NiO for the cathode). [15] The electrochemical reactions that take place in the MCFC are slightly different to those previously mentioned for fuel cell systems:



The cathode in MCFCs therefore requires CO<sub>2</sub>, which is generally supplied by mixing some of the anode exhaust with the cathode fuel supply. [14]

Solid oxide fuel cells (SOFCs), contain a dense ceramic electrolyte and operate at high temperatures (600-1100°C). [1] SOFCs employ a solid oxide as an electrolyte, typically yttria-stabilized zirconia (YSZ). The established anode material is Ni-YSZ cermet, where a cermet is a ceramic material impregnated with metal. The most commonly employed cathode material is currently Ln<sub>1-x</sub>Sr<sub>x</sub>MnO<sub>3</sub> (LSM). [16] The high operating temperature has a number of advantages. It allows internal reforming, promotes electrocatalysis with non-precious metals and produces high quality heat as a by-product which can be utilised for co-generation further increasing the systems efficiency. Co-generation is when the heat produced by the cell is also used to generate power, for example by using the exhaust gas to operate a turbine. [1]

## 1.2 Solid Oxide Fuel Cells

### 1.2.1 Cell Configurations

A number of SOFC geometries have been investigated and currently the planar and tubular arrangements are the established systems. Both of these geometries have a number of advantages and disadvantages. The tubular design shown in Figure 1.2 was pioneered by Westinghouse Electric Corporation (now Siemens Westinghouse Power Corporation or SWPC) in the late 1970s. [2] The inner layer of the tubular arrangement is the cathode. In previous generations of TSOFC (Tubular SOFC), there was a support tube which air

diffused through, though the current generation of TSOFCs are air electrode-supported. [17] The next layer is the electrolyte, typically YSZ. The external layer is the fuel electrode (anode). [17] Tubular configured cells have low volumetric power density and high production costs. These have been the major problems limiting their development since their inception. [17] The low volumetric power density is the result of the large voids within the cells to allow for efficient gas flow within the system and also, the long conduction path for electrical charge through each cell. [2]

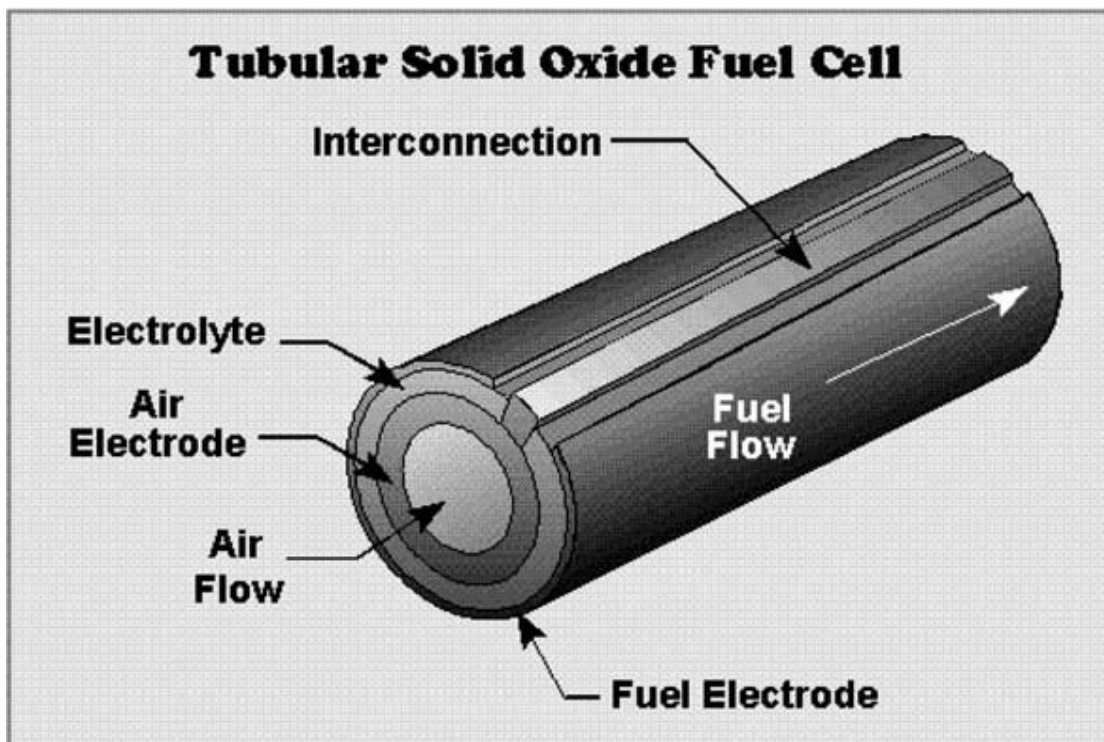


**Figure 1.2** Siemens-Westinghouse tubular SOFC design. Tube diameter is approximately 22 mm [17]

The planar geometry is shown in Figure 1.3. The mechanical properties are relatively poor compared to those of the tubular cells and there is a need for high temperature gas-tight seals. Planar SOFCs have been found to be brittle under tension, with the tensile strength of zirconia (typically >90% of the electrolyte) in SOFCs being only around 20% of the compressive strength. [2] The gas tight seals, ensure that the gas and fuel mixtures are kept separate. As a result a number of glass ceramic materials have been developed to ensure gas tight sealing. [16] A number of companies including Rolls Royce (UK), Global Thermoelectric (Canada), SOFCo (USA) and Sulzer Hexis (Switzerland) are developing

planar cells. [18] The planar arrangement enables a series arrangement of cells, vastly reducing the current path compared to tubular cell and resulting in comparatively much lower ohmic losses. Consequently, planar cells have much higher power densities, as well as allowing established production methods to be employed such as tape casting and screen printing, reducing costs. [2]

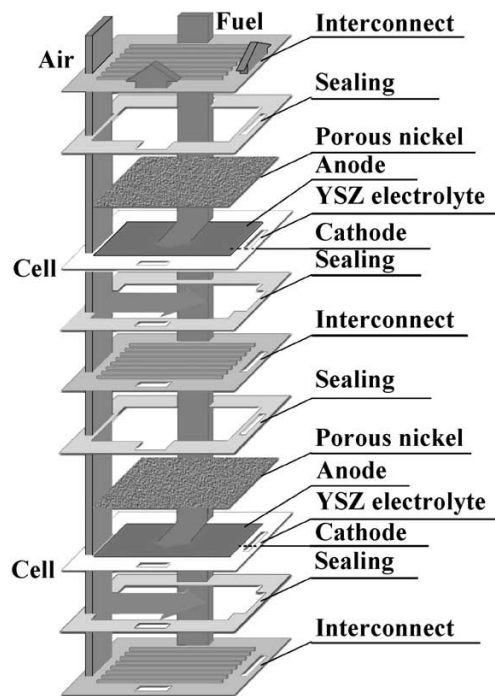


**Figure 1.3** Schematic diagram of a planar SOFC stack. A stack is a collection of individual cells combined with any peripheral requirements, such as sealants between cells as well as the air and fuel supply. [16]

### 1.3 SOFC Components

Each of the components used in a SOFC system has to fulfil a number of roles and as a result is required to possess a number of physical, chemical and performance criteria. In order to reduce the complexity of the description required, the following explanation is geared towards the planar SOFC geometry.

During the manufacture of SOFCs the electrolyte is deposited by tape casting with the electrodes then deposited onto the electrolyte. [19] Both the electrolyte and electrodes typically require very high temperature sintering stages of up to 1550°C. [19] As a result all components are required to withstand the thermal cycling and high temperatures under

which the cell operates and is manufactured. In relation to this the thermal expansion coefficient of materials used in the SOFC are required to be similar. A difference in the thermal expansion coefficient of the materials employed in the cell can lead to the various layers of the cell peeling apart and cracking as their relative size varies over the operational temperature range. [1] The materials employed in SOFC are required to be strong and tough. [1] As has been previously mentioned the tensile strength of zirconia is much lower than the compressive strength. As a result of this planar SOFCs are more susceptible to mechanical failure. It is possible to improve the mechanical strength of YSZ by using low doping levels of yttria (~3 mol%) to produce the tetragonal form with good mechanical strength, as opposed to the 8-10 mol% used to achieve higher ionic conductivity. [18]

### **1.3.1 Electrolyte**

The electrolyte separates the two electrodes and so as a result is required to encompass some properties not found in the electrodes. The electrolyte is required to be dense to prevent the fuel and oxygen source from mixing. An electrolyte also must have very good ionic conductivity to enable the swift and efficient transfer of ions between electrodes with as minimal cell impedance as possible. [20] At the same time as being a good ionic conductor the electrolyte needs to be an electronic insulator, to minimise leakage currents between the anode and cathode, which would reduce the cell efficiency. There are a large variety of materials that have been investigated for use as SOFC electrolytes. This area has been reviewed in depth by Fergus. [20]

A number of doped ceramics have been employed as electrolytes in SOFCs. Variation in the composition of the material can also lead to defects which are known as extrinsic defects. Extrinsic defects can be induced by doping a pure material with aliovalent impurities. These are impurity atoms that have a different valency to those naturally present in the lattice structure [21]. An example of this is the addition of  $Y_2O_3$  to a  $ZrO_2$  lattice to form YSZ. The natural Zr ion has a +4 formal charge associated with the atom whereas the yttria ions only have a +3 charge. As a result for every two yttria ions added to the lattice structure one  $O^{2-}$  vacancy must be created in order to maintain the charge balance. In the case of YSZ the vacancies created are regarded as the mobile species in

ionic conduction so the creation of these vacancies greatly increases the overall ionic conduction of the material. [21]

Yttria-stabilised zirconia (YSZ) is currently the most widely employed electrolyte material for SOFCs. [22] YSZ is a lattice of  $ZrO_2$  that is doped with typically 8%  $Y_2O_3$ , so the result is an increase in the number of  $O^{2-}$  vacancies in the material lattice.

The addition of a small amount of yttria to the zirconia lattice has the effect of stabilising the conductive cubic fluorite phase and increasing the number of  $O^{2-}$  vacancies in the lattice, increasing the ionic conductivity. [20] The conductivity of YSZ has been shown to increase with yttria content up to around 8 mole % yttria before dropping away at higher concentrations. [20] This has been attributed to the association of Schottky point defects. This results in the point defects becoming less mobile and as a result the conductivity decreases. [20] Other dopants have also been used with zirconia. Scandia in particular shows promising properties, outperforming the ionic conduction of YSZ in a number of studies. [20]

Ceria doped typically with either gadolinium (CGO) or samarium also forms the fluorite structure and has higher ionic conductivity, particularly at lower temperatures, as well as lower polarization resistance. [23] The ionic conduction of CGO has been shown to increase with increasing gadolinium up to 25%, before decreasing hereafter. This has resulted in ceria being used as a SOFC electrolyte material. CGO however has been shown to be electronically conductive. This is of particular concern at higher temperatures ( $>700^\circ C$ ) and low oxygen partial pressures. [20]

The final established SOFC electrolyte material is strontium and magnesium doped lanthanum gallate,  $La_{1-x}Sr_xGa_{1-y}Mg_yO_3$  (LGSM). LGSM has been shown to have similar conductivity to CGO over a range of temperatures and better conductivity than YSZ. LSGM is also not as electronically conductive as CGO at low oxygen partial pressures making it preferable in such conditions. LSGM has a perovskite structure which is the same as many cathode materials. Interdiffusion between the cathode and electrolyte has been shown. This has the eventual effect of degrading the properties of both components after operation. [20]

There are a number of materials that have been proposed to replace YSZ as an electrolyte material in SOFCs all of which have associated advantages and disadvantages. As with all components the performance of the electrolyte can only be assessed as part of a whole system, as interactions with the anode and cathode must be considered.

### 1.3.2 Anode

The anode is the fuel electrode. Anode material require a porosity of between 20 and 40% in order to facilitate the mass transport of both the reactant gas into, and the resultant product gases away from, the cell. [1] Anodic materials are also required to be stable in reducing conditions and to have high electronic conductivity. Currently anodic materials are typically made by impregnating the electrolyte material with NiO, which is then reduced to Ni metal before operation. This approach means that the thermal expansion of the resultant anode material is compatible with that of the electrolyte. [1]

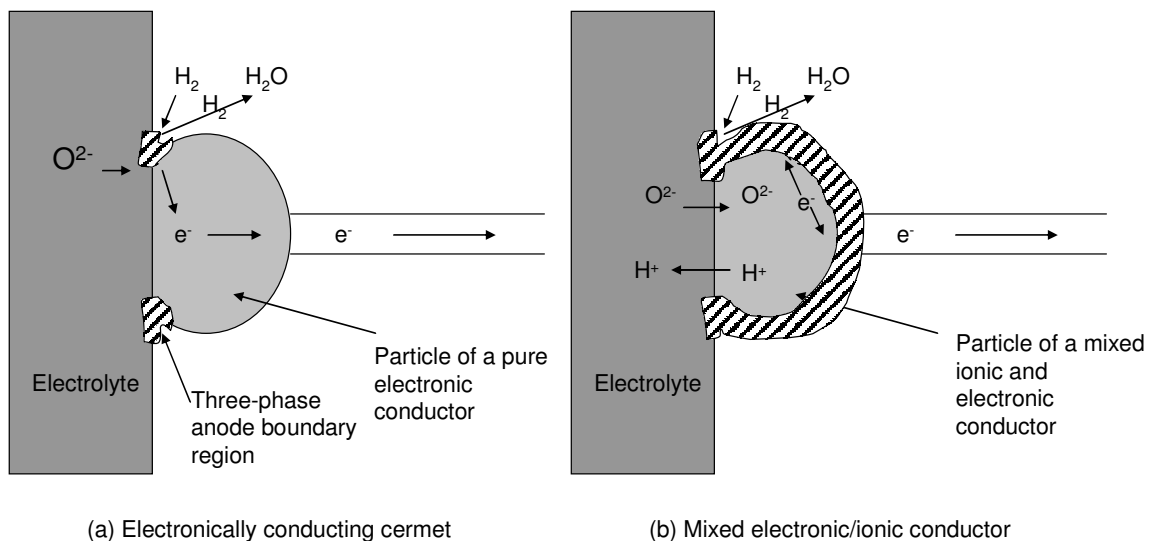


**Figure 1.4** An illustration of three-phase boundary regions in electronically and electronic/ionically conducting SOFC anode materials. [adapted from 2]

There has been a large amount of research into anode materials that enable the direct utilisation of methane in the cell. [19, 21, 22, 24-28,] The electrochemical reaction occurs at the TPB, which is the line at which the ionic conducting phase, electron conducting phase and gas phase all meet. [22] In systems where the electrodes are pure electronic

conductors (ie ionic insulators), the only sites where the fuel can be oxidised is where the electrolyte meets the catalytically active sections of the electrode. If the anode material is a mixed electronic and ionic conductor then ions can pass from the electrolyte through the electrode. This increases the extent of the TPB as shown in Figure 1.4 and hence the number of sites at which the fuel can be oxidised.

### 1.3.3 Cathode

As with the anode, the cathode has a porous structure to facilitate the rapid mass transport of reactant gases. [2] The most common cathode material is currently the p-type semiconductor, Strontium-doped lanthanum manganite  $(La_{1-x}Sr_x)MnO_{3-x/2}$  (LSM). A range of other materials may be employed. As with the anode, of particular interest are perovskite structures which are mixed oxide ion and electronic conductors. The mixed oxide ion and electronic conductors are of particular relevance for lower-temperature SOFCs as the polarization of the cathode increases significantly as the operating temperature is decreased. [2]

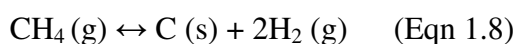
### 1.3.4 Interconnect Materials

The interconnect is the material which is used to connect neighbouring fuel cells. The interconnect can be metal though expensive 'inconel' type stainless steels are required for cells with operating temperatures of 800-1000°C. The thermal expansion coefficient of conventional steels differs from that of the YSZ electrolyte. As a result, a number of alloys such as Cr-5Fe-1Y<sub>2</sub>O<sub>3</sub> Siemens/Plansee alloy, which is an yttria based system doped with chromium and iron, have been developed. [2] However, these alloys have been shown to poison the cathode with chromium under cathodic operating conditions. This results in the rapid deactivation of the cathode. Metal interconnects can also form oxide coatings, on their surfaces which limit their electrical conductivity. [2]

Certain ceramic materials have been employed as interconnect materials, lanthanum chromite being the preferred option. [2] Magnesium or other alkaline earth metals can be used to substitute some of the lanthanum in order to improve the electronic conductivity of the material. [2]

## 1.4 Anode Development

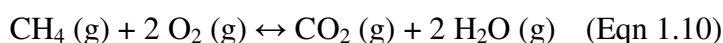
SOFCs based on a YSZ electrolyte have been shown to be highly efficient for use with hydrogen. [1, 29] Ni-based anodes have been developed for use in such SOFCs. However, the use of hydrocarbon fuel with these anodes is problematic as Ni is an excellent catalyst for the formation of graphite filaments in dry hydrocarbons at elevated temperatures. [6] Carbon formation is the result of either methane dissociation (Eqn 1.8) or the Boudouard reaction (Eqn 1.9): [24]

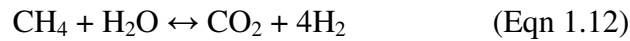
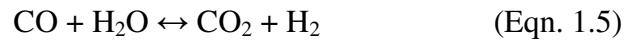
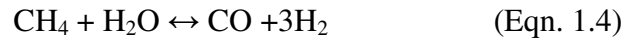


This carbon deposition can lead to the rapid and irreversible deactivation of such anodes. The carbon source is deposited onto the metal surface, dissolution of the carbon into the metal bulk before the carbon precipitates out as a fibre on the metal surface. [22] The formation of these carbon fibres on porous Ni cermets can lead to cermet fracture, as a result of the stresses exerted by the fibres. [22] As a result, hydrocarbons must be externally reformed, or steam added to the fuel mixture to reduce carbon deposition by internal reforming. In order to improve the efficiency of SOFC systems there has been research into improving the catalyst materials employed.

### 1.4.1 Operation of SOFCs Using Hydrocarbon Fuels

The internal reforming of hydrocarbons in the anode compartment is a complex system that involves a number of different reactions. For example the oxidation of methane ( $\text{CH}_4$ ) is often displayed as a total oxidation (Eqn 1.10). However as previously mentioned in Section 1.4, methane cracking (Eqn.1.8), the Boudouard reaction (Eqn.) and also the reduction of methane (Eqn 1.11) can all lead to the deposition of carbon on the catalyst. In order to reduce the extent of carbon deposition on the anode, steam is often added to the methane. This promotes the steam reforming of methane (Eqn. 1.4) and WGS reactions (Eqn. 1.5 and Eqn. 1.12)





Gorte and McIntosh, [22] stipulated that there are two possible approaches for using hydrocarbons within SOFC systems. The first was the use of conventional Ni-based anodes under closely controlled conditions under which carbon deposits do not form. The second approach was the use of new anode materials which do not catalyse carbon formation.

#### 1.4.2 SOFC with Ni-Based Anodes

Ni-YSZ cermet anodes are employed in the most developed SOFC systems, that is, the systems closest to commercialisation. [22] The Ni cermets are relatively easy to fabricate and have good electronic and catalytic activity thanks to the Ni. The YSZ component provides support which reduces sintering and provides ionic conductivity, allowing the  $\text{O}^{2-}$  ions to diffuse further into the anode. [22]

Methane is generally the only hydrocarbon that can be internally reformed by Ni based anodes. [22] Steam is added to the methane flow. A steam-methane ratio of greater than 2:1 is required. The addition of steam promotes the steam-reforming of the methane which reduces the extent of carbon deposition. [22] The addition of trace amounts (up to 1 vol %) of metal such as Co, Cu, and Ag were shown to reduce the formation of carbonaceous deposits observed on Ni-YSZ anodes. [24]

Higher hydrocarbon fuels require  $\text{H}_2\text{O}/\text{C}$  ratios much higher than that required for methane. [22] The steam reforming of methane is an endothermic process. As a result of this if methane is directly used in the cell then cold spots can form which can reduce the performance of parts of the anode. [22]

Murray et al [26] reported the optimal operating temperature of a SOFC operating using dry methane as the range 500-700°C. This was due to the fact that below this range carbon was deposited via Eqn. 1.8 and above this range via Eqn. 1.9.

In laboratory conditions a number of groups have been able to operate SOFCs with Ni based anodes that directly use methane as a fuel. However in such studies the cells have been closely monitored and tightly controlled. In a stack system such control would be difficult to maintain especially if the system were subjected to a variable load. [22]

### **1.4.3 Ceramic Anodes**

The problem of carbon deposition on Ni anodes arises owing to the characteristics that make it an effective anode material. Ni is one of the most efficient steam reforming catalysts and also one of the best catalysts for the formation of carbon. As a result it may be necessary to investigate materials which, while being good electronic conductors, are poor reforming catalysts. As a result, a number of metal oxides have been considered as anodes. They do not catalyse the formation of carbon and have high melting temperatures so are resistant to sintering. Some metal oxides exhibit mixed electronic and ionic conductivity, greatly increasing the TPB area. [18, 22]

Doped ceria, generally containing  $\text{Sm}_2\text{O}_3$  or  $\text{Gd}_2\text{O}_3$  (GDC), has been investigated for use as a SOFC anode material. Ceria has very high ionic conduction and significant electronic conductivity above  $600^\circ\text{C}$ . [30] It is possible to obtain higher electronic conductivities by using metal oxides which have the perovskite structure ( $\text{ABO}_3$ , where A and B are cations with a combined charge of +6). The perovskite structure is able to accommodate high dopant levels, which can be used to alter the structural stability, catalytic activity and the electronic and ionic conductivity of the material. [22] Many of the standard cathode materials, such as LSM, have a perovskite structure. [22] This has also led to research into the possibility of developing symmetrical cells, with Bastidas et al. showing that  $(\text{La}_{0.75}\text{Sr}_{0.25})\text{Cr}_{0.5}\text{Mn}_{0.5}\text{O}_3$  (LSCM) was an effective redox stable electrode in conditions applicable to both the anode and the cathode. [31] Such perovskite based anodes work particularly well with electrolytes of a similar structure such as Sr- and Mg-doped  $\text{LaGaO}_3$  (LSGM). [30]

## **1.5 Summary**

The high theoretical efficiency of fuel cell systems makes them a highly attractive option for the generation of electrical energy. The high operating temperature and relatively

simple nature of the SOFC system makes it an exciting technology especially when the waste heat produced can be utilised. Currently, most SOFC systems use H<sub>2</sub> as a fuel. This limits the operation of such systems due to the problems with the production, transportation and storage of clean H<sub>2</sub>. The direct use of hydrocarbons as a fuel source would reduce the complexity, and hence the cost of SOFC systems. The currently employed Ni based anodes are prone to carbon deposition which may lead to cracking of the anode when operated with hydrocarbon fuels. The development of new anode materials which have the required stability, compatibility with other cell components, catalytic activity and electronic conductivity is possibly the major materials problem to be addressed in SOFC development. [18]

## 1.6 References

- [1] A. Boudghene-Stambouli, E. Traversa, *Renewable and sustainable Energy Reviews*, 6, **2002**, 433
- [2] J. Larminie, A. Dicks, *Fuel Cell Systems Explained*, 2<sup>nd</sup> ed., Wiley
- [3] J. Hetland, G. Mulder, *International Journal of Hydrogen Energy*, 32, **2007**, 736
- [4] R.J. Gorte, S. Park, J.M. Vohs, C. Wang, *Advanced Materials*, 12, **2000**, 1465
- [5] K. Kordesch, J. Gsellmann, M. Cifrain, S. Voss, V. Hacker, R. R. Aronson, C. Fabjan, T. Hejze, J. Daniel-Ivad, *Journal of Power Sources*, 80, **1999**, 190
- [6] G.F. McLean, T. Niet, S. Prince-Richard, N. Djilali, *International Journal of Hydrogen Energy*, 27, **2002**, 507
- [7] G. Mulder, P. Coenen, A. Martens, J. Spaepen, *International Journal of Hydrogen Energy*, 33, **2008**, 3220
- [8] S. Lister, G. McLean, *Journal of Power Sources*, 130, **2004**, 61
- [9] B. Smitha, S. Sridhar, A.A. Khan, *Journal of Membrane Science*, 259, **2005**, 10
- [10] K. Sopian, W.R.W. Daud, *Renewable Energy*, 31, **2006**, 719
- [11] N.W. Deluca, Y.A. Elabd, *Journal of Polymer Science: Part B: Polymer Physics*, 44, **2006**, 2201
- [12] N. Sammes, R. Bove, K. Stahl, *Current Opinion in Solid State and Materials Science*, 8, **2004**, 372
- [13] J.C. Yang, Y.S. Park, S.H. Seo, H.J. Lee, J.S. Noh, *Journal of Power Sources*, 106, **2002**, 68

- [14] P. Tomczyk, *Journal of Power Sources*, 160, **2006**, 858
- [15] J.P.P. Huijsmans, G.J. Kraaij, R.C. Makkus, G. Rietveld, E.F. Sitters, H.Th.J. Reijers, *Journal of Power Sources*, 86, **2000**, 117
- [16] T.-L. Wen, D. Wang, H.Y. Tu, M. Chen, Z. Lu, Z. Zhang, H. Nie, W. Huang, *Solid State Ionics*, 152, **2002**, 399
- [17] C. Haynes, *Journal of Power Sources*, 109, **2002**, 365
- [18] J. T. S. Irvine, A. Sauvet, *Fuel cells*, 3-4, **2001**, 205
- [19] S. Park, R.J. Gorte, J.M. Vohs, *Journal of the Electrochemical Society*, 148 (5), **2001**, A445
- [20] J.W. Fergus, *Journal of Power Sources*, 162, **2006**, 30
- [21] A. R. West, *Basic Solid State Chemistry*, 2<sup>nd</sup> ed, Wiley
- [22] S. McIntosh, R. J. Gorte, *Chem. Rev.*, 104, **2004**, 4845.
- [23] B. Dalslet, P. Blennow, P.V. Hendriksen, N. Bonanos, D. Lybye, M. Mogensen, *J. Solid State Electrochem.*, 10, **2006**, 548
- [24] J. Maček, B. Novosel, M. Marinšek, *Journal of the European Ceramic Society*, 27, **2007**, 487
- [25] M. Mogensen, S. Skaarup, *Solid State Ionics*, 86-88, **1996**, 1151
- [26] E.P. Murray, T. Tsai, S.A. Barnett, *Nature*, 400, **1999**, 649
- [27] R.J. Gorte, J.M. Vohs, S. McIntosh, *Solid State Ionics*, 175, **2004**, 1
- [28] S. Park, R.J. Gorte, J.M. Vohs, *Applied Catalysis A: General*, 200, **2000**, 55
- [29] Cracium R., Park S., Gorte R.J., Vohs J.M., Wang C., Worrell W.L., *Journal of The Electrochemical Society*, 146, **1999**, 4019
- [30] S. Tao, J.T.S. Irvine, J.A. Kilner, *Adv. Mater.*, 17, **2005**, 1734
- [31] D.M. Bastidas, S. Tao, J.T.S. Irvine, *J. Mater. Chem.*, 16, **2006**, 1603

**Chapter 2. Temperature  
Programmed Studies and  
Catalysis Background**

## **2.1 Introduction**

This chapter provides a background to the catalytic studies presented in this thesis. The majority of the results presented in this thesis were obtained using temperature programmed methods. This chapter introduces the range of temperature programmed techniques outlining the data obtained from each type of experiment as well as the advantages and limitations of each technique. There is also a brief summary of the theory behind the other experimental techniques employed as part of this thesis. The literature is reviewed in order to provide a background to materials which have previously been studied for use as SOFC anode materials. As the materials investigated during this study were copper impregnated Ce/Zr mixed oxides the literature was investigated for research on any similar materials that has been conducted previously.

## **2.2 Temperature Programmed Techniques**

### **2.2.1 Introduction**

Temperature programmed (TP) techniques were pioneered by Amenomiya and Cvetanovic [1], who applied Temperature Programmed Desorption (TPD) experiments to the study of catalysts. Schwartz and Falconer [2] published a review of transient techniques to investigate methanation on supported nickel catalysts outlining the use of the other main TP techniques, TP reaction (TPRx), TP surface reaction (TPSR), TP reduction (TPR(d)) and TP oxidation (TPO).

During this study, all the TP techniques employed used the same reactor and detector set-up which will be described fully in Chapter 3. The gases employed and the procedures undertaken did vary between experiments and these are described in Chapter 3.

### **2.2.2 Temperature Programmed Desorption (TPD)**

#### **2.2.2.1 Experimental Procedure**

TPD is the simplest of the TP techniques. A small sample typically of 10-200 mg, is situated in a reactor that is to be heated by a furnace. An inert gas such as He, Ar or N<sub>2</sub> is then passed over the catalyst bed and the sample is heated in a linear fashion with time. Species will desorb from the sample as it is heated and can be detected downstream, by a

quadrupole mass spectrometer (QMS), gas chromatography or a thermal conductivity detector (TCD). [3]

Amenomiya and Cvetanovic [1] identified six separate steps, involved in a TPD: (1) pre-treatment of the catalyst, (2) preadsorption of the adsorbate, where the adsorbate is the probe molecule which is deposited onto the sample surface and subsequently desorbed. (3) Evacuation of the apparatus after the adsorption to remove the physically adsorbed gas; that is the gas which is very weakly attached to the sample due to induced dipole (van de Waals) interactions. (4) Programmed desorption of the residual chemisorbed gas into the stream of a carrier gas. This is an inert gas (typically He or Ar) continuously passed over the sample in order to remove any species released from the sample. The chemisorbed gas is the part of the adsorbate which is strongly bound to the sample. Generally this will be by ionic or covalent bonding. (5) Detection of the desorbed gas in the carrier and (6) trapping and analysis of the desorbed gas to establish its identity.

#### **2.2.2.2 Theory**

The theory behind TPD, as well as methods for extracting adsorption parameters and the applications of TPD have been extensively studied. [1-12] TPD experiments provide information about the strength of interaction of species with the surface of the solid sample or catalyst being investigated. [5] The desorption spectrum is a record of concentration of observed species against time over the duration of the experiment. [8] As the catalyst is heated during a TPD experiment, adsorbed gases desorb and are then carried away by the carrier gas. In simple theoretical treatments, the temperature of the gas and sample in the system are assumed to be equivalent at all times independent of bed position. [11] The rate of desorption increases with temperature, initially at an exponential rate as shown in Figure 2.1. The continuous desorption of the adsorbed species results in the surface sites becoming depleted. As a result, the rate of increase of desorption slows and the rate of desorption reaches a maximum or peak, before dropping back down to zero, if the sample is heated to a sufficiently high temperature to remove all the adsorbed gas. [3]

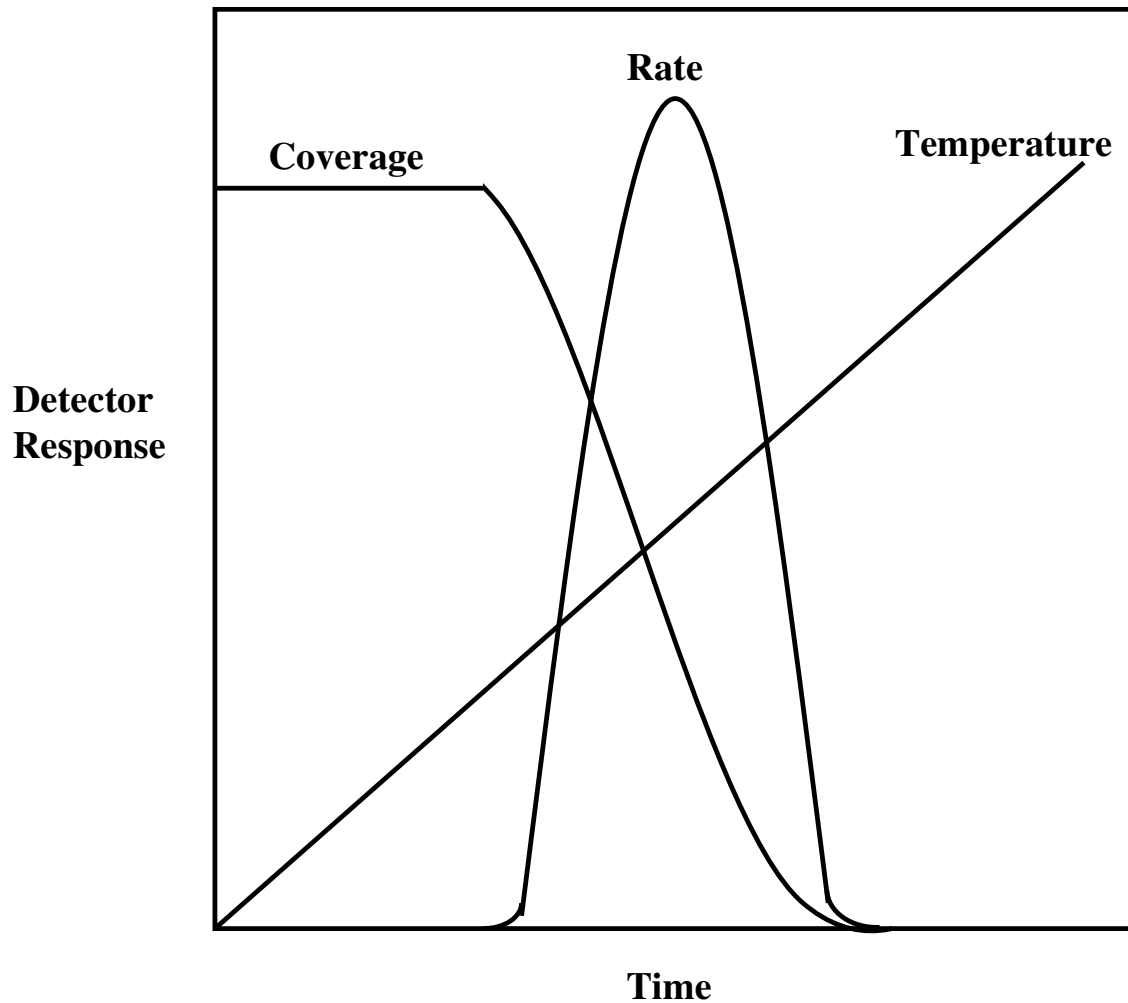


**Figure 2.1** Dependence of surface coverage, desorption rate and temperature on time during a TPD experiment (adapted from [3]).

Linear heating rates are invariably used in TPD experiments. The complexity of the system involved during TPD experiments means that for mathematical simplicity it is necessary to use simplified models, which can be expected to approach experimental results under appropriate conditions. [8] If a linear heating rate is therefore applied to a system where first-order desorption is predicted then the material balance of a presorbed probe molecule on a solid adsorbent which is subsequently subjected to TPD into a carrier gas is given by:

$$-v_m \frac{\partial \theta}{\partial t} = v_m k_d \theta - k_a C(1 - \theta) \quad (\text{Eqn 2.1})$$

and

$$FC = V_s v_m k_d \theta - V_s k_a C(1-\theta) \quad (\text{Eqn 2.2})$$

In these expressions,  $v_m$  is the amount of the probe molecule adsorbed per unit volume of the solid phase. The surface coverage is shown by  $\theta$ ,  $k_d$  is the rate constant of desorption,  $k_a$  is the rate constant of adsorption,  $C$  is the concentration of the probe molecule in the carrier gas,  $F$  is the carrier gas flow rate and  $V_s$  is the volume of the solid phase. [8] With all of these values measured in standard S.I. units. If it is assumed that there is negligible re-adsorption of the probe molecule then the coverage of the sample can be shown by:

$$\frac{d\theta}{dT} = -\frac{\theta A}{\beta} \exp(-E_d / RT) \quad (\text{Eqn 2.3})$$

Where  $\beta$  is the heating rate. The shapes of the peaks obtained from TPD experiments from a homogeneous surface with negligible readsorption will depend on the ratio of  $E_d/T_m$  where  $E_d$  is the activation energy of desorption and  $T_m$  is the observed temperature of the peak maximum. If the observed results differ drastically from the predicted results it can be assumed that the desorption process is more complex or that there is significant diffusion in the carrier gas stream which leads to peak broadening. [8] However if there is significant readsorption then the following expression applies for  $K_M$ :

$$K_M = \frac{\beta V_a}{F} (1-\theta_M)^2 \frac{\Delta H}{RT_M^2} \quad (\text{Eqn 2.4})$$

This is true where  $K=k_d/k_a$  is the equilibrium constant of desorption,  $\Delta H$  is the heat of desorption and subscript  $M$  is used to denote quantities at the peak maximum.

The shape and position of the desorption features in the TPD spectrum can be affected by diffusional resistances, readsorption, [5, 11] and flow rates of the carrier gas as well as desorption kinetics, making interpretation complex. Hertz et al. [5] simulated the effect of readsorption at low flow rates, using a carrier gas and also at high flow rates which involved desorption into a vacuum. They found that when using the carrier gas the accumulation of the gaseous probe molecule (CO) led to extensive readsorption within the sample markedly increasing the temperature of the desorption peak. With the high flow rate (vacuum) system, it was gaseous CO accumulated in the sample as a result of

diffusional limitations that controlled the rate of desorption. [5] The conclusions that were drawn from the results of Hertz et al [5] was that adsorption effects are unavoidable during any form of TPD experiment and that indeed at many points in the experiment adsorption and desorption compete to the extent that the adsorption equilibrium was approached. Rieck and Bell [11] investigated how the rate of carrier gas flow affected the results obtained by TPD experiments by desorbing CO from catalyst beds with different particle sizes (diameter varied from 0.04 cm to 0.20 cm). They showed that increasing the flow rate of the carrier gas (flow rates varied from 0.1 to 5.0 cm<sup>3</sup>s<sup>-1</sup>) during a TPD resulted in the spectrum having sharper desorption peaks at lower temperatures. They surmised that by increasing the carrier gas flow rate readsorption of the probe molecule further down the catalyst bed was reduced. As a result the probe molecules were released from the catalyst bed at lower, more consistent temperatures (hence the sharper peaks).

Most real catalyst systems are energetically heterogeneous and display a complex TPD spectrum containing multiple peaks and shoulders. [7] These spectra are the result of samples containing a number of different sites to which the probe molecule can bind, each of which may have a different binding energy for the probe molecule. The more tightly bound the probe molecule is to the site the higher the temperature that will be required to displace it. The shapes and positions of the peaks are related in a fundamental way to the desorption process, providing information on the manner in which the gas is adsorbed. [8] The area of each peak can be calibrated by using a gas flow of known composition in order to determine the abundance of adsorbed species present.

### **2.2.3 Temperature Programmed Reduction (TPR)**

TPR experiments only differ from TPD with regard to the gas employed in the system. TPRs employ a reducing gas such as H<sub>2</sub> or CO, generally in a flow of the carrier gas; 5% H<sub>2</sub>/Ar was employed in this study. The remainder of the experiment is conducted as per the TPD. The sample is heated in a linear fashion and the products monitored by the detector downstream of the reactor. Samples studied in TPR experiments are typically pre-treated to ensure they are in their oxidised form. As the sample is heated the oxygen present in the sample will react with the reducing gas (such as H<sub>2</sub> or CO) to release an oxidised product (H<sub>2</sub>O or CO<sub>2</sub>). The surface sites and the material bulk may both be reduced during a TPR experiment. Thus the TPR spectrum may be sensitive to the sample preparation route

employed. [13] Typical TPR spectra contain multiple peaks. The temperature of each relates to the accessibility and ease of reduction of the site. If calibrated, as described previously in relation to TPDs, the amount of oxygen evolved by the sample can be calculated, providing data on the reducibility of the sample as well as its oxygen storage capacity (OSC).

#### **2.2.4 Temperature Programmed Reaction (TPRx)**

TPRx experiments are used to study the interaction of a reactive gas, for example, CH<sub>4</sub>, with a catalyst. A wide range of gases can be employed for TPRx experiments. As the experiments undertaken as part of this thesis made use of CH<sub>4</sub> that is the reactant which will be focused on. The reaction of CH<sub>4</sub> is likely to take place in a number of different ways. The first of these is the partial oxidation of CH<sub>4</sub> to CO, H<sub>2</sub> and H<sub>2</sub>O which may then lead to the total oxidation of CH<sub>4</sub> to CO<sub>2</sub> and H<sub>2</sub>O, both these reactions are ascribed to the CH<sub>4</sub> reacting with surface oxygen from the sample. The second reaction pathway is methane dissociation. Here, methane may form monatomic H and unsaturated carbon species which are commonly deposited on the oxide. [14] The final anticipated pathway for CH<sub>4</sub> consumption is the Water Gas Shift (WGS) reaction this is where CO, reacts with water to form CO<sub>2</sub> and H<sub>2</sub>.

#### **2.2.5 Temperature Programmed Oxidation (TPO)**

In order to determine the nature and extent of any carbon deposition, samples can be oxidised in a TPO experiment. A gas containing O<sub>2</sub> is passed over the sample as it is heated. This oxidises any carbon species deposited on the catalyst during the TPRx. The number of surface states of carbon is revealed by the number of peaks present in the TPO. [14] The area of the carbon peaks evolved reveals the amount of carbon deposited in each type of surface state.

### **2.3 Experimental Considerations**

There are a number of factors that must be considered, to ensure the accuracy of results obtained in TP experiments. [3] Adsorbents that are desorbed from the sample may be

adsorbed further down the catalyst bed or within the TP apparatus. This can result in broadening of the peaks obtained as well as a shift in peak position to higher temperatures.

A large sample is likely to cause a temperature gradient in the catalyst bed. This is particularly an issue for thermally insulating samples. Such a gradient would result in reactions taking place at different times across the catalyst bed, leading to broad, poorly resolved peaks. A low gas flow rate, or a large system volume downstream of the catalyst bed can result in a discrepancy between the sample temperature and the detection of the signal corresponding to that temperature. A low flow rate increases the extent to which desorbed species are readsorbed on the catalyst bed. [11] A large system volume downstream of the reactor, means that the desorbed gas has further to travel to the detector. This leads to a time lag between desorption and detection increasing the observed desorption temperature.

These effects can be minimised by using a sufficiently high gas flow rate, minimising the system volume downstream of the reactor, using a small mass of sample and heating the apparatus downstream of the reactor to prevent the re-adsorption of species after they have been desorbed from the catalyst sample.

There are a variety of detectors that are employed as part of a TP system such as a QMS, Gas Chromatograph (GC) and Thermal Conductivity Detector (TCD).

## **2.4 Light-off Experiments**

In light-off curves the conversion of a reaction is plotted against temperature. [15] There are a range of approaches that can be used to generate such curves. A series of isothermal, steady state experiments can be conducted at a number of temperatures and conversion plotted against temperature. Alternatively, as in this work, the temperature can be ramped at a constant rate and reactant and product concentrations measured continuously. This allows for quick measurement, especially if the detector is situated in-line. Conversion plots are generally S-shaped with an initial exponential conversion before the amount of reactant present becomes a limiting factor. The light-off temperature is the temperature at which a pre-determined proportion of reactants are converted to products. There does not appear to be a universally applied point at which the light-off temperature is taken. Values used range from 10-90% conversion. Light-off plots allow a relatively quick and easy

technique to investigate catalytic activity for a range of different reactant mixtures or to allow the comparison of a range of different catalysts for use in the same reaction.

## 2.5 Theory of Scanning Electron Microscopy (SEM) and Energy-dispersive X-ray Spectroscopy (EDX)

The typical set up of an SEM system is shown in Figure 2.2. Electrons are energised by a filament, typically tungsten. The electrons are then accelerated by an electrostatic field from the electron gun down the column of the microscope. The incident (electron) beam passes through a series of lenses, the first of which are condenser lenses which adjust the sample brightness. The objective (final) lens is used to set the sample magnification. The electron beam interacts with the sample leading to the production of a number of signals such as secondary electrons, back-scattered electrons and characteristic X-rays. These signals can then be used to define amongst other things the surface topography and composition. The SEM detects secondary electrons. These secondary electrons have very low energy approximately 50eV. As a result those that reach the detector are from the surface of the sample typically up to a depth of a few nm. The secondary electrons are then collected and the signal amplified in order to generate an image representative of the area being investigated. [16]

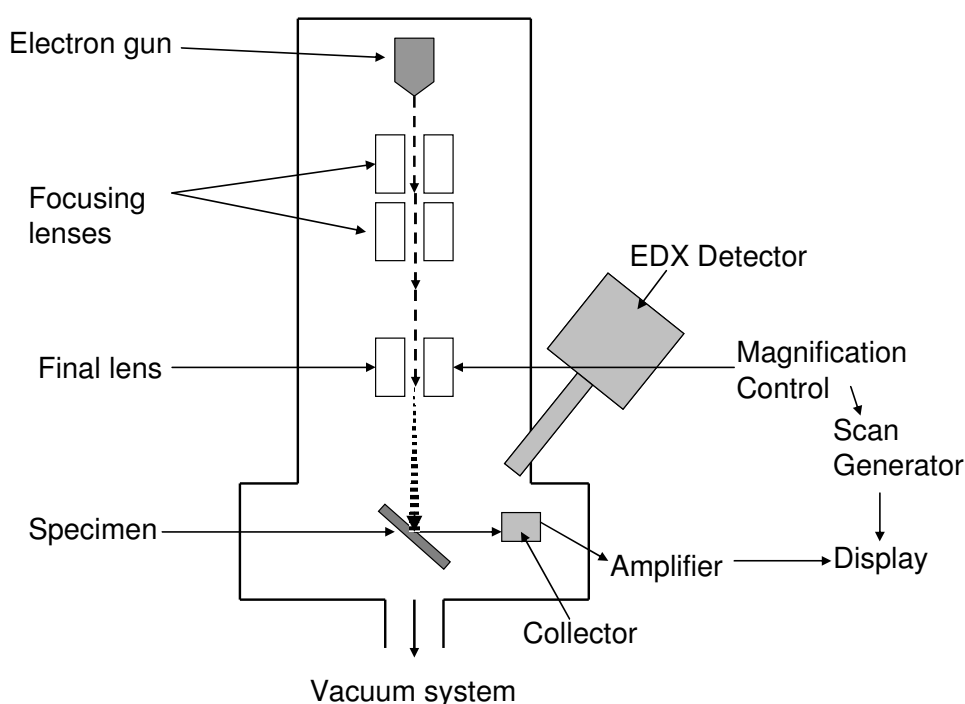


**Figure 2.2** A block diagram of a typical SEM system.

Energy-dispersive X-ray Spectroscopy (EDX) is an elemental analysis or chemical characterisation technique. EDX involves the analysis of the x-rays emitted by a sample in response to it being struck by the charged particles of the electron beam. As each element has a unique distribution of electronic energy levels, the x-rays are characteristic of the element's electronic structure, allowing elemental identification. The incident beam may excite an electron from one of the discrete inner shells. This electron is then ejected from the sample and leaves behind an electron hole. An electron from a higher energy outer shell then fills the electron hole, with the difference in energy between the higher and lower energy shells released as a x-ray. This x-ray can then be detected by an energy dispersive spectrometer, which can identify the characteristic x-ray and so identify the elements present.

## 2.6 XRD Theory

X-ray diffraction provides an overall, average picture of the structure of a material. It cannot usually detect any localised defects or define the position of small quantities of dopants. [17]

The X-rays are generated by the electrical heating of a filament, which is generally tungsten. The filament emits electrons which are accelerated by a high potential difference (20-50 kV). These electrons then bombard the anode, causing the anode to generate a spectrum of 'white' X-radiation. [17]

W.H. and W.L. Bragg, conducted experiments with the intention of using X-ray crystal diffraction as a technique to determine crystal structure. The first structure that they determined in this way was that of NaCl in 1913. [17] The X-ray diffraction is similar to a 'reflection' from the planes of atoms present in a structure. Figure 2.3 shows the conditions assigned by Bragg for X-rays to be reflected by a crystal. The black spots on the diagram show a section through the crystal with the parallel Miller indices  $hkl$  with interplaner spacing of  $d_{hkl}$  are represented by the black lines. The X-rays are shown by the green lines are incident to the planes at the angle  $\theta_{hkl}$ . The X-rays are scattered by atoms in the lattice but in order for them to form a beam of reasonable intensity which can be detected, they must arrive in phase or reinforce one another. The Bragg equation (Eqn 2.5) relates the

spacing between crystal planes to the  $\theta$  angles at which the reflections from these planes are observed

$$n\lambda = 2d_{hkl}\sin\theta_{hkl} \quad (\text{Eqn 2.5})$$

Where  $n$  is an integral number of wavelengths and  $\lambda$  is the wavelength of the X-rays.

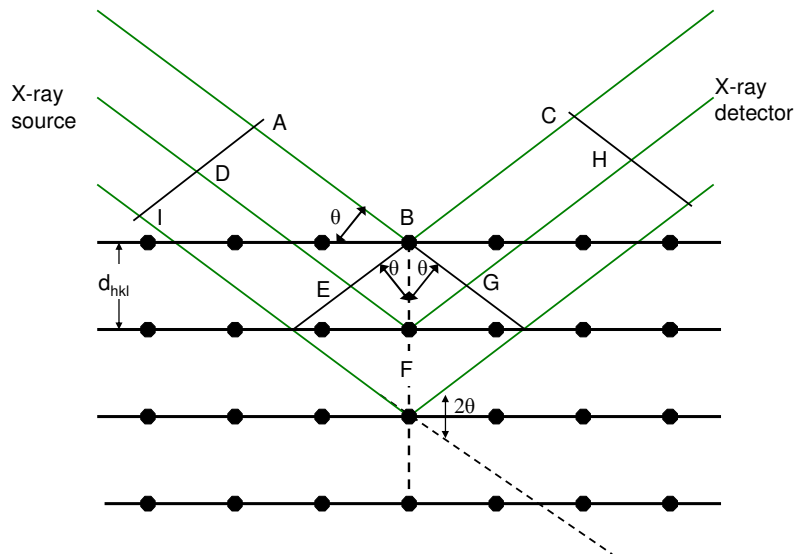


**Figure 2.3** Bragg reflections that result from a set of crystal planes with the spacing  $d_{hkl}$ . (adapted from [17])

## 2.7 Ceria-Zirconia Mixed Oxides

### 2.7.1 Introduction

Materials containing  $\text{CeO}_2$  and  $\text{ZrO}_2$  have been investigated extensively for a range of applications, primarily as automotive Three-Way Catalysts (TWCs) [18-29]. TWCs are used to convert CO, hydrocarbons (HC) and  $\text{NO}_x$  from vehicle exhaust into  $\text{CO}_2$ ,  $\text{H}_2\text{O}$  and  $\text{N}_2$ , respectively. The increasingly strict vehicle emissions legislation in both Europe and America has led to extensive investment and development of these materials. Extreme efficiency and durability are required of the current generation of TWCs. [18]

The structural properties and phase diagram of the  $\text{CeO}_2$ - $\text{ZrO}_2$  system are still a matter of investigation. [30] Zirconia has three polymorphic phases: monoclinic ( $T < 1170^\circ\text{C}$ ), tetragonal ( $1170 < T < 2370^\circ\text{C}$ ) and cubic ( $T > 2370^\circ\text{C}$ ). [31] It is also possible to obtain both

the tetragonal and cubic phases at room temperature with the addition of dopant oxides in sufficient levels. [31] Fuentes and Baker have recently reported on the phase of Ce-Zr oxides of the composition included in this thesis. [32] Using Rietveld refinements the oxides containing 10, 25, 50 and 75 mol % CeO<sub>2</sub> displayed a tetragonal structure (P4<sub>2</sub>/nmc space group). Increasing the ceria concentration up to 90 mol % led to the formation of a cubic structure (Fm3m space group). [32]

The introduction of the smaller Zr<sup>4+</sup> cation (ionic radius 0.84 Å) into the CeO<sub>2</sub> lattice (ionic radius 0.97 Å), enhances the efficiency of the Ce<sup>4+</sup> -Ce<sup>3+</sup> redox couple. This is due to the formation of defects throughout the material which increase the oxygen mobility and diffusion through the lattice. [33] The ‘best’ structure and composition of the Ce<sub>x</sub>Zr<sub>1-x</sub>O<sub>2</sub> for TWC applications would ideally have the lowest reduction temperature, the highest rate of oxygen transfer and the highest degree of reducibility as well as being thermally and chemically stable. [18]

The redox behaviour and stability of a range of CeO<sub>2</sub>-ZrO<sub>2</sub> compositions have been shown to be affected by a large range of factors such as structure, [19] texture, [18] phase homogeneity [34] and sample pre-treatment. Sun and Sermon [34] showed that the textural stability of a material could be enhanced by increasing the phase purity.

The best-performing CeO<sub>2</sub>-ZrO<sub>2</sub> composition, in terms of redox behaviour and thermal stability has varied widely between studies, with CeO<sub>2</sub> rich, ZrO<sub>2</sub> rich and 50:50 compositions all being reported as showing the best activity and/or stability. [25, 35, 36] This is not surprising, however, since a wide range of compositions, preparation routes and methods of analysis have been employed. Therefore, there does not appear to be a single composition which will provide the best results across the board.

### **2.7.2 Three-Way Catalysis (TWC)**

The emissions permitted for passenger vehicles in Europe were reduced to 1g of CO/km in 2005 with US Tier 2 legislation also requiring durability up to 180,000km. [37] As a result of these increasingly strict emissions regulations there has been constant research into improving the efficiency and durability of TWCs. Ceria is a well established component in three way auto-motive catalysts, generally being present as a promoter, alongside a

precious metal active phase and an alumina support. [38] Pure ceria has been replaced in most systems by Ce-Zr mixed oxides which have been shown to have greater stability under high temperature operating conditions. [38] This prevents the loss of oxygen storage capacity (OSC), increasing the life time of the catalytic system. [38] The OSC of the material is its ability to absorb and release oxygen under fuel-lean and fuel-rich conditions, respectively. [37]

The contribution that Ce-Zr mixed oxides of varying composition would make to the activity of TWCs was investigated by González-Velasco et al. [29] They observed the general trend of increasing activity for CO and C<sub>3</sub>H<sub>6</sub> oxidation with increasing cerium content. Highest activity in this study was observed for the 80/20 (Ce-Zr) oxide. [29] Below 1023°C González-Velasco et al. concluded that both CO and C<sub>3</sub>H<sub>6</sub> reacted mainly with oxygen from the lattice. [29] Above 1023°C the WGS reaction and hydrocarbon reforming were felt to have a large contribution to the activity of the system.

Zhao et al. [26] investigated how the surface area of Ce<sub>0.67</sub>Zr<sub>0.33</sub>O<sub>2</sub> samples prepared by a citric sol-gel method affected the OSC of the material. Four samples of varying surface areas (between 56 m<sup>2</sup> g<sup>-1</sup> and 9 m<sup>2</sup> g<sup>-1</sup>) were prepared by either redox cycling (reduced at 800°C in 5% H<sub>2</sub>/N<sub>2</sub> then re-oxidised in air at 500°C) or exposing the material to a flow of steam and air at 800°C. These treatments also had the affect of increasing the crystallite size within the Ce-Zr samples (from 73Å to a maximum of 133Å). The Dynamic Oxygen Storage Capacity (DOSC) generally increased with the surface area of the samples, when investigated using CO oxidation. [26]

The reduction of lead and sulphur levels in gasoline has led to a shift in the active phase metals employed for TWCs. There has been complete or partial substitution of Pt by Pd in the traditional Pt/Rh catalyst systems. [39] As a result, Pt/Rh, Pt/Pd/Rh, Pd/Rh and Pd-only systems are commercialised. [23]

### **2.7.3 Preferential CO Oxidation in Excess Hydrogen**

The preferential oxidation of CO (CO-PROX) is a reaction that has received a great deal of interest. PEMFCs operate using CO-free hydrogen as the Pt catalysts that are employed in the electrodes are poisoned by CO levels of 10-100ppm. An efficient catalyst would

therefore enable the use of syngas (synthesis gas a mixture of CO and H<sub>2</sub>) with PEMFCs. A number of precious metal based catalysts have been employed for the selective oxidation of CO, such as metal oxide supported Au catalysts [40] and alumina supported Pt-group metal catalysts. [41] CuO/CeO<sub>2</sub> systems are regularly employed in this role owing to their high selectivity and activity for CO oxidation [42-44] The Cu based systems have been shown to be more active and much more selective than Pt based catalysts and while being less active than Au catalysts they are much more selective. [43]

Caputo et al., [24] employed a 4 wt% CuO/CeO<sub>2</sub> sample produced using wet impregnation of ceria. This proved to be a highly effective catalyst for the preferential oxidation of CO in a flow of 0.5 vol% CO, 0.5 vol % O<sub>2</sub> and 50% H<sub>2</sub> with the balance N<sub>2</sub>, at low temperature (70-110°C). However the conversion of H<sub>2</sub> increased with increasing temperature faster than the rate of CO conversion, up to the point where it consumed all the available oxygen and this became rate limiting for CO conversion. [42] Manzoli et al. reported similar observations during PROX reactions (CO 1%, O<sub>2</sub> 1%, H<sub>2</sub> 0-50%, balance He) using Cu/CeO<sub>2</sub> catalysts (prepared by incipient impregnation of copper nitrate). [44] There was initially significant conversion of CO to CO<sub>2</sub> up to 130°C, above this temperature the CO<sub>2</sub> levels began to decline as H<sub>2</sub> was converted to water. All oxygen present was consumed at around 170°C. Above this temperature the CO levels increased as the H<sub>2</sub> was preferentially oxidised. [44]

Zheng et al. [45] employed H<sub>2</sub>-TPR to determine the states of CuO and CeO<sub>2</sub> present in a CuO/CeO<sub>2</sub> system. The TPR pattern they reported, for 6.30 wt % CuO/CeO<sub>2</sub> displayed four peaks, two high intensity peaks at 160 (I) and 210°C (II) and two broad peaks of lower intensity at 400-500 (III) and 700-900°C (IV). Peak I was attributed to finely dispersed CuO which strongly interacted with the CeO<sub>2</sub>, with II resulting from bulk CuO. The higher temperature peaks observed by Zheng et al. closely correspond to those for pure CeO<sub>2</sub>, with peak III being attributed to H<sub>2</sub> reaction with surface capping oxygen and peak IV being the reaction of H<sub>2</sub> with oxygen from the bulk. [31, 37, 39] Chen et al. compared a selection of CuO impregnated (1-10 wt % Cu, incipient impregnation) Ce<sub>0.9</sub>Zr<sub>0.1</sub>O<sub>2</sub> oxides. [43] They reported low temperature peaks at around 137°C for all CuO loadings, with the intensity of these peaks increasing with copper loading. This represented a promotion in the reduction in CuO as pure CuO was reduced at 340°C. [43]

## 2.7.4 Direct Oxidation of Hydrocarbons Leading to SOFC Anode Development

As was discussed in Section 1.4, the current Ni based anodes prevent the direct use of hydrocarbon fuels as they catalyse carbon deposition which leads anode deactivation and ultimately cell failure. [46-51]

The extensive research that has been done into  $\text{CeO}_2$ ,  $\text{ZrO}_2$  and  $\text{Ce}_x\text{Zr}_{1-x}\text{O}_2$  mixed oxide systems has shown these materials to be thermally and chemically very stable as well as being catalytically active. [52-54] The high activity of the system with regard to the oxidation of hydrocarbons (HCs), has resulted in a number of researchers investigating the system for the combustion of HCs. [33, 46-64]

In order to improve the catalytic activity and electronic conductivity of the anode a metallic active phase is added. Copper provides good electronic conductivity for the anode while being relatively inert with regard to carbon deposition reactions. [50] Qu et al. [60] investigated two  $\text{ZrO}_2$ -supported copper (5 wt% wet impregnation) based catalysts. They found that the temperature at which the catalysts were reduced (during TPR experiments), and the activity of the catalyst for the oxidation of methane primarily depended on the phase composition and physiochemical properties of the support. [60] One of the  $\text{ZrO}_2$  supports contained homogeneous, spherical particles with an average particle size about 10 nm, with a large Specific Surface Area (SSA) of  $54.36 \text{ m}^2 \text{ g}^{-1}$ . The second  $\text{ZrO}_2$  support had larger irregular particles and a much smaller SSA of only  $2.22 \text{ m}^2 \text{ g}^{-1}$ . The high surface area sample was shown to be more active for the oxidation of methane. The high surface area catalyst converted 50% of the methane present in a 1:2 ratio mixture of methane and oxygen by  $404^\circ\text{C}$ , this was  $90^\circ\text{C}$  lower than the temperature at which the low surface area catalyst achieved 50% methane conversion. [60] The TPR of the high surface area catalyst displayed a shoulder and two peaks at 180, 188 and  $258^\circ\text{C}$  respectively. These reduction peaks were assigned to the reduction of small CuO particles, isolated copper ions and copper clusters, and the bulk copper oxide respectively. The TPR observed for the lower surface area catalyst displayed a broad peak with a maximum at  $311^\circ\text{C}$  and also a small peak at  $240^\circ\text{C}$ . These peaks were assigned to the reduction of the bulk copper oxide and copper clusters respectively. [54] The increase in the reducibility of the high SSA catalyst was thought to be due to superior dispersal of copper through the sample. [60] Dongare et al. prepared a range of CuO- $\text{ZrO}_2$  samples with CuO loadings of up to 33 mol% using sol-

gel synthesis. [65] They reported incorporation of copper into the  $\text{ZrO}_2$  lattice at concentrations up to 5 mol%. Above 5 mol%, around half the copper loading was incorporated into the  $\text{ZrO}_2$  lattice with the remainder remaining as extra lattice copper. [65] Catalysts prepared using this technique were found to be superior to either  $\text{CuO}$ ,  $\text{ZrO}_2$  or  $\text{CuO}$  supported on  $\text{ZrO}_2$  for the oxidation of methane. [65]

Relatively large amounts (21 at %) of copper have been shown to substitute into the fluorite  $\text{CeO}_2$  lattice. This effect however, depends largely on the preparation technique used. Fuerte et al [50] showed substitution into the lattice for materials prepared by microemulsion coprecipitation but no incorporation of copper into the ceria lattice for materials of the same composition prepared using a freeze-drying technique. [50] The incorporation of copper into the  $\text{CeO}_2$  lattice would be expected to lead to a large decrease in the lattice parameter, as the ionic radius of  $\text{Cu}^{2+}$  (0.73 Å) is much smaller than that of  $\text{Ce}^{4+}$  (0.97 Å). However the substitution of  $\text{Ce}^{4+}$  with  $\text{Cu}^{2+}$  increased the number of oxygen vacancies leading to only a small decrease in the lattice parameter. [50]

There has been a large amount of research in a range of  $\text{CeO}_2$  and  $\text{Ce}_x\text{Zr}_{1-x}\text{O}_2$  systems impregnated with copper by Gorte and co workers. [61-64, 66-70] The addition of  $\text{ZrO}_2$  to  $\text{CeO}_2$  in the  $\text{Cu-CeO}_2\text{-YSZ}$  system was shown by Ahn et al [61] to enhance the thermal stability of the material when operated in humidified  $\text{H}_2$ . The mechanism, through which the addition of Zr stabilised the anode material, was not well understood though the explanation offered was that the reducibility of the material was improved with the addition of  $\text{ZrO}_2$ . [61] The performance of  $\text{Ni-YSZ}$  and  $\text{Cu-CeO}_2\text{-YSZ}$  anodes was compared by Costa-Nunes et al. [64] when operating under  $\text{H}_2$  and  $\text{CO}$ . The  $\text{Ni-YSZ}$  anodes were found to be very effective when operating under  $\text{H}_2$  but showed extremely poor performance when operating under  $\text{CO}$ . The  $\text{Cu-CeO}_2\text{-YSZ}$  on the other hand showed comparable performance for both fuels. As a result the copper impregnated anodes would be able to directly use syngas (a mixture of  $\text{CO}$  and  $\text{H}_2$  normally produced by coal gasification) as a fuel source. [64] Jung et al. [63] increased the dispersal of copper in the  $\text{Cu/CeO}_2\text{/YSZ}$  system by adding urea to the aqueous  $\text{Cu}(\text{NO}_3)_2$  solutions used for the wet impregnation of samples. It was stipulated that the addition of urea would lead to more homogeneous copper dispersal within the sample, which was indeed the observed result. [63]

He et al [62] studied the effect that synthesis conditions had on the performance of Cu-CeO<sub>2</sub>-YSZ anodes. Samples containing copper were prepared using wet-impregnation. One set of samples was calcined at 500°C in air before being reduced at 500°C in H<sub>2</sub>. The second set of samples were impregnated and then reduced in H<sub>2</sub> with no calcination step. They found that copper samples that were reduced without calcination had a much more even dispersion of copper which was well connected and provided an efficient current conduction path at low (20 wt%) copper loadings. The same study also showed the importance of the ceria calcination temperature, with deactivation reported for samples calcined at 1000°C. He et al [62] concluded that it is the ceria phase which is the crucial component in the Cu-CeO<sub>2</sub>-YSZ system, the performance of which was strongly influenced by the ceria salt used in material preparation and by the calcination temperature. Indeed He et al felt that preferential carbon deposition provided an electron conduction pathway after operation of the cell under *n*-butane, improving the electric conductivity of Cu/CeO<sub>2</sub>-YSZ anodes. [62] Lee et al. [70] investigated bi-metallic Cu-Ni and Cu-Co impregnated CeO<sub>2</sub>-YSZ anodes. The CeO<sub>2</sub>-YSZ materials were impregnated with 20 wt% metal (Cu, Ni and Co), using wet impregnation of nitrate salts. The bi-metallic systems displayed improved performance compared to Cu-based anode, in terms of power density for operation with H<sub>2</sub> fuel at 700°C. The addition of Cu to the Ni and Co also reduced the level of carbon deposition experienced by the anode when operated using *n*-butane. [70]

A wide range of mixed oxide compositions have been shown to be effective catalysts for direct combustion of hydrocarbons. Larrondo et al. [52] investigated a range of Ce<sub>x</sub>Zr<sub>1-x</sub>O<sub>2</sub> (x = 0.9-0.5) oxide compositions, as shown in Table 2.1, for H<sub>2</sub> and dry CH<sub>4</sub> direct oxidation reporting favourable results for all oxide compositions as shown in Table 2.1. The two major peaks observed-T1 and T3-, the positions of which varied depending on sample composition, were assigned to reduction of surface and bulk oxygen from the sample, respectively. [52]

**Table 2.1** Peak temperatures for H<sub>2</sub> TPR profiles for Ce<sub>x</sub>Zr<sub>1-x</sub>O<sub>2</sub> (x = 0.9-0.5) oxides from [52]. In the nomenclature Z stands for Zr. The amount of Zr present is shown by the first number (5, 3, 1 relates to 50, 30 and 10 mol% respectively) and the second figure shows the calcinations temperature (600°C or 800°C respectively).

Peak	Z56 (°C)	Z36 (°C)	Z16 (°C)	Z58 (°C)	Z38 (°C)	Z18 (°C)
T1	187	181	108	194	247	197
T2	-	-	472	-	-	494
T3	569	530	719	582	597	747

A range of other metals have also been used in anodes for direct hydrocarbon utilisation. Hibino et al. [71] prepared a range of materials based on gadolinium-doped ceria (GDC), with 1-9 wt% Ru. The Ru was found to be highly effective for reforming un-reacted hydrocarbons at 600°C when operated with dry methane, ethane and propane. [71] Kharton et al. investigated a range of ceria-based anodes for the direct oxidation of methane. [k] They used Pt as an active phase with Ce<sub>0.45</sub>Zr<sub>0.45</sub>La<sub>0.10</sub>O<sub>2-δ</sub> (CZLO) and Ce<sub>0.8</sub>Gd<sub>0.2</sub>O<sub>2-δ</sub> (CGO). Kharton reported Pt modified CZLO as displaying significant activity for the partial oxidation of methane. As a result they stipulated it is an interesting material for use in SOFC anodes operated using natural gas as a fuel. [72]

## 2.8 Summary

Ce/Zr mixed oxides systems have been shown to have increased thermal stability and catalytic activity for the oxidation of hydrocarbons, when compared to CeO<sub>2</sub> and ZrO<sub>2</sub> supported systems. This research has been primarily with regard to TWC for automotive applications. However the activity and stability displayed by Ce/Zr systems has led to research into diversifying the use of these oxides. At least two of the potential uses for these systems, are in relation to fuel cell applications; as a catalyst for the CO-PROX reaction and as an anodic material in SOFCs.

The stability and effectiveness of a variety of Ce/Zr systems has been studied. The general consensus appears to be that increasing the ceria content of the oxide leads to an increase in the OSC of the material. However, the increasing ceria content also appears to reduce the thermal stability of the resultant oxide. Research into a large range of Ce/Zr oxide compositions in one study is sparse. Whereas a number of studies have shown the activity

of the oxides to be strongly effected by the preparation route, and SSA. This means that results across a range of studies are not directly comparable.

There are a range of different metals supported on the Ce/Zr oxides from Pt/Rh, Pt/Pd/Rh, Pd/Rh and Pd in automotive catalysts to CuO for preferential CO oxidation. Copper was chosen as an active phase as it had been shown across a range of studies to decrease carbon deposition on supported oxides when used as supported copper or as part of a bi-metallic system.

Copper has also been shown to be able to substitute into lattice sites in both ZrO<sub>2</sub> and CeO<sub>2</sub> systems. The incorporation of copper into lattice sites is very sensitive to the preparation technique used, but levels of up to 21 at% copper substituted into the CeO<sub>2</sub> lattice have been reported. The incorporation of copper into the support has also been shown to increase the activity of the resultant catalysts. This has led to interest in using Cu-Ce/Zr systems as SOFC anodes.

## 2.9 Aims

The aims of the work undertaken as part of this study are as follows

- i. Investigate a range of Ce/Zr oxides of varying composition prepared using a novel process established in the group by Fuentes. A range of temperature programmed techniques were to be utilised to establish the reduction and reaction behaviour of the materials prepared.
- ii. To prepare a number of copper impregnated materials based on the Ce/Zr oxides. Two copper impregnation techniques and a range of copper loadings were investigated to establish which materials gave the best catalytic performance in terms of redox activity and activation of CH<sub>4</sub>. These materials are intended for use as anode catalysts in SOFCs. Ce/Zr oxides have been shown to be highly active and durable catalysts with regard to the oxidation of hydrocarbons and CO.

## 2.10 References

- [1] Y. Amenomiya, R.J. Cvetanovic, *J. Phys. Chem.* 67, **1963**, 144.
- [2] J.A. Schwarz, J.L. Falconer, *Catalysis Today*, 7, **1990**, 1
- [3] J.L. Falconer, J.A. Schwartz, *Catal. Rev. –Sci Eng.*, 25 (2), **1983**, 141
- [4] S. Bhatia, I. Beltramini, D.D. Do, *Catal Today* 7, **1990** 309
- [5] R.K. Herz, J.B. Kiela, S.P. Marin, *Journal of Catalysis*, 73, **1982**, 66
- [6] R.J. Gorte, *Journal of Catalysis* 75, **1982**, 164
- [7] F. Villeras, L.J. Michot, G. Gerard, J.M. Cases, W. Rudzinski, *J. Therm. Anal. Cal.*, 55, **1999**, 511
- [8]. R.J. Cvetanovic, Y. Amenomiya, *Catal. Rev.-Sci. Eng.*, 6(1), **1972**, 21
- [9] J.L.G. Fierro, J.F. Garcia De La Banda, *Catal. Rev.-Sci. Eng.*, 28, **1986**, 265
- [10] R.A. Demmin, R.J. Gorte, *Journal of Catalysis*, 90, **1984**, 32
- [11] J.S. Rieck, A.T. Bell, *Journal of Catalysis*, 85, **1984**, 143
- [12] D.M. Jones, G.L. Griffin, *Journal of Catalysis*, 80, **1983**, 40
- [13] H. Vidal, S. Bernal, J. Kašpar, M. Pijolat, V. Perrichon, G. Blanco, J.M. Pintado, R.T. Baker, G. Colon, F. Fally, *Catalysis Today*, 54, **1999**, 93
- [14] I.S. Metcalfe, R.T. Baker, *Catalysis Today*, 27, **1996**, 285
- [15] F. Duprat, *Chem. Eng. Sci.*, 57, **2002**, 901
- [16] J.P. Eberhart, *Structural and Chemical Analysis of Materials*, Wiley, **1991**
- [17] L. Smart, E. Moore, *Solid State Chemistry: An Introduction*, 2<sup>nd</sup> edi., Chapman and Hall
- [18] R. Di Monte, J. Kašpar, *Catalysis Today*, 100, **2005**, 27
- [19] J. Kašpar, P. Fornasiero, G. Balducci, R. Di Monte, N. Hickey, V. Sergo, *Inorganica Chimica Acta*, 349, **2003**, 217
- [20] Y. Guo, G. Lu, Z. Zhang, S. Zhang, Y. Qi, Y. Liu, *Catalysis Today*, 126, **2007**, 296
- [21] Z. Zhang, Y. Zhang, Z. Mu, P. Yu, X. Ni, S. Wang, L. Zheng, *Applied Catalysis B: Environmental*, 76, **2007**, 355
- [22] G. Colon, M. Pijolat, F. Valdivieso, H. Vidal, J. Kašpar, E. Finocchio, M. Daturi, C. Binet, J.C. Lavalley, R.T. Baker, S. Bernal, *J. Chem Soc. Faraday Trans.*, 94, **1998**, 3717
- [23] S. Bernal, G. Blanco, J.J. Calvino, J.M. Gatica, P. Omil, J.M. Pintado, *Topics in Catalysis*, 28, **2004**, 31
- [24] R. Di Monte, J. Kašpar, *Topics in Catalysis*, 28, **2004**, 47

- [25] S. Bernal, G. Blanco, M.A. Cauqui, M.P. Corchado, C. Larese, *Catalysis Today*, 53, **1999**, 607
- [26] M. Zhao, M. Shen, J. Wang, *Journal of Catalysis*, 248, **2007**, 258
- [27] T. Masui, K. Minami, K. Koyabu, N. Imanaka, *Catalysis Today*, 117, **2006**, 187
- [28] J. Kašpar, P. Fornasiero, *Journal of Solid State Chemistry*, 171, **2003**, 19
- [29] J.R. González-Velasco, M.A. Gutiérrez-Ortiz, J.-L. Marc, J.A. Botas, M.P. González-Marcos, G. Blanchard, *Applied Catalysis B: Environmental*, 22, **1999**, 167
- [30] R. Di Monte, J. Kašpar, *J. Mater. Chem.*, 15, **2005**, 633
- [31] V.R. Mastelaro, V. Briois, D.P.F. de Souza, C.L. Silva, *Journal of the European Ceramic Society*, 23, **2003**, 273
- [32] R.O. Fuentes, R.T. Baker, *J. Phys. Chem. C*, 113, **2009**, 914
- [33] D. Terribile, A. Trovarelli, C. de Leitenburg, A. Primavera, G. Dolcetti, *Catalysis Today*, 47, **1999**, 133
- [34] H. Vidal, J. Kašpar, M. Pijolat, G. Colon, S. Bernal, A. Cordon, V. Perrichon, F. Fally, *Applied Catalysis B: Environmental*, 27, **2000**, 49
- [35] M. Fernandez Garcia, A. Martinez Arias, A. Iglesias Juex, C. Belver, A.B. Hungria, J.C. Conesa, J. Soria, *J. Catal.*, 194, **2000**, 385
- [36] F. Zamar, A. Trovarelli, C. de Leitenburg, G. Dolcetti, *J. Chem. Soc. Chem Commun.*, **1995**, 965
- [37] J. Kašpar, P. Fornasiero, *Journal of Solid State Chemistry*, 171, **2003**, 19
- [38] A.B. Hungria, N.D. Browning, R.P. Erni, M. Fernández-Garcia, J.C. Conesa, J.A. Pérez-Omil, A. Martinez-Arias, *Journal of Catalysis*, 235, **2005**, 251
- [39] H.S. Gandhi, G.W. Graham, R.W. McCabe, *J. Catal.*, 216, **2003**, 433
- [40] S.E. Collins, J.M. Cies, E. del Rio, M. Lopez-Haro, S. Trasobares, J.J. Calvino, J.M. Pintado, S. Bernal, *J. Phys. Chem. C*, 111, **2007**, 14371
- [41] D.H. Kim, M.S. Lim, *Appl. Catal. A: Gen.*, 224, **2002**, 27
- [42] T. Caputo, L. Lisi, R. Pirone, G. Russo, *Ind Eng. Chem. Res.*, 46, **2007**, 6793
- [43] Y.-Z. Chen, B.-J. Liaw, H. -C. Chen, *International Journal of Hydrogen Energy*, 31, **2006**, 427
- [44] M. Manzoli, R. Di Monte, F. Boccuzzi, S. Coluccia, J. Kašpar, *Applied Catalysis B: Environmental*, 61, **2005**, 192
- [45] X. -C. Zheng, S. -P. Wang, S. -R. Wang, S. -M. Zhang, W.-P. Huang, S.-H. Wu, *Materials Science and Engineering C*, 25, **2005**, 516
- [46] S. McIntosh, R. J. Gorte, *Chem. Rev.*, 104, **2004**, 4845.

- [47] J. Maček, B. Novosel, M. Marinšek, *Journal of the European Ceramic Society*, 27, **2007**, 487
- [48] M. Mogensen, S. Skaarup, *Solid State Ionics*, 86-88, **1996**, 1151
- [49] E.P. Murray, T. Tsai, S.A. Barnett, *Nature*, 400, **1999**, 649
- [50] A. Fuerte, R.X. Valenzuela, L. Daza, *Journal of Power Sources*, 169, **2007**, 47
- [51] S. Park, R.J. Gorte, J.M. Vohs, *Journal of the Electrochemical Society*, 148(5), **2001**, A443
- [52] S. Larrondo, M.A. Vidal, B. Irigoyen, A.F. Craievich, D.G. Lamas, I.O. Fabregas, G.E. Lascalea, N.E.W. de Reça, N. Amadeo, *Catalysis Today*, 107-108, **2005**, 53
- [53] L.F. Liotta, G. Di Carlo, G. Pantaleo, G. Deganello, *Applied Catalysis B: Environmental*, 70, **2007**, 314
- [54] L.M. Gomez-Sainero, R.T. Baker, I.S. Metcalfe, M. Sahibzada, P. Concepcion, J.M. Lopez Nieto, *Applied Catalysis A: General*, 294, **2005**, 177
- [55] S. Eriksson, S. Rojas, M. Boutonnet, J.L.G. Fierro, *Applied Catalysis A: General*, 326, **2007**, 8
- [56] M.R. Kantserova, T.K. Shashkova, S.N. Orlik, *Theoretical and Experimental Chemistry*, 42, **2006**, 197
- [57] G. Águila, F. Gracia, J. Cortés, P. Araya, *Applied Catalysis B: Environmental*, 77, **2008**, 325
- [58] M. Labaki, J. –F. Lamonier, S. Siffert, E.A. Zhilinskaya, A. Aboukaïs, *Colloids and Surfaces A: Physiochem. Eng. Aspects.*, 227, **2003**, 63
- [59] S. Saitzek, S. Villain, G. Nolibé, J.R. Gavarri, *Applied Surface Science*, 253, **2007**, 7490
- [60] F.F. Qu, W. Chu, L.M. Shi, M.H. Chen, J.Y. Hu, *Chinese Chemical Letters*, 18, **2007**, 993
- [61] K. Ahn, H. He, J.M. Vohs, R.J. Gorte, *Electrochemical and Solid-State Letters*, 8 (8), **2005**, A414
- [62] H. He, J.M. Vohs, R.J. Gorte, *Journal of the Electrochemical Society*, 150 (11), **2003**, A1470
- [63] S. Jung, C. Lu, H. He, K. Ahn, R.J. Gorte, J.M. Vohs, *Journal of Power Sources*, 154, **2006**, 42
- [64] O. Costa-Nunes, R.J. Gorte, J.M. Vohs, *Journal of Power Sources*, 141, **2005**, 241
- [65] T. Hibino, A. Hashimoto, M. Yano, M. Suzuki, M. Sano, *Electrochimica Acta*, 48, **2003**, 2531

- [66] S. An, C. Lu, W.L. Worrell, R.J. Gorte, J.M. Vohs, *Solid State Ionics*, 175, **2004**, 135
- [67] M.D. Gross, J.M. Vohs, R.J. Gorte, *Journal of Electrochemical Society*, 154, **2007**, B694
- [68] C. Lu, W.L. Worrell, J.M. Vohs, R.J. Gorte, *Journal of the Electrochemical Society*, 150 (10), **2003**, A1357
- [69] C. Lu, W.L. Worrell, R.J. Gorte, J.M. Vohs, *Journal of the Electrochemical Society*, 150 (3), **2003**, A354
- [70] S.-I. Lee, J.M. Vohs, R.J. Gorte, *Journal of the Electrochemical Society*, 151 (9), **2004**, A1319
- [71] M.K. Dongare, A.M. Dongare, V.B. Tare, E. Kemnitz, *Solid State Ionics*, 152, **2002**, 455
- [72] V.V. Kharton, A.A. Yaremchenko, A.A. Valente, E.V. Frolova, M.I. Ivanovskaya, J.R. Frade, F.M.B. Marques, J. Rocha, *Solid State Ionics*, 177, **2006**, 2179

# **Chapter 3. Experimental Details**

### 3.1 Introduction

This chapter contains a summary of the material preparation methods and apparatus utilised for materials characterisation. It also contains details of initial temperature programmed experiments and subsequent adjustments used to analyze and improve the performance of the equipment and details of the calibration processes employed.

### 3.2 Material Preparation

Powder samples of a number of mixed Ce/Zr oxides were utilised in this work, some impregnated with copper. These were prepared by one of three fabrication routes. The materials fabricated were either pure (“bare”) Ce/Zr oxides, Ce/Zr oxides which were impregnated with copper by the process of incipient wetness or Ce/Zr oxides which were impregnated with copper during preparation of the oxide. All of the materials analysed as part of this work were prepared by the author.

#### 3.2.1 Oxide Preparation

$\text{Ce}_{0.1}\text{Zr}_{0.9}\text{O}_2$  (ZCe10),  $\text{Ce}_{0.25}\text{Zr}_{0.75}\text{O}_2$  (ZCe25),  $\text{Ce}_{0.5}\text{Zr}_{0.5}\text{O}_2$  (ZCe50),  $\text{Ce}_{0.75}\text{Zr}_{0.25}\text{O}_2$  (ZCe75),  $\text{Ce}_{0.9}\text{Zr}_{0.1}\text{O}_2$  (ZCe90) and  $\text{CeO}_2$  oxides were synthesised from nitrate precursors using a technique established in the group by Fuentes. [1] Zirconium dinitrate oxide (99.9%, Alfa Aesar) and cerium nitrate hexahydrate (99.5%, Alfa Aesar) were weighed in the ratio appropriate for the preparation of 0.1 moles of the relevant oxide (Table 3.1) before being dissolved separately in 50ml of  $\text{H}_2\text{O}$  under stirring for 30 min. The two cation solutions were then combined and left to mix under stirring for 30 min. To the cation solution, anhydrous citric acid (99.5%, Alfa Aesar) was added in a quantity appropriate to give a molar ratio of citric acid (CA): total oxide (TO) of 2:1. The solution was allowed to homogenise for 12 hours before the temperature was increased to  $80^\circ\text{C}$  at a rate of  $5^\circ\text{C min}^{-1}$  and maintained at  $80^\circ\text{C}$  for 30 min, under stirring on a hot plate. This led to the elimination of excess water and the formation of a transparent gel which became increasingly viscous over time. The gel was then transferred to a muffle furnace where it was heated from 80 to  $250^\circ\text{C}$  at a rate of  $2^\circ\text{Cmin}^{-1}$  and was maintained at  $250^\circ\text{C}$  for 1h. This led to the production of foam with the evolution of the remaining water and  $\text{NO}_2$ . The resulting foam-like powder was then heated at a rate of  $2^\circ\text{Cmin}^{-1}$  to  $500^\circ\text{C}$  and was

maintained at 500°C for 1h. All powders produced by this technique were a uniform yellow colour, with ZCe25 and ZCe50 being slightly darker, and the CeO<sub>2</sub> sample having the lightest colour.

**Table 3.1** – Masses of nitrates used in preparation of 0.01 moles of the Ce/Zr mixed oxides.

Oxide Composition	Ce(NO <sub>3</sub> ) <sub>3</sub> .6H <sub>2</sub> O (g)	ZrO (NO <sub>3</sub> ) <sub>2</sub> .xH <sub>2</sub> O (g)	Citric Acid (g)
ZCe90	3.91	0.27	3.84
ZCe75	3.26	0.67	3.84
ZCe50	2.17	1.33	3.84
ZCe25	1.09	2.00	3.84
ZCe10	0.43	2.40	3.84

### 3.2.2 Copper Impregnation

Copper impregnation was conducted using two separate techniques, incipient wetness and impregnation during fabrication of the oxide. A three part nomenclature was devised in order to allow the rapid organisation and recognition of these samples. For example, 5-50-I would represent a sample containing 5 wt% copper (5), on the ZCe50 (50) mixed oxide, with the copper added by the incipient wetness technique (I). Samples which had copper added during the preparation of the oxide were assigned the suffix D. The copper content of the samples was calculated as a wt% of the final reduced catalyst.

#### 3.2.2.1 Incipient Wetness

Incipient wetness is a technique which relies on capillary action to draw the solution containing the copper salt into the oxide. The calcined oxide samples prepared as explained in Section 3.2.1. were used. The relevant amount to result in 2 wt%, 5 wt%, 7 wt% or 10 wt% final Cu content of copper nitrate trihydrate (98%, Alfa Aesar) dissolved in acetone was added dropwise to 0.5 g of the oxide. The solution was added dropwise to the oxide powder until the powder began to change colour. This was then ground using an agate pestle and mortar and allowed to dry before more of the copper solution was added. Once all of the required copper solution had been added to the sample it was heated to 250°C at a

rate of  $2^{\circ}\text{Cmin}^{-1}$  and was maintained at  $250^{\circ}\text{C}$  for 1h. As will be discussed in Section 5.5. this was found to be an inadequate temperature for total decomposition of the copper nitrate, as a result samples were subsequently heated to  $500^{\circ}\text{C}$  at a rate of  $2^{\circ}\text{Cmin}^{-1}$  and maintained at  $500^{\circ}\text{C}$  for 1h. The two different calcination treatments were indicated by a slight alteration to the previously stated nomenclature with I or II being added to the terms for the incipient wetness samples for those calcined at  $250^{\circ}\text{C}$  and  $500^{\circ}\text{C}$ , respectively.

After calcination and grinding in a pestle and mortar for one minute the powders were all of uniform colour ranging from a greyish green for 5-10-I to dark brown for 5-90-I. Generally as the copper loading increased the powders darkened, changing from yellow/green (2 wt%) to brown (5 wt%, 7 wt%) to grey/brown (10 wt%).

### **3.2.2.2 Impregnation During Preparation**

Oxide samples containing 5 wt% copper were synthesised directly from nitrate precursors in a synthesis adapted from Terribile. [2] Zirconium dinitrate oxide (99.9%, Alfa Aesar), cerium nitrate hexahydrate (99.5%, Alfa Aesar) and copper nitrate trihydrate (98%, Alfa Aesar) were weighed in the ratio applicable to the compound being prepared before being dissolved separately in  $\text{H}_2\text{O}$  under stirring. The three cation solutions were then combined and left to mix under stirring for 30 minutes. To the cation solution, anhydrous citric acid (99.5%, Alfa Aesar) was added in order to give a final molar ratio of citric acid (CA): total oxide (TO) of 2:1. The solution was allowed to homogenise for 12 h before the temperature was increased to  $80^{\circ}\text{C}$  at a rate of  $5^{\circ}\text{C min}^{-1}$  and maintained at  $80^{\circ}\text{C}$  for 30 min. This led to the elimination of excess water and the formation of a transparent gel which became increasingly viscous over time. The gel was then transferred to a muffle furnace where it was heated from  $80^{\circ}\text{C}$  to  $250^{\circ}\text{C}$  at a rate of  $2^{\circ}\text{Cmin}^{-1}$  and was maintained at  $250^{\circ}\text{C}$  for 1h, leading to the formation of a foam and the evolution of the remaining water and  $\text{NO}_2$ . The resulting material was then heated to  $500^{\circ}\text{C}$  at a rate of  $2^{\circ}\text{Cmin}^{-1}$  and was maintained at  $500^{\circ}\text{C}$  for 1h. After this calcination step the materials were ground in a pestle and mortar for one minute. The powders produced had uniform colour ranging from dark green (5-10-D) to dark brown (5-90-D).

### **3.3 Scanning Electron Microscopy (SEM)**

Calcined powders were studied by Scanning Electron Microscopy (SEM) using a Jeol JSM 5600 SEM with a tungsten filament and a CCD camera. Images were collected in the magnification range  $\times 100$  -  $\times 5000$  using an accelerating voltage of 5 - 30 kV and a small spot size generally between 18-26. Samples were mounted onto the specimen holder using cut to fit, electronically conducting carbon adhesive discs. Energy-Dispersive X-ray spectroscopy (Oxford Inca) (EDX) was utilised to investigate the distribution of elements within the samples.

### **3.4 X-ray Diffraction (XRD)**

X-ray diffraction (XRD) was used to confirm the crystal structure of the oxides and investigate materials for unwanted large collections of copper species in the calcined powders. The machine used to collect the patterns was a Stoe STADI-P powder diffractometer which used a copper anode, producing monochromated x-rays at a wavelength of 1.5406 Å. Samples to be investigated were mounted on a sandwich of mylar discs greased with Vaseline. Readings were made by step-scanning with a step size of  $0.1^\circ$  and a step counting time of 5 sec. The instrument contained a collimator, which is a device used to filter the X-rays so improving the resolution of the pattern obtained. The problem with excluding some of the X-rays is that the pattern obtained is less intense so such a device can only be used on a machine with a strong initial signal. The collimator had the effect of adding two peaks at  $2\theta = 22$  and  $24^\circ$  which should therefore be discounted from the final pattern.

### **3.5 BET Surface Area Analysis**

BET was used to investigate the specific surface area of the materials produced. The technique is named after the pioneers of the technique, Brunauer, Emmett and Teller. [3] A Micromeritics ASAP 2020 machine was employed to determine the Specific Surface Area (SSA) of powder samples. BET adsorption/desorption isotherms were also acquired for nitrogen at 77K. The sample was heated and degassed, to remove foreign molecules. Controlled doses of  $N_2$  were then adsorbed onto the sample. The sample was then maintained at 77K and subjected to a wide range of pressures in order to generate the

adsorption/desorption isotherms. The adsorption or desorption of nitrogen molecules from the samples led to pressure variations. By knowing the area occupied by one adsorbed molecule and using an adsorption model it is possible to calculate the SSA of a sample.

### 3.6 Temperature Programmed Apparatus

The schematic representation of the apparatus utilised in this work is shown in Figure 3.1. The system was based on that used by Baker and Metcalfe, [4] and consisted of two separate frames. All equipment was designed and built in house. The first frame housed five gas lines. The first of these was attached to oxygen (SGE 1/8" oxygen trap) and water (1/8" Safe Glass Moisture Trap, CRS systems) filters. All the filters had 1/8" brass on/off valves (Swagelok) situated at either end in order to protect the filters during any subsequent adjustment of the systems' configuration. After the filters, the line passed to a mass flow controller (UNIT 7300, calibrated for N<sub>2</sub>, maximum flow rate of 250 ml min<sup>-1</sup>). This first gas line was primarily used as the carrier gas line (Ar). Three further gas lines passed through a similar series of valves and filters and into a four way selection valve (Swagelok, 5-way switching ball valve), which allowed the relevant flow to be selected. Typically, these gas lines were used for dilute hydrogen (5% H<sub>2</sub>/Ar), methane (5% CH<sub>4</sub>/Ar) and oxygen (5% O<sub>2</sub>/Ar). The O<sub>2</sub>/Ar line had no oxygen trap. A calibration gas mixture was also connected to one of the inlet ports of the four way selection valve. This mixture was formulated so that the mass spectrometer could be calibrated for several species. A mass flow controller (UNIT 7300, calibrated for N<sub>2</sub> max flow rate 600ml min<sup>-1</sup>) was placed in-line after the selection valve in order to regulate the flow of gas. All tubing utilised on the first frame was 1/8" stainless steel tubing (SGE). The carrier gas and the selected treatment or calibration gas both passed into a two-way switching valve (Rheodyne 3000-038) positioned on the second frame. The design of this valve meant that flows from the two mass flow controllers would be continuous with one flow directed to vent and one to the rest of the apparatus. In this way the samples could be pre-treated with one gas and then the flow switched to an alternate gas with no delay or risk of air entering the equipment. The gas going to vent passed through a rotameter (Cole-Palmer, 50ml) and a bubble flow meter so that the flow rate could be measured if required. The other gas flow passed through a liquid injection port. This consisted of a 1/16" stainless steel T-junction, with two of the arms of the T being assigned to the gas entering and exiting the junction and the third holding a 1/16" tubing to 1/4" (Swagelok) reducing fitting. The 1/4" fitting

contained two septa which created a gas tight seal. This arrangement allowed pulses of water of known volume to be injected into the system through the septa, using a 1.0 $\mu$ l gas-tight syringe (SGE, 1BR-7) in order to calibrate the mass spectrometer. Downstream of the liquid injection port all tubing was heated using a heating cord which was wound around the tubing to prevent water or other species from condensing in the apparatus.

Next in line was a 6 way switching valve (Rheodyne, 7 port stainless steel switching valve), downstream from which all tubing was 1/16" glass-lined tubing (SGE, 0.8mm I.D.) the reason for this was two-fold. First, it reduced the volume of the system and hence the time lag between desorption of a species from the sample and its detection in the mass spectrometer. Second, it had the effect of minimising any adsorption of products onto the inner walls of the system. The Rheodyne switching valve could direct the gas flow to either one of the two reactors or the by-pass line. An identical valve after the reactors was used to select the desired flow path. The by-pass line was simply an uninterrupted, heated piece of glass-lined tubing through which a flow could be diverted whilst the micro-reactors were being attached or removed.

The reactor arrangement is shown in Figure 3.2. The quartz micro-reactors were built in-house and consisted of 1/4" o.d. tubes which broadened out to 1/2" o.d. in the centre. In this central bubble there was a quartz frit on which the sample was located (Figure 3.3). Typical sample mass was 50 mg. This ensured that the quartz frit was completely covered in sample without there being excessive depth of catalyst bed which may have resulted in re-adsorption of desorbed species in the downstream part of the catalyst bed. The nature of the micro-reactor employed meant that only powder samples were suitable for investigation as they were required to fit through the thin neck of the micro-reactor. The micro-reactor was attached using 1/4" to 1/16" reducing union compression fittings (SGE) at the bottom and a three way reducing union which consisted of 2  $\times$  1/16" ports and one 1/4" port (SGE). Each of these employed graphite ferrules due to the high temperatures to which they would be subjected.

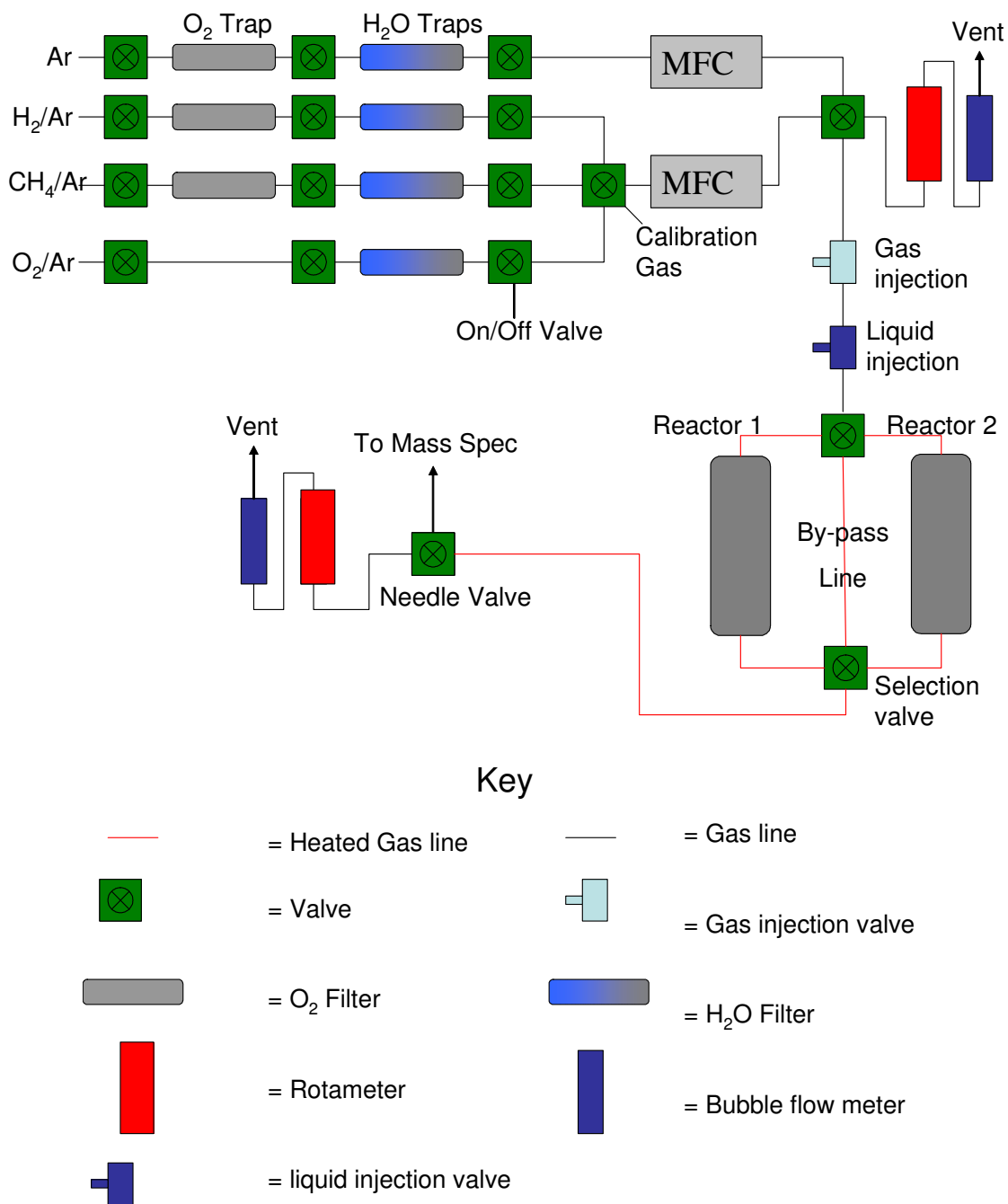


**Figure 3.1** Apparatus for temperature programmed experiments.

The furnaces were both designed and built in-house, they consisted of a 300 mm by 25 mm i.d. quartz tube encased in a 115 mm diameter steel shell containing insulation. Two K-type thermocouples were employed. One was located in the centre of the furnace tube and regulated the power input to the furnace and a second thermocouple was held in position against the outside of the reactor next to the quartz frit on which the sample was located. The reading from the second thermocouple was logged by the computer attached to the

mass spectrometer. During a heating programme the top and bottom of the micro-reactor were surrounded with kaowool insulation which served the dual purpose of ensuring a better heat distribution within the furnace as well as enabling the micro-reactor to be secured centrally within the quartz tube. After passing through the reactor and selection valve the gas passed through a 1/16" needle valve which enabled a small proportion of the gas to be fed to the mass spectrometer via a heated 1/32" capillary, with the remainder going to vent through the rotameter and bubble flow meter mentioned above.

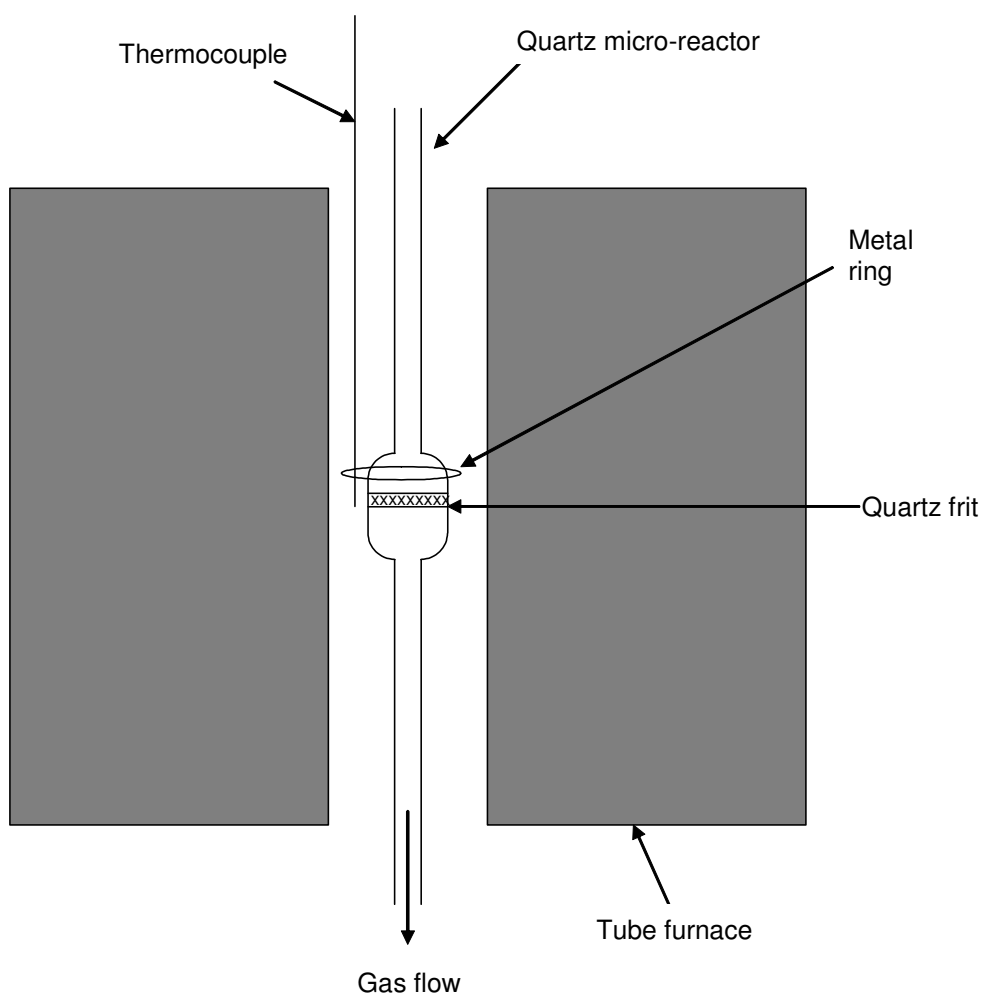


**Figure 3.2** Furnace and reactor arrangement.

There were five gases or gas mixtures employed during this investigation. These were provided from gas cylinders (BOC). These cylinders were connected via pressure regulators and Swagelok on/off valves to the experimental rig. All lines were 1/8" PTFE tubing with PTFE ferrules. Pure Ar (BOC, standard grade) was employed as a carrier gas for desorption experiments and also during water calibration measurements with oxygen

and H<sub>2</sub>O filters employed as previously stated. The gas mixtures employed were 5% H<sub>2</sub>/Ar, 5% CH<sub>4</sub>/Ar and 5% O<sub>2</sub>/Ar (all BOC, standard grade) and a calibration gas mixture containing 0.1023% ethane, 0.1032% ethene, 1.02% CO<sub>2</sub>, 2.01% H<sub>2</sub>, 2.03% CO, 0.46% O<sub>2</sub> and a balance of Ar (BOC, certification level +/- 5% analytical accuracy). The typical flow rate employed during experiments was 50 ml min<sup>-1</sup>. This was regulated by the mass flow controllers which were set using a calibration factor table obtained from Brookes instruments for each gas mixture employed. To check the accuracy of the calibration factors the flow rate was also measured using a bubble flow meter and flow rates were recorded.

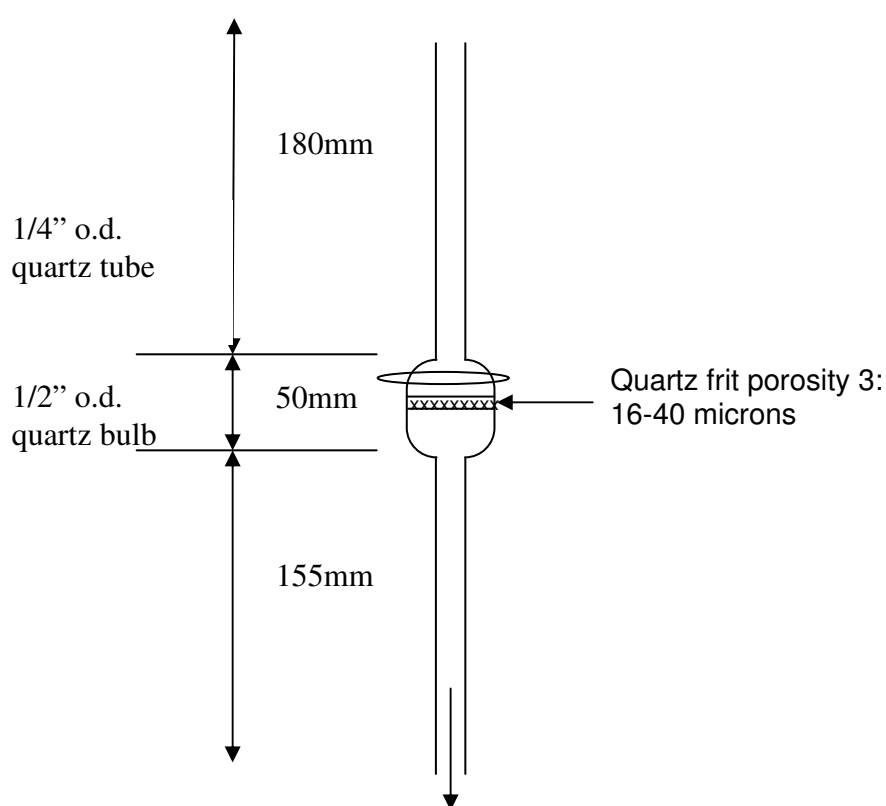


**Figure 3.3** Quartz micro-reactor.

### 3.7 Temperature Programmed Experiments

There were five distinct temperature programmed experimental procedures employed in this work which all required slight variations in how the equipment was utilised. Calcined oxide samples were used in a series of temperature programmed experiments in order to investigate their redox behaviour, catalytic activity, stability at high temperature and

oxygen storage capacity. Powder samples were prepared as described in Section 3.2, with the final step being calcination for 1h at 500°C.

Samples were ground into fine powders using a pestle and mortar and small amounts (~50 mg) used in order to minimise temperature and concentration gradients within the catalyst bed as well as reducing any effects arising from water production. Each day, the mass spectrometer was calibrated for water by injecting 0.2 µl pulses of liquid water and by using the calibration gas mixture. Gas flow rates were approximately 50 ml min<sup>-1</sup>, the heating rate was 5°C min<sup>-1</sup> and the maximum temperature was typically 800°C. The five primary experiments conducted are outlined in the following sections.

### **3.7.1 Temperature Programmed Desorption (TPD)**

TPD experiments involved a flow of inert gas (Ar, BOC Standard grade, 50 ml min<sup>-1</sup>) being passed over the sample (50 mg). The gas flow was established through the reactor and left for roughly 30 min to equilibrate. The sample was heated from room temperature in a linear fashion at 5°C min<sup>-1</sup> to the maximum temperature (typically 800°C). Once the target temperature had been reached, the sample was allowed to cool to room temperature with the gas flow maintained (Ar). TPD experiments were employed in order to identify any adsorbed species which were present on the samples as prepared. The experiments also served a secondary purpose of giving an indication as to how the materials were affected by thermal cycling.

### **3.7.2 Temperature Programmed Reduction (TPR)**

TPR experiments involved the reduction of a sample (50 mg) using a flow of a reducing gas (5% H<sub>2</sub>/Ar, 50 ml min<sup>-1</sup>). The gas flow was established through the reactor and left for roughly 30 min to equilibrate. The sample was heated in a linear fashion at 5°C min<sup>-1</sup> to the maximum temperature (typically 800°C). The temperature was maintained at the maximum temperature for 1 h in order to extend the time during which the sample was reduced. On completion of the program the sample was allowed to cool back to room temperature. Samples were either subjected to TPRs as prepared or after a TPD experiment, in which case the TPRs are referred to as TPD/Rs. Monitoring H<sub>2</sub> consumption and H<sub>2</sub>O production

as well as calculating the area of the corresponding peaks revealed the temperature at which the samples were reduced and the extent to which they were reduced, respectively.

### **3.7.3 Temperature Programmed Reaction (TPRx)**

TPRx experiments involved the reaction of samples (50 mg) with a flow of a reactive gas (in this work 5% CH<sub>4</sub>/Ar, 50 ml min<sup>-1</sup>). The gas flow was established through the reactor and left for roughly 30 min to equilibrate, then heated in a linear fashion at 5°C min<sup>-1</sup> to the maximum temperature (800-900°C). The temperature was maintained at the maximum temperature for 1 h in order to extend the time during which reaction took place. On completion of the program the sample was allowed to cool back to room temperature under a flow of the reaction gas.

### **3.7.4 Temperature Programmed Oxidation (TPO)**

TPO experiments were conducted on samples after a TPRx experiment. A flow of oxidative gas (5% O<sub>2</sub>/Ar, 50 ml min<sup>-1</sup>), was established after the sample (50 mg) had been allowed to cool back to room temperature. The gas flow was left for roughly 30 min to equilibrate. The sample was then heated in a linear fashion at 5°C min<sup>-1</sup> to the maximum temperature (800-900°C). As the sample was heated, species that had been deposited during the TPRx were oxidised and the resulting CO and CO<sub>2</sub> emissions recorded by the QMS. TPO experiments revealed the extent of any carbon deposition on the samples that occurred during the TPRx.

### **3.7.5 Lightoff Experiments**

In Lightoff experiments a stoichiometric 2:1 ratio flow of CH<sub>4</sub> and O<sub>2</sub> was established (with a combined flow rate of 50 ml min<sup>-1</sup>). Samples (50 mg) were pre-reduced in a flow of H<sub>2</sub> (5% H<sub>2</sub>/Ar, 50 ml min<sup>-1</sup>, 5°C min<sup>-1</sup> to 500°C) to ensure they were in their active form. After the stoichiometric flow had been established and allowed to equilibrate (30 min) samples were heated in a linear fashion (5°C min<sup>-1</sup>) to the maximum temperature (800-900°C). The samples catalysed oxidation of the methane leading to a decrease in the partial pressure of the reactants (CH<sub>4</sub> and O<sub>2</sub>), which were converted to either CO<sub>2</sub> and H<sub>2</sub>O, when total oxidation occurred, or CO and H<sub>2</sub> when there was only partial oxidation of the

reactants. Another possibility was the deposition of carbon species onto the catalyst which would likely reduce its activity. The more active the sample the lower the temperature at which the reaction occurred and also the lower the temperature at which the reaction would reach maximum conversion. The lightoff temperature was taken as the point at which 10% of maximum conversion was reached. [5]

### 3.8 Detector Settings

The detector utilised in this work was a quadrupole mass spectrometer (QMS) (European Spectrometry Systems). The QMS system had two detectors: a Secondary Electron Multiplier (SEM) and a Faraday detector. The software required a recipe to be prepared. The recipe contained information as to the frequency of scans (typically set as every 3 sec). Number of scans to be taken (10,000), the mass to charge ratios ( $m/q$ ) to be monitored, the maximum range at which the species were monitored and the detector to be used. Up to 16 different channels or  $m/q$  values could be recorded simultaneously. In a typical recipe there were 12 masses monitored at:  $m/q = 2$  ( $H_2$ ), 12 (C), 14 (N), 15 ( $CH_3$ ), 16 (O or  $CH_4$ ), 18 ( $H_2O$ ), 28 ( $N_2$  or CO), 30 (ethane or NO), 32 ( $O_2$ ), 40 (Ar) and 44 ( $CO_2$ ). The maximum range for each species was typically set to  $10^{-7}$ ,  $10^{-8}$  and  $10^{-9}$  mBar. The lower the maximum range the more accurate and sensitive the readings would be. However if the detected level of the species rose above that of the range set then that channel would become saturated and the reading would flat line along the maximum level until the level dropped back below this maximum. A further channel was used to record the signal from the thermocouple attached to the reactor during the course of each experiment.

The spectrometer was set daily following an established procedure to ensure that all results were directly comparable. The multiplier voltage of the SEM was set to 1600 V after a range of experiments was run to establish the sensitivity of the QMS to accelerator voltage (Figure 3.4). As can be seen from Figure 3.4, the SEM detector response initially increased gradually with increasing voltage, before a sharp increase in response at voltages above 1700 V. As a result any experiment run with a voltage higher than 1600 V had a tendency to give values for some species that were above the maximum for the SEM detector ( $9.99 \times 10^{-7}$  mBar). Typically, this occurred for the  $m/q = 18$  trace ( $H_2O$ ) during reduction experiments. It was established that 1600 V was the highest voltage that could be utilised without the detector readings for the species being monitored going off the scale during the

course of an experiment. The flow that was diverted to the mass spectrometer was re-adjusted each morning using the leak detect option of the QMS software and a flow of Ar. The needle valve was adjusted until the partial pressure of Ar in the QMS detector read  $8.0 \times 10^{-7}$  mBar. The Leak Detect option provided a very quick response to any adjustment which is why it was utilised for this calibration.

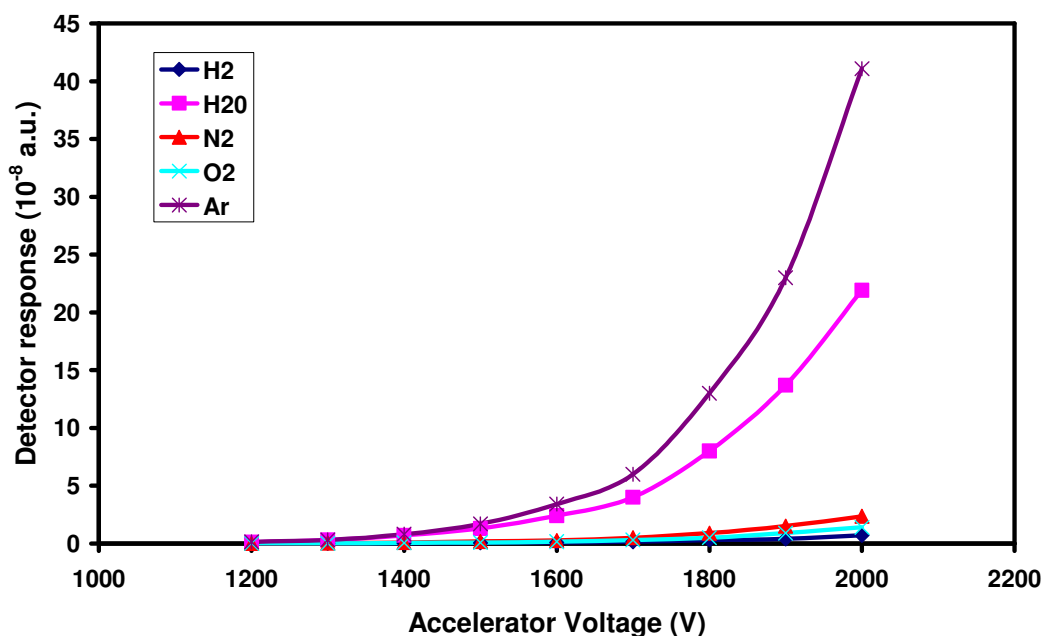


**Figure 3.4** QMS response depending on accelerator voltage.

### 3.8.1 Mass Spectrometry

Mass spectrometry is a technique used to analyse the chemical composition of a sample. The components of the sample molecule are ionized to generate charged fragments. These are then detected according to their mass-to-charge ratio. All mass spectrometer types consist of three important components: an ion source to convert the molecules into ions, a mass-analyser, which sorts the molecules according to their  $m/q$  ratios by applying either a magnetic or an electric field, and a detector which records the quantity of each ion present.

### 3.8.2 Detector Calibration

The QMS was calibrated using the calibration gas described in Section 3.6, a flow of which was established and once the signal had stabilised it was left to run for roughly 10 min. In order to calibrate for water, 10 pulses of 0.2  $\mu$ l were injected from which the average

volume was obtained. This allowed the calibration of the QMS reading for water, CO<sub>2</sub>, CO, ethane, ethane, H<sub>2</sub> and O<sub>2</sub>.

For the water calibrations, the area under the water trace was calculated using integration. In order to calculate the area the data points relating to gas partial pressure were each added to the subsequent data point with the result being divided by 2 to give an average value. The average value was then multiplied by the x-axis value (time). The area values for the desired temperature range were then added in order to provide the area under the plot. This technique was also used to calculate the area of the calibration water pulses. The areas for the pulses were then averaged in order to provide the peak area used for calibration. With the moles produced during an experiment calculated using Eqn 3.1:

$$\frac{AET}{ACT} \times \text{moles per calibration} = \text{moles per experiment} \quad (\text{Eqn 3.1})$$

Where AET is the Area under Experimental Trace and ACT is the Area under Calibration Trace.

### 3.8.3 Data Manipulation

The data from the TP runs was recorded as a MIM file. In order for the data to be read by Excel, the postscript file from each run was converted into two separate ASCII files. One of the ASCII files would contain the data from all the partial pressure traces, with the other contained the readings from the thermocouple. The ASCII files could then easily be transferred straight into Excel. In order to convert the data in the ASCII file into the temperature during the experiment Eqn 3.2 was used:

$$T = 2^{-15} \cdot r \cdot mT \quad (\text{Eqn 3.2})$$

Where r was the recorded value and mT is the maximum temperature set in the QMS software. Experiments were routinely plotted with both time and temperature values on the x-axis. The y-axis trace values were plotted on both a linear and logarithmic scale with plots specific to certain reactions being plotted if necessary (for example H<sub>2</sub> and O<sub>2</sub> traces on scales to make changes comparable for TPR experiments).

### 3.8.4 Thermocouple Adjustments

The position of the thermocouple was adjusted after it was discovered that the thermocouple, when positioned within the micro-reactor, caused some reaction of the gas employed, particularly in the TPRx experiments and the subsequent TPO experiments. Figure 3.5 shows the carbon species evolved during a TPO after a TPRx experiment. The amount of CO<sub>2</sub> evolved during the TPO when the thermocouple was positioned in the reactor, as opposed to outside it was considerably greater. The presence of CO<sub>2</sub> in the TPO where the thermocouple was positioned outside the reactor suggests that there may have been some gas phase reaction of the CH<sub>4</sub>.

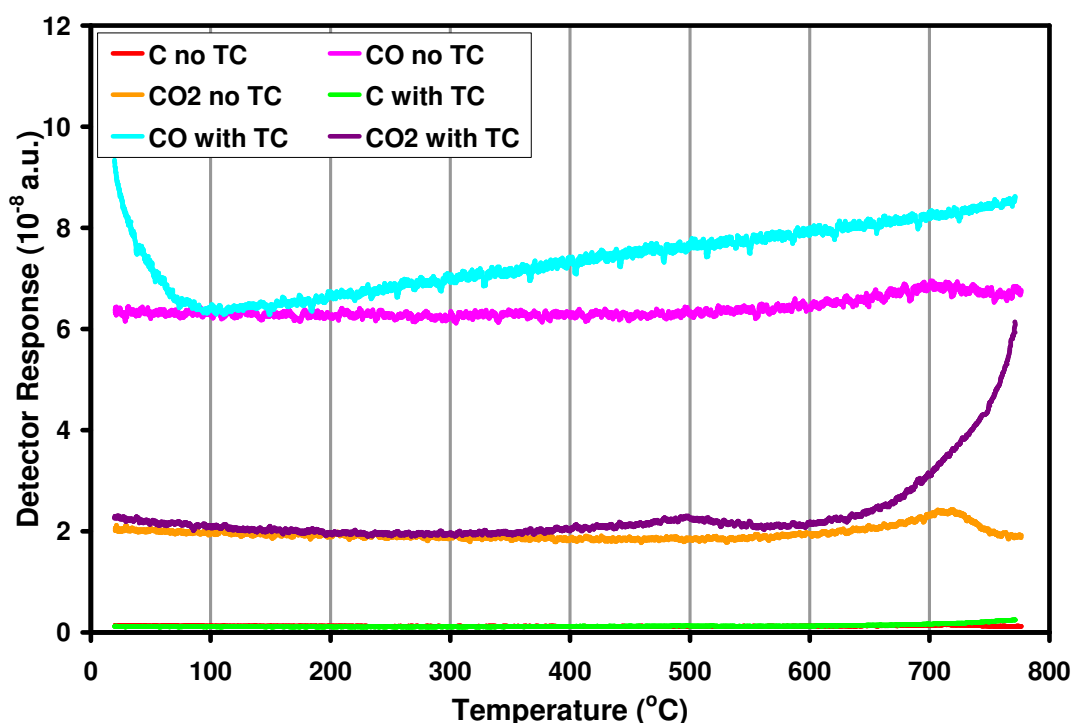


**Figure 3.5** Carbon species evolved during a TPO following a TPRx.

The initial large CO peak in Figure 3.5 for the sample with the thermocouple is due to the QMS being left for insufficient time to equilibrate before the commencement of the TPO. It may be the case that there was residual highly active carbon species from the TPRx which reacted with the oxygen when the flows were switched, all such species were consumed below 100°C.

In the light of these results, the thermocouple was therefore removed from within the quartz micro-reactor and attached to the outside of the reactor at the level of the quartz frit.

Electrical tape was used to support the weight of the thermocouple at the top of the reactor fitting and the thermocouple itself was secured against the outside of the micro-reactor bulb using steel wire. Figure 3.6 shows the thermocouple readings with the thermocouple positioned on the in-side and out-side of an empty micro-reactor. The micro-reactor was subjected to a typical heating ramp to 800°C at a rate of 5°C min<sup>-1</sup>. The two readings were found to be comparable, showing that there was little influence on the results of using the thermocouple outside the reactor.

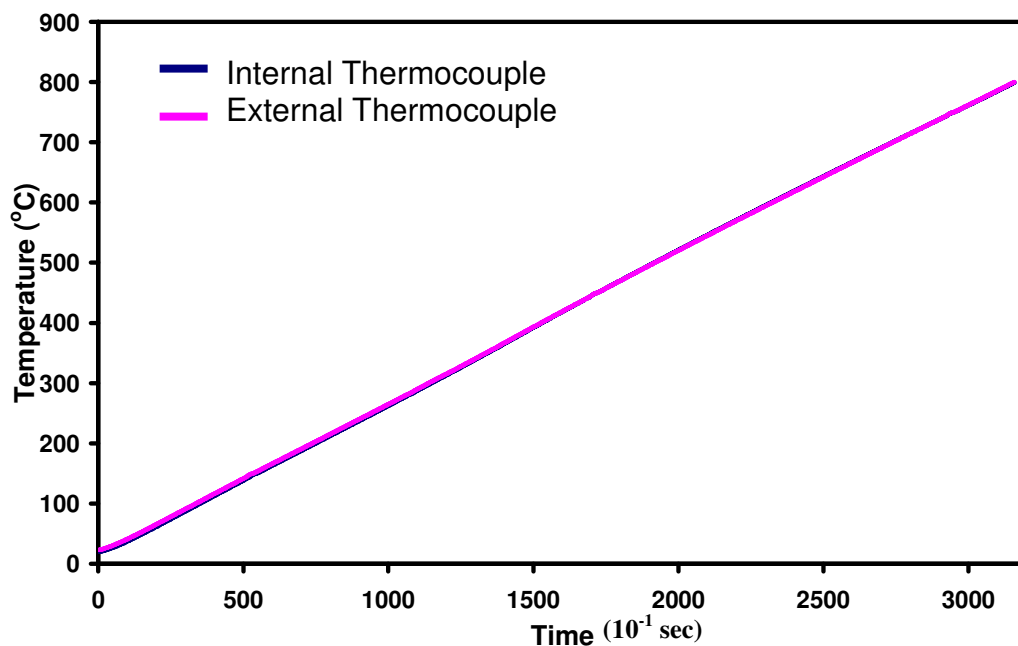


**Figure 3.6** Comparison of temperature readings with the thermocouple positioned inside and outside the micro-reactor during a blank TPRx.

### 3.8.5 Lightoff Modifications

The lightoff experiments conducted required the mixing of the 5% CH<sub>4</sub>/Ar and 5% O<sub>2</sub>/Ar flows at regulated levels which was impossible with the equipment configured as designed. It was therefore necessary to alter the layout of the equipment to facilitate the necessary mixing of gases. The modified layout is shown in Figure 3.7. The Ar line which had passed through the first mass flow controller (MFC) was diverted straight to the switching valve which meant that the flow had to be regulated using the regulator on the gas cylinder. This freed up MFC1 through which was diverted the 5% O<sub>2</sub>/Ar line. The flows after the two mass flow controllers were then combined using an 1/8" brass T piece before being fed into the selection valve. This arrangement allowed the flowrate of CH<sub>4</sub>/Ar and O<sub>2</sub>/Ar to be

closely monitored and adjusted as applicable to allow the 1:2 ratio of the gases to be maintained at the required flow rate of  $50\text{ml min}^{-1}$  for the mixture.

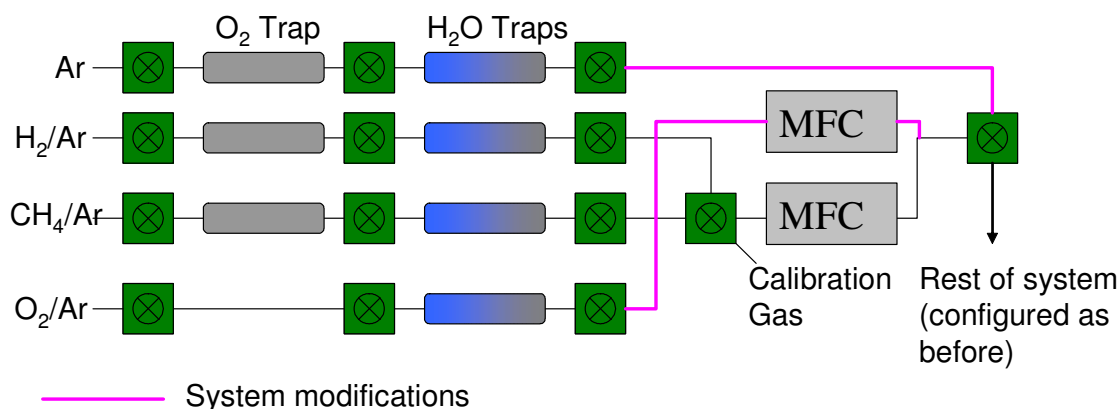


**Figure 3.7** Modifications to gas lines for lightoff experiments.

### 3.8.6 Further Modifications

There were two further modifications to the equipment not previously mentioned. Firstly the glass lined tubing initially utilised (SGE, 0.5mm I.D.) was found to be prone to blockages and so was subsequently replaced by tubing of slightly larger internal diameter (SGE 0.8mm I.D.). The first batch of micro-reactors was not uniform in shape and so influenced the reproducibility of the results. Subsequent batches of reactors were uniform and had a slightly longer neck at the upper end. This had the effect of moving the fittings slightly higher out of the furnace, protecting them against undue heating and so making them easier to handle especially after experiments.

## 3.9 References

- [1] R.O. Fuentes, R.T. Baker, *J. Phys. Chem. C*, 113, **2009**, 914
- [2] D. Terribile, A. Trovarelli, C. de Leitenburg, A. Primavera, G. Dolcetti, *Catalysis Today*, 47, **1999**, 133
- [3] S. Brunauer, P.H. Emmett, E. Teller, *J. Am. Chem. Soc.*, 60, **1938**, 309
- [4] R.T. Baker, I.S. Metcalfe, *Ind. Eng. Chem Res.*, 34, **1995**, 1558
- [5] F. Duprat, *Chem. Eng. Sci.*, 57, **2002**, 901

# **Chapter 4. Ceria-Zirconia Oxides as Catalyst Supports**

## 4.1 Introduction

The experiments described in this chapter were intended to investigate how varying relative concentration of ceria in the Ce/Zr mixed oxides prepared as described in Section 3.2.1 affected their structure and redox behaviour. A range of compositions was investigated:  $\text{Ce}_{0.1}\text{Zr}_{0.9}\text{O}_2$  (ZCe10),  $\text{Ce}_{0.25}\text{Zr}_{0.75}\text{O}_2$  (ZCe25),  $\text{Ce}_{0.5}\text{Zr}_{0.5}\text{O}_2$  (ZCe50),  $\text{Ce}_{0.75}\text{Zr}_{0.25}\text{O}_2$  (ZCe75) and  $\text{Ce}_{0.9}\text{Zr}_{0.1}\text{O}_2$  (ZCe90). The aim was to identify which compositions would provide the most active catalyst support.

## 4.2 Characterisation

### 4.2.1 Scanning Electron Microscopy

The as-prepared oxide samples (that is calcined at 500°C for 1 h then ground in a pestle and mortar for 1 min) were analysed using the SEM. EDX analysis of all oxide compositions was also carried out in order to establish the dispersal of Ce and Zr within the powders.

There were numerous hemi-spherical depressions, between 2-5µm in diameter, throughout all of the powders as shown in Figure 1.1. These depressions were formed during preparation of the powders by the gas that was evolved. These depressions greatly increase the surface area of the powders and should therefore increase the activity of the powders. All of the powders examined using SEM displayed a high degree of agglomeration throughout the sample. The low ceria content samples, Figure 1.1 (a) and (b), tended to display an angular morphology. The higher ceria samples displayed a more rounded morphology, with increased occurrence of the bubble shaped depressions.

The EDX results for the high and low ceria containing samples are shown in Figures 4.2 and 4.3. As would be expected the EDX trace for Zr in Figure 4.2 (d) displayed a very strong signal. The dark areas observed on the trace are from areas where the sample is thicker as opposed to areas of poor dispersal. This is confirmed by the slightly darker traces observed for both O and Ce, though the effect of the increasing sample thickness was relatively minor for these elements. The same kind of result was observed for the high Ce containing samples in Figure 4.3 (b), where there was a much stronger signal observed

for Ce than the other elements. All of the samples investigated displayed a uniform dispersion of ceria and zirconia throughout.

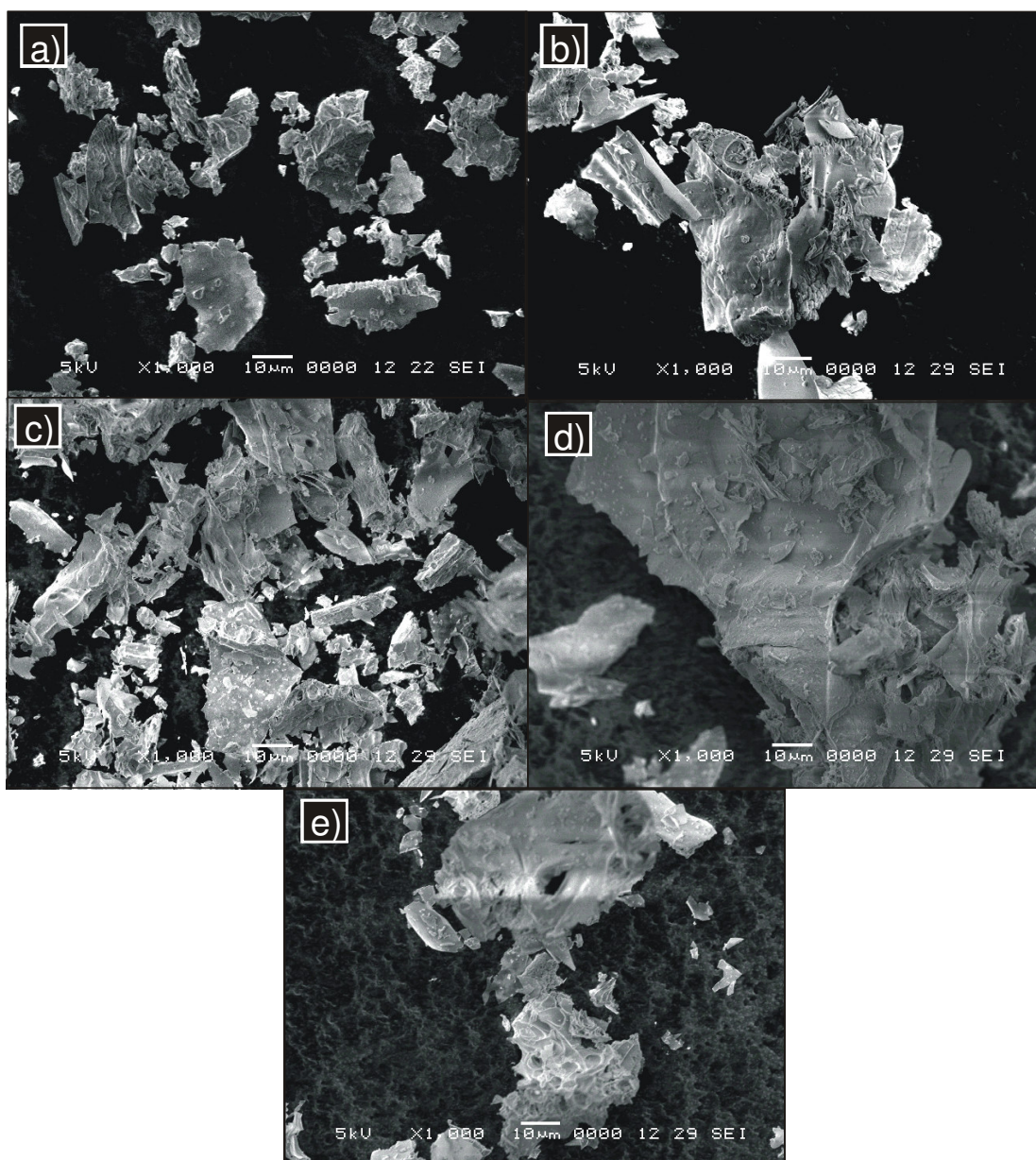


**Figure 4.1** SEM images of as-prepared samples, a) ZCe10, b) ZCe25, c) ZCe50, d) ZCe75, e) ZCe90.

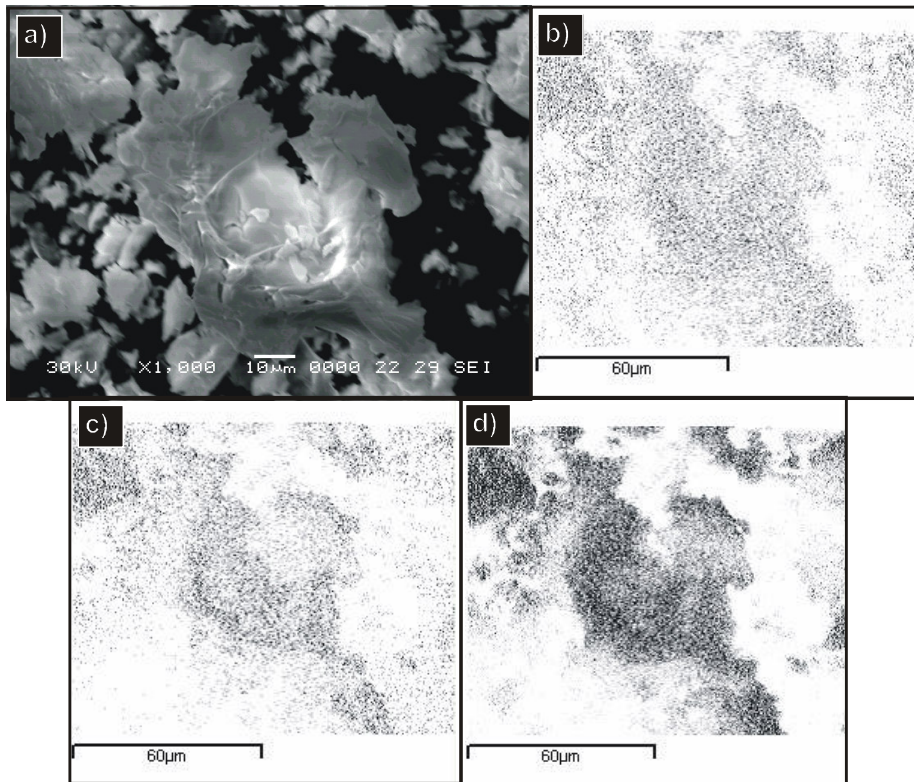


**Figure 4.2** SEM image and elemental maps of (b) Ce, (c) O, (d) Zr for ZCe10.

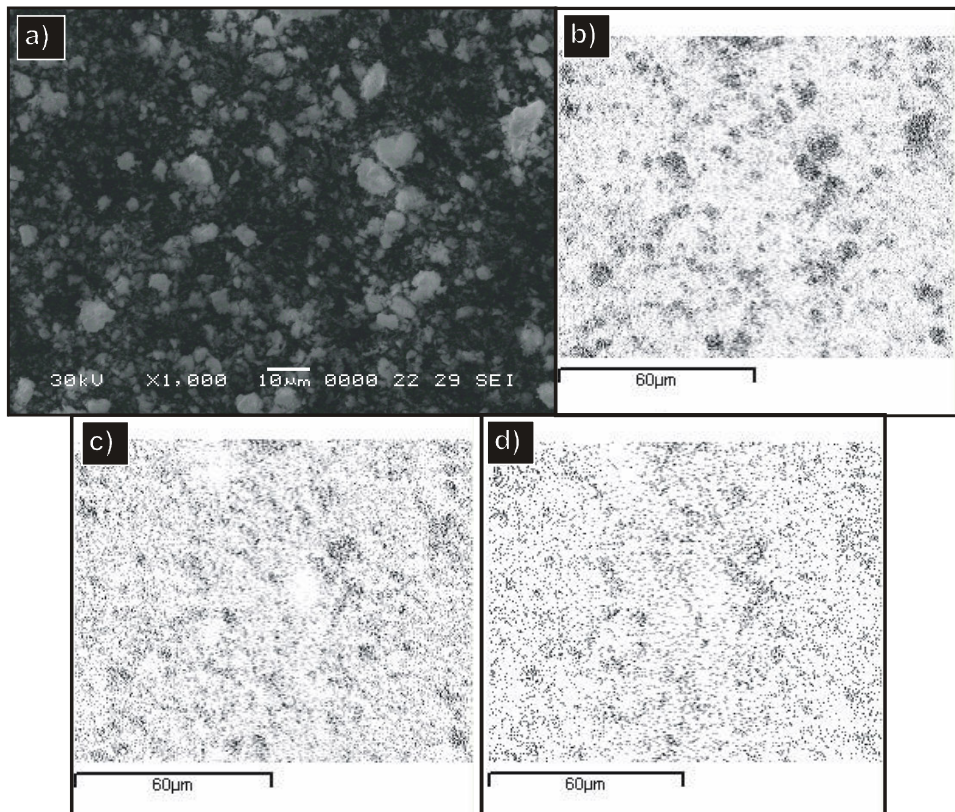


**Figure 4.3** SEM image and elemental maps of (b) Ce, (c) O, (d) Zr for ZCe90.

### 4.3 BET Surface Area Analysis

The specific surface areas (SSA) of the calcined samples was analysed using the BET technique and are plotted in Figure 4.4. The SSAs for the low ceria samples were comparable ( $ZCe10 = 31.8 \text{ m}^2\text{g}^{-1}$ ,  $ZCe25 = 31.2 \text{ m}^2\text{g}^{-1}$ ). High SSA values were found for  $ZCe50 (52.6 \text{ m}^2\text{g}^{-1})$ ,  $ZCe75 (47.6 \text{ m}^2\text{g}^{-1})$  and  $ZCe90 (46.0 \text{ m}^2\text{g}^{-1})$ .

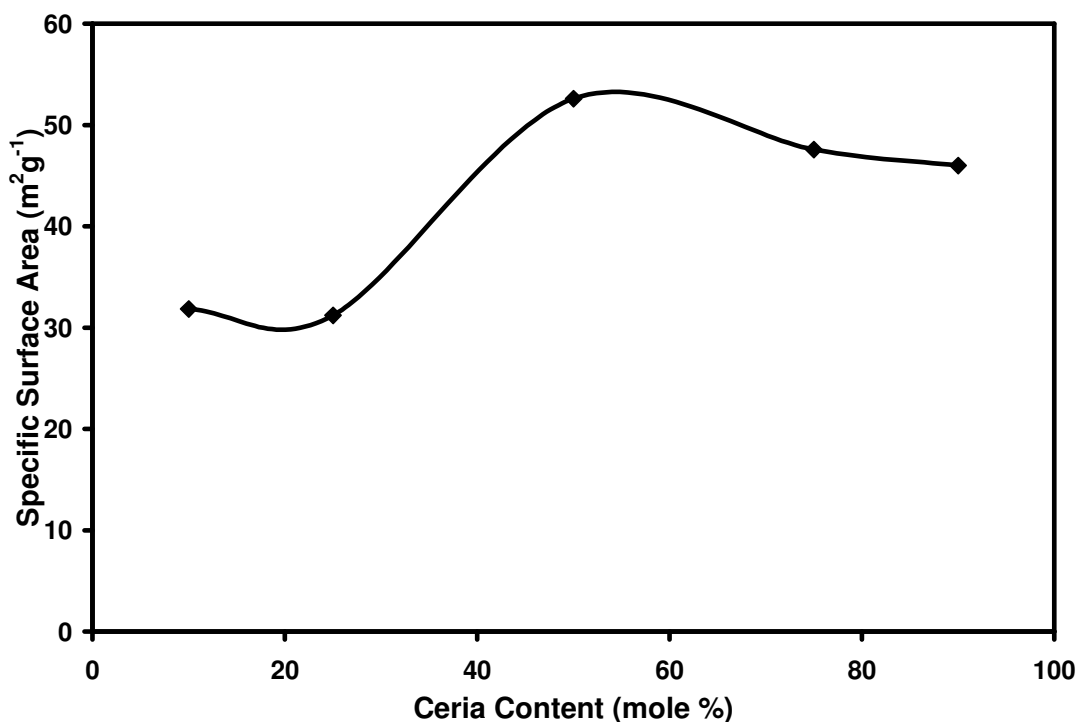


**Figure 4.4** BET specific surface areas for the as-prepared powder samples ground in a pestle and mortar.

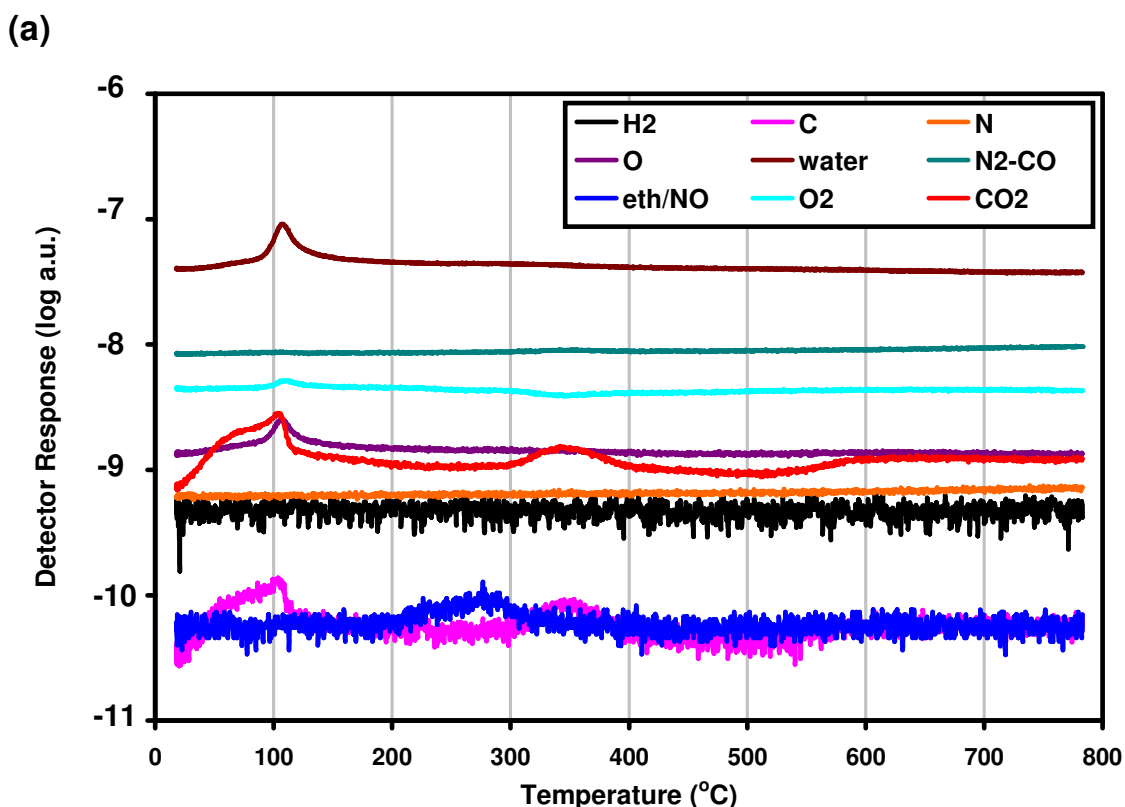
### 4.4 Temperature Programmed Studies

The equipment and procedures for temperature programmed experiments are outlined in Section 3.6. Twelve m/q traces were monitored during temperature programmed experiments. The m/q values chosen for investigation were 2 ( $\text{H}_2$ ), 12 (C), 14 (N), 15 ( $\text{CH}_3$ ), 16 (O or  $\text{CH}_4$ ), 18 ( $\text{H}_2\text{O}$ ), 28 ( $\text{N}_2$  or CO), 30 (ethane or NO), 32 ( $\text{O}_2$ ), 40 (Ar), 44 ( $\text{CO}_2$ ) and 46 ( $\text{NO}_2$ ). The results of these experiments are detailed in the following section for all oxide compositions.

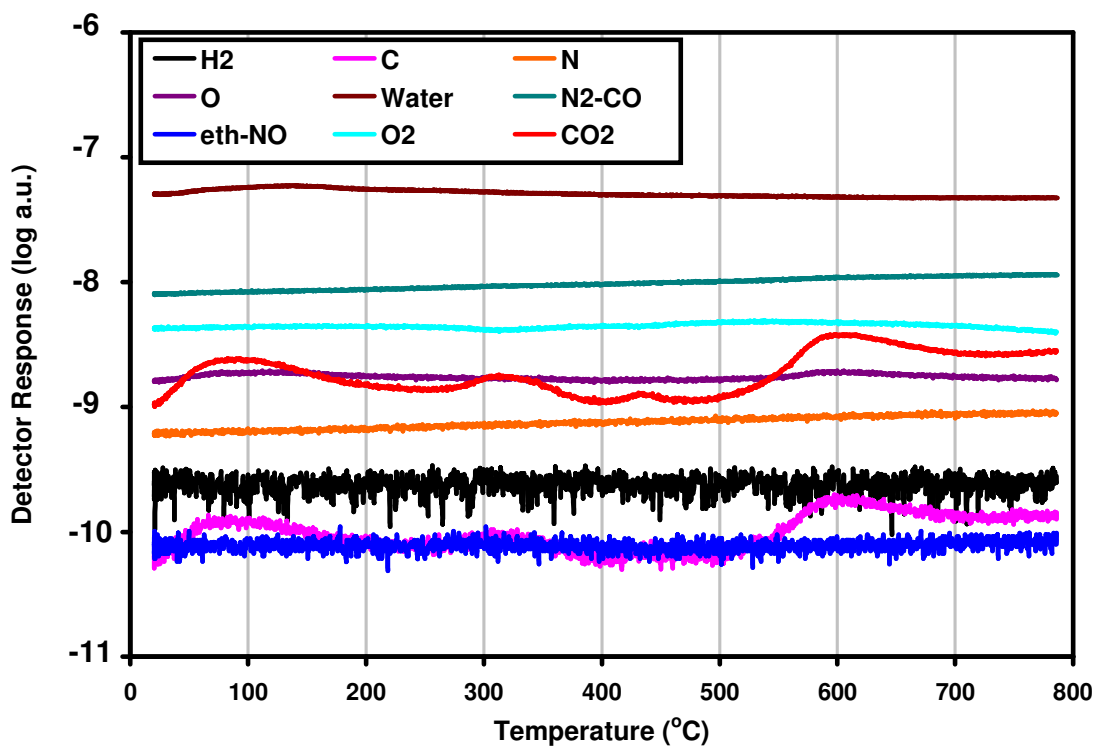
#### 4.4.1 Temperature Programmed Desorption

As the samples were heated in the TPD experiments adsorbed species were released from the sample and were detected by the QMS. A number of  $m/q$  signals were recorded. The main species of interest were water as well as a number of oxygen - (O, CO, O<sub>2</sub> and CO<sub>2</sub>), nitrogen - (N<sub>2</sub>, N and NO<sub>2</sub>) and carbon-containing (C, CO and CO<sub>2</sub>) compounds.

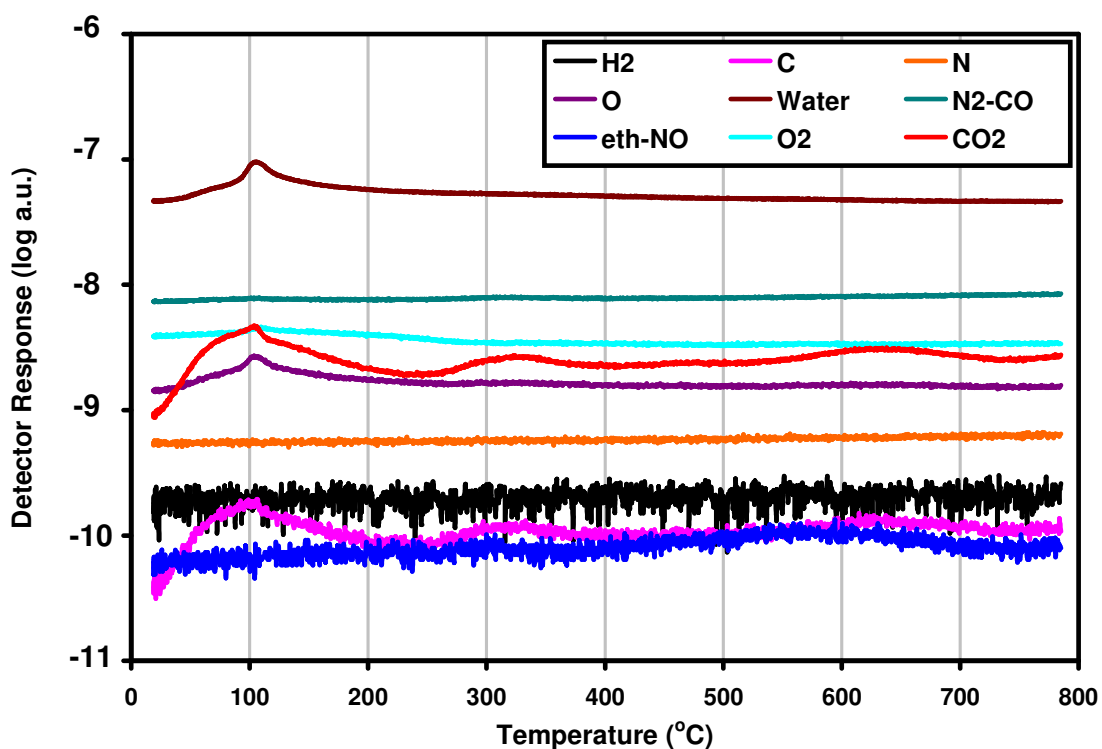
TPD results for the as-prepared oxide samples (Figure 4.5) displayed a sharp peak in  $m/q = 18$  and a smaller peak mirroring this signal in  $m/q = 16$ , at about 105°C. This is characteristic of evolution of water which is then partially broken down in the QMS to give atomic O. The trace for  $m/q = 2$  showed no changes in the TPD. The relatively constant hydrogen signal over the duration of the TPD implies that the water is definitely the result of desorption and not sample reduction.



(b)



(c)



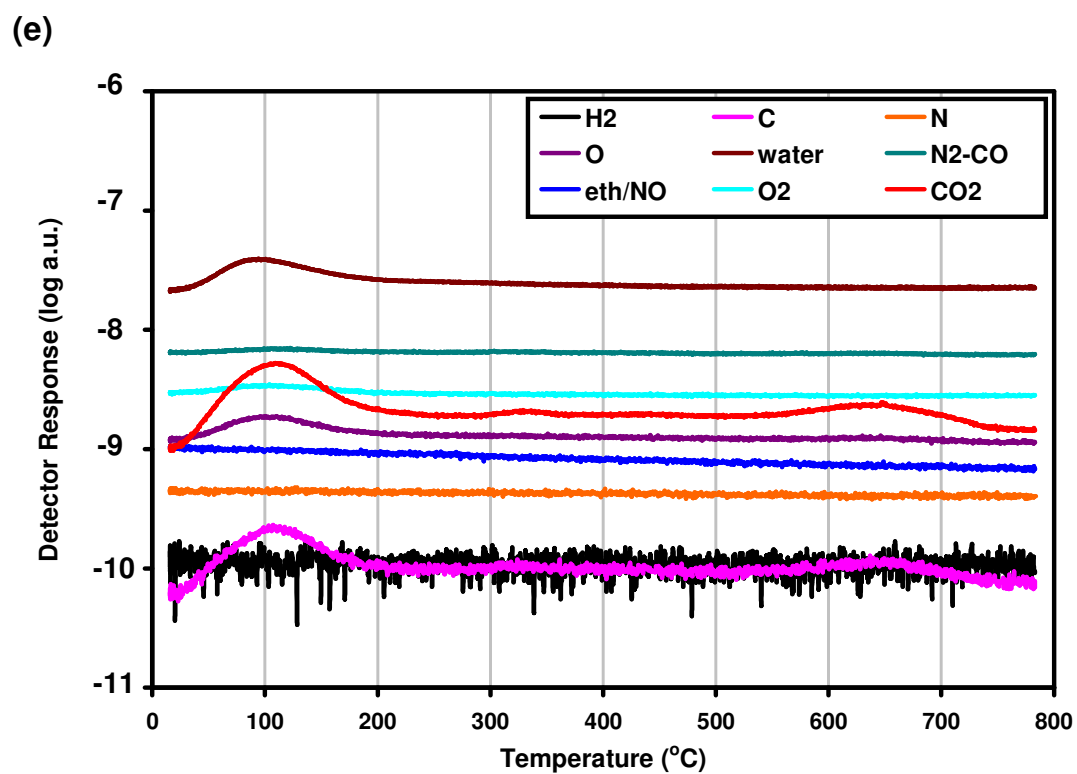
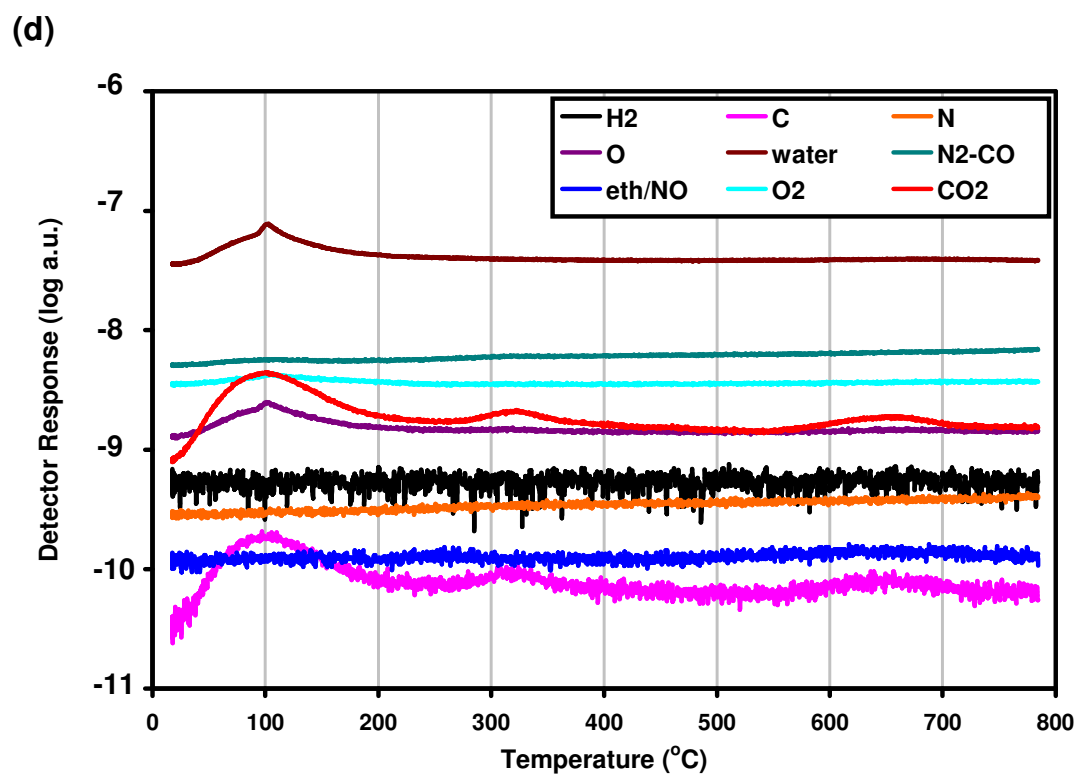


**Figure 4.5** TPD traces for as prepared (a) ZCe10, (b) ZCe25, (c) ZCe50, (d) ZCe75, (e) ZCe90.

The traces for nitrogen - and oxygen - containing species were closely monitored, as variations in these readings could show the presence of an air leak into the experimental system. Peaks were observed in the O traces at around 100°C which can be attributed to the decomposition of desorbed water in the QMS. There were also small O<sub>2</sub> peaks at around this temperature, particularly for ZCe10 (Fig 4.5(a)). This may have been due to the release of atmospheric oxygen adsorbed onto the oxide, [1] as is discussed in Chapter 6. There were increases observed in m/q = 14 (N) and m/q = 28 (N<sub>2</sub>) above 600°C. These two traces suggest evolution of nitrogen. The m/q = 30 (NO) trace also showed a peak for three of the samples, ZCe10, ZCe75 and ZCe90, at around 280°C. The evolution of N – containing species may be due to the nitrates used in the preparation of the samples not being fully decomposed during calcination at 500°C. The residual nitrate appears to have decomposed at the higher experimental temperatures. The NO<sub>2</sub> signal (m/q = 46) was also recorded but no significant change was observed so these are omitted. The amount of nitrogen species evolved during the TPDs was very small.

For clarity the m/q = 44 (Figure 4.6) and m/q = 18 (Figure 4.7) signals have been plotted together for all oxide compositions. The carbon species evolved during TPDs of the oxides appears to be primarily in the form of CO<sub>2</sub>, with the slight changes in the m/q = 28 (CO/N<sub>2</sub>) signal corresponding to small increases in the m/q = 14 (N) level, as the residual nitrates are decomposed. All of the samples investigated gave multiple CO<sub>2</sub> signals during TPD experiments. There were three separate peaks observed in the m/q = 44 signal at about 105, about 315 and 600-650°C, suggesting either the presence of three separate carbon species, or carbon species present at several types of surface site. The m/q = 44 peaks had corresponding peaks at m/q = 12 suggesting the release of CO<sub>2</sub> and its subsequent decomposition in the QMS to give C. All samples gave low, medium and high temperature features which varied in intensity and relative intensity between individual samples. This was most pronounced in ZCe25 (Figure 4.6(b)), which displayed a relatively small low temperature peak (at about 100°C) but much larger high temperature peak (at about 600°C). The medium temperature peak was fairly uniform in intensity and temperature for all samples. At higher temperatures the carbon containing species released are primarily in the form of CO<sub>2</sub> as shown in the m/q = 44 traces in Figure 4.5.

For ZCe75, there was also (Figure 4.6(d)) a contribution to the  $m/q = 44$  trace from the decomposition of the remaining nitrate used in the sample preparation at temperatures above 600°C. This is confirmed by the corresponding increase in the  $m/q = 14$  (N) trace at these temperatures.

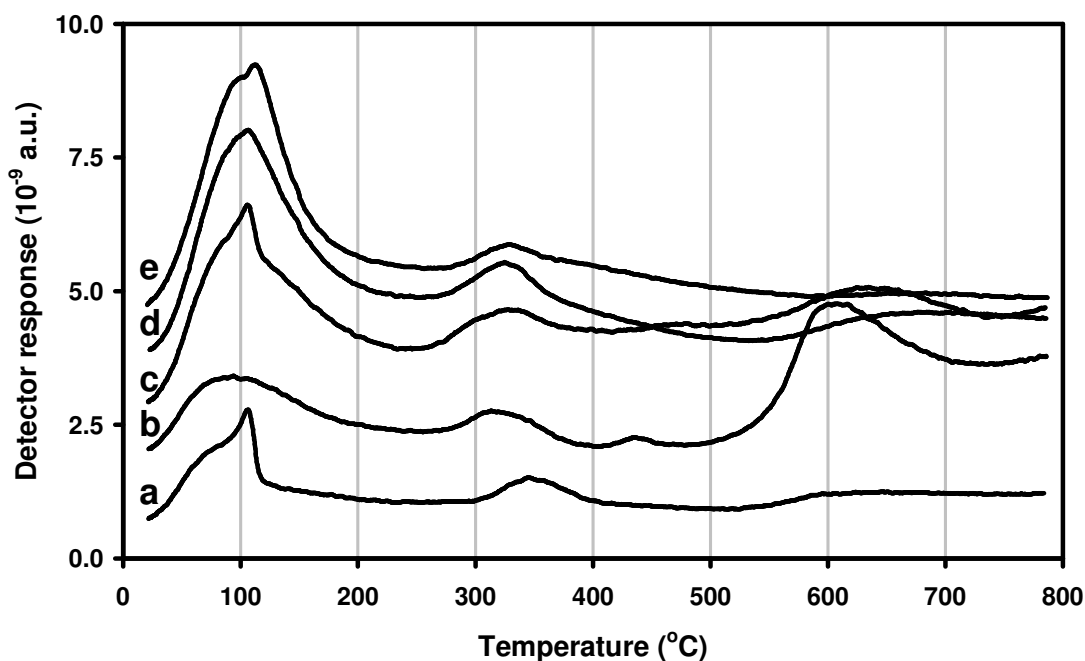


**Figure 4.6** CO<sub>2</sub> traces from TPD experiments on as-prepared (a) ZCe10, (b) ZCe25, (c) ZCe50, (d) ZCe75, (e) ZCe90.

In Figure 4.7, the  $m/q = 18$  (H<sub>2</sub>O) signal consistently showed low temperature desorption of water at about 100°C in all samples. With the exception of ZCe25, which showed minimal water desorption, the amount of water desorbed at this temperature generally increased with increasing ceria concentration up to ZCe75.

While the ZCe25 water trace (Figure 4.7(b)) displayed minimal desorption of water the traces for the other oxides were relatively consistent. The preparation and storage of all the oxides was consistent so it is not known why ZCe25 would be the only material not to display significant water desorption. The fact that ZCe25 also had a pronounced high temperature peak for CO<sub>2</sub> evolution which again contrasted with the other oxides suggests that this sample does appear to vary from the other compositions.

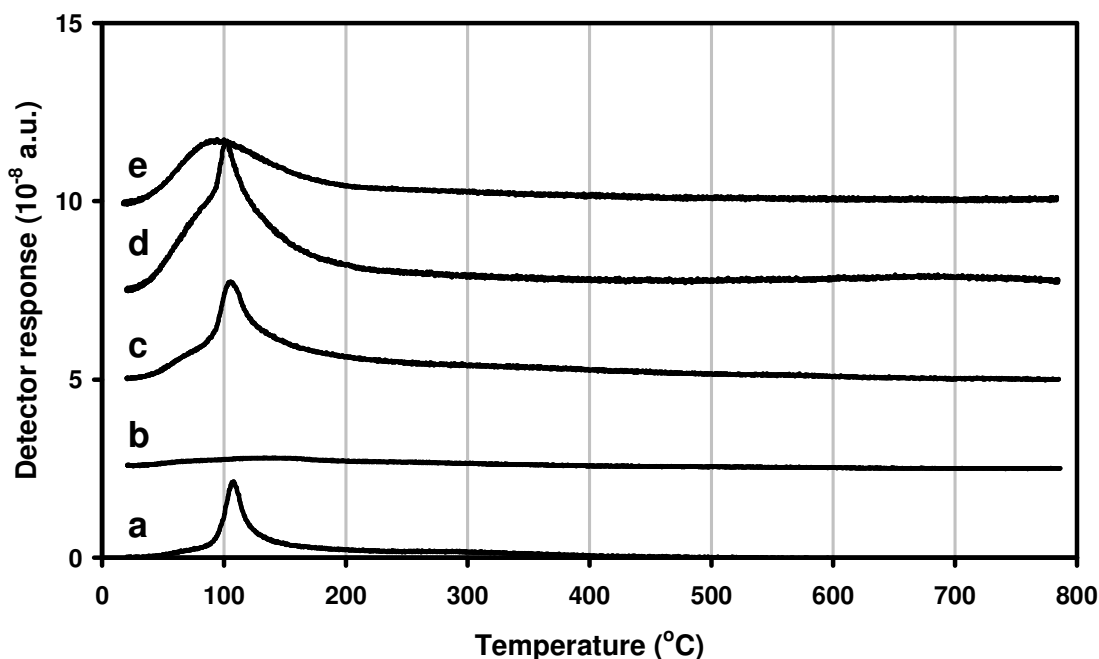


**Figure 4.7** H<sub>2</sub>O traces from the TPDs of as-prepared (a) ZCe10, (b) ZCe25, (c) ZCe50, (d) ZCe75, (e) ZCe90.

#### 4.4.2 Temperature Programmed Reduction

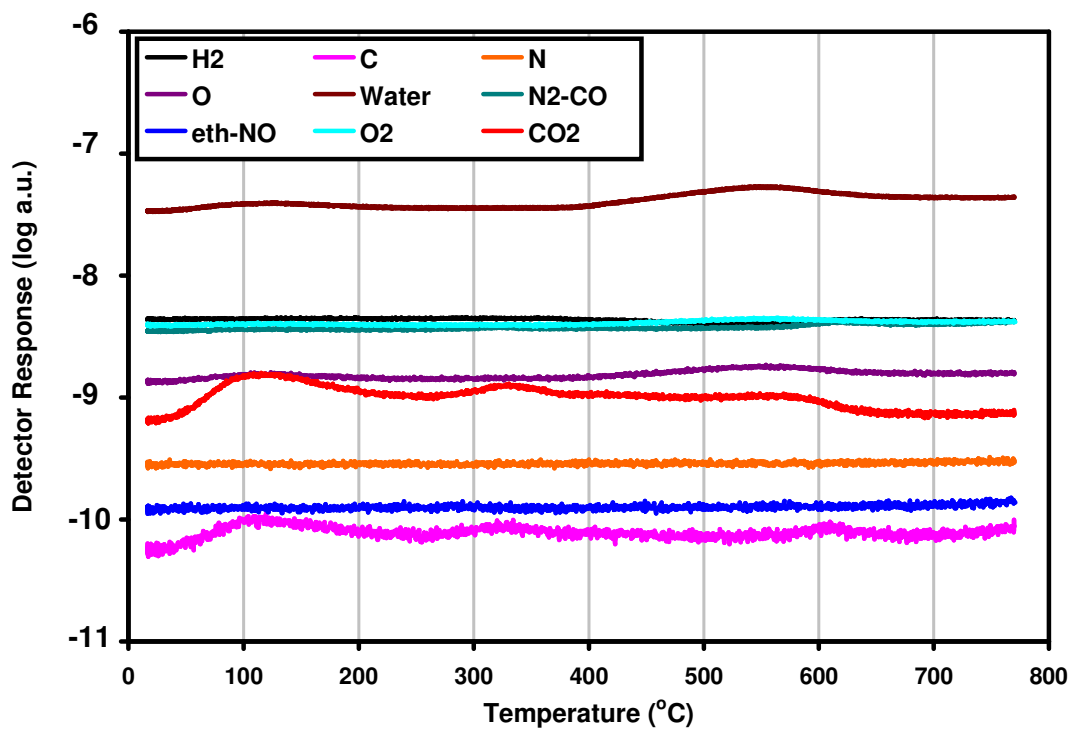
TPR experiments enabled the investigation of the oxygen storage capacity of the sample (shown by the amount of water evolved) and the availability of the oxygen present (shown by the temperature of any water evolution peaks). It was established that the as-prepared samples contained carbon species and adsorbed water (Figure 4.8(a)). To allow for accurate determination of experimental sample reduction, TPD experiments were undertaken prior to the TPRs to remove any adsorbed species (Figures 4.6 and 4.7). Of primary concern was adsorbed water because the evolution of adsorbed water would falsely increase the apparent extent of reduction of the oxide samples.

##### 4.4.2.1 The Effect of TPDs prior to TPRs

TPRs were conducted on as-prepared samples and also on samples after TPD (to 800°C at 5°C min<sup>-1</sup> which are referred to as TPD/R experiments). Plots of all TPD/Rs undertaken on the mixed oxide samples are included as Appendix 1 for completeness. The effect of the TPD experiment on the traces obtained during the TPR experiments is quite distinct and is

shown in Figure 4.8. The  $m/q = 28$  ( $N_2$ ) levels were much more constant in the TPD/R than in the TPR results and there was a dramatic decrease in  $CO_2$  evolved, with only one small peak in the TPD/R compared to three significant peaks in the TPR.

(a)



(b)

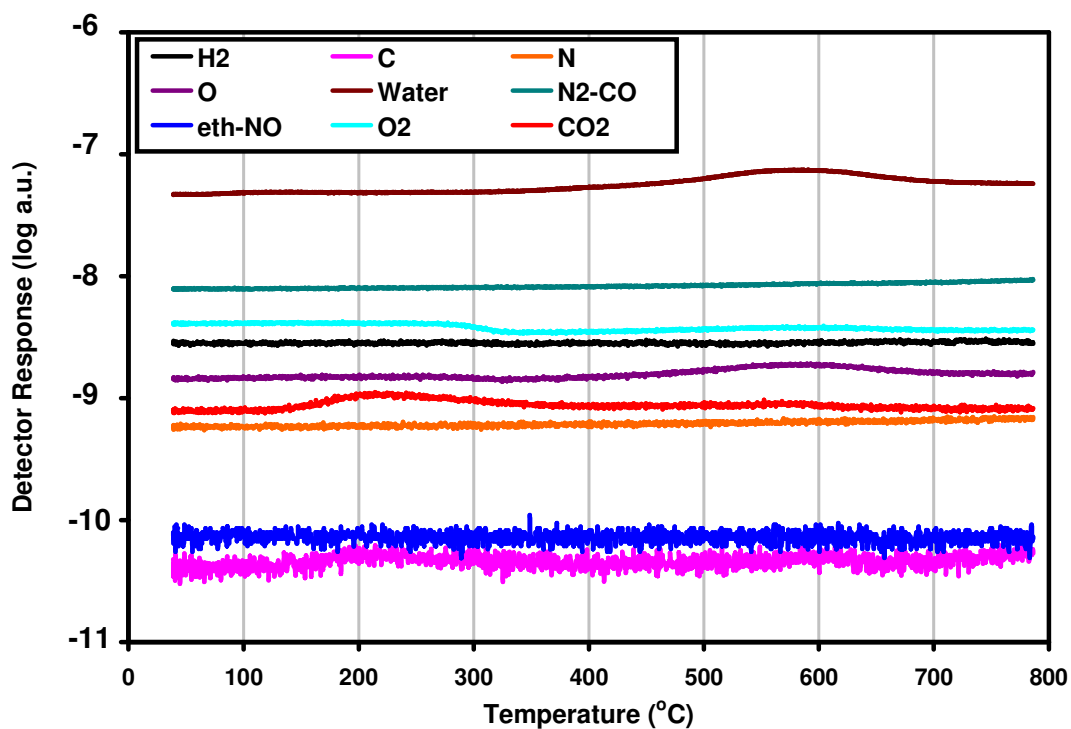


**Figure 4.8** a) TPR of ZCe50 sample as prepared, b) TPD/R of ZCe50.

The position of the CO<sub>2</sub> peak observed in the TPD/R does not correspond to any of the peaks observed in the TPR. It may be the case that the thermal cycling involved in the TPD changed the environment in which the remaining carbon was present. The low temperature water peak observed during the straight TPR experiment was also absent or at least drastically reduced for the TPD/Rs. The high temperature H<sub>2</sub>O peaks were generally slightly reduced in terms of area for the TPD/Rs compared to the TPRs as well as being shifted to higher temperatures. This will be further discussed in the next section.

During the TPR experiment, traces for  $m/q = 18$  and  $m/q = 2$  were monitored closely to ensure correlation between H<sub>2</sub> consumption and water production (Figure 4.9). There was significant evolution of water between 50-150°C for which there was no corresponding decrease in H<sub>2</sub> (Figure 4.10) implying that this water was not produced by reduction of the sample.

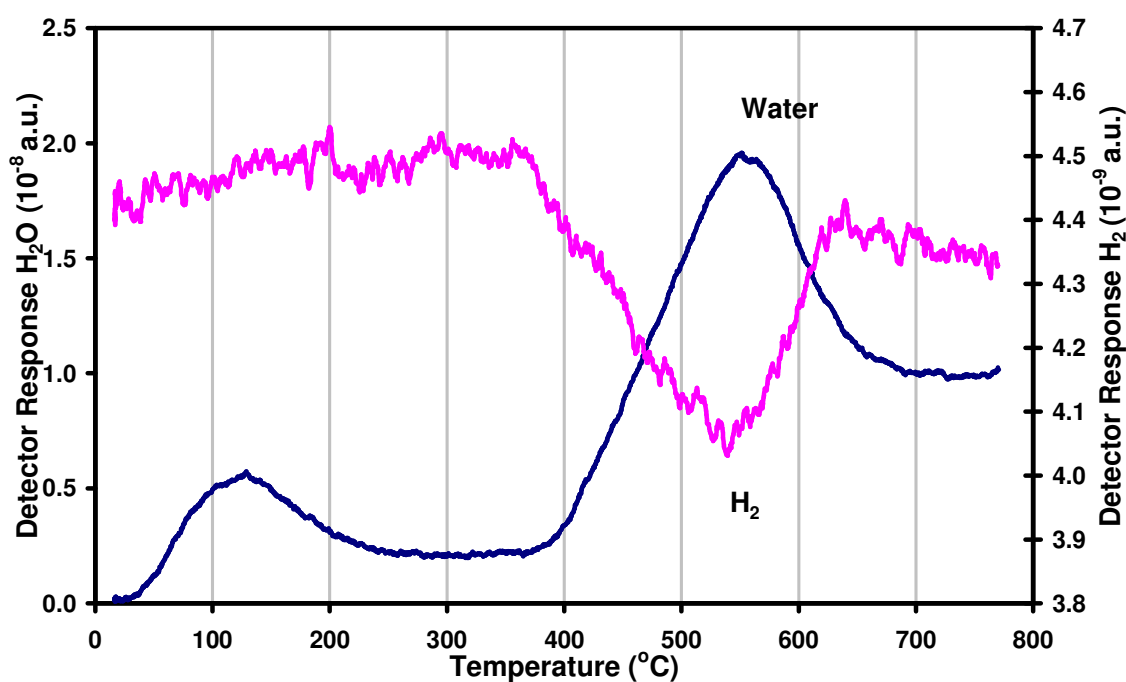


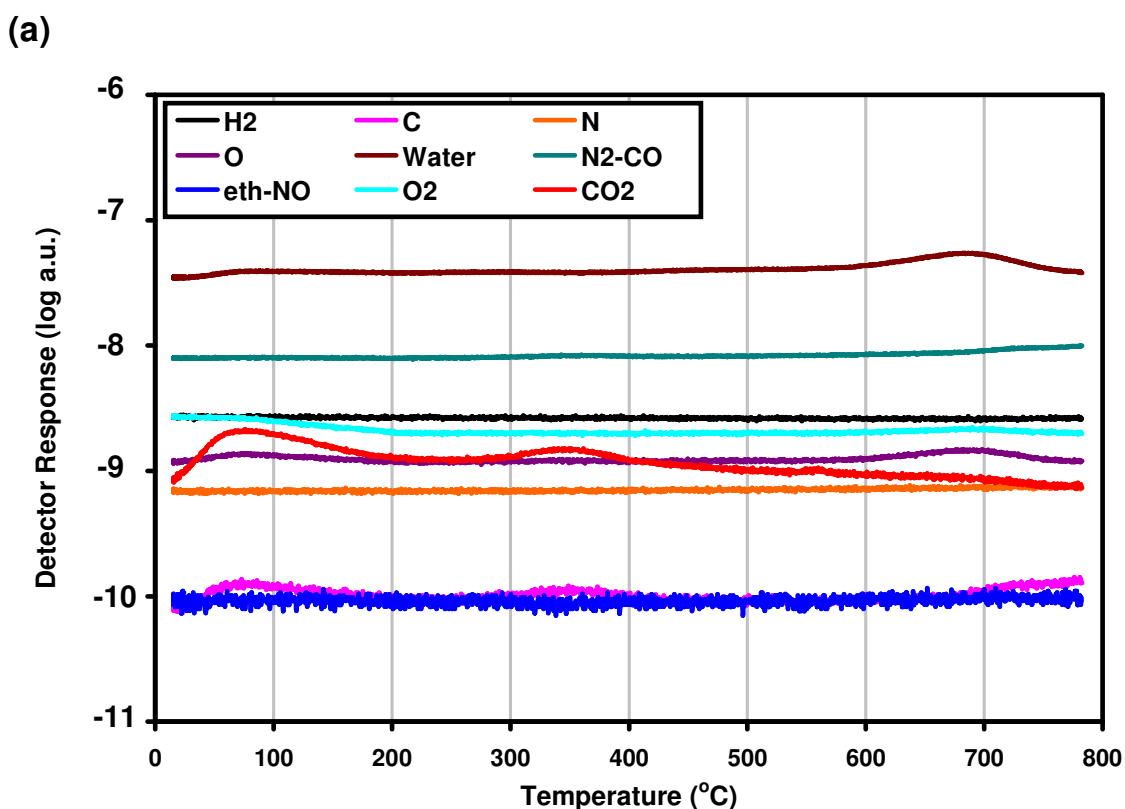
**Figure 4.9** Water and hydrogen traces from TPR of as-prepared ZCe50 sample.

This effect was observed for all samples to some degree but was most pronounced in high ceria concentration samples (Figure 4.11). Low temperature water and hydrogen traces were on very different scales because the QMS was much less sensitive to hydrogen than to water. In order to directly compare the two traces the hydrogen signal was amplified and smoothed (using a 10 point moving average) in order to reduce the noise present in the raw

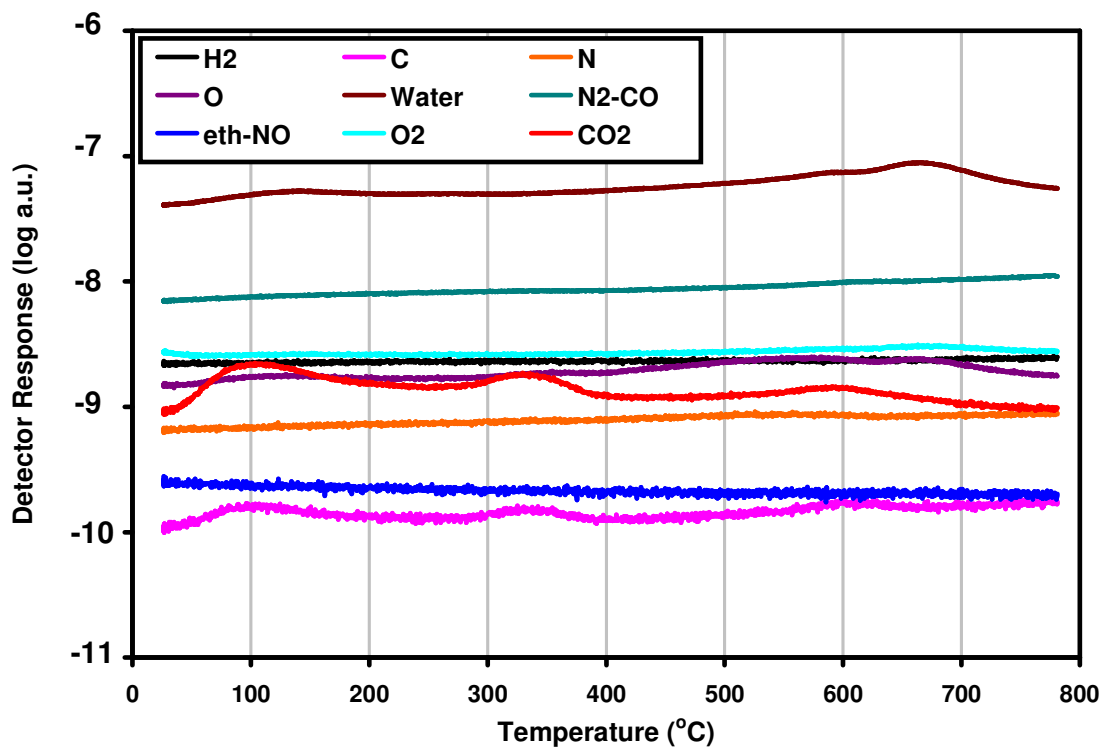
data. True reduction peaks were observed in the TPRs at higher temperatures, in the range 550-700°C and here it is clear that H<sub>2</sub> is consumed and H<sub>2</sub>O evolved simultaneously. The temperature at which reduction occurred decreased with increasing ceria concentration up to the ZCe50 sample, before increasing slightly thereafter.

#### 4.4.2.2 The Effect of Mixed Oxide Composition on TPRs

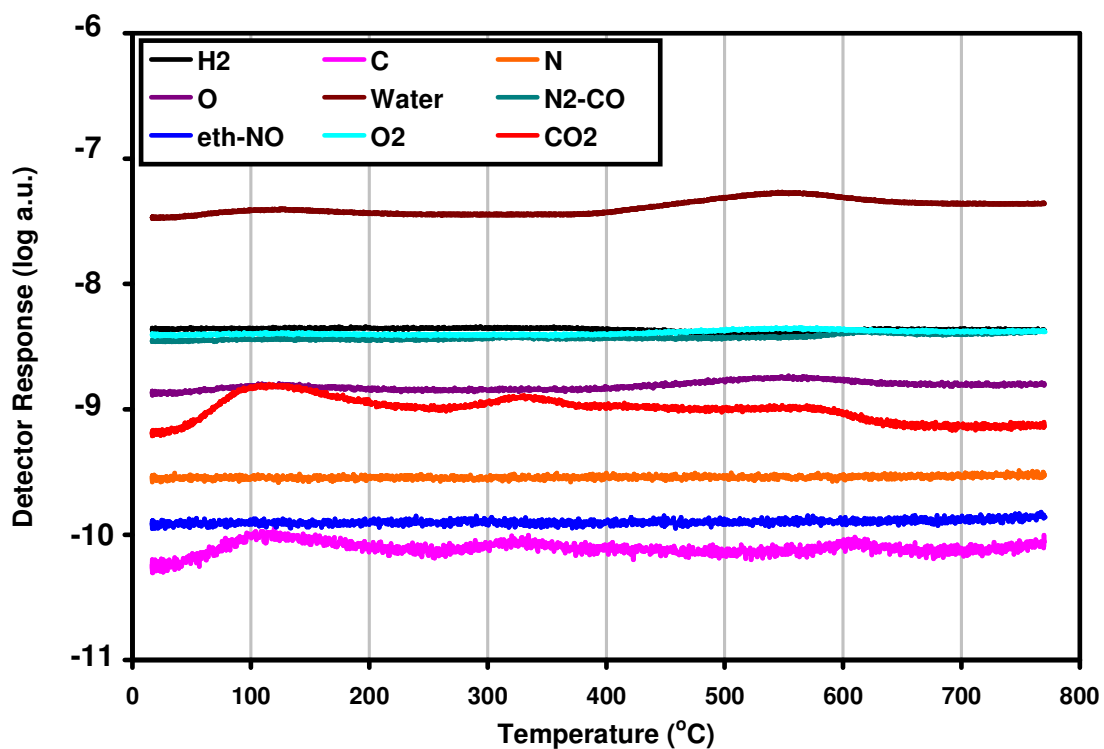
The large low temperature desorption of water in the TPR results meant that determining the extent of sample reduction was difficult because the apparent extent of reduction would be artificially increased by the desorption. In order to rectify this a TPD was performed on the oxide samples (as described in Section 4.3.1) before TPR experiments. As a result, the adsorbed H<sub>2</sub>O was desorbed in the TPD and not in the subsequent TPR. TPRs obtained in this way are presented in Figure 4.12 and referred to as TPD/Rs. These traces were used to obtain a more accurate estimate of the extent of reduction of the oxides.

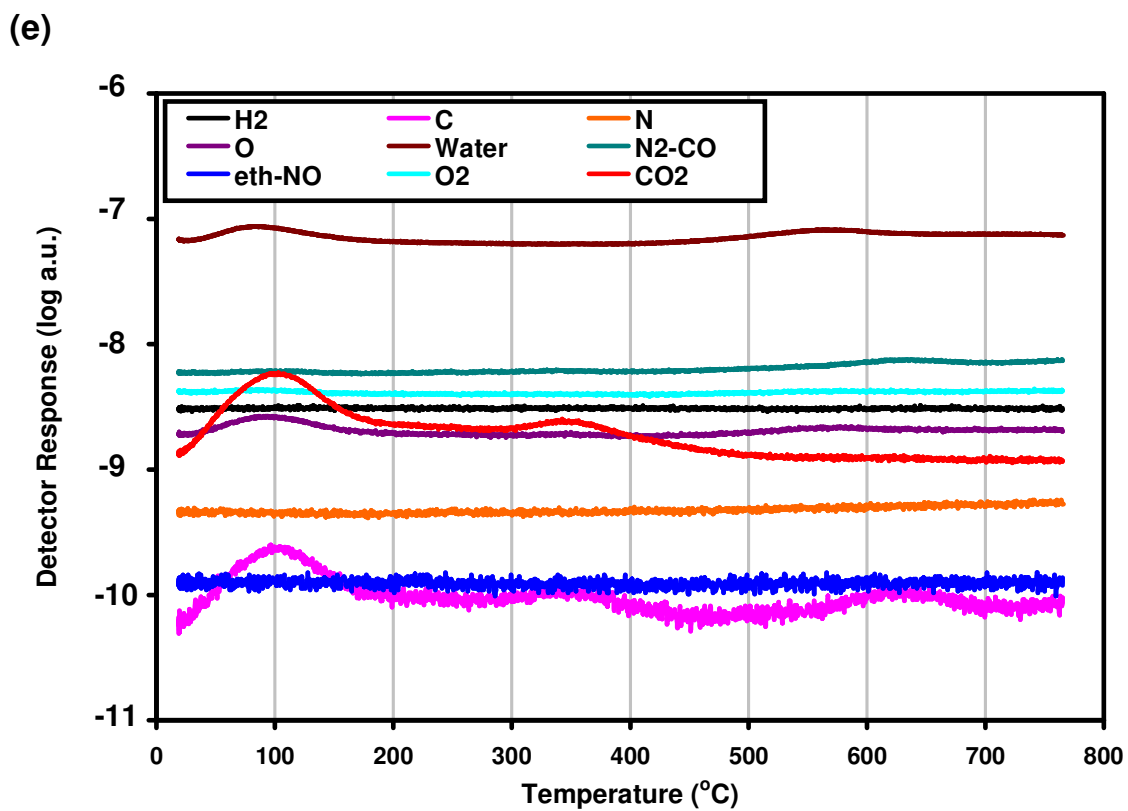
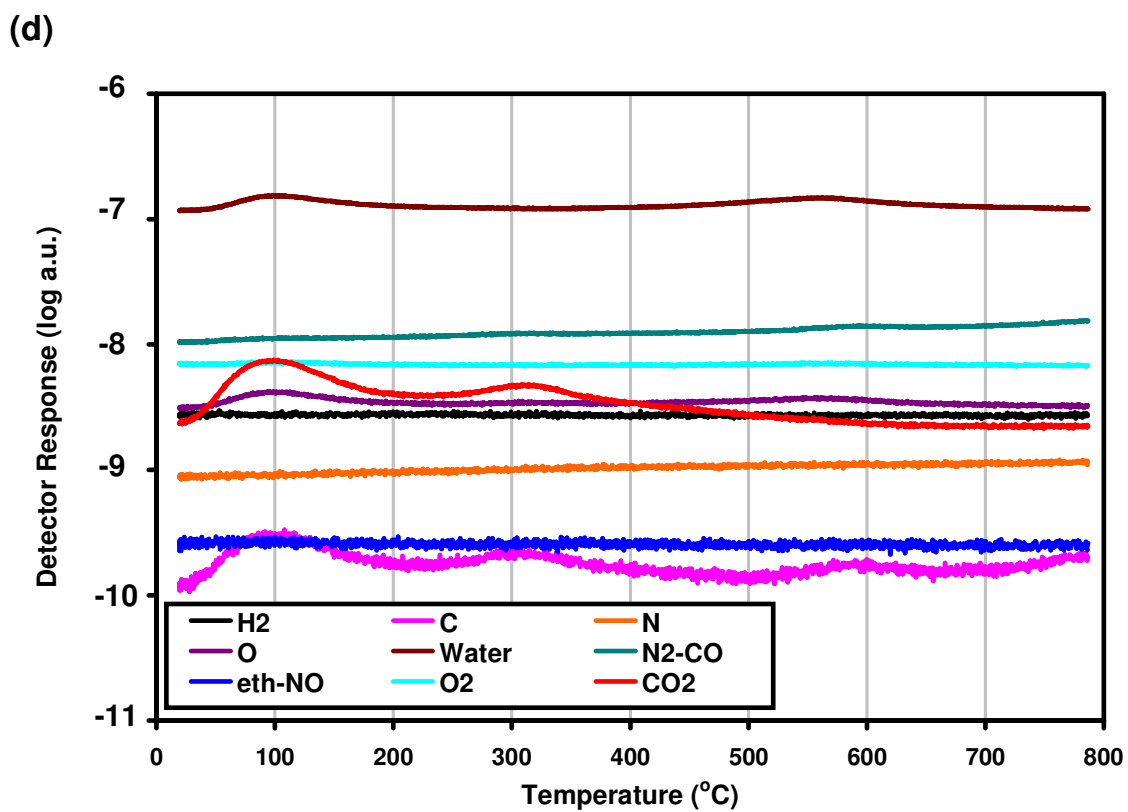


(b)



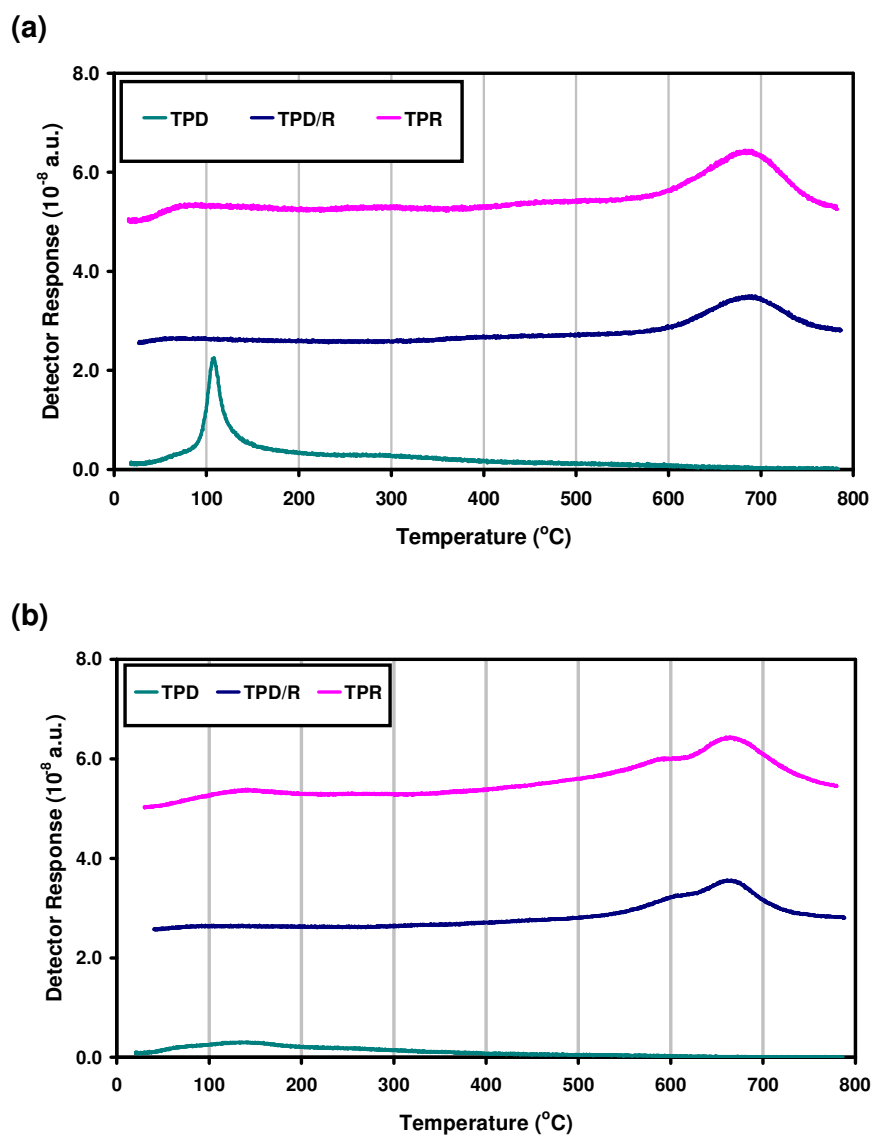
(c)





**Figure 4.10** TPR traces for as-prepared (a) ZCe10, (b) ZCe25, (c) ZCe50, (d) ZCe75, (e) ZCe90.

TPD, TPR and TPD/R water traces have been plotted on the same axis in order to reveal any effect of the thermal cycling due to the TPD and are shown in Figure 4.11. The TPRs showed less low temperature water production than the TPDs, which is surprising as the amount of water adsorbed in the samples would be expected to be identical for both sets of runs. The TPR experiments were performed before the TPD and TPD/R experiments. It may be the case that small amounts of atmospheric water were adsorbed onto the sample during the intervening period. The samples were kept in sealed containers so any adsorption of atmospheric species should be minimal.



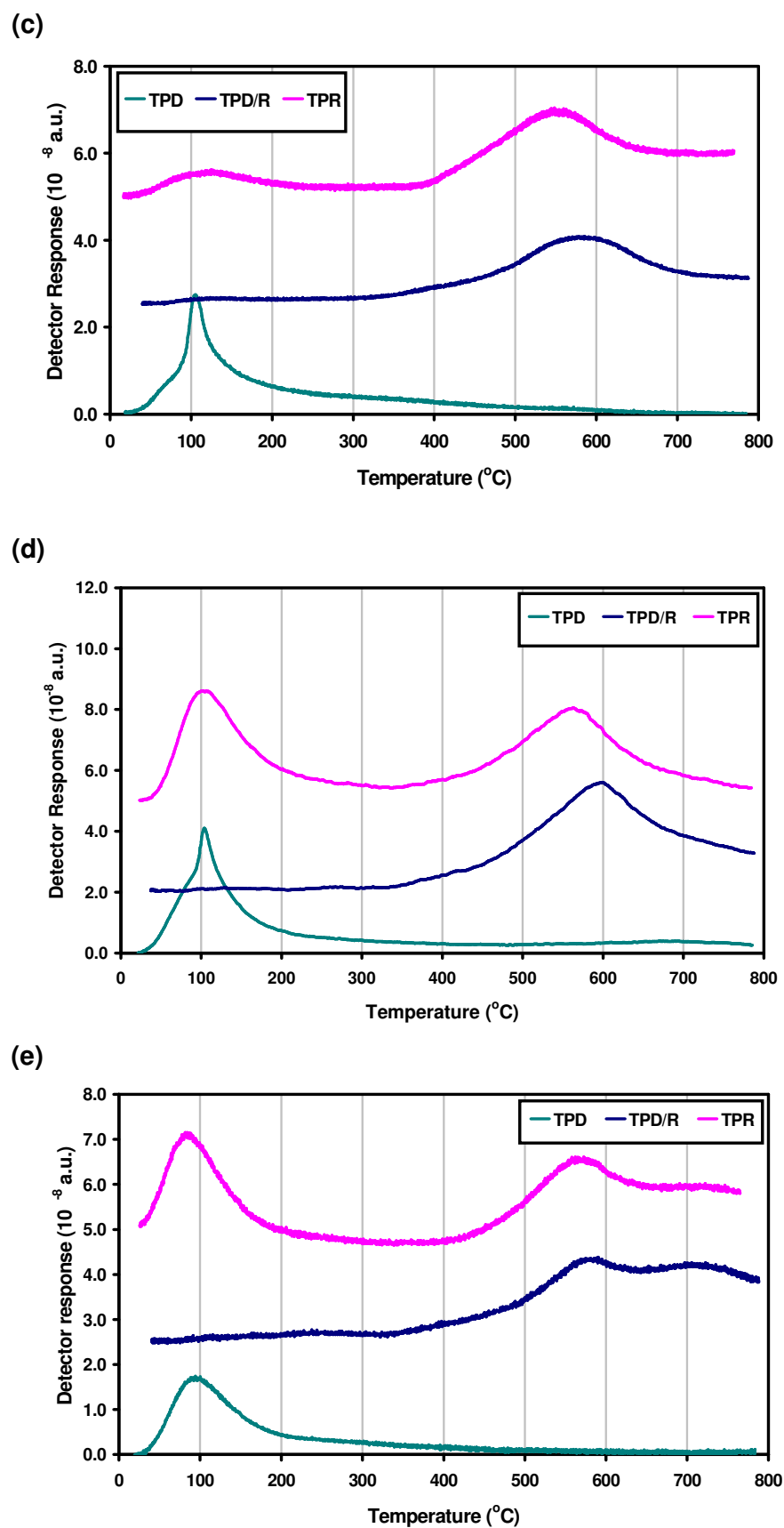


**Figure 4.11** Water traces from TPD, TPD/R and TPR experiments plotted for (a) ZCe10, (b) ZCe25, (c) ZCe50, (d) ZCe75, (e) ZCe90.

In order to allow direct comparison between samples the water traces from the TPRs (Figure 4.12) and TPD/Rs (Figure 4.13) were plotted for all mixed oxide compositions. The TPD experiments have the effect of drastically reducing if not completely eradicating the low temperature water peak observed in the straight TPRs. It is a reasonable conclusion that the low temperature water peaks observed are due to desorption. The high temperature peaks were observed at slightly increased temperatures in the TPD/Rs compared to those observed from the straight TPRs. The positions of the reduction peaks for the TPR and TPD/R experiments are plotted as a function of mole % CeO<sub>2</sub> in Figure 4.14.

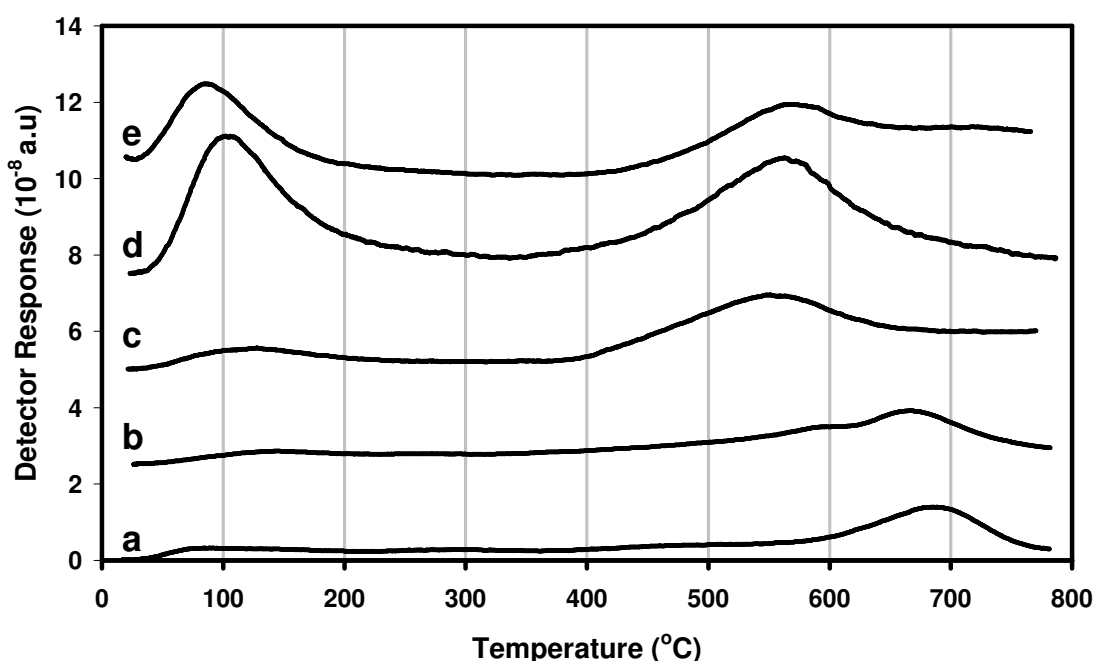


**Figure 4.12** Water traces from TPRs conducted on as-prepared Zr/Ce oxides (a) ZCe10, (b) ZCe25, (c) ZCe50, (d) ZCe75, (e) ZCe90.

The water traces from the straight TPRs all showed low temperature water peaks at around 100°C which are most pronounced for the high (mole %) ceria samples (Figure 4.12(d) and (e)). The low temperature peaks observed for the ZCe10, ZCe25 and ZCe50 samples were markedly smaller. All samples also displayed high temperature evolution of water (between 500-800°C). These peaks relate to the reduction of the samples. The temperature of this reduction peak varied with material composition. ZCe50 had the lowest temperature reduction peak (557°C) closely followed by ZCe75 (567°C) and ZCe90 (572°C). The high temperature water peak observed for the samples with low ceria contents were at higher

temperatures. The peak for ZCe25 was the lower (667°C) and ZCe10 had the highest temperature water peak (685°C). A number of the samples displayed multiple high temperature peaks. This was most pronounced in ZCe25 (Figure 4.12(b)) where there was a distinct shoulder on the high temperature peak (at 598°C) and ZCe90 which displayed a second high temperature peak (at 717°C).

TPD/R runs showed minimal low temperature water evolution since the adsorbed water present in the straight TPR runs had been desorbed during the TPD. The high temperature water peaks were all at a slightly increased temperature and were less pronounced than those for the straight TPRs (Figure 4.13). The high temperature water peak positions showed a similar pattern for the TPD/R runs as that observed in the straight TPRs. ZCe90 had the lowest temperature reduction peak (581°C) closely followed by ZCe50 (589°C) and ZCe75 (598°C).

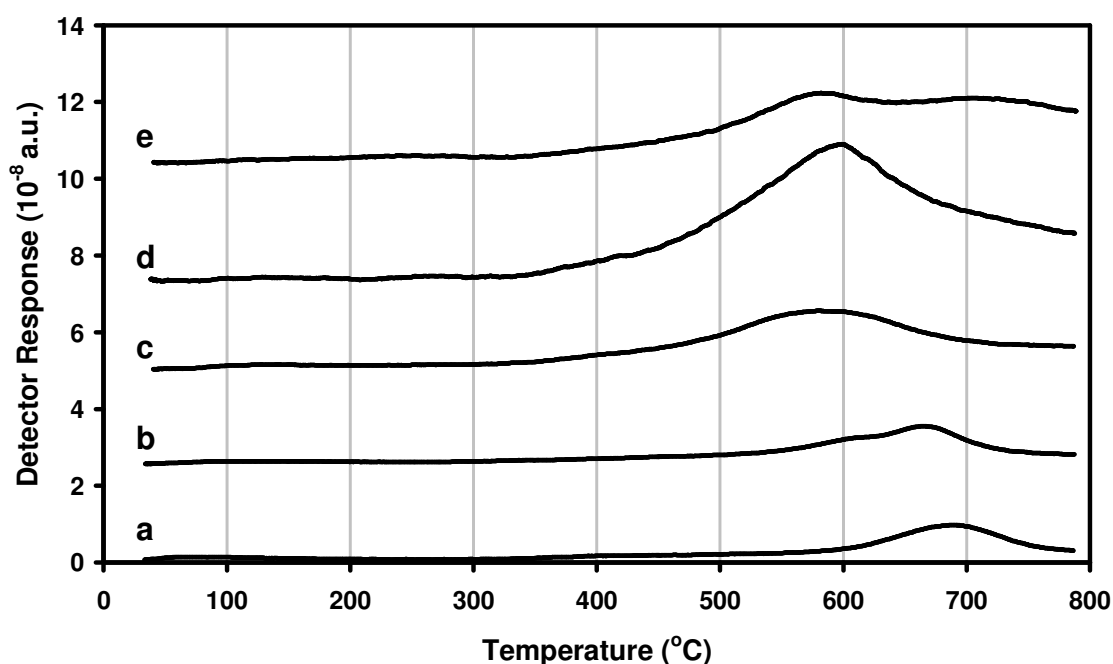


**Figure 4.13** Water traces from TPD/Rs for (a) ZCe10, (b) ZCe25, (c) ZCe50, (d) ZCe75, (e) ZCe90.

The high temperature water peak observed for the low (mole %) ceria samples were again at higher temperatures than in the TPR results. The peak for ZCe25 was the lower (666°C) and the peak for ZCe10 was the highest overall (690°C). The high temperature water peaks observed in the TPD/Rs differed from those in straight TPRs for all of the oxide

compositions. This was attributed to a thermal cycling effect which appeared to have less effect on the samples of low ceria content. The peak reduction temperature observed for the TPD/Rs compared to the TPRs decreased by 1°C for ZCe25 following the TPD and increased by 5°C for ZCe10.

The effect of the TPD experiments and the thermal cycling involved can be clearly seen in the positions of the high temperature peaks in Figure 4.14. The biggest differences in the peak reduction temperatures between the TPR and the TPD/R results was shown by ZCe50 (32°C) and ZCe75 (31°C). The changes in peak reduction temperature for the remaining samples were small (+5°C for ZCe10, -1°C for ZCe25, +9°C for ZCe90). The positions of the local maxima (shoulders and additional peaks) were again very similar in the TPR and TPD/R spectra. These minor peaks were generally much smaller than the main reduction peaks.

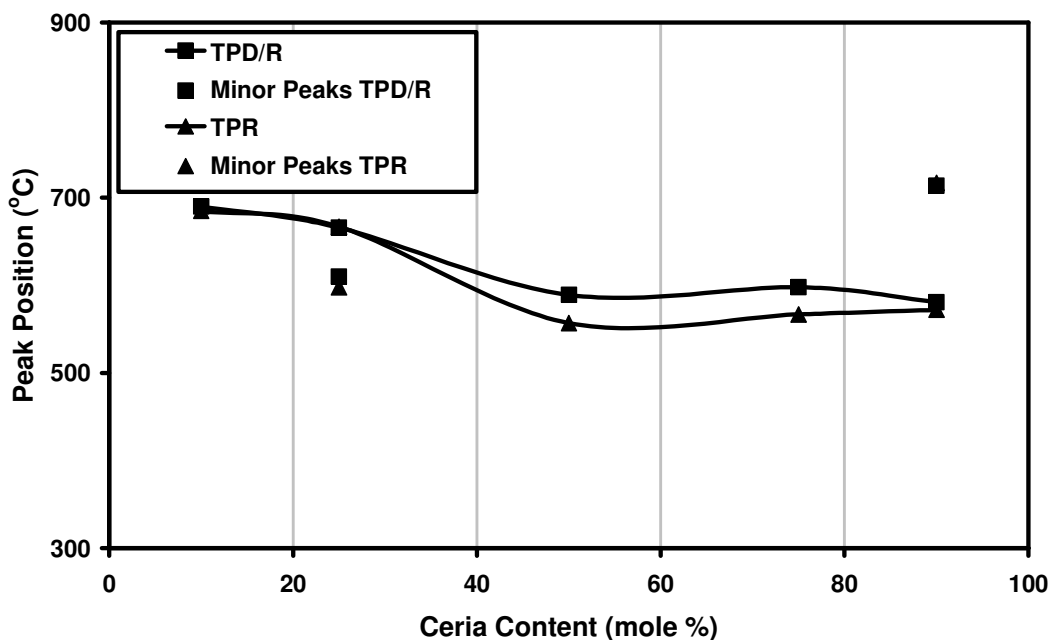


**Figure 4.14** Reduction peak positions taken from the TPR and TPD/R results for ZCe solid solutions.

The amount of water evolved during the reduction experiments was calculated over the entire length of the run by measuring the total area beneath the water traces and using the water calibration obtained as described in Section 3.6.3. In Figure 4.15 the number of moles of water produced during the TPR runs is plotted for both straight TPR and TPD/R

results. As the value is calculated over the entirety of the experiment there is a large gap between the water produced by the two different types of experiments because the straight TPRs contain a contribution from the desorbed water. For comparison, the theoretical maximum amount of water produced if the samples were 100% reduced was also plotted. The theoretical maximum was obtained by calculating the moles of Ce present in each sample to be investigated. It was assumed that all Ce present in the oxide was present as  $Ce^{4+}$  and that this was reduced to  $Ce^{3+}$  during the course of the TPR. The amount of oxygen that would be removed and hence the amount of  $H_2O$  that would be produced was calculated.

The number of moles of water produced approached the theoretical maximum for the low ceria content materials before dipping below the theoretical line for the samples with higher ceria contents. As would be expected, the straight TPR runs evolved more water than the TPD/R runs. The moles of water evolved increased with ceria concentration up to ZCe75 before declining slightly to ZCe90. The TPD/R traces provide the best indication of the reduction behaviour of these materials as the water produced is unlikely to be due to desorption but only to sample reduction. The numbers of moles of water produced were converted into a percentage of the theoretical maximum yield where it was assumed that all Ce is present as  $Ce^{4+}$  and was reduced to  $Ce^{3+}$  by the  $H_2$  (Table 4.1).

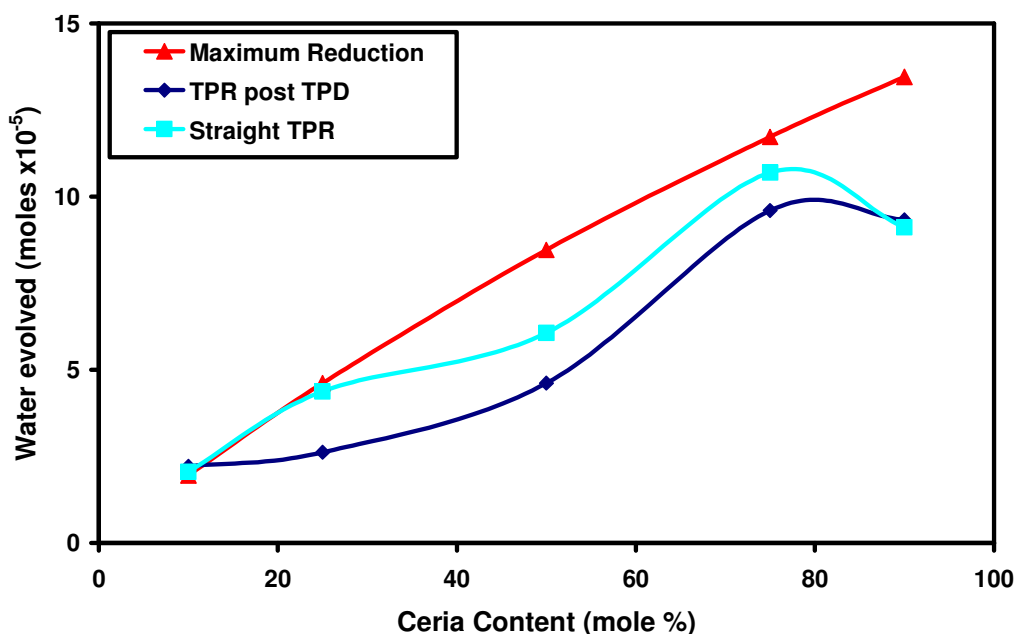


**Figure 4.15** Moles of water produced during TPR and TPD/R of ZCe mixed oxides. Maximum theoretical water evolution is also plotted for comparison.

**Table 4.1** Peak positions and water production data for TPR and TPD/R experiments on Ce/Zr mixed oxides.

Mole % Cerium	Experiment Type	Major peak (°C)	Minor peak (°C)	Moles of water (10 <sup>-5</sup> )	% of theoretical maximum
10	TPR	685	530	2.05	105.2
	TPD/TPR	690	390	2.21	113.1
25	TPR	667	598	4.38	94.8
	TPD/TPR	666	610	2.62	56.7
50	TPR	557	-	6.06	71.6
	TPD/TPR	589	-	4.61	54.5
75	TPR	567	-	10.70	91.2
	TPD/TPR	598	-	9.60	81.9
90	TPR	572	717	9.12	67.5
	TPD/TPR	581	714	9.33	69.3

The number of moles of water produced (Figure 4.15) gives an indication of the oxygen storage capacity of the materials, as the water is produced when oxygen from the sample reacts with the H<sub>2</sub> gas. Materials with higher ceria contents would be expected to produce more water as it is the Ce<sup>4+</sup> which is reduced. However whilst the information gained in this way is important, the extent to which the materials are reduced is also revealing. Figure 4.16 shows a very different trend to that observed in Figure 4.15. As in Figure 4.15, the straight TPRs generally showed a higher percentage of total theoretical water evolution, because of the inclusion of desorbed water. The ZCe10 sample showed water production over 100% in the TPR and TPD/R. This was due to the low ceria content of these samples. Any adsorbed water present in the sample would greatly increase the percentage of water produced.

As for Figure 4.15, the TPD/R runs provided the most reliable information on extent of sample reduction. The largest theoretical yield for TPD/R runs was for ZCe10 (105%), then ZCe75 (82%), so, despite the fact that ZCe75 produced more than four times the amount of water as the ZCe10 sample in the TPD/Rs, the extent of reduction was actually lower. ZCe25 (57%) and ZCe50 (55%) were again comparable with ZCe90 (69%) having the third highest percentage of theoretical water production.

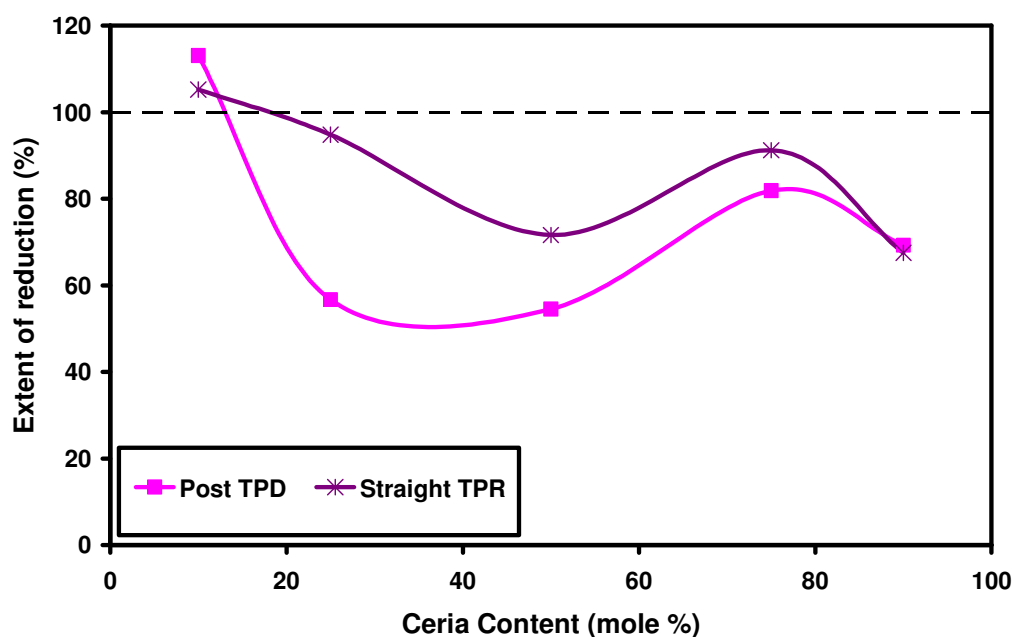


**Figure 4.16** Water produced during the TPR and TPD/Rs for all ZCe mixed oxide compositions as a percentage of the maximum theoretical yield.

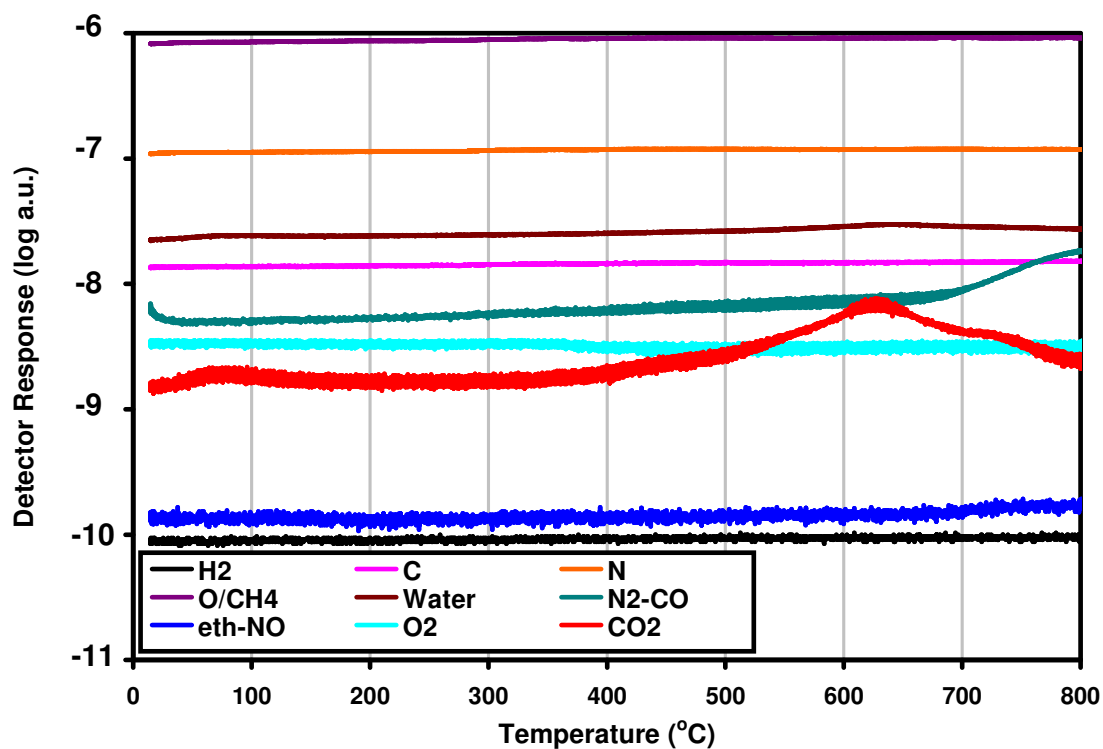
#### 4.4.3 Temperature Programmed Reaction

Temperature programmed reaction (TPRx) experiments used a reactive gas (5% methane in Ar) in the place of H<sub>2</sub>. The reactive gas would then be oxidised by the oxygen contained in the sample. TPRx experiments of only two of the oxide samples were run as it was felt that alternative experiments could provide more useful data.

The TPRx experiments were run on as-prepared samples. As a result, both displayed low temperature water and CO<sub>2</sub> peaks at about 100°C as observed in the TPD and TPR runs. ZCe50 (Figure 4.17(a)) displayed a large CO<sub>2</sub> peak (at about 615°C) which was attributed to the complete oxidation of the CH<sub>4</sub> by the oxygen in the sample. Both samples displayed high temperature H<sub>2</sub> and CO production around 850°C with a corresponding decrease in CH<sub>4</sub>. This suggests that partial oxidation of the CH<sub>4</sub> had occurred at these temperatures. This was more pronounced for ZCe90. From these results it appeared that ZCe50 displayed complete oxidation and then at higher temperature partial oxidation. In contrast the TPRx run on ZCe90 showed minimal evidence of total oxidation but a greater amount of high temperature partial oxidation. The release of residual NO from ZCe50 was also observed at

high temperature (860°C), which was attributed to the decomposition of the remaining nitrate used in the preparation of the sample.

(a)



(b)

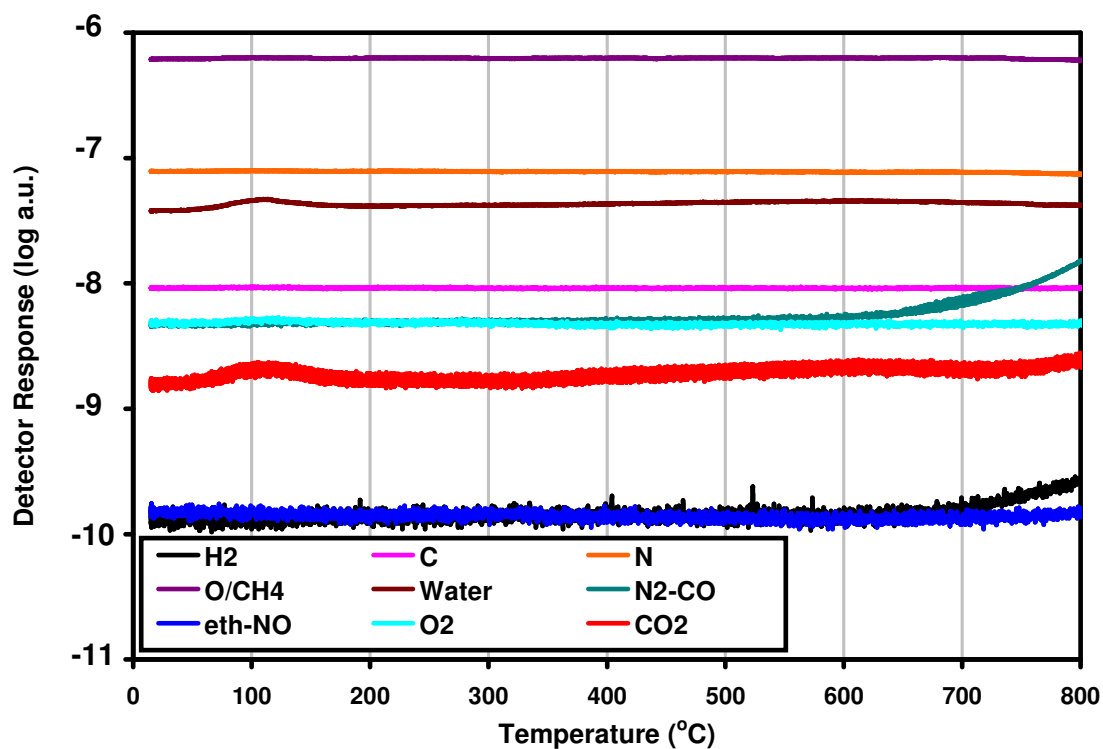
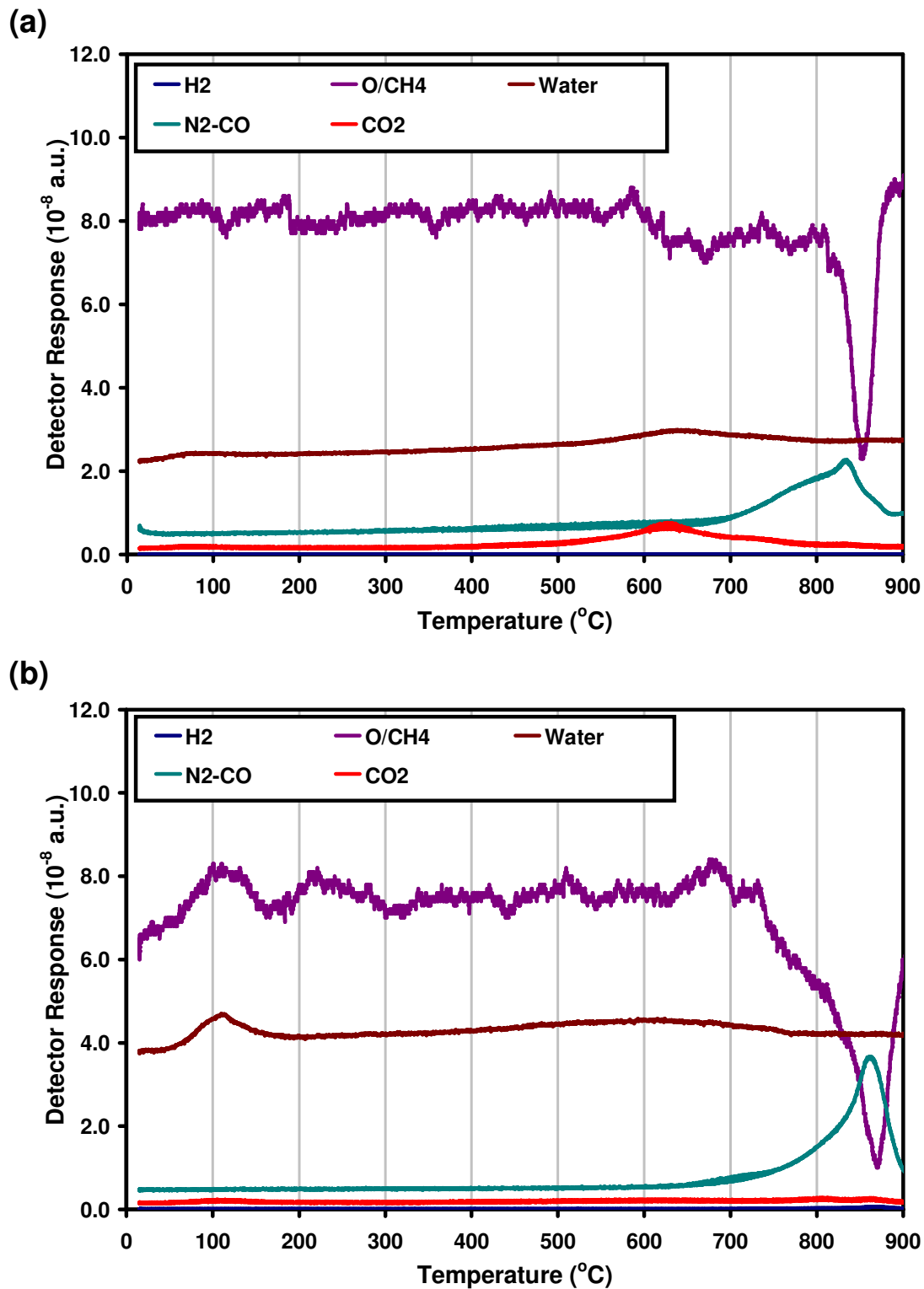


Figure 4.17 Log TPRx traces for as-prepared a) ZCe50 b) ZCe90.

The logarithmic plots shown in Figure 4.17 showed a number of the traces effectively, but made it very difficult to discern the changes in CH<sub>4</sub> levels. Therefore, the CH<sub>4</sub> traces were shifted down the y-axis and plotted on a linear scale in Figure 4.16 to show how they correspond to the other traces.



**Figure 4.18** Linear TPRx traces for as-prepared a) ZCe50 b) ZCe90.

#### 4.4.4 Temperature Programmed Oxidation

TPO runs were performed on samples that had been subjected to a TPRx experiment, as described in the previous section, in order to establish the nature and quantity of species deposited on the sample during the reaction with methane. Results are shown in Figure 4.19 (logarithmic y-axis scale) and Figure 4.20 (linear y-axis scale).

The TPO results for ZCe50 showed large peaks for CO<sub>2</sub>, CO and C at 300°C and a corresponding dip in O<sub>2</sub>, as well as a set of smaller peaks at around 590°C. This implies that large amounts of carbon species had been deposited onto the ZCe50 during the TPRx. ZCe90 also displayed two peaks for carbon species (280°C and 690°C), though these peaks were smaller than those observed for ZCe50. For both samples there was a relatively minor dip in the O<sub>2</sub> level, before the second much larger decrease in the O<sub>2</sub> level. This first dip was therefore thought to result from either oxidation of the oxide sample, or from the oxidation of surface carbon deposits. The carbon deposits were then further oxidised and released from the sample as the temperature was increased.

During the TPRx experiment on ZCe90 the dip in CH<sub>4</sub> corresponded with an increase in the CO level, suggesting that there was sufficient oxygen in the sample to allow for the partial oxidation of the CH<sub>4</sub> over the applicable temperature range. For the ZCe50 sample, however, the major dip in CH<sub>4</sub> was at a slightly higher temperature than the main CO peak. In this case, the major CH<sub>4</sub> consumption corresponds with production of H<sub>2</sub>. This suggests that the methane was converted into carbon deposits on the oxide surface, with the resultant release of H<sub>2</sub> (Figure 4.17(b)). The levels of the H<sub>2</sub> trace is much lower than for other species due to the low sensitivity of the QMS to H<sub>2</sub>. The ZCe50 might be expected to experience greater carbon deposition than ZCe90, as the ZCe90 sample would have nearly twice the amount of available oxygen. The amount of carbon deposited in the TPRx experiments was calculated to be in the ratio 2.2:1 for ZCe50 to ZCe90, respectively.

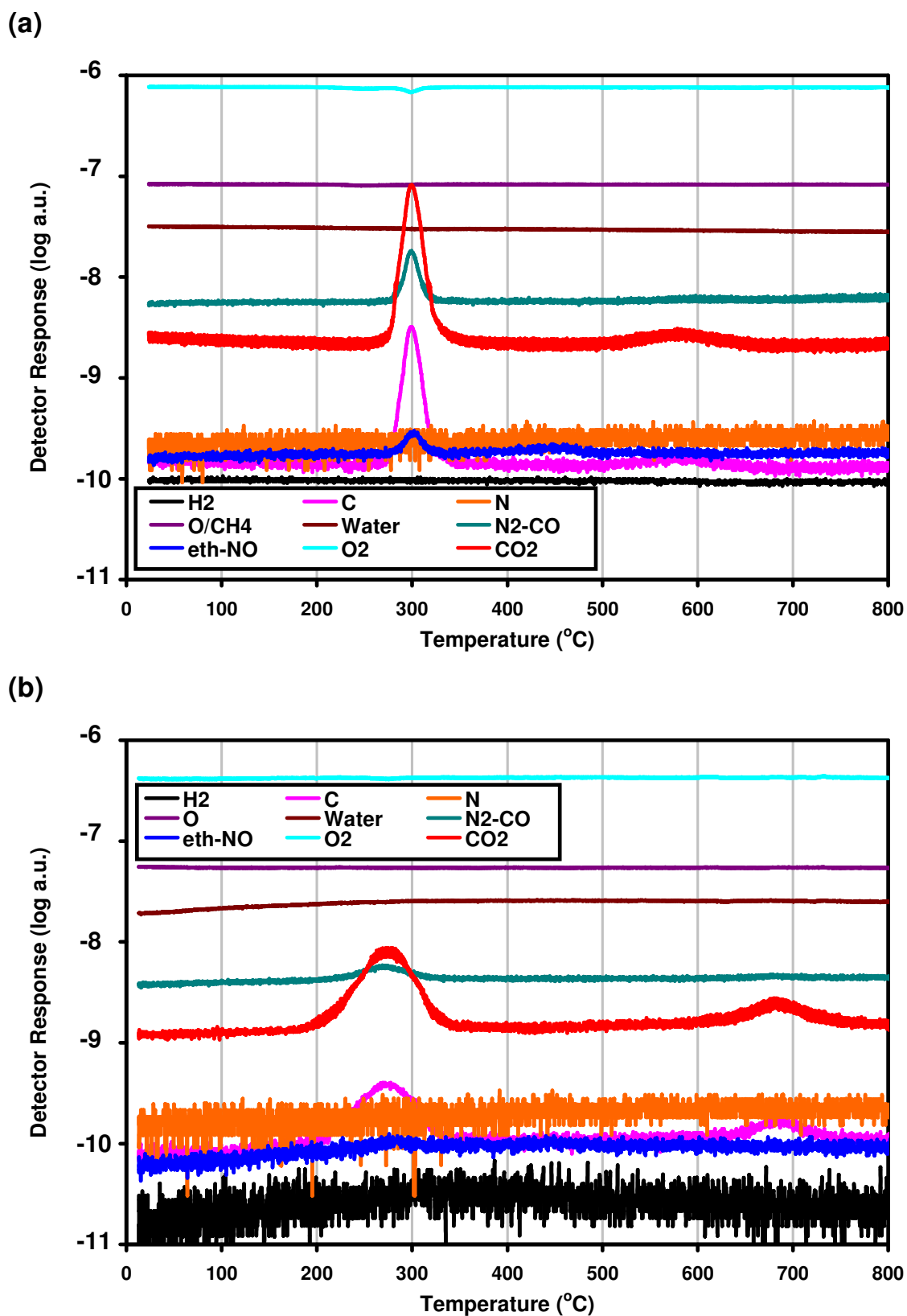


**Figure 4.19** Log TPO traces for (a) ZCe50 and (b) ZCe90, after TPRx experiments.

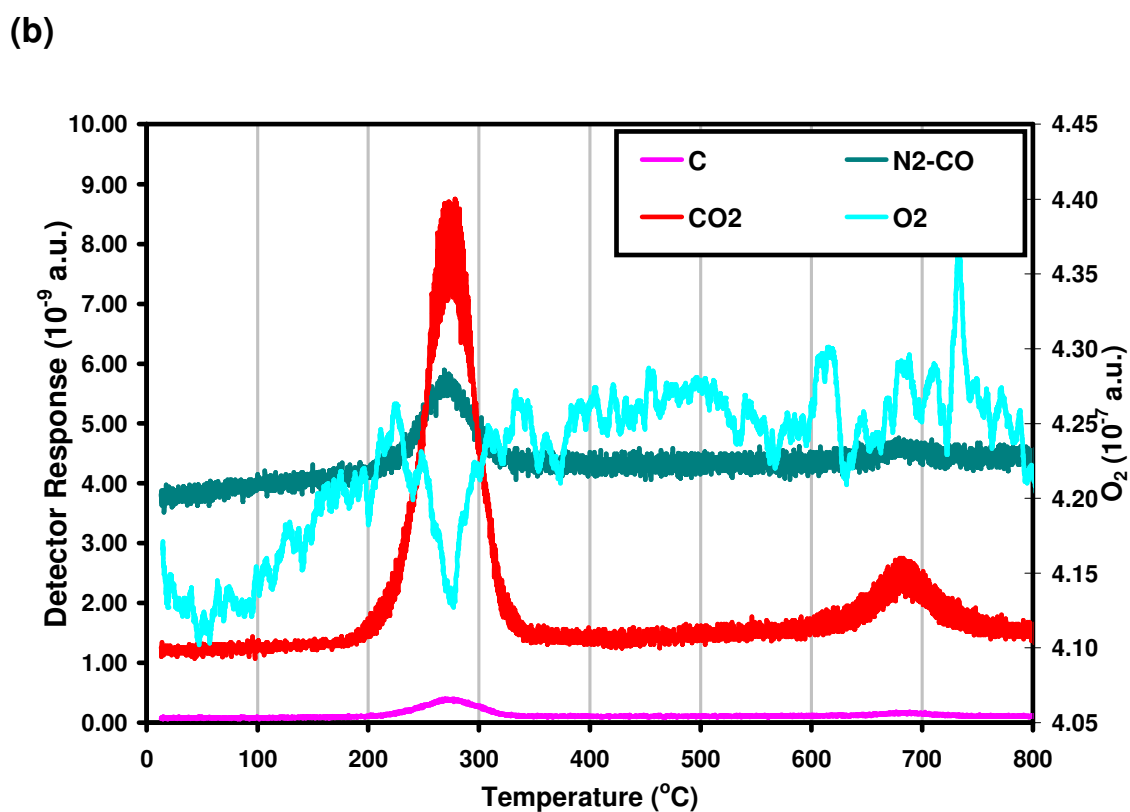
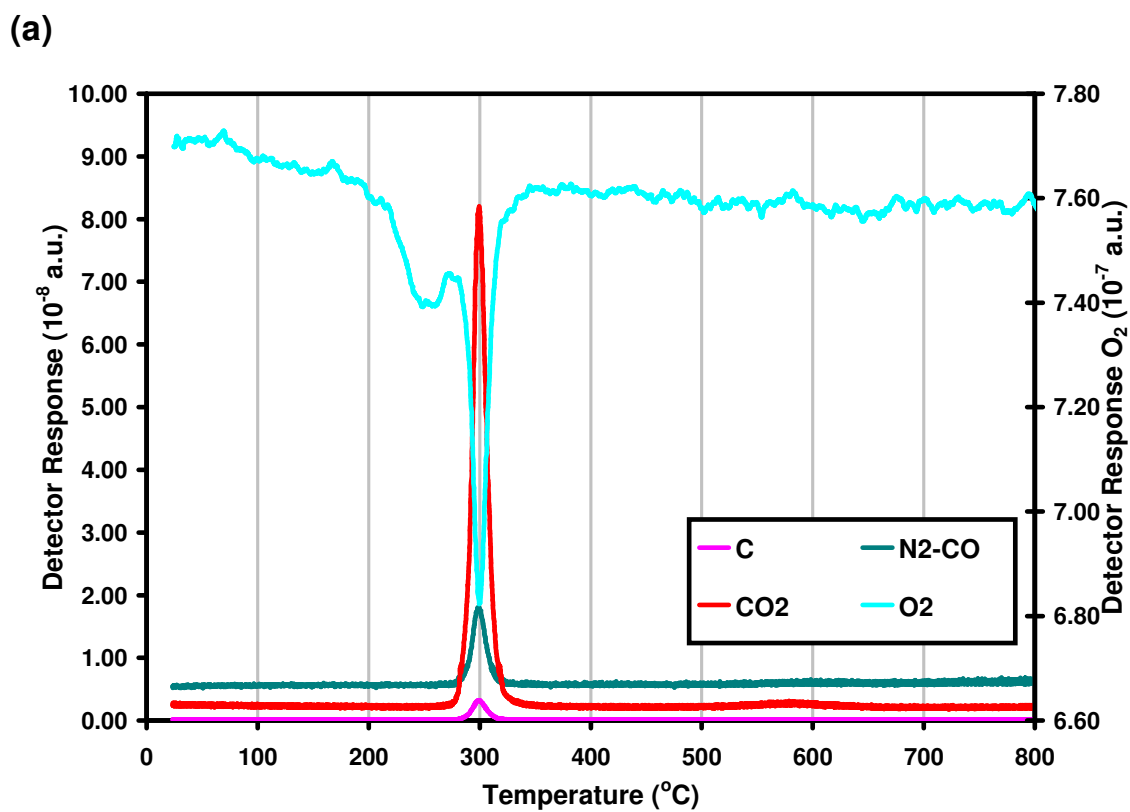


**Figure 4.20** Linear TPO traces for (a) ZCe50 and (b) ZCe90 after TPRx experiments.

#### 4.4.5 Lightoff Experiments

Lightoff experiments involved passing a stoichiometric (2:1 ratio) gas mixture of CH<sub>4</sub> and O<sub>2</sub> over pre-reduced catalysts (catalysts were heated to 500°C at 5°C min<sup>-1</sup> and maintained at 500°C for 1 h). In the lightoff experiments, the Zr/Ce solid solutions were studied as well as CeO<sub>2</sub> for comparison. The lightoff point was defined as the temperature at which 10% of maximum conversion of the reactants had taken place.

A typical lightoff plot is shown in Figure 4.21, a lightoff run using an empty reactor is included as Figure 4.22, with the remaining plots included as Appendix 2. It can be seen that two distinct reactions take place during the experiment in Figure 4.21. The partial pressures of the reactants at m/q = 14 (N/CH<sub>2</sub>), 15 (CH<sub>3</sub> and overlap with 16), 16 (O and CH<sub>4</sub>) and 32 (O<sub>2</sub>) start off flat before beginning to decrease at around 450°C. The traces continue to decrease at an approximately uniform rate until at around 860°C they stabilise with the exception of m/q = 15 which dips sharply. The initial products are CO<sub>2</sub> and water. CO<sub>2</sub> is produced from around 430°C and H<sub>2</sub>O and CO from around 450°C. These traces rise in a uniform manner before stabilising above 700°C. So to summarise, the CH<sub>4</sub> is reacting with the O<sub>2</sub> to form CO<sub>2</sub> and water (Eqn 4.1).

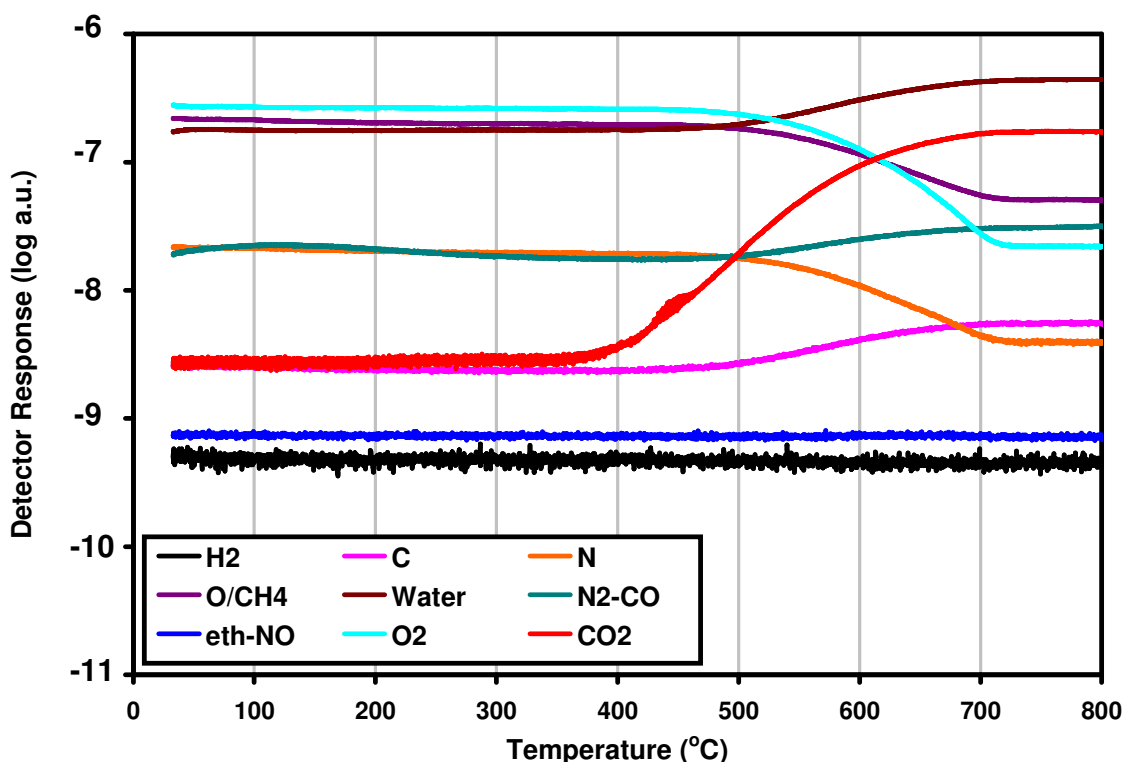
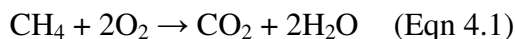
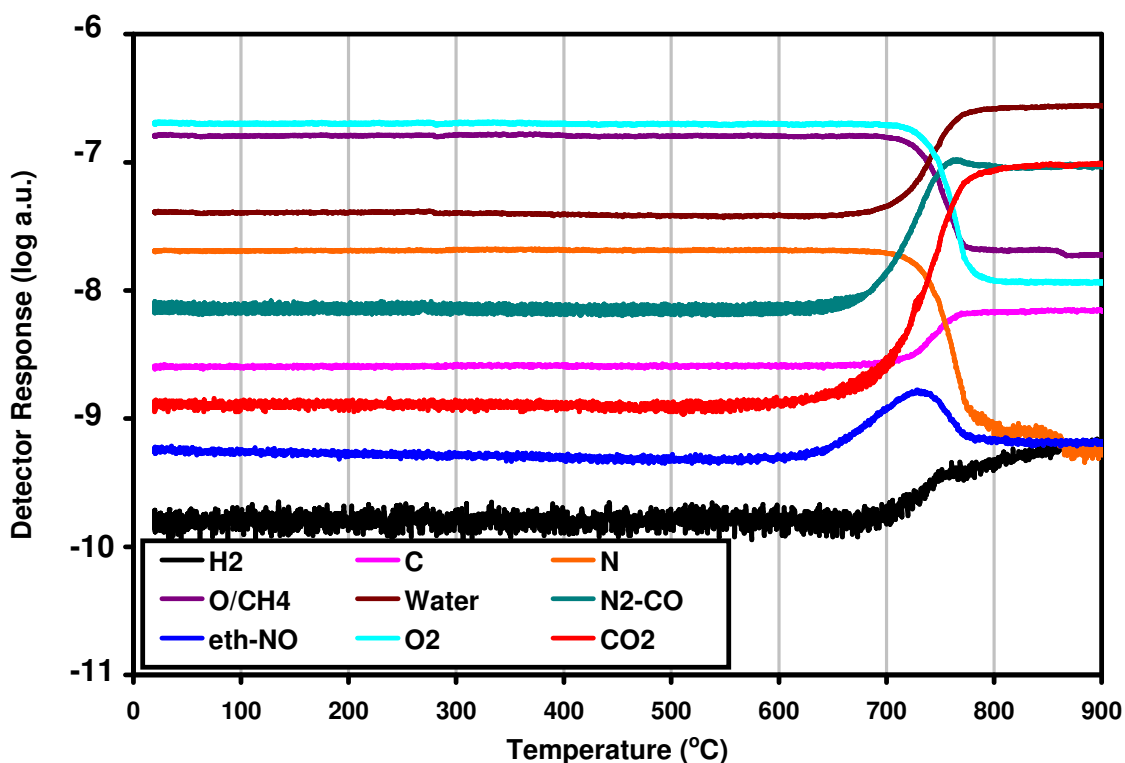


Figure 4.21 Lightoff plot of ZCe50 sample pre-reduced at 500°C.

As seen in the following linear light-off plots (Figure 4.23-4.28) there was also a second reaction taking place above 850°C, in which there is an increase in the CO and H<sub>2</sub> traces and a corresponding decrease in m/q = 14, 15 16 and 44. This is likely the result of the steam reforming of methane taking place to produce CO and H<sub>2</sub> (Eqn 4.2).



In order to determine the extent of gas phase reaction in these experiments a lightoff experiment was run using an empty micro-reactor. The results are shown in Figure 4.22. At around 700°C there were large increases in the levels of H<sub>2</sub>, H<sub>2</sub>O, CO and CO<sub>2</sub> with corresponding decreases in CH<sub>4</sub> and O<sub>2</sub>. Traces became stable above 800°C and for the remainder of the experiment.



**Figure 4.22** Lightoff plot for experiment run using an empty reactor.

The lightoff reactions were probably the most complex reactions investigated. Six traces have been separated out from the lightoff data (Figure 4.23 – 4.28) in order to present them more clearly and compare them for all mixed oxide compositions as well as for CeO<sub>2</sub>.

Because of the complexity that is inherent in the lightoff traces, the most relevant traces have been plotted for all the materials tested in order to make the data as accessible as possible. The reactants, O<sub>2</sub> and CH<sub>4</sub> are plotted in Figure 4.23 and Figure 4.24, respectively. The reactant levels for all samples remained approximately constant up to 400°C. The most active of the materials then began to catalyse the reaction between the CH<sub>4</sub> and O<sub>2</sub>.

As would be expected, the traces of both reactants showed the same order of activity for the catalysts tested. The most active was ZCe75, which was noticeably more active than the other compositions. ZCe25 and ZCe50 were the next active and it was very difficult to tell the traces corresponding to these two materials apart. ZCe90 was the next active material and ZCe10 the least active of the mixed oxides. Once the ZCe10 had started to catalyse the reaction, however, the rate of increase of reaction rate with temperature was higher than for the ZCe90, which it overtook, in terms of conversion, at around 550°C. The CeO<sub>2</sub> prepared by the same method as the other materials was much less active than the mixed oxides that were employed in this investigation. The O<sub>2</sub> levels decreased before levelling out at close to zero between 700 and 810°C, depending on the material. The CH<sub>4</sub> traces displayed a similar initial pattern before a second sharp dip between 815 and 880°C, again depending on the material.

The CO<sub>2</sub> and water traces, Figure 4.25 and Figure 4.26 respectively, were, to an extent, the mirror images of the initial reactant traces. That is, they began to increase at some point above 400°C, (the exact temperature depending on the material). They also displayed the same order of activity, namely ZCe75 > ZCe25 ~ ZCe50 > ZCe10 > ZCe90 > CeO<sub>2</sub>. As for the methane trace, both the water and CO<sub>2</sub> traces display a dip, to some extent, for all material compositions at some point between 815 and 890°C. In the case of CO<sub>2</sub>, despite the dip, the level is still well above the initial background amount for all materials. It is unlikely that the CO<sub>2</sub> is actually reacting and the dip is just the result of another carbon species being created. It seems likely that the water is being consumed in the steam reforming of methane at high temperature (above 800°C) to generate CO and H<sub>2</sub>.

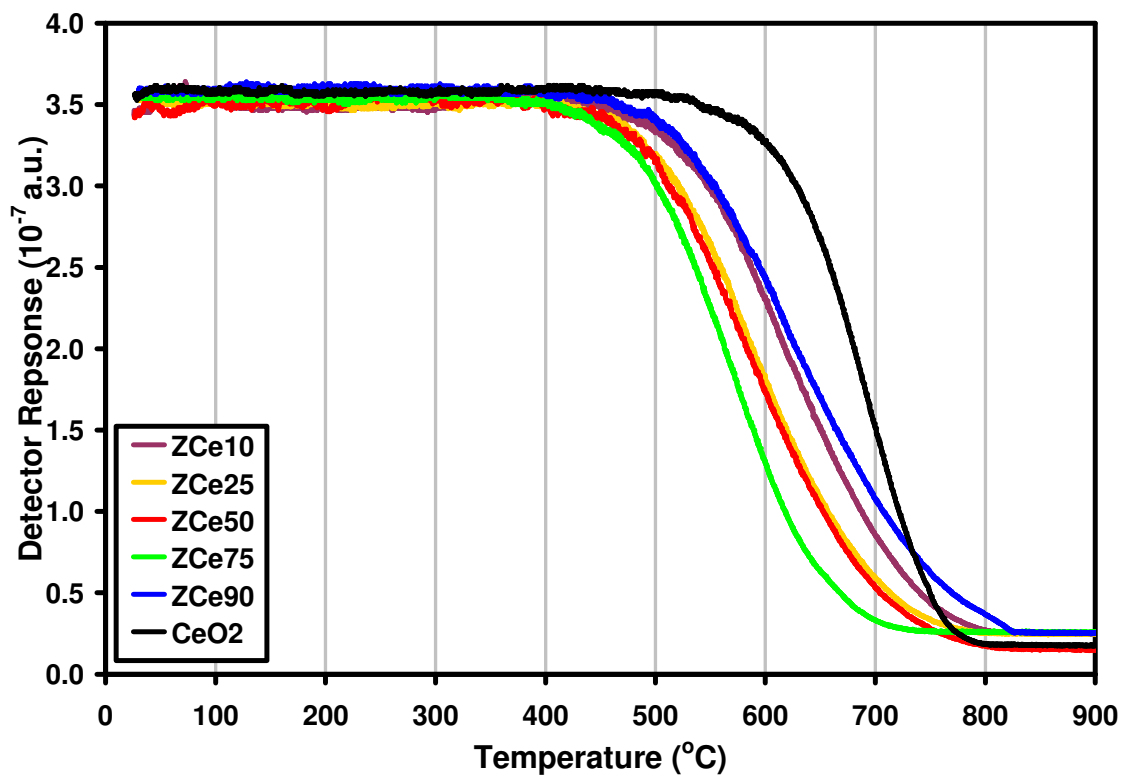


Figure 4.23 O<sub>2</sub> traces from lightoff experiments on ZCe mixed oxides and CeO<sub>2</sub>.

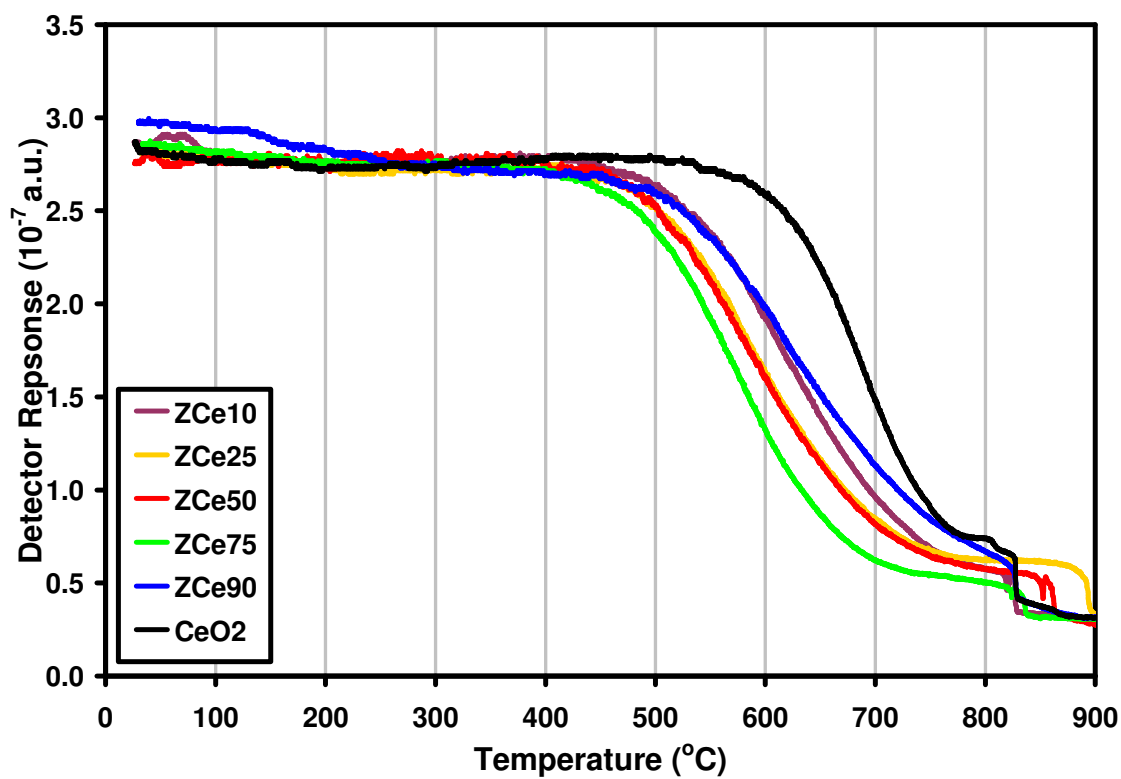


Figure 4.24 CH<sub>4</sub> traces from lightoff experiments on ZCe mixed oxides and CeO<sub>2</sub>.

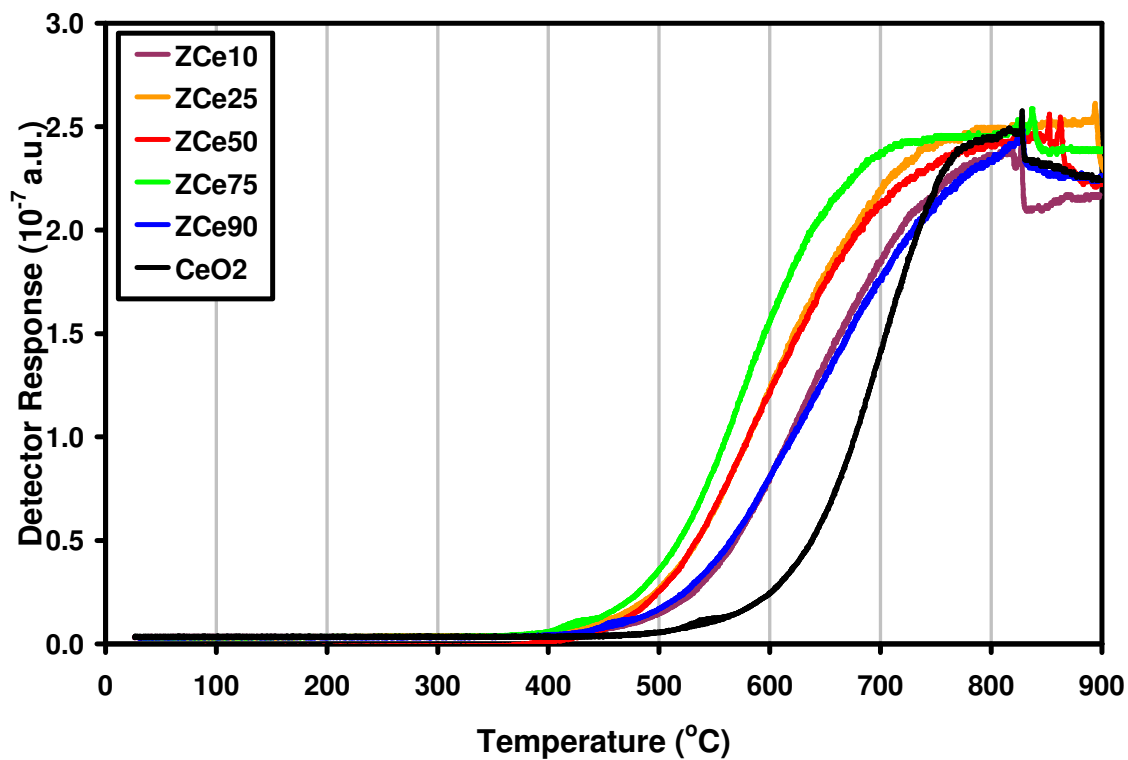


Figure 4.25 CO<sub>2</sub> traces from lightoff experiments on ZCe mixed oxides and CeO<sub>2</sub>.

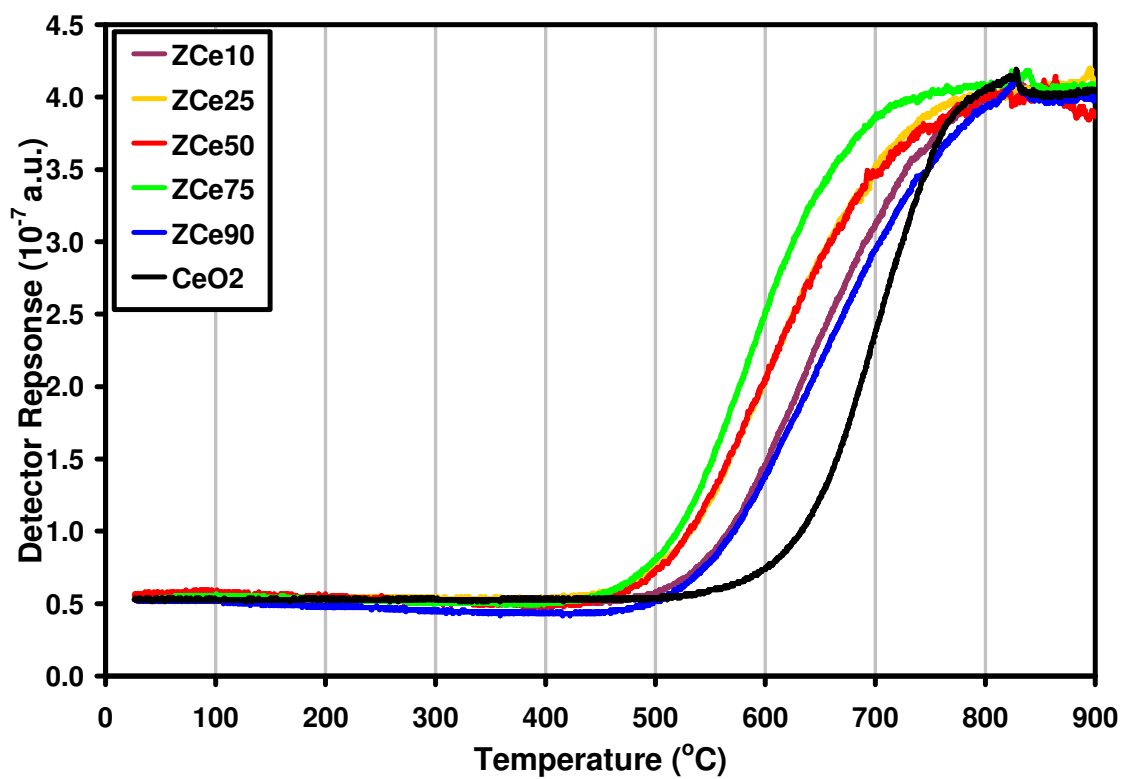
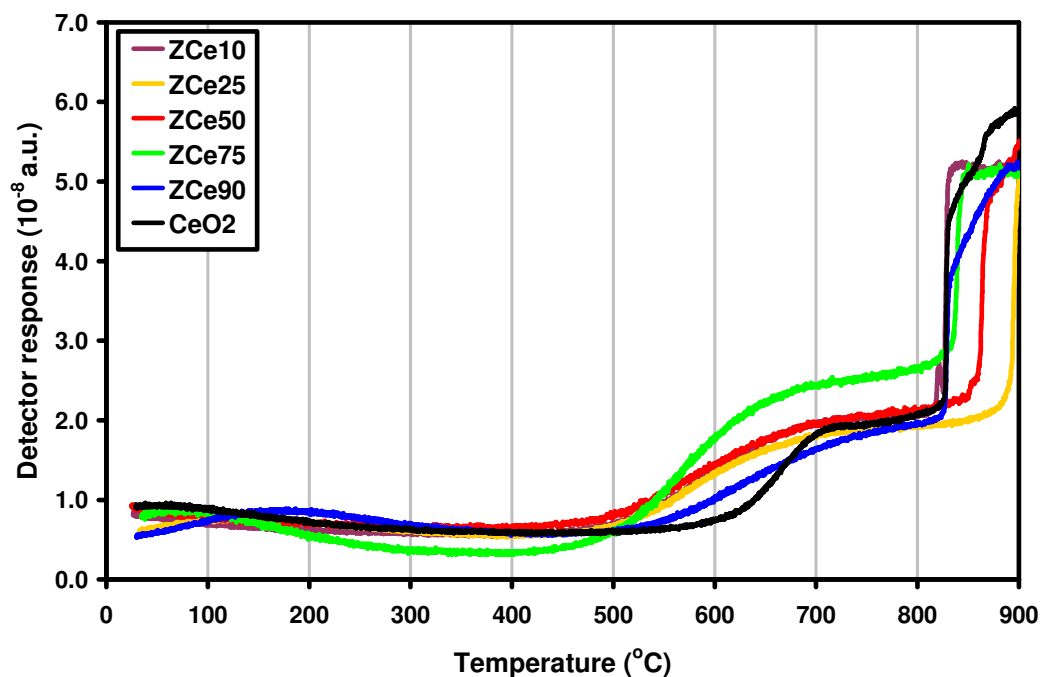
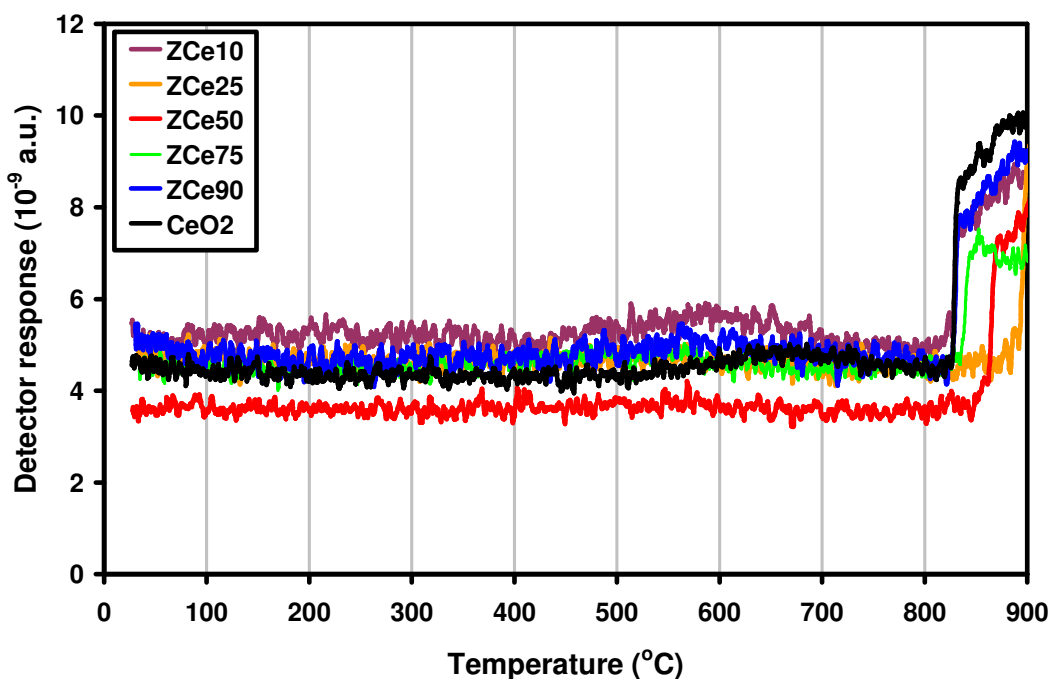


Figure 4.26 H<sub>2</sub>O traces from lightoff experiments on ZCe mixed oxides and CeO<sub>2</sub>.



**Figure 4.27** CO traces from lightoff experiments on ZCe mixed oxides and CeO<sub>2</sub>.



**Figure 4.28** H<sub>2</sub> traces from lightoff experiments on ZCe mixed oxides and CeO<sub>2</sub>.

The CO and H<sub>2</sub> traces in Figures 4.27 and 4.28, respectively, reveal the temperature at which the steam reforming of methane occurred. The levels and temperatures at which CO and H<sub>2</sub> are produced vary suggesting the materials have varying selectivity for the steam reforming of methane. CO is also produced at lower temperatures (450°C for ZCe75),

though there was no corresponding H<sub>2</sub> signal so it is likely that this CO is the result of the breakdown of CO<sub>2</sub> in the QMS. All materials displayed two distinct CO peaks: an initial peak which is attributable to oxidation of CH<sub>4</sub> and then a very sharp high temperature (815-890°C) peak due to steam reforming. CeO<sub>2</sub>, ZCe90 and ZCe10 all show this second peak at the same temperature (around 820°C) closely followed by ZCe75 (830°C) before a large gap to ZCe50 (870°C) and ZCe25 (890°C).

The lightoff temperature, which is defined in this work as the temperature at which 10% of the maximum conversion of the reactants had taken place, was calculated and is plotted in Figure 4.29 in order to compare the activities of the different catalysts.

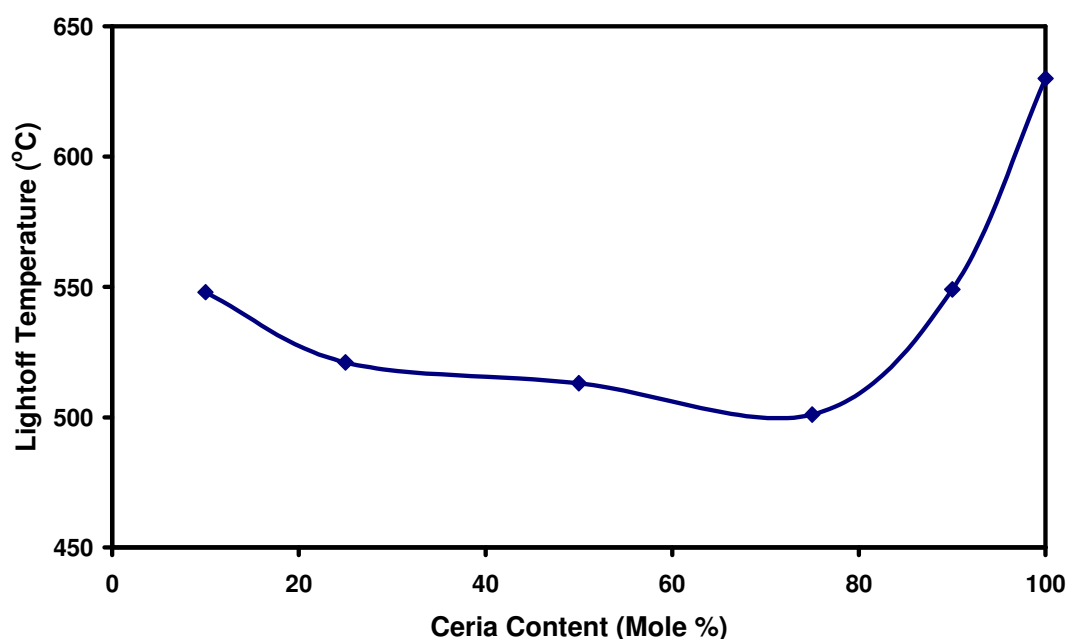


**Figure 4.29** Lightoff temperatures obtained from O<sub>2</sub> consumption trace for mixed oxides and CeO<sub>2</sub> in a 2:1 mixture of O<sub>2</sub> and CH<sub>4</sub>.

The activity of the catalysts appeared to increase with increasing ceria content (mole%) up to ZCe75 before tailing off sharply with CeO<sub>2</sub> having the highest lightoff temperature by almost 80°C. Hence the mixed oxides all appear to be far more active than pure CeO<sub>2</sub> for catalysing the oxidation of methane.

CH<sub>4</sub> and CO<sub>2</sub> levels displayed good correlation for the temperature at which they decreased and increased respectively. There was also correlation between the temperature at which O<sub>2</sub> decreased and H<sub>2</sub>O was produced. However, the latter were consistently around 20°C

higher than the temperature observed for the carbon species, for all oxide samples, as shown in Table 4.2 and Figure 4.30.

**Table 4.2** Lightoff temperatures obtained from O<sub>2</sub> and CH<sub>4</sub> consumption, and H<sub>2</sub>O and CO<sub>2</sub> production traces for mixed oxides and CeO<sub>2</sub> in a 2:1 mixture of O<sub>2</sub> and CH<sub>4</sub>.

ZCe	O <sub>2</sub>	H <sub>2</sub> O	CH <sub>4</sub>	CO <sub>2</sub>
10	548	554	528	530
25	521	520	503	497
50	513	521	503	498
75	501	509	486	481
90	549	558	523	523
100	630	622	617	600

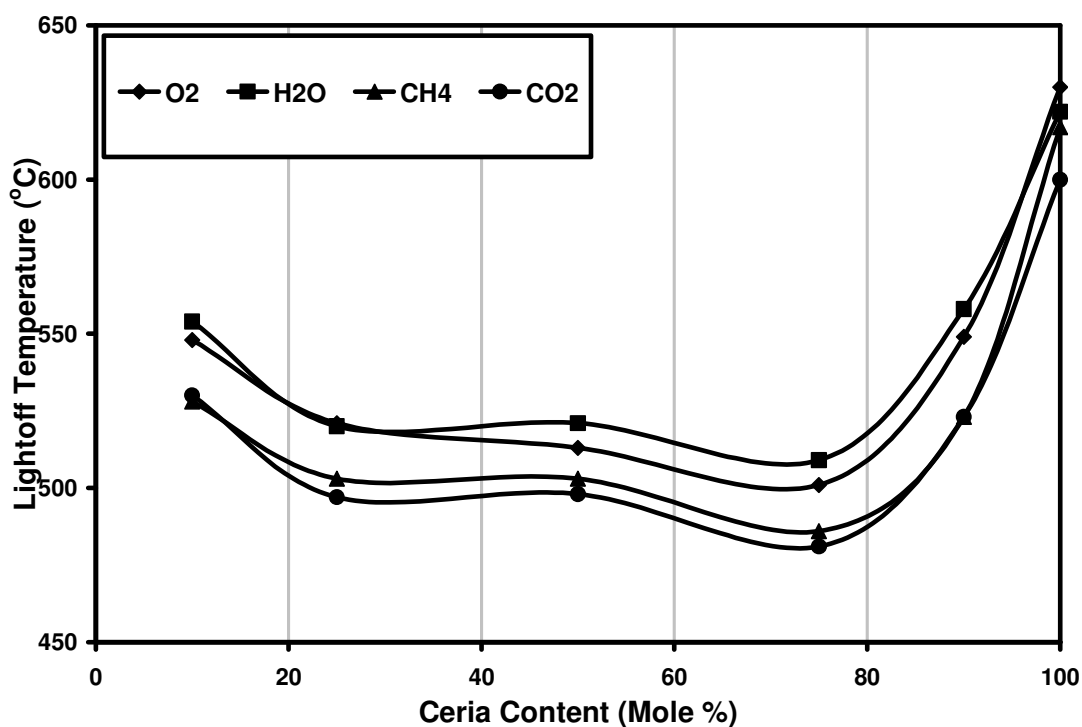


**Figure 4.30** Lightoff temperatures obtained from O<sub>2</sub> and CH<sub>4</sub> consumption, and H<sub>2</sub>O and CO<sub>2</sub> production traces for mixed oxides and CeO<sub>2</sub> in a 2:1 mixture of O<sub>2</sub> and CH<sub>4</sub>.

All samples used in the lightoff experiments were pre-reduced at 500°C for 1 h in 5% H<sub>2</sub>/Ar. The TPR results displayed in Section 4.3.2 showed that this was an insufficient temperature to reduce any of the oxides (ZCe50 the most active oxide was reduced at

550°C). As a result the initial lag between the temperature at which CH<sub>4</sub> and O<sub>2</sub> partial pressures decrease may have been due to the methane being reduced by oxygen that was present in the oxide to form CO<sub>2</sub>. The H that was released from the methane was then retained on the catalyst surface as OH<sup>-</sup>. This accounts for the slight increase in the temperature at which H<sub>2</sub>O is produced, relative to CH<sub>4</sub> consumption. This is a mechanism similar to that proposed by Driscoll et. al. [2] for the oxidation of hydrocarbons over oxide-based catalysts, shown as Figure 4.31. Driscoll et al proposed the direct formation of hydroxide radicals on the oxide surface. If these radicals are relatively stable then it may not have been until a large amount of the oxide was reduced that the hydroxide groups reacted with each other to release H<sub>2</sub>O.

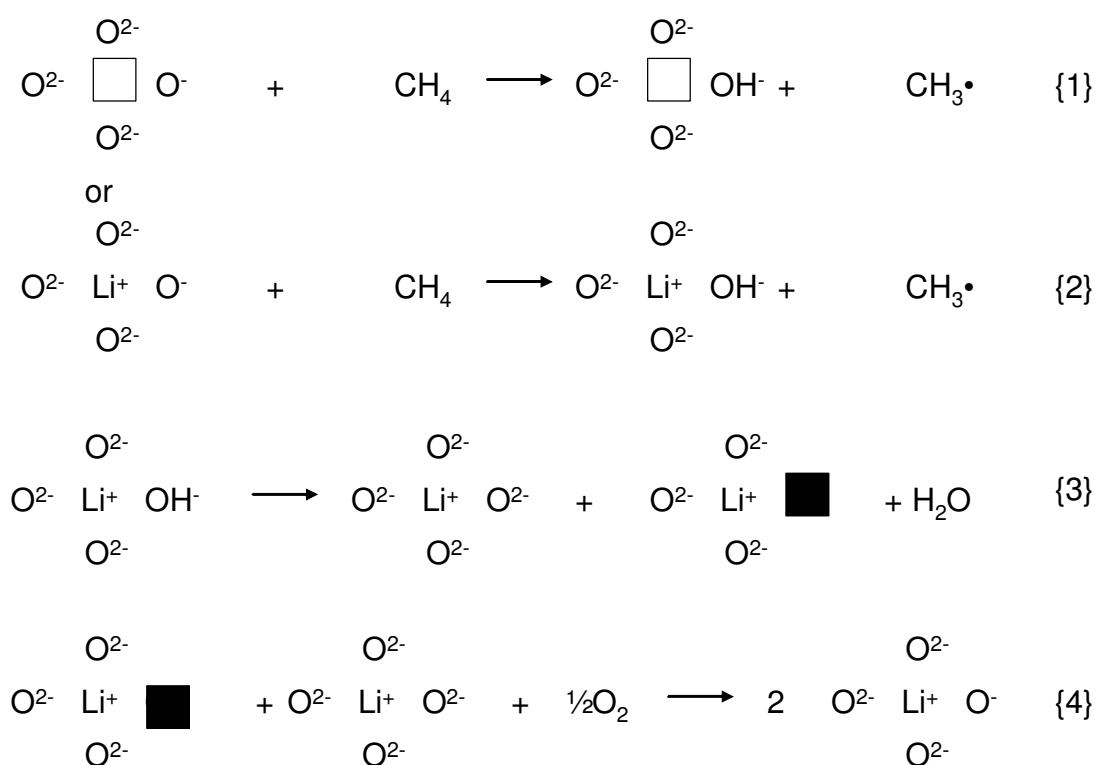


**Figure 4.31** Schematic representation of the catalytic cycle proposed by Driscoll et. al. [2]. □ and ■ represent vacancies for cations and anions respectively.

## 4.5 Summary

The redox behaviour and catalytic activity of five different Zr/Ce oxides and CeO<sub>2</sub> have been investigated using a series of temperature programmed experiments.

The desorption experiments revealed that the as-prepared samples contained carbon species, nitrogen species and water in varying amounts.

The presence of adsorbed water in the as-prepared samples impacted on efforts to calculate the extent of reduction of the catalysts. As a result, TPD/R experiments were run to eliminate these adsorbed species before the TPR experiments.

Samples containing at least 50% ceria (mole%) were all reduced at similar temperatures (581-598°C in the TPD/Rs), with the lower ceria content samples being reduced at higher temperatures (666-690°C in the TPD/Rs).

The thermal cycling associated with the TPD experiments led to an increase in the reduction temperature in the subsequent TPR for most samples. This effect varied from a 5°C to a 30°C increase in reduction peak position. The exception to this was ZCe25 which displayed a decrease in reduction peak position in the TPD/R compared to the TPR. This change was very small (-1°C) and is within experimental error.

ZCe75 produced the greatest amount of water per unit mass in both the TPR and TPD/R experiments. The highest percentage of theoretical water yield was observed for the ZCe10 sample, although this sample also produced the least water in absolute terms.

As-prepared samples with low ceria contents, especially, contained large amounts of residual water, which greatly influenced the calculation of total water production.

Lightoff experiments allowed comparison of the catalytic activity of the samples. The most active sample was found to be ZCe75. The remaining oxides were divided into two comparable groups: ZCe25 and ZCe50 and ZCe10 and ZCe90, the least active.

CeO<sub>2</sub> prepared in the same way as the mixed oxides was studied in the lightoff experiments for comparison. This showed that even the least active mixed oxides had a lightoff temperature 80°C lower than that of the pure oxide.

As a result of the experiments described in this chapter the ZCe75 and ZCe50 oxides would appear to be the most promising catalyst support materials. Both materials have high SSAs, relatively good activity for the oxidation of methane and high ceria content improving the OSC of the material.

#### 4.6 References

- [1] C. Li, K. Domen, K. Maruya, T. Onishi, *J. Am. Chem. Soc.*, 111 (20), **1989**, 7683
- [2] D.J. Driscoll, W. Martir, J. -X. Wang, J.H. Lunsford, *J. Am. Chem. Soc.*, 107, **1985**, 58

**Chapter 5. Copper  
Impregnated Ceria-  
Zirconia Oxides**

## 5.1 Introduction

The Ce/Zr oxides investigated in Chapter 4, which were named according to the ceria mole % content of the sample, ie ZCe25 contained 25 mole % Ce, were impregnated with copper by employing two different preparative routes. These were wet impregnation (I), using copper nitrate dissolved in acetone, and impregnation of the copper during the preparation of the oxide (D) by adding copper nitrate to the cerium and zirconium nitrates. Low loadings of copper were used (2, 5, 7, and 10% by weight). These materials were investigated using SEM, XRD, BET and a variety of temperature programmed techniques .in order to investigate their catalytic performance. The results of these investigations are described below.

## 5.2 SEM images and Elemental Maps

The 5, 7 and 10 copper wt% as prepared powders for all oxide compositions, were investigated using SEM. EDX was also used to investigate the distribution of the elements Ce, Cu, O and Zr within the samples. In all cases, there was a slight disparity between the size of the SEM images and elemental maps, though all the major particles were readily identifiable. This was caused by the EDX and the SEM detectors having slightly different geometries.

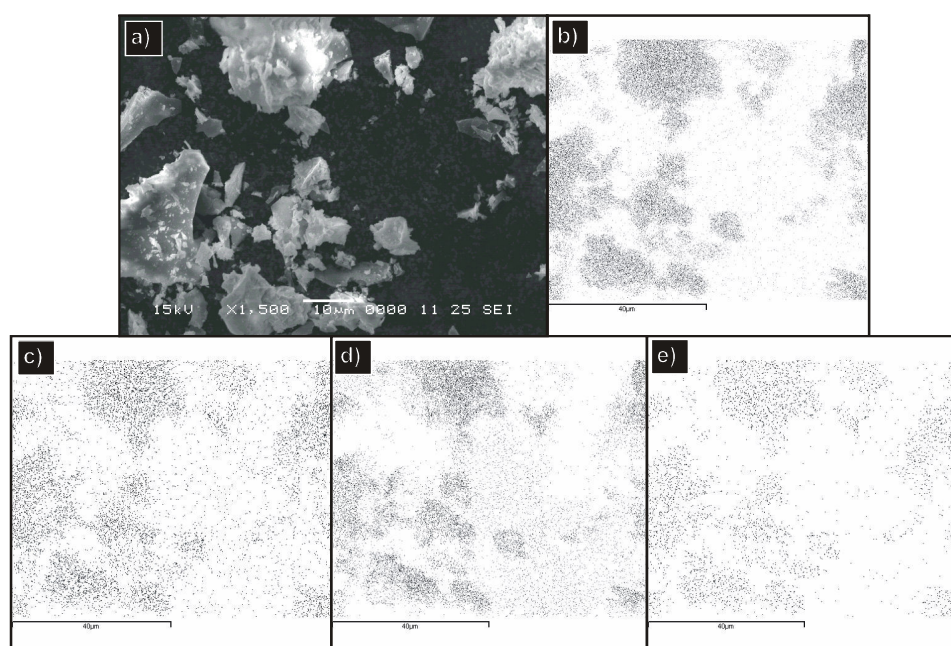


**Figure 5.1** (a) SEM image and elemental maps of (b) Ce, (c) Cu, (d) O, (e) Zr for 5-50-D.

Oxide samples impregnated with 5 wt% copper during oxide preparation (Figure 5.1) showed a uniform dispersion of copper implying that there were no obvious large copper oxide particles. This was true for all of the samples prepared by the direct (D) method (5-10-D, 5-25-D, 5-50-D, 5-75-D and 5-90-D).

Samples containing 2, 5, 7 and 10 wt% copper, were prepared by the incipient wetness (I) method. The samples containing 5 wt% copper generally showed even copper distribution throughout the samples. Figure 5.2 shows a SEM image and the EDX maps for the 5-50-I (II) powder. There was an even distribution of all the elements present which suggests good distribution of the copper throughout the entire oxide sample. The impregnation was undertaken with the aim of depositing as small copper particles as possible with the understanding that an even coating of small copper particles would greatly increase the interaction between the Cu metal and the oxide phase increasing the activity of the catalyst. When a lower copper loading was used (2 wt%) the desired even distribution of copper throughout the oxide sample was attained. For the higher copper loadings, however (7-10 wt%) the impregnation technique did not produce the desired results and all samples displayed some areas of high copper concentration.

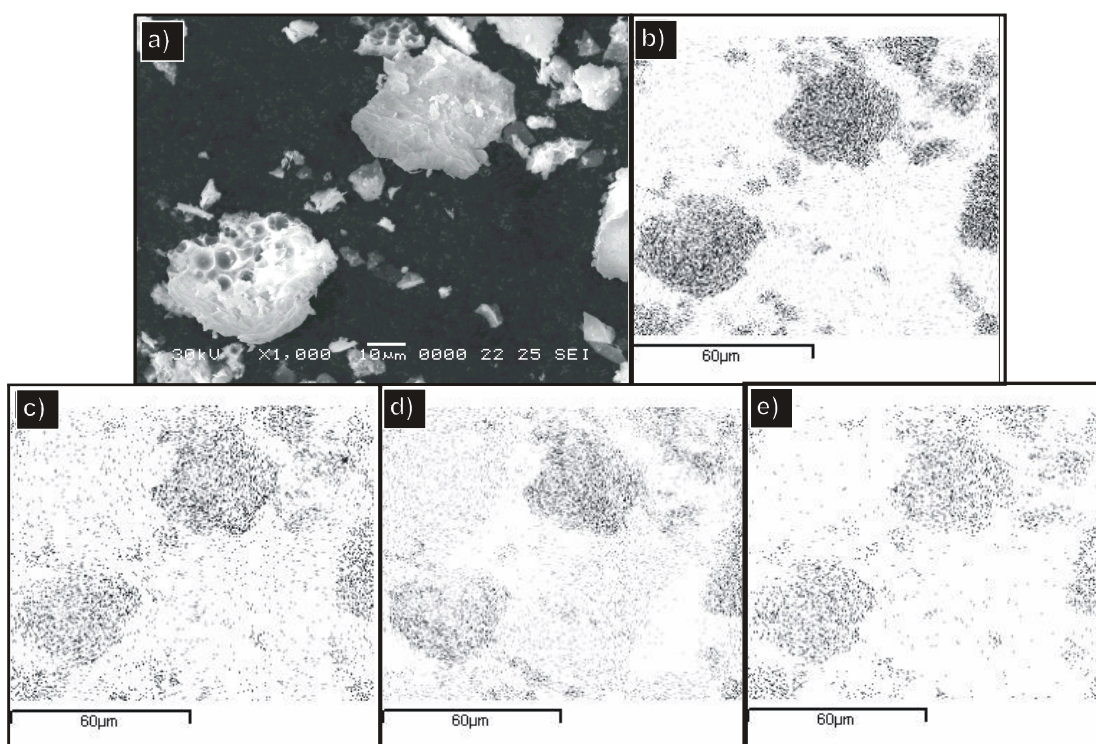


**Figure 5.2** (a) SEM image and elemental maps of (b) Ce, (c) Cu, (d) O, (e) Zr for 5-50-I (II).

Not all 5 wt% I samples displayed the desired copper dispersion, with only ZCe75 and ZCe90 showing no evidence of copper particles. There were some dark areas observed on the 5-10-I (II) EDX map for copper. On inspection at higher magnification (Figure 5.3) the presence of large copper containing agglomerations was confirmed. There were also similar copper oxide particles observed for 5-25 and 5-50-I (II) samples. These Cu particles were relatively rare (roughly 1 observed for every 3 areas investigated at  $\times 1,000$  magnification for the 5-10-I (II) sample) and their rate of occurrence declined with increasing ceria content of the oxides. Repeating the preparation of the I copper samples produced similar results. The oxides which were most prone to the formation of the copper particles were those known to have the lowest specific surface area, which will be discussed further in Section 5.4. This suggests that the surface area of particularly the ZCe10 and ZCe25 oxides was insufficient for the desired dispersal of the copper nitrate within the sample. As a result the copper solution appears to have ‘pooled’ in some areas resulting in the presence of copper agglomerations.

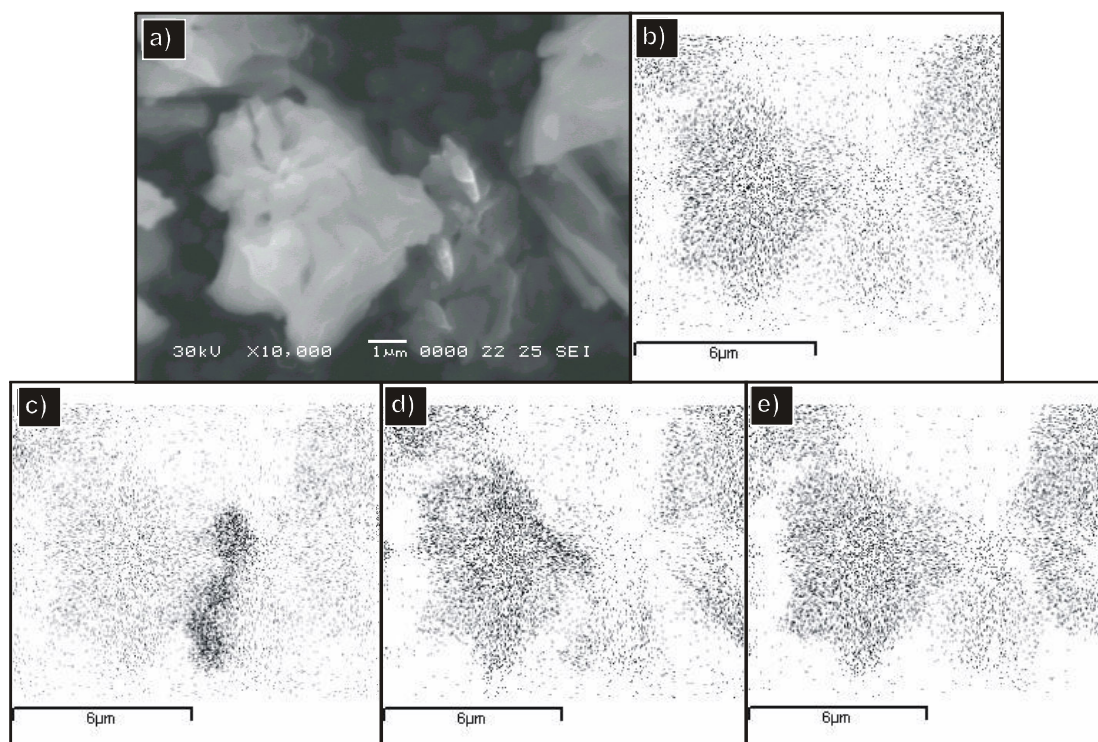


**Figure 5.3** (a) SEM image and elemental maps of (b) Ce, (c) Cu, (d) O, (e) Zr for 5-10-I (II).

The 7 wt% copper I samples as shown in Figure 5.4 displayed areas of even copper distribution as well as a number of large copper particles.

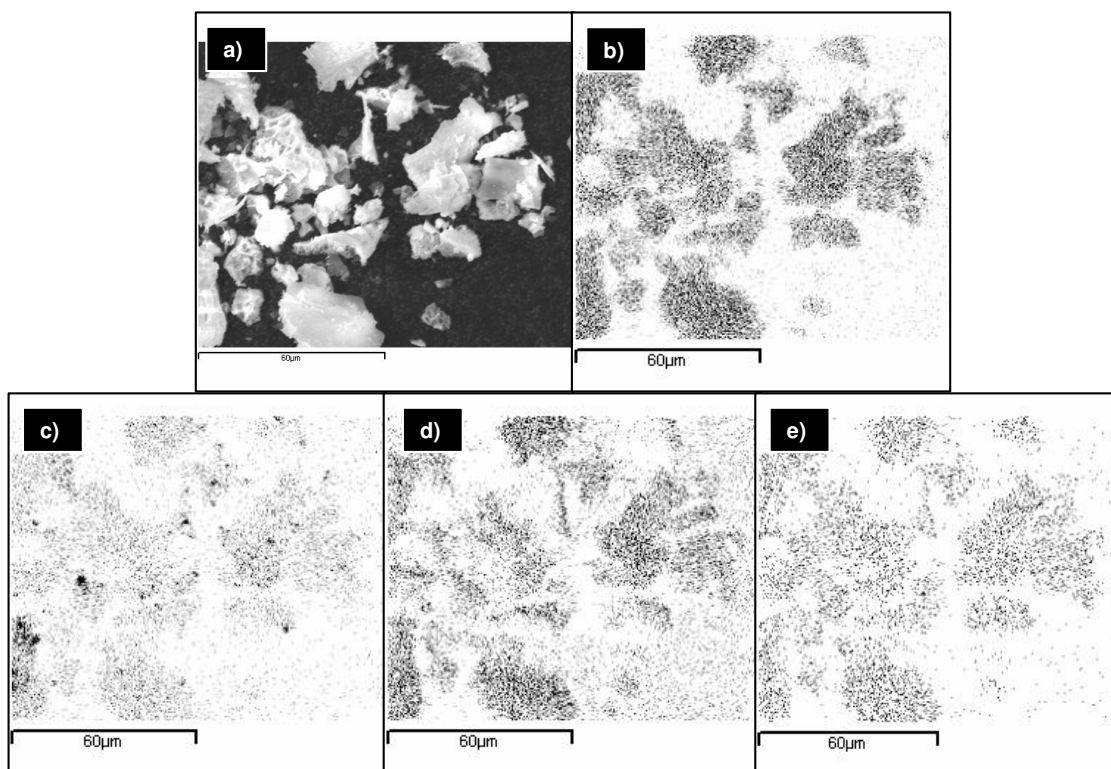


**Figure 5.4** (a) SEM image and elemental maps of (b) Ce, (c) Cu, (d) O, (e) Zr for 7-50-I (II).

As shown in Figure 5.5, the 10 wt% I copper samples also displayed large areas of even copper distribution. There were also numerous examples of sizable copper particles throughout the samples. A good example of this is the EDX map in Figure 5.5 (c). Whilst large areas of the plot showed reasonable copper dispersion through the sample there are a number of dark areas, one of which is highlighted. The maximum loading that is viable whilst achieving the desired uniform copper distribution using the I technique appears to be 5 wt% and even then there are some small copper deposits observed for the oxides with lower surface areas. The large areas of evenly dispersed copper suggests that these samples will still perform well as catalysts but the larger copper particles would be expected to be less active.

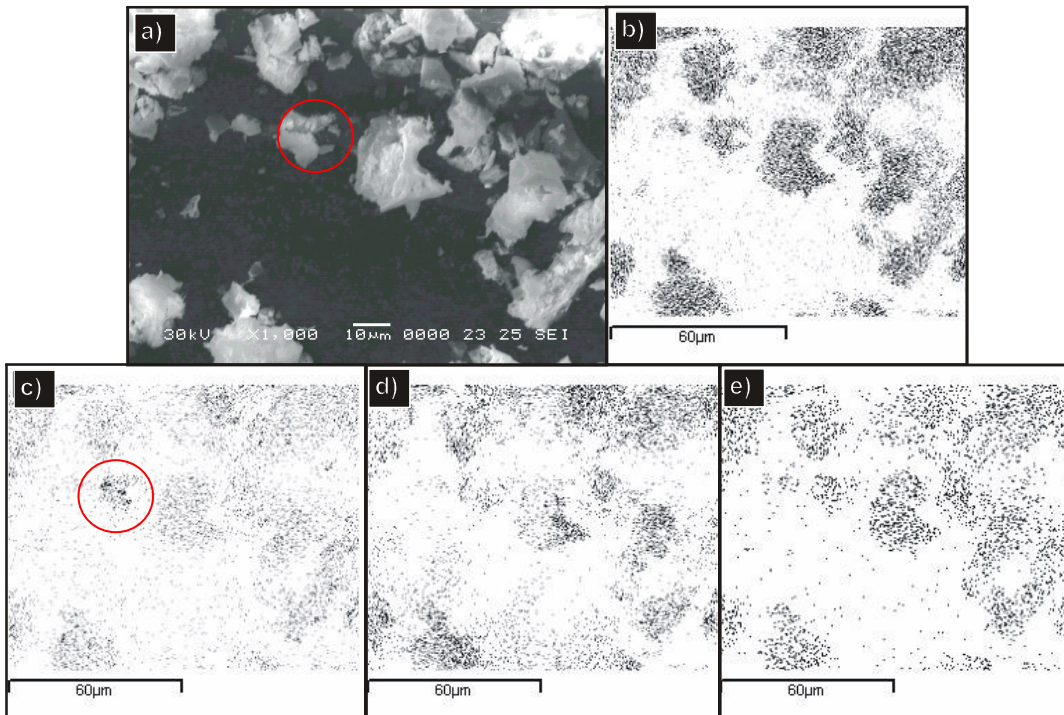


**Figure 5.5** (a) SEM image and elemental maps of (b) Ce, (c) Cu, (d) O, (e) Zr for 10-50-I (II).

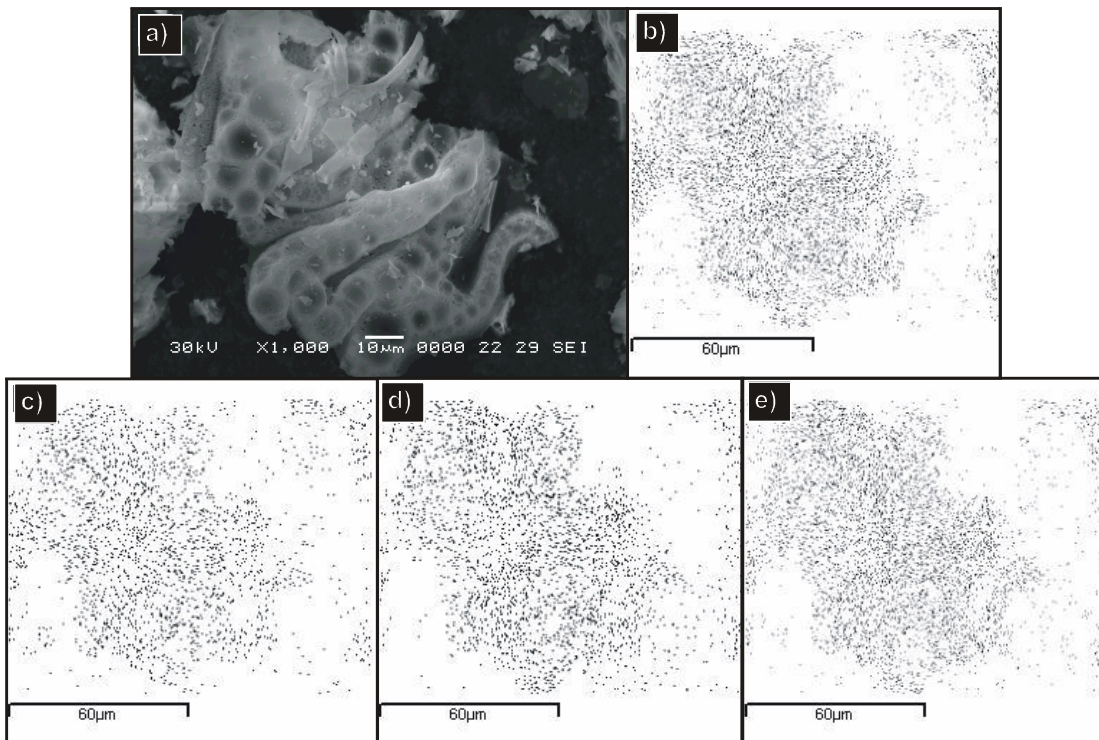


**Figure 5.6** (a) SEM image and elemental maps of (b) Ce, (c) Cu, (d) O, (e) Zr for 10-50-D.

Figure 5.6 shows a 10 wt% D copper sample. Throughout all of the areas investigated using EDX on this sample there were no observed copper agglomerations. It appears that the D technique enables the preparation of uniform samples with higher copper loadings than those achievable through the I preparation route.

### 5.3 XRD

Figure 5.6 shows the XRD patterns collected for all oxide compositions as well as all 5 wt% copper impregnated samples. The peaks observed at  $2\theta = 22$  and  $24^\circ$  are the result of the collimator, as described in Chapter 3 and can be discounted. The impregnation of copper during the preparation of the oxide appears to have minimal impact on the crystal structure of the oxide. The patterns for the impregnated samples correlate closely with those of the bare oxides. For the D 5 wt% impregnated samples there were no peaks that would be attributed to either CuO or Cu observed. This suggests that any copper crystallites present must be very small (nanoparticles) and as a result produce very broad peaks which are difficult to distinguish. The second possibility is that the concentration of the Cu and CuO phases is very low. This would result in very small peaks which would be hard to distinguish. The majority of the 5-I samples did display a peak at  $2\theta = 39^\circ$  attributed to CuO, the most pronounced of these was for 5-10-I (Figure 5.7(e)). This was the sample that displayed the highest concentration of copper agglomerations by the EDX elemental maps.

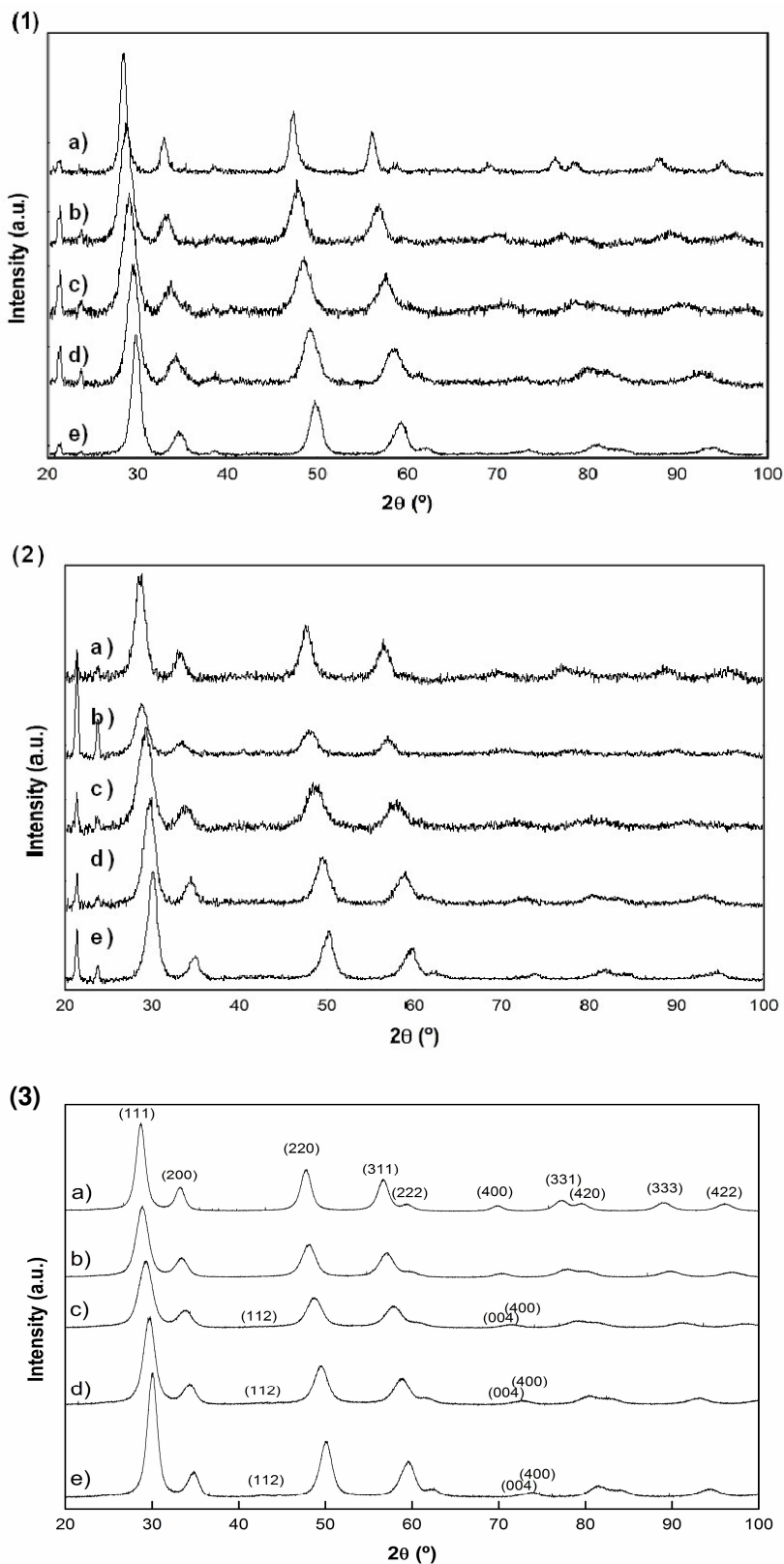


**Figure 5.7** XRD patterns for 5 wt% copper impregnated oxides, prepared by (1) Wet-Impregnation, (2) Direct impregnation during preparation and (3) Bare oxide patterns collected by Fuentes [1] are included for comparison (a) ZCe90, (b) ZCe75, (c) ZCe50, (d) ZCe25 and (e) ZCe10 calcined at 500°C for 1 h.

## 5.4 BET Surface Area Analysis

BET surface area analysis was used to investigate how impregnating the oxides with copper by the different techniques affected the specific surface area (SSA) of the samples. The BET results shown in Figure 5.8 reveal an interesting relationship between the samples prepared by different techniques. The SSAs of the I samples were consistently higher than for the bare oxides. This was most pronounced in ZCe10 (31.8 m<sup>2</sup>g<sup>-1</sup> before impregnation and 54.4 m<sup>2</sup>g<sup>-1</sup> after impregnation). The wet impregnation had the effect of making the SSAs for the materials more uniform with a difference of 21.4 m<sup>2</sup>g<sup>-1</sup> between ZCe25 and ZCe50 for the oxides and a difference of only 14.6 m<sup>2</sup>g<sup>-1</sup> between the impregnated samples. The effect of the impregnation during preparation was very pronounced. The surface area for 5-10-D (63.5 m<sup>2</sup>g<sup>-1</sup>, an increase of 31.7 m<sup>2</sup>g<sup>-1</sup> on the bare oxide), 5-25-D (51.5 m<sup>2</sup>g<sup>-1</sup>, + 20.3 m<sup>2</sup>g<sup>-1</sup>) and 5-50-D (69.8 m<sup>2</sup>g<sup>-1</sup>, + 17.2 m<sup>2</sup>g<sup>-1</sup>) were all significantly increased.

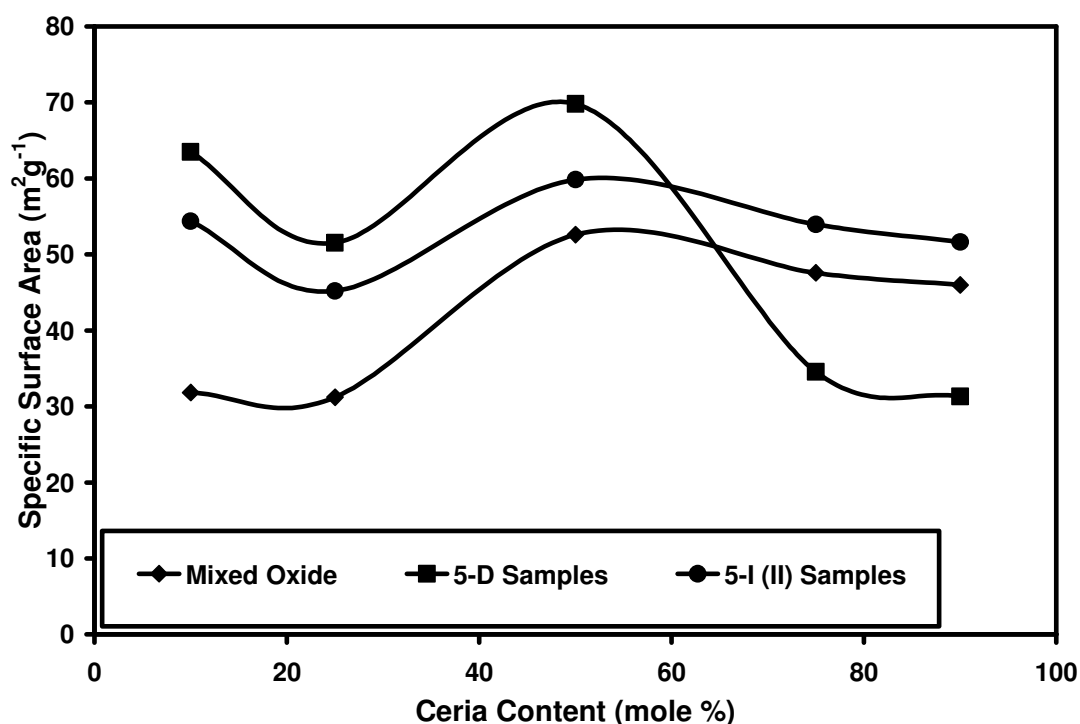


**Figure 5.8** BET SSA values for bare oxides, 5 wt% I samples and 5 wt% D samples. All samples were first calcined at 500°C for 1 hr and then ground in a pestle and mortar for 1 min.

Two samples however displayed a decrease in SSA from the bare oxide, with the addition of copper. These were 5-75-D ( $34.6 \text{ m}^2\text{g}^{-1}$ , a decrease of  $13.1 \text{ m}^2\text{g}^{-1}$  on the bare oxide) and 5-95-D ( $31.3 \text{ m}^2\text{g}^{-1}$ , -  $14.7 \text{ m}^2\text{g}^{-1}$ ). These results suggest that the effect of the D method is quite complex, and that the single step preparation/impregnation (method D) seems to result in noticeably different materials from those produced by the two step preparation/impregnation (method I).

## 5.5 Temperature Programmed Studies

The equipment and procedures for TP experiments are outlined in Sections 3.6 and 3.7. In order to investigate the effect the preparation technique had on materials properties a range of materials of the same composition were examined: 5-10, 5-25, 5-50, 5-75, 5-90 and 10-50 samples were prepared by both the I and D techniques. In addition, to establish the effect of copper loading over a range of oxide compositions, samples with 2 and 7 wt% copper content were prepared by the I technique, though not all of these materials were tested extensively.

### 5.5.1 Temperature Programmed Desorption

A summary of the TPD experiments is included in the following section. All experimental plots have been included as Appendix 3 for completion.

#### 5.5.1.1 Effect of Calcination Temperature

Figure 5.8(a) shows the traces for a typical TPD for an I sample calcined at  $250^\circ\text{C}$  (5-50-I). As for the bare oxides, there was initial desorption of water (at around  $100^\circ\text{C}$ ), though the extent of this water desorption was much lower for the copper impregnated samples. A series of  $\text{CO}_2$  peaks (at about 100, 235 and  $695^\circ\text{C}$ ) were also observed for this sample and a number of large NO peaks were observed at around 240 and  $350^\circ\text{C}$ . These features will be discussed further in the following section.

It was initially felt that  $250^\circ\text{C}$  would be a high enough calcination temperature to decompose the copper nitrate used to impregnate the oxides. The TPD trace for 5-50-I (I) (Figure 5.9(a)) showed large  $m/q = 32$  ( $\text{O}_2$ ),  $m/q=30$  (NO),  $m/q = 28$  ( $\text{N}_2$ ) and  $m/q = 14$  (N) peaks. As these peaks were not present in the bare oxide TPD traces it was apparent that

the nitrates used to impregnate the copper into the oxides had not been fully decomposed after calcination at 250°C. The calcination temperature was raised to 500°C, which was the temperature used for the calcination of the bare oxides and the D samples (Figure 5.9(c)) neither of which displayed desorption of nitrogen species to any significant extent.

The effect of the change of calcination temperature, from 250°C to 500°C, can be clearly seen in the TPD (Figure 5.9(b)) in which the large peaks for nitrogen containing species are absent. In the TPD for 5-50-I (II) (calcined at 500°C), there was initial desorption of water around 100°C, and four distinct CO<sub>2</sub> peaks were observed (80, 420, 675, 767°C) as a result of the decomposition of residual organic precursors. There were also peaks for  $m/q = 16$  (O) and  $m/q = 32$  (O<sub>2</sub>) corresponding to the highest temperature CO<sub>2</sub> peak. The detection of O corresponding to CO<sub>2</sub> would be expected to be due to decomposition of the CO<sub>2</sub> in the QMS. The presence of O<sub>2</sub> at the same temperature however suggests that there is something else taking place. There were also no corresponding peaks observed for the bare oxide so desorption of O<sub>2</sub> can be related to the presence of the copper. A possible scenario, which will be discussed further in Chapter 6, is that labile oxygen species formed by the addition of the copper to the oxides are able to desorb from the sample at high temperature (around 750°C). These oxygen species would also then react with any residual carbon on the surface of the powder explaining the corresponding CO<sub>2</sub> and C peaks.

The TPD trace of 5-50-D (Figure 5.9(c)) was similar in many respects to that of the 5-50-I (II) sample which was also calcined at 500°C. There were a number of differences observed for these materials of the same composition prepared by two different preparation routes. There was again initial evolution of water which peaked at 77°C before tailing off gradually over the rest of the experiment. With the exception of the peak which is present at 420°C for 5-50-I (II) the CO<sub>2</sub> trace for 5-50-D was comparable to that of 5-50-I (II) with a large initial peak (90°C) and a shoulder (544, 660°C) which led up to the largest peak at 714°C.

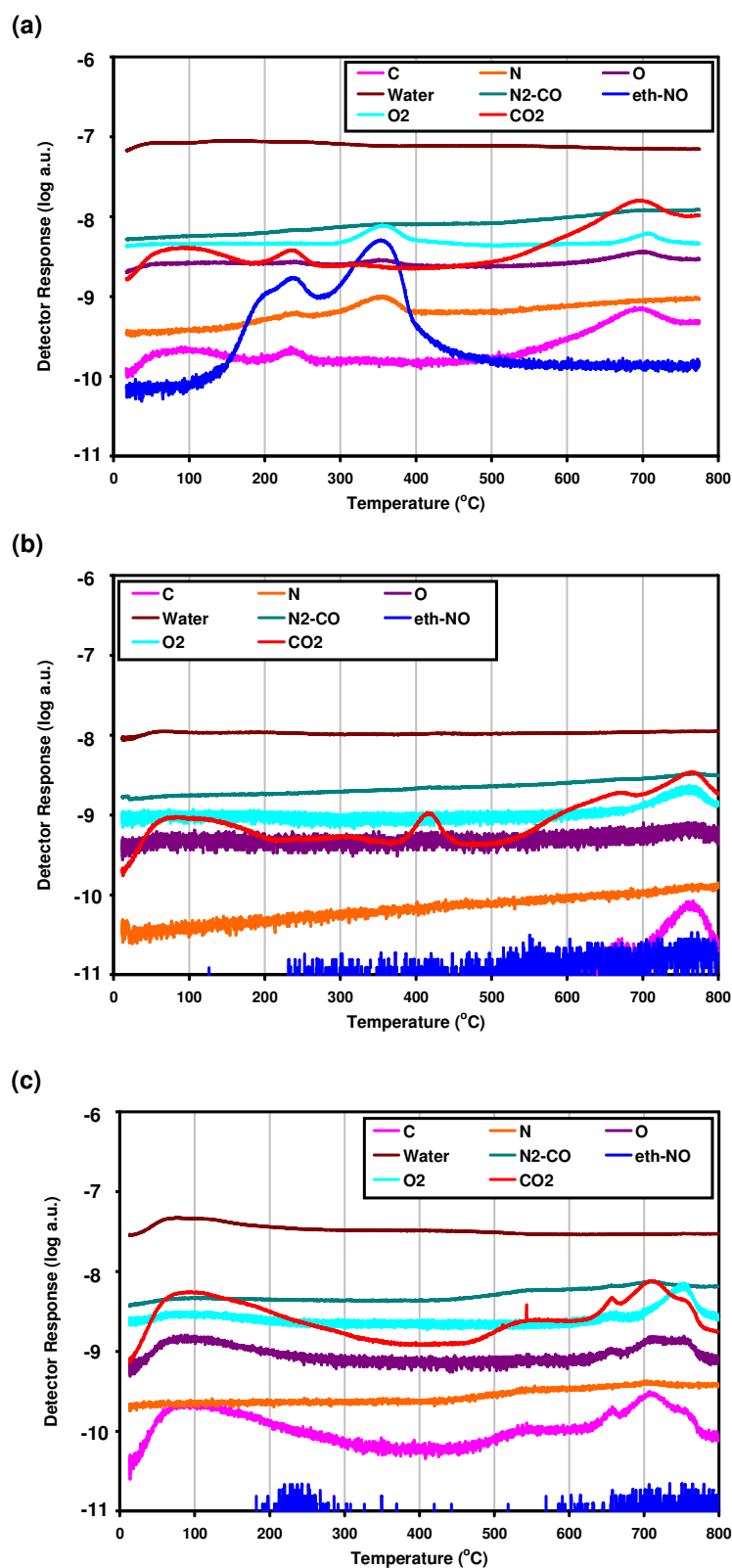


**Figure 5.9** TPD traces for as-prepared (a) 5-50-I (I), (b) 5-50-I (II), (c) 5-50-D.

The  $m/q = 44$  ( $\text{CO}_2$ ) trace is mirrored by  $m/q = 16$  (O) and  $m/q = 12$  (C), which can be assigned to the breakdown of  $\text{CO}_2$  in the QMS. There was also another  $m/q = 32$  ( $\text{O}_2$ ) peak

(756°C). In this instance as the large CO<sub>2</sub> peak was shifted to a slightly lower temperature (714°C) the two peaks no longer corresponded. This suggests that oxygen from the sample was desorbed during the TPDs for both samples. The m/q = 32 peak corresponded with a smaller m/q = 16 peak but to no consistent change in any other trace. This suggests that it is O<sub>2</sub> that was being evolved from the sample. Desorption of oxygen from the sample during TPD experiments would impact on any calibration measurements in subsequent TPD/Rs, as the amount of oxygen that was present in the samples before reduction would be overestimated.

### 5.5.1.2 Effect of Mixed Oxide Composition

For clarity the m/q = 44 (Figure 5.10), m/q = 32 (Figure 5.11) and m/q = 18 (Figure 5.12) signals have been plotted for all 5 wt% copper impregnated oxide compositions. The signals for m/q = 44 and 32 were both smoothed, using a 10 point moving average, to reduce the noise present in both traces. All of the samples investigated evolved multiple CO<sub>2</sub> peaks during TPD experiments. The m/q = 44 (CO<sub>2</sub>) signal was similar for 5-10-D, 5-25-D, 5-75-D and 5-90-D samples with an initial peak between 75 and 100°C, a second peak at around 600°C and a high temperature peak above 750°C. The trace for 5-50-D had three pronounced high temperature peaks at 660, 713 and 755°C. These peaks were not observed for any other sample although they proved to be reproducible for 5-50-D. The m/q = 44 peaks had corresponding peaks at m/q = 12 suggesting the release of CO<sub>2</sub> and its subsequent decomposition in the QMS to give C, confirming the m/q = 44 signal was due to the evolution of CO<sub>2</sub>.

The copper impregnated oxides displayed desorption of O<sub>2</sub> at high temperature as shown in Figure 5.11. This suggested that these catalysts were likely to be reduced much more easily than the bare oxides, as the oxygen in the samples was released readily even in an inert atmosphere. There was also initial O<sub>2</sub> evolution observed for all the 5-D samples at around 100°C and also to a much lesser degree in the 5-I samples. It was felt to be unlikely, at this low temperature, that the desorption was due to the evolution of lattice oxygen. As there were corresponding peaks observed for the bare oxides it has been surmised that the initial desorption was due to the release of O<sub>2</sub> species adsorbed onto the samples, as is discussed further in Chapter 6. The high temperature peak above 700°C varies in both temperature and magnitude as the oxide composition changes. Low ceria samples, 5-10-D and 5-25-D,

displayed almost equivalent peaks at roughly 725°C. As was shown for the CO<sub>2</sub> traces, 5-50-D had a much larger peak than that observed for any of the other samples, at around 760°C. There was a small peak shown at around 660°C which was also observed for 5-90-D. The trace for 5-90-D corresponds closely to that of 5-50-D but the peaks observed are approximately half the area. The 5-75-D sample displayed the smallest O<sub>2</sub> desorption peak of all the materials tested, at around 680°C.

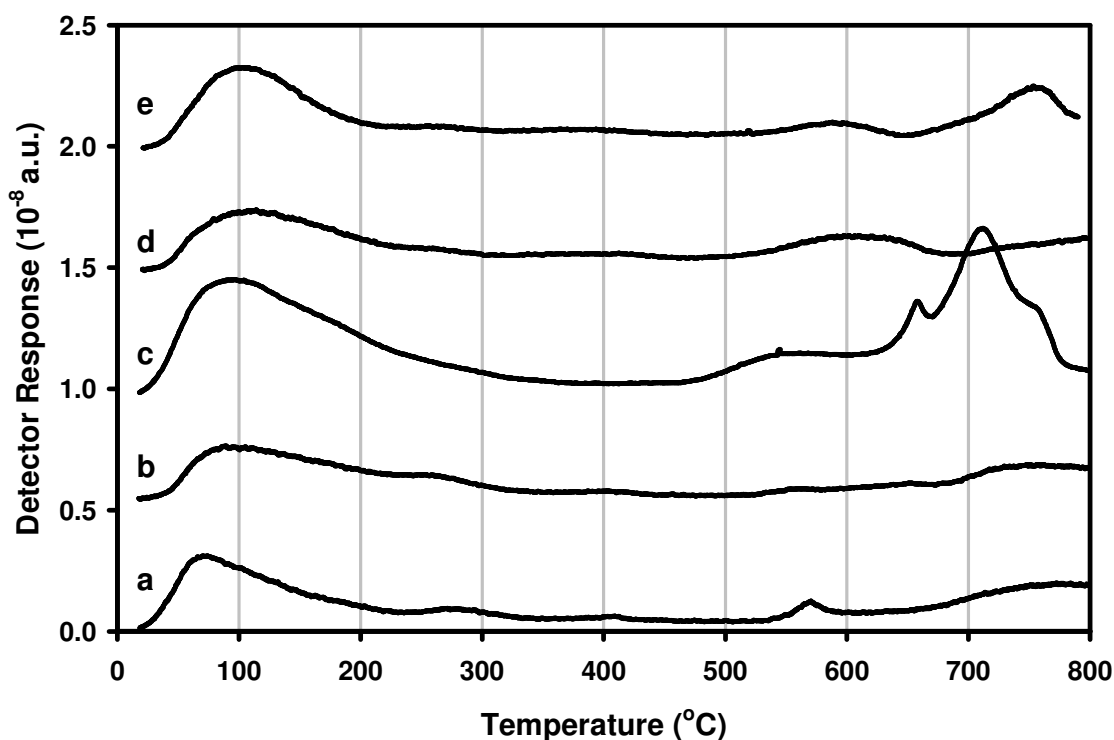


**Figure 5.10** CO<sub>2</sub> traces ( $m/q = 44$ ) from TPDs of as-prepared (a) 5-10-D, (b) 5-25-D, (c) 5-50-D, (d) 5-75-D, (e) 5-90-D.

The area of the O<sub>2</sub> desorption peaks was calculated for all the samples tested. The amount of O<sub>2</sub> desorbed was then quantified by comparing the peak areas calculated to the traces from the calibration gas as described in Section 3.8.1. The O<sub>2</sub> trace from the calibration gas corresponded to a known amount of O<sub>2</sub> (as the volume and composition of the calibration gas corresponding to the trace were both known). By comparing the area of the TPD and calibration gas traces for O<sub>2</sub> it was possible to calculate the moles of oxygen which were desorbed during experiments and the data is displayed in Figure 5.13. The moles of O<sub>2</sub> desorbed were then calculated as a % of the theoretical O<sub>2</sub> content of the sample. The amount of O<sub>2</sub> that could be released through sample reduction was based on the

assumptions that all copper was present as CuO and reduced to Cu and all Ce was initially present as Ce<sup>4+</sup> and reduced to Ce<sup>3+</sup>.

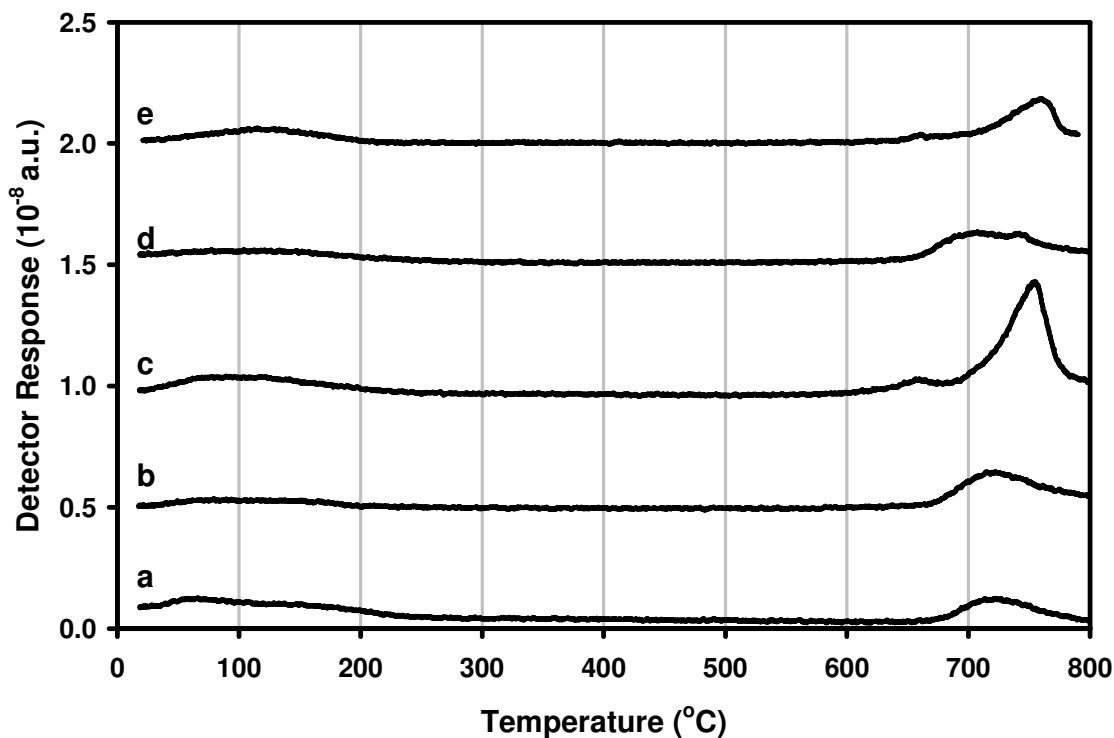


**Figure 5.11** O<sub>2</sub> traces (m/q = 32) from the TPDs of as-prepared (a) 5-10-D, (b) 5-25-D, (c) 5-50-D, (d) 5-75-D, (e) 5-90-D.

The amount of O<sub>2</sub> desorbed for the I samples increased with increasing ceria content of the oxide to 5-75-I (II), before decreasing for 5-90-I (II), as shown in Figure 5.13. The rate at which desorption increased was initially large before remaining constant between 5-50-I (II) and 5-75-I (II). For the D samples the highest desorption was seen for 5-50-D which displayed a large high temperature peak at 750°C. 5-10-D displayed the second highest amount of O<sub>2</sub> desorption, though the majority of this was evolved below 200°C. It was thought to be unlikely that the O<sub>2</sub> evolved at low (<200°C) was the result of the sample being reduced in the Ar flow. 5-25-D, 5-75-D and 5-90-D all desorbed similar amounts of O<sub>2</sub>. Increasing the copper loading was expected to lead to greater O<sub>2</sub> desorption from the impregnated samples as there would be more CuO present, which it has been surmised was the source of the O<sub>2</sub>. In order to establish if this was the case a series of 50-I (II) samples of varying copper loadings were analysed. There was only slight increase in the evolution of O<sub>2</sub>, on going from the 2 to the 5 wt% copper samples, before a massive increase for 7-50-I (II), from which roughly two and a half times the amount of O<sub>2</sub> was desorbed when

compared to 5-50-I (II). The amount of O<sub>2</sub> desorbing from the sample actually decreased when the copper loading was changed from 7 to 10 wt%. This is displayed in Figure 5.14. The 7-50-I (II) sample has a much broader high temperature desorption peak. The effect of using the D as opposed to the I copper impregnation technique was to increase the amount of O<sub>2</sub> desorbed for all oxide compositions. The increase was most pronounced in the low ceria samples (5-10, 5-25 and 5-50), with the higher ceria oxide samples (5-75 and 5-90) showing comparable desorption.

Figure 5.12 shows the  $m/q = 18$  (H<sub>2</sub>O) signals corresponding to desorption of water from samples impregnated with 5 wt% copper during preparation. All samples showed low temperature water desorption. The temperature at which the desorption maximum occurred rose with increasing ceria content, from 64°C for 5-10-D to 120°C for 5-90-D. There was a slight increase in the area of the peaks with increasing ceria content which agrees with the results obtained for the bare oxides. However the amount of water obtained during TPD experiments involving copper impregnated samples was drastically lower than that obtained from the bare oxides. The high temperature peaks observed for some of the bare oxides were not observed for the copper impregnated samples.

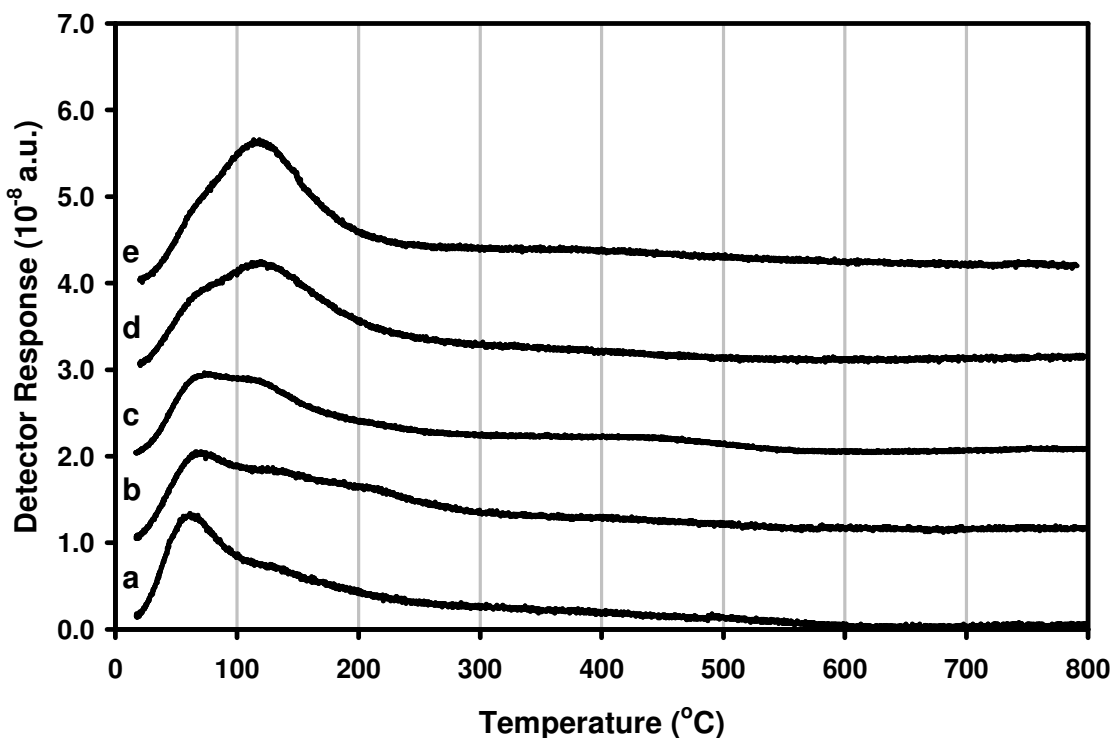


**Figure 5.12** H<sub>2</sub>O traces ( $m/q = 18$ ) from the TPDs of as-prepared (a) 5-10-D, (b) 5-25-D, (c) 5-50-D, (d) 5-75-D, (e) 5-90-D.

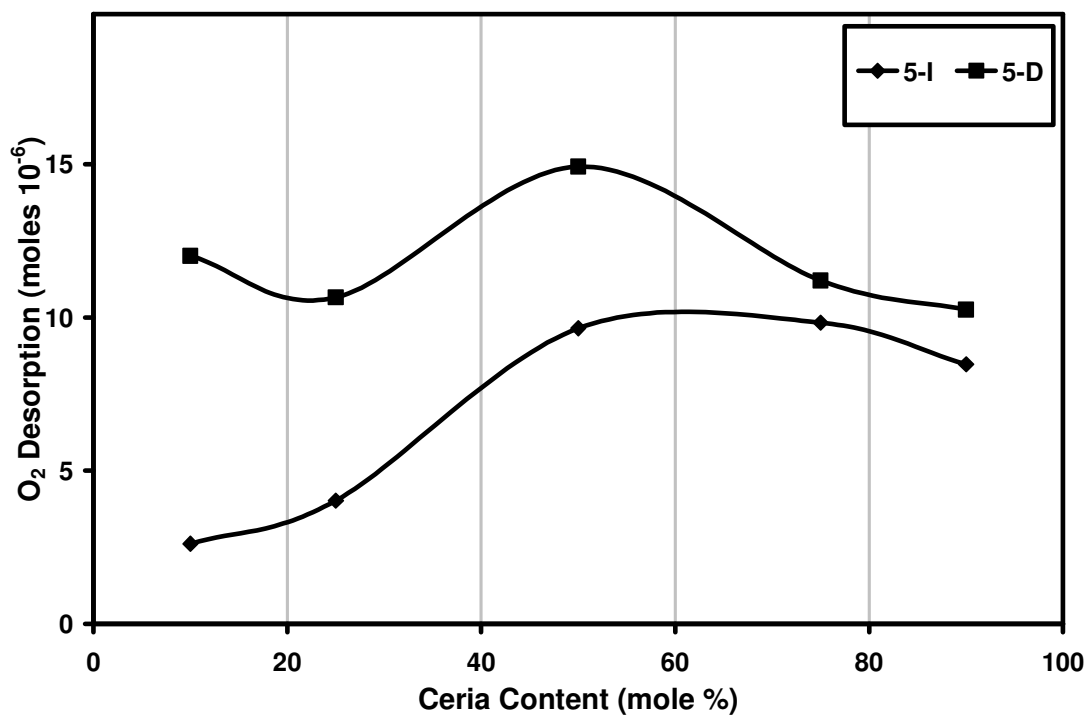


**Figure 5.13** Moles of O<sub>2</sub> desorbed during TPD of 5-I and 5-D samples.

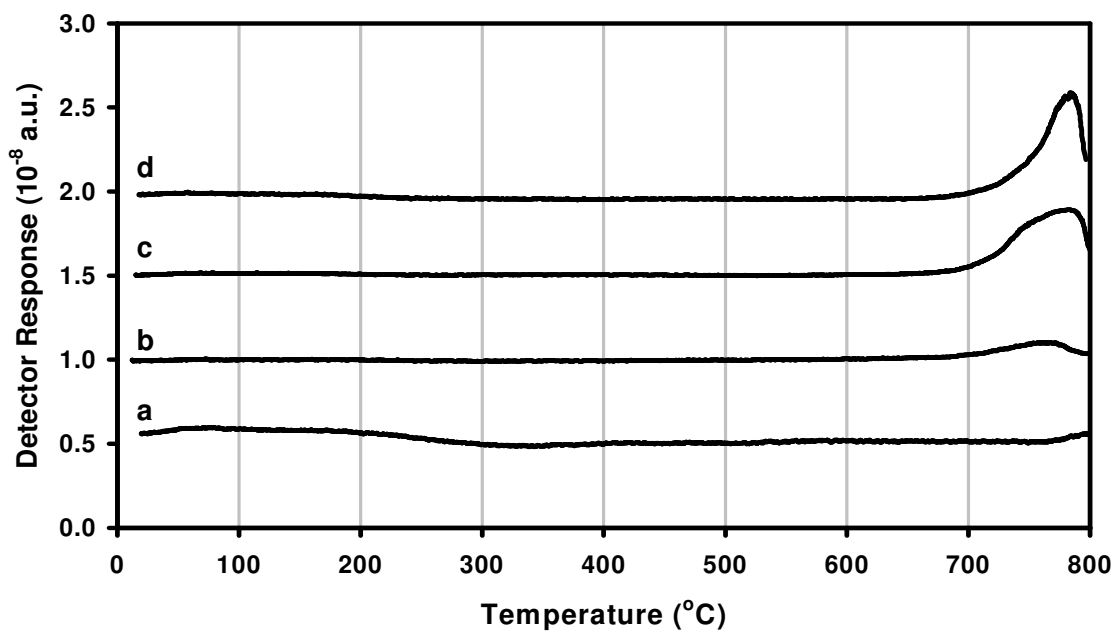


**Figure 5.14** O<sub>2</sub> traces from the TPDs of as-prepared (a) 2-50-I (II), (b) 5-50-I (II), (c) 7-50-I (II), (d) 10-50-I (II).

The effect of increasing the copper content of the impregnated mixed oxide on the amount of O<sub>2</sub> desorbed is shown in Figure 5.14. The temperature at which the O<sub>2</sub> was desorbed was relatively consistent, peaking at around 780°C. Oxygen evolution was minimal for the 2 wt% impregnated sample and increased progressively as Cu loading increased. This seems to confirm the observation that the desorption of O<sub>2</sub> is due to highly active CuO sites, from which the O<sub>2</sub> is readily released even in an inert atmosphere.

### 5.5.2 Temperature Programmed Reduction

TPR experiments enabled the investigation of the oxygen storage capacity of the sample (shown by the amount of water evolved) and availability of the oxygen present (shown by the temperature of any water evolution peaks). All experimental plots are included as Appendix 4 for completeness. It was established by TPD that the samples as prepared contained carbon species and adsorbed water (Figures 5.11 and 5.12). There was also desorption of oxygen at high temperatures (above 700°C, Figures 5.11 and 5.14) for all copper-containing samples. The oxygen desorption was most pronounced in samples with higher copper content. As a result, accurate determination of the extent of reduction of the samples was problematic. Using straight TPR measurements, on the as-prepared samples, would mean that desorbed water would lead to an artificial increase in the calculated extent of the sample reduction. TPD/R measurements would underestimate the true extent of reduction due to the oxygen desorption during TPDs. As a result the amount of water evolved during the TPRs, TPD/Rs and the amount of O<sub>2</sub> evolved during TPDs were all calculated in order to ensure as accurate a calculation of the sample reduction as was possible.

#### 5.5.2.1 Effect of the Copper Impregnation Technique

In order to establish the effect of the oxide on the impregnated copper TPRs were performed on nanoparticulate CuO (NanoArc 97.5%, S.A. 25-40 m<sup>2</sup>g<sup>-1</sup>, 23-37 nm) and on CuO prepared from Cu(NO<sub>3</sub>)<sub>2</sub>·3H<sub>2</sub>O (calcined at 250°C for 1hr and subsequently 500°C for 1hr, with a heating rate of 2°C min<sup>-1</sup>). The resulting traces are shown in Figure 5.15. The nanopowder showed water evolution at low temperature (<100°C), the main reduction peak being at 165°C. The main reduction peak had corresponding O (m/q=16) and O<sub>2</sub> (m/q=32) peaks. The former of which is explained by decomposition of water in the QMS, the latter

was thought to result from the release of labile oxygen species from the copper. There were two distinct shoulders to the water peak. The lower of these was at 150°C and for the higher temperature shoulder the water trace remained fairly constant at an elevated level between 180 and 300°C before tailing off. The breadth of the peaks is probably due to a range of particle sizes being present in the material. There was also a peak observed for NO (m/q=30) at around 160°C which is thought to be the decomposition of remaining nitrate used in sample preparation.

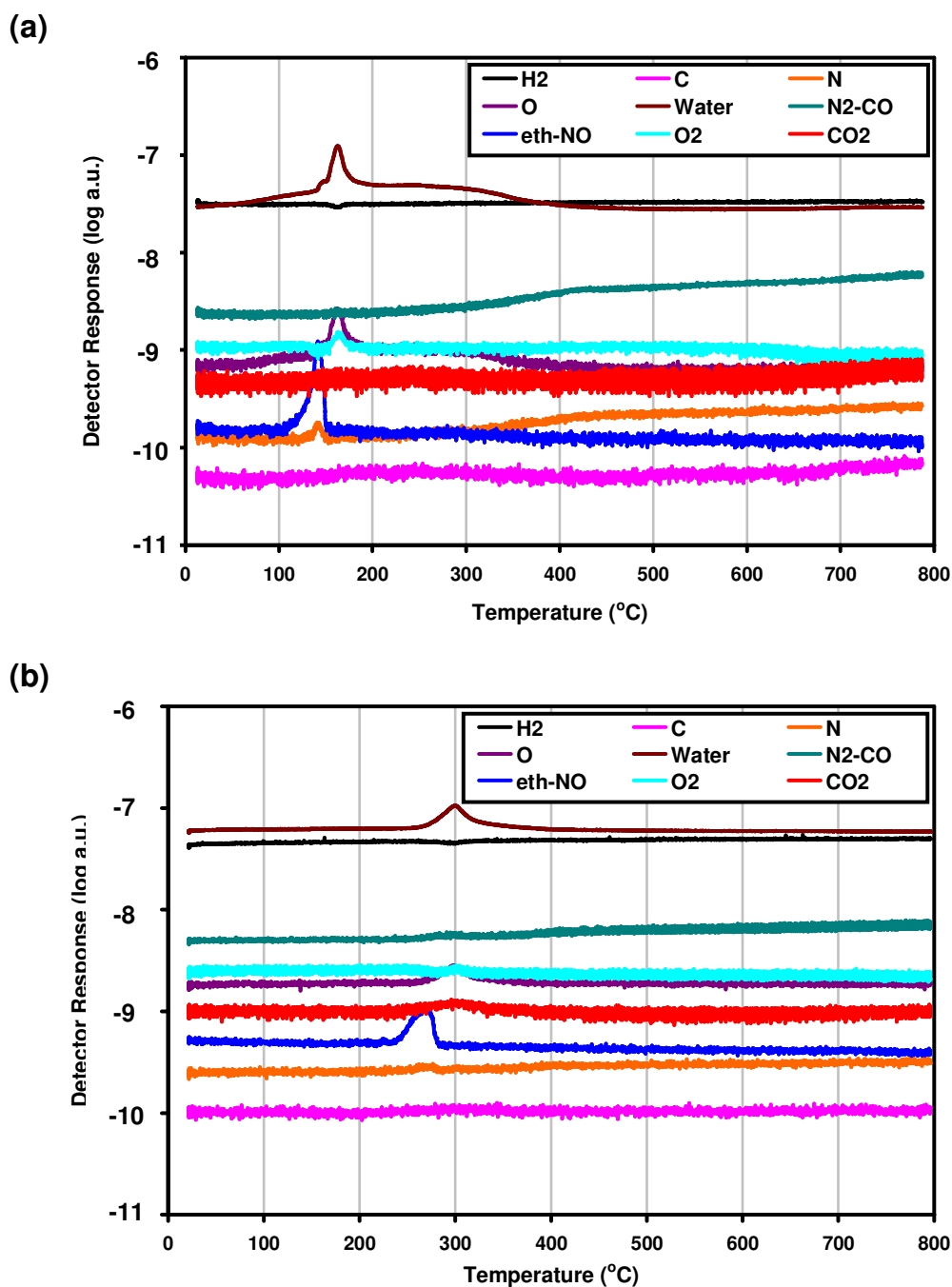


**Figure 5.15** TPR traces of (a) CuO nano-powder (b) CuO prepared from  $\text{Cu}(\text{NO}_3)_2 \cdot 3\text{H}_2\text{O}$ .

For the CuO prepared from the nitrate the majority of the traces remained constant for the duration of the TPR. The only peaks of note observed were for NO ( $m/q = 30$ ) at 270°C, and for water at 300°C. The higher temperature of the main reduction peak for the sample from the nitrate compared to the nano-powder is likely to be because of the higher SSA of the nano-powders. The CuO obtained from the nitrate was likely to have a lower SSA and is shown to be less active. The residual nitrate used to produce the copper might be expected to be released in the form of NO<sub>2</sub> (Eqn 5.1). The trace for NO<sub>2</sub> was negligible for the duration of the TPR, however, with only NO being detected. It may therefore have been the case that the NO<sub>2</sub> that was released during the nitrate decomposition reacted with the H<sub>2</sub> flow as shown in Eqn 5.2. The other alternative would be the mechanism of decomposition of the copper nitrate to have been that proposed by Burleson et al. [2] for the decomposition of zirconium nitrate (Eqn 5.3).



The two alternative copper impregnation routes gave rise to samples with similar reduction profiles as shown in Figure 5.16. As with all the TPR experiments the hydrogen trace appeared stable on this scale and indeed it was not until it was enlarged greatly that any H<sub>2</sub> consumption troughs were seen.

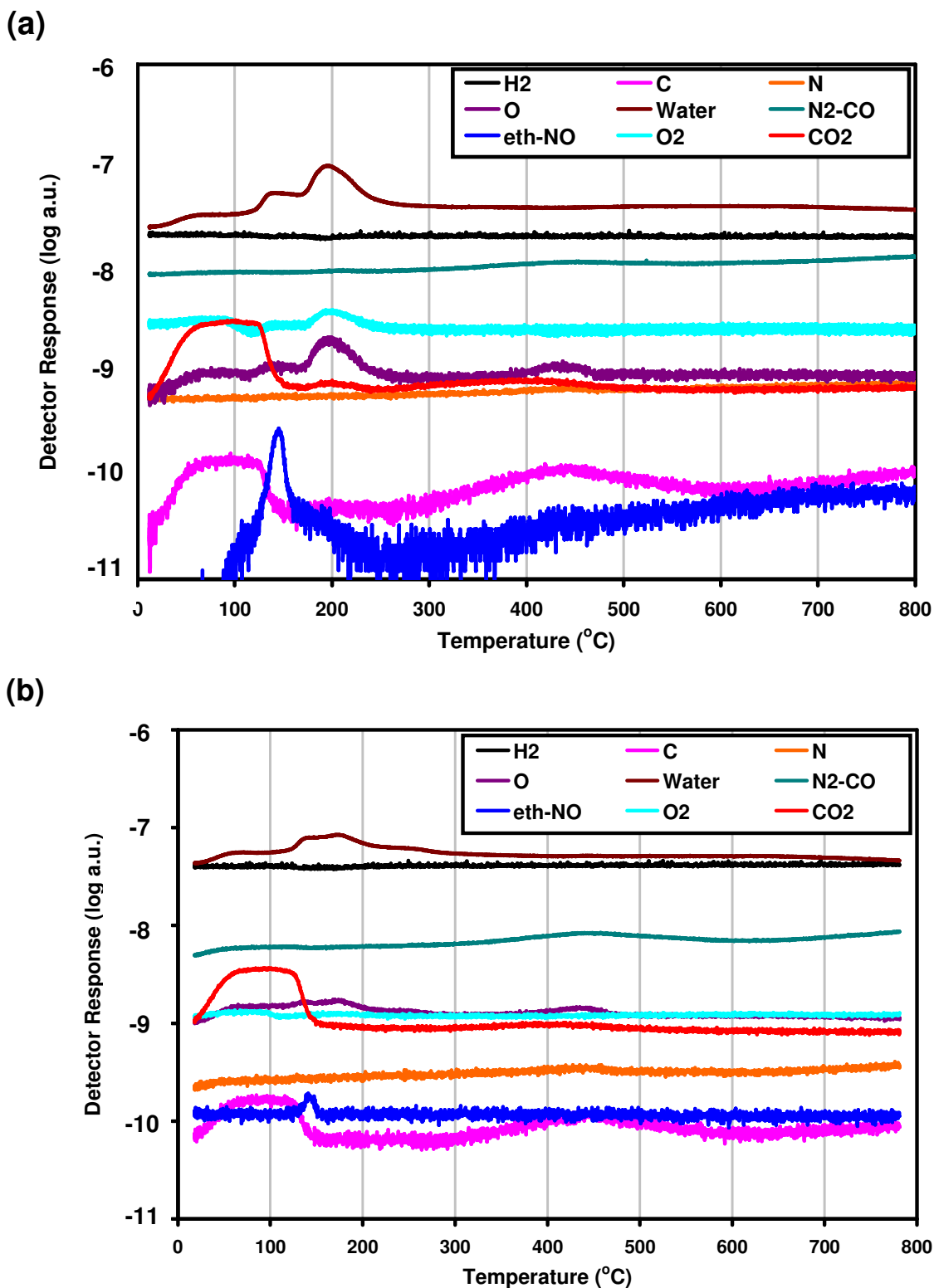


**Figure 5.16** TPR traces of as-prepared (a) 5-50-I (II) and (b) 5-50-D.

The  $m/q = 12$  (C) trace followed quite closely the  $\text{CO}_2$  trace at low temperature with a large peak between 60-120°C. Carbon traces also displayed a peak at around 440°C which was reflected in the  $m/q = 28$  (CO) trace for the I and D samples. The perceived high

temperature peak in the  $m/q = 28$  trace seems to have been due to the gradual increase in the level of  $N_2$  during the reaction which was mirrored by N.

There was a small amount of NO ( $m/q = 30$ ) released in the TPRs of both samples shown in Figure 5.16, which was a result of the release of the remaining nitrate precursor from the preparation techniques. The  $m/q = 28$  trace ( $N_2$  or CO) increased with temperature for all the materials independent of preparation route. These traces varied depending on the material and showed a number of distinct peaks (at around 450 and 750°C for the 5-50 samples). With any increase in nitrogen levels the first concern was a leak in the system but the oxygen levels were stable at these temperatures and also there was no additional reduction taking place at the higher temperatures which would occur if air (and hence  $O_2$ ) was entering the system. Both  $m/q = 12$  and  $m/q = 14$  showed peaks corresponding to peaks in the  $m/q = 28$  trace, suggesting that small amounts of nitrogen species remaining from the copper nitrate impregnation as well as carbon species remaining from the preparation were decomposing.

The water traces for both materials showed reduction was taking place at a much lower temperature (peak reduction at 180°C for 5-50-D and 200°C for 5-50-I (II)) than that displayed by the bare oxide (560°C for ZCe50). The water traces for both materials displayed two distinct peaks which varied in position and relative size depending on the impregnation technique. With regard to the ZCe50 samples, for 5-50-I (II) the second water peak was over twice the height of the first peak. This was not the case for 5-50-D in which the second peak was only slightly larger than the first. This suggests that the D impregnation technique was more effective at ensuring a high dispersion of the readily reduced states. That is a higher proportion of the copper impregnated was in the active state almost in a 1:1 ratio compared to 1:2 for the wet impregnated sample of the same composition.

### **5.5.2.2 Effect of Oxide Composition**

In order to clearly display the effect of oxide composition on reduction temperature, the water traces for the straight TPRs for all 5 wt% copper impregnated samples were plotted (Figure 5.17 and Figure 5.18). Initial water desorption was observed for all samples

irrespective of preparation technique or oxide composition typically peaking around 75°C. For the I samples there were two distinct low temperature reduction peaks, that is, water peaks that corresponded to H<sub>2</sub> consumption. The first reduction peak (1) was consistently around 135°C. The area of this initial reduction peak generally increased with the increasing ceria content of the oxide. The exception to this was 5-90-I (II) where the reduction peak became a small shoulder on the second reduction peak. The second peak (2) generally moved to slightly lower temperatures with increasing ceria content (from 200°C for 5-10-I (II) to 170°C for 5-90-I (II)), with the exception of 5-10-I (II) which displayed the second peak at a slightly lower temperature than that observed for 5-25-I (II). The relative area of the second peak also increased with the ceria content. Two samples also displayed large high temperature peaks (3 and 4): 5-10-I (II) at 490°C and 5-90-I (II) at 720°C, while the other samples only displayed very small higher temperature peaks. These high temperature peaks were likely due to the low copper loading (5 wt%) being insufficient to cover all the oxide support in the sample. Therefore, bulk material was present whose reduction could not be catalysed by Cu species. This assertion is supported by the fact that the peak was at a similar temperature to minor peaks observed in the reduction of the bare oxide (530°C for ZCe10 and 715°C for ZCe90).

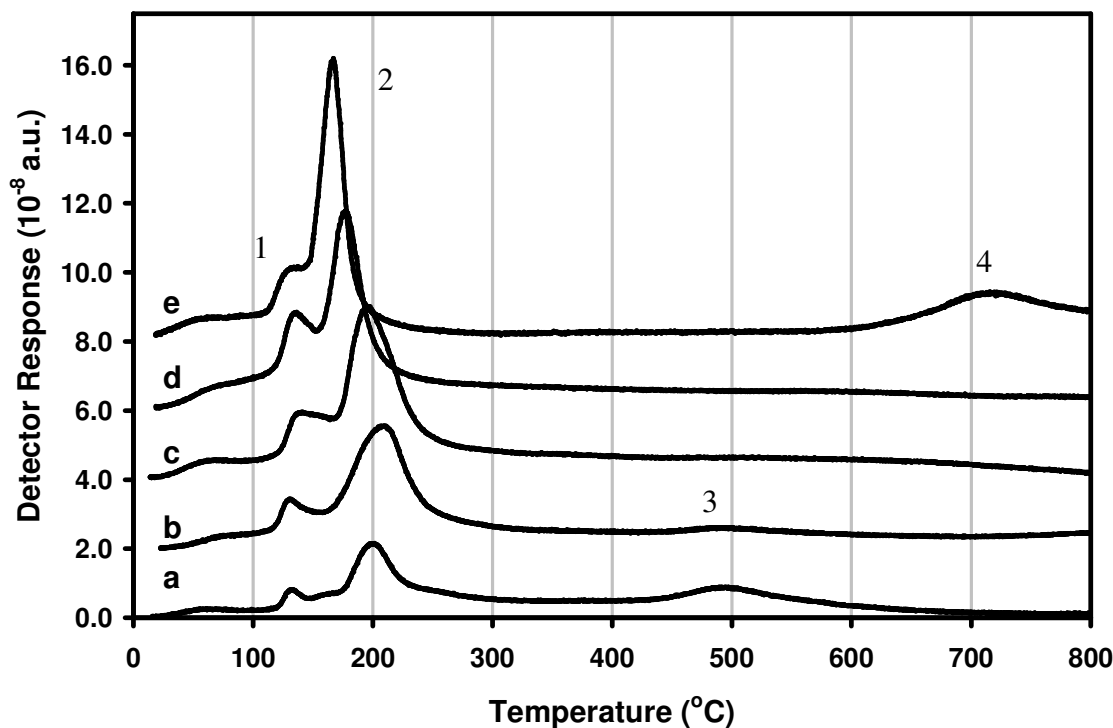


**Figure 5.17** TPR water traces for as-prepared (a) 5-10-I (II), (b) 5-25-I (II), (c) 5-50-I (II), (d) 5-75-I (II), (e) 5-90-I (II).

As observed with the 5-I samples, there were also two reduction peaks observed for all materials prepared using the D method. For all the D samples, the main reduction peak temperatures were found to be lower than for I materials of the same composition. The difference in peak reduction temperature between the I and D samples varied with oxide composition and ranged from a decrease of 20°C for the ZCe50 samples to a maximum decrease in the peak reduction temperature of 60°C for ZCe10.

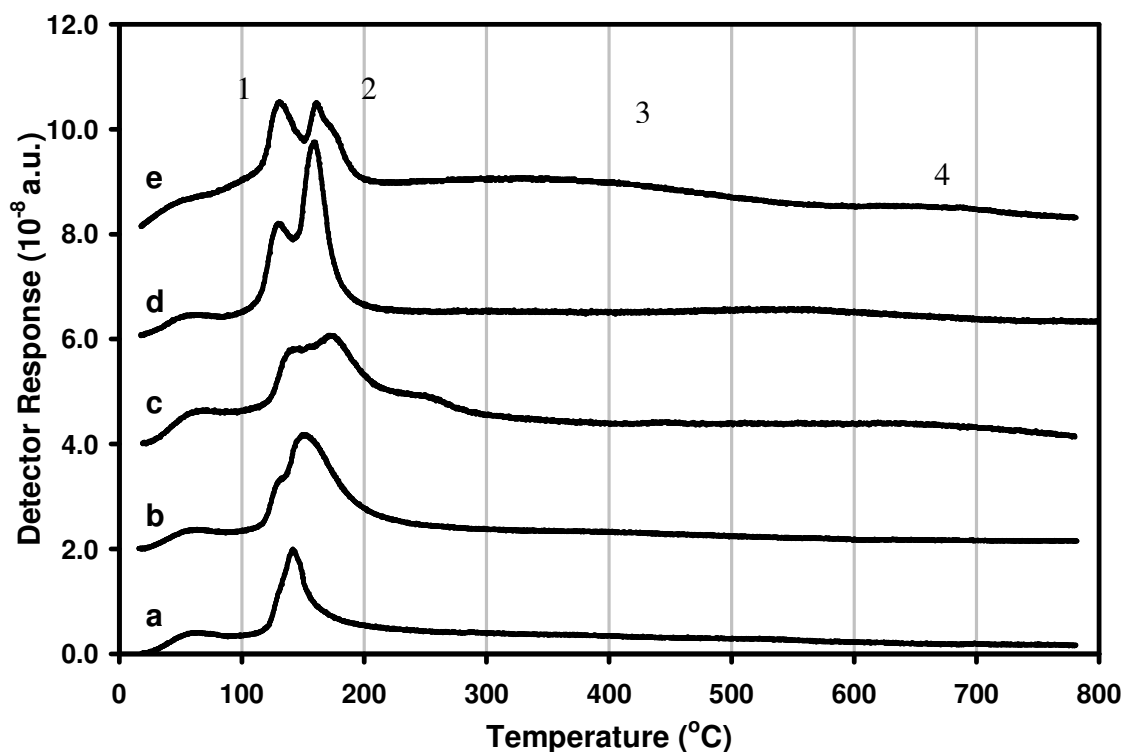


**Figure 5.18** TPR water traces for as-prepared (a) 5-10-D, (b) 5-25-D, (c) 5-50-D, (d) 5-75-D, (e) 5-90-D.

Despite the large change in the position of the second reduction peak (2) observed on altering the impregnation route, the lower temperature peak (1) remained consistent (within  $\pm 5^\circ\text{C}$ ) for the two preparation routes. As a result, for 5-10-D and 5-25-D, these peaks appeared as shoulders on the second reduction peak. This shift in the position of the second reduction peak (2) for 5-10-D was such that the first peak (1) is not easily discernable. The relative size of the lower temperature peaks increased for all of the 5-D materials. This was most pronounced for 5-90-D for which the lower temperature reduction peak was larger than the second reduction peak.

Figure 5.19 shows the moles of water evolved for the 5 wt% Cu impregnated samples in TPR and TPD/R experiments. Water evolved during the TPD experiments is not included. For the I as-prepared samples the amount of water produced during the TPR experiments increased with increasing ceria concentration up to 5-50-I (II). There was then a slight decrease in water production for 5-75-I (II) and 5-90-I (II), the latter of which had only the third highest water produced for the 5-I (II) samples. For the TPD/R runs however there was again an increase in the water evolved from 5-10-I (II) to 5-25-I (II) with the rest of the samples 5-50-I (II), 5-75-I (II) and 5-90-I (II) producing roughly equivalent amounts of water. The TPD/R results consistently contained less water evolution than the TPR results. This was a result of the desorption of water during the TPD previously discussed in Section 5.5.1, as well as the desorption of O<sub>2</sub> during the TPDs which is discussed further in Section 5.5.2.4.

During the TPRs the as-prepared D samples showed increased water production from 5-10-D to 5-50-D before declining for 5-75-D with 5-90-D producing the greatest amount of water for the 5-D samples. The TPDs again decreased the amount of water evolved from the samples with the TPD/Rs containing less water evolution than the TPRs.

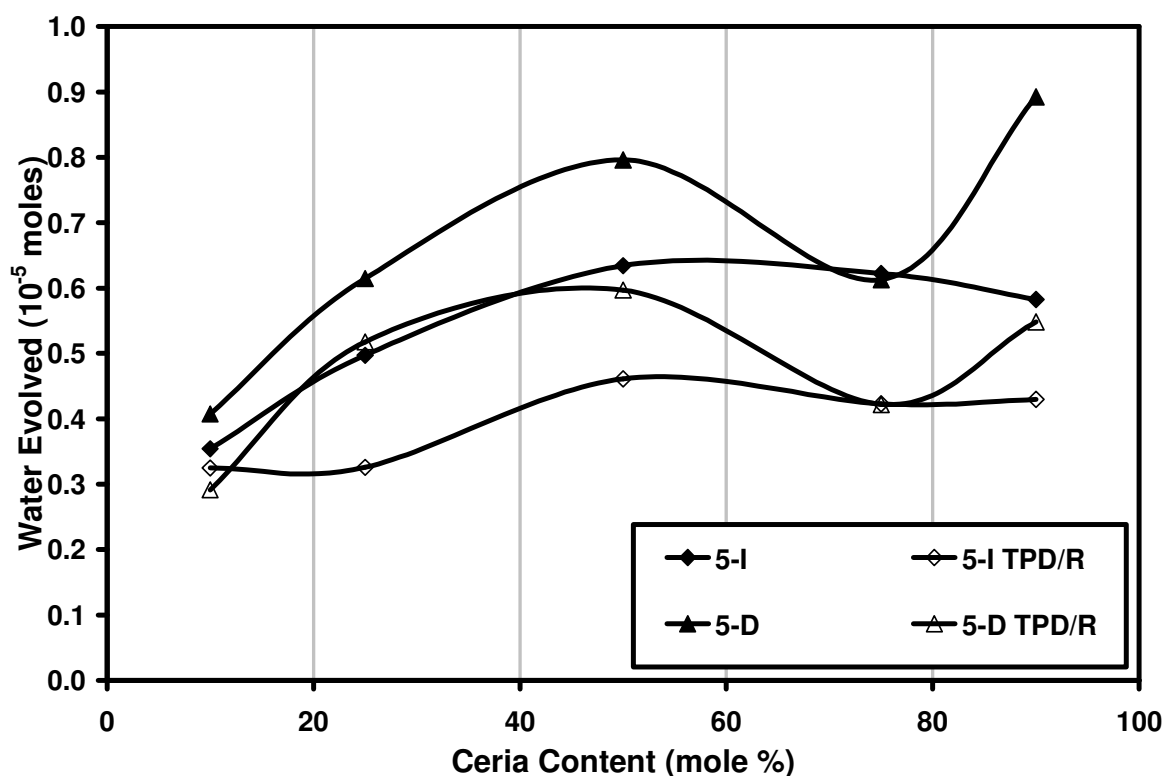


**Figure 5.19** Moles of water produced during TPR and TPD/R of 5 wt% copper impregnated mixed oxides.

### 5.5.2.3 Effect of Copper Loading

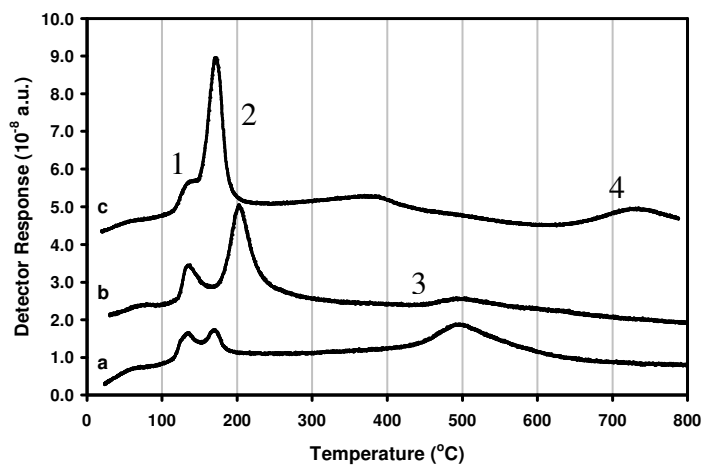
Samples were prepared containing 2, 5, 7 and 10 wt% copper to investigate the effect that the copper loading had on the reduction profile of the catalysts. The 5 wt% copper impregnated samples were discussed in Section 5.5.2.2.

Figure 5.20 shows the water traces for a number of the 2 wt% copper samples which were impregnated using the incipient wetness method. All of these samples displayed large high temperature peaks. These peaks were located at 495°C for 2-10-I (II), 500°C for 2-50-I (II) and 2-90-I (II) displayed two peaks at 390°C and 735°C. These peaks are similar to reduction peaks observed for the bare oxides in Section 4.3.2.2. As a result the high temperature reduction peaks observed (3 and 4), were attributed to areas of the Ce/Zr support on which there was no copper present to catalyse the reduction as a result of the low copper loading. The assignment of these peaks is discussed further in Chapter 6. As observed with the other copper impregnated samples, there were two low temperature reduction peaks. The position of the first of these peaks is within +/- 5°C of the corresponding peaks for the 5% copper impregnated samples (Figure 5.21).

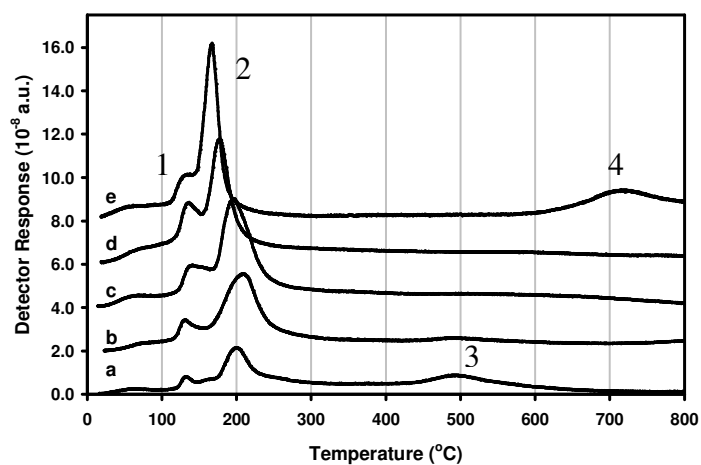
For the ZCe50 and ZCe90 samples, apart from the peaks at high temperatures the only effect of the reduced Cu loading was to diminish the peak area. This can be explained by the smaller amount of copper present to be reduced. The presence of the large high temperature peaks is a result of insufficient copper loading to ensure that the copper was distributed over the whole surface of the oxide. As a result there are in effect areas of bare oxide present in the sample which are reduced at higher temperature. The 2-10-I (II) trace is more difficult to explain, but was repeatable. The large peak at 495°C implies poor copper coverage for large areas of the sample, which is to be expected with the low copper loading. This behaviour was also displayed by 5-10-I (II). The first low temperature reduction peak is consistent with that observed for other impregnated samples but the second low temperature peak is 30°C lower than that observed in the 5 wt% copper impregnated ZCe10 sample. The decrease in the temperature at which the second reduction peak was observed may be because the CuO was present as smaller particles at the lower loading, with these smaller particles being more readily reduced. Again the reasoning behind this will be discussed in detail in Chapter 6.

The water traces for the 5 wt% copper impregnated I samples are plotted in Figure 5.21. All samples displayed two distinct low temperature reduction peaks. The first reduction peak (1) was consistently around 135°C. The second peak (2) generally moved to slightly lower temperatures with increasing ceria content with the exception of 5-10-I (II) which displayed the second peak at a slightly lower temperature than that observed for 5-25-I (II). Two samples also displayed large high temperature peaks (3 and 4): 5-10-I (II) at 490°C and 5-90-I (II) at 720°C, with the other samples only displaying very small higher temperature peaks.

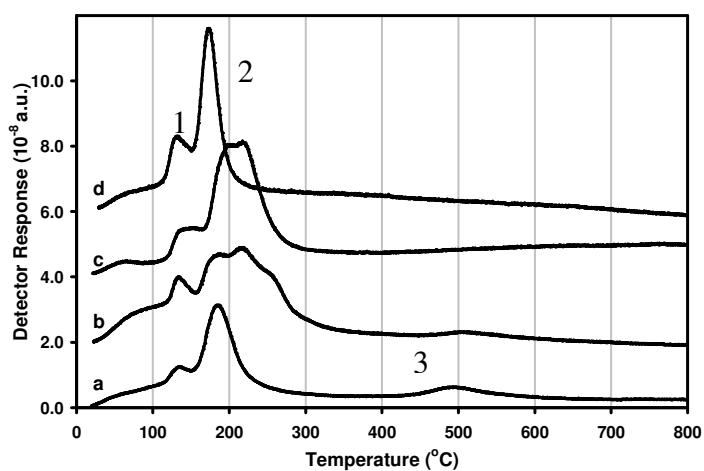
The water traces for the 7 wt% copper impregnated samples are plotted in Figure 5.22. As had been previously observed, the copper loading has minimal effect on the temperature of the first reduction peak (1) with the position of the low temperature peak being between 133 and 141°C for all the materials investigated. The 7 wt% copper samples, (as with the 10 wt% samples) 7-25-I (II) and 7-50-I (II), both displayed multiple or broadened reduction peaks at around 200°C (2). The EDX maps had revealed large copper agglomerations for some of the 5-I samples and all of the 7-I and 10-I samples (Figure 5.3-5.5). These larger copper agglomerations were unlikely to be as active as the smaller species with higher SSAs. These multiple environments in which the copper was present throughout the material appeared to result in multiple reduction peaks.



**Figure 5.20** TPR water traces for as-prepared (a) 2-10-I (II), (b) 2-50-I (II), (c) 2-90-I (II).

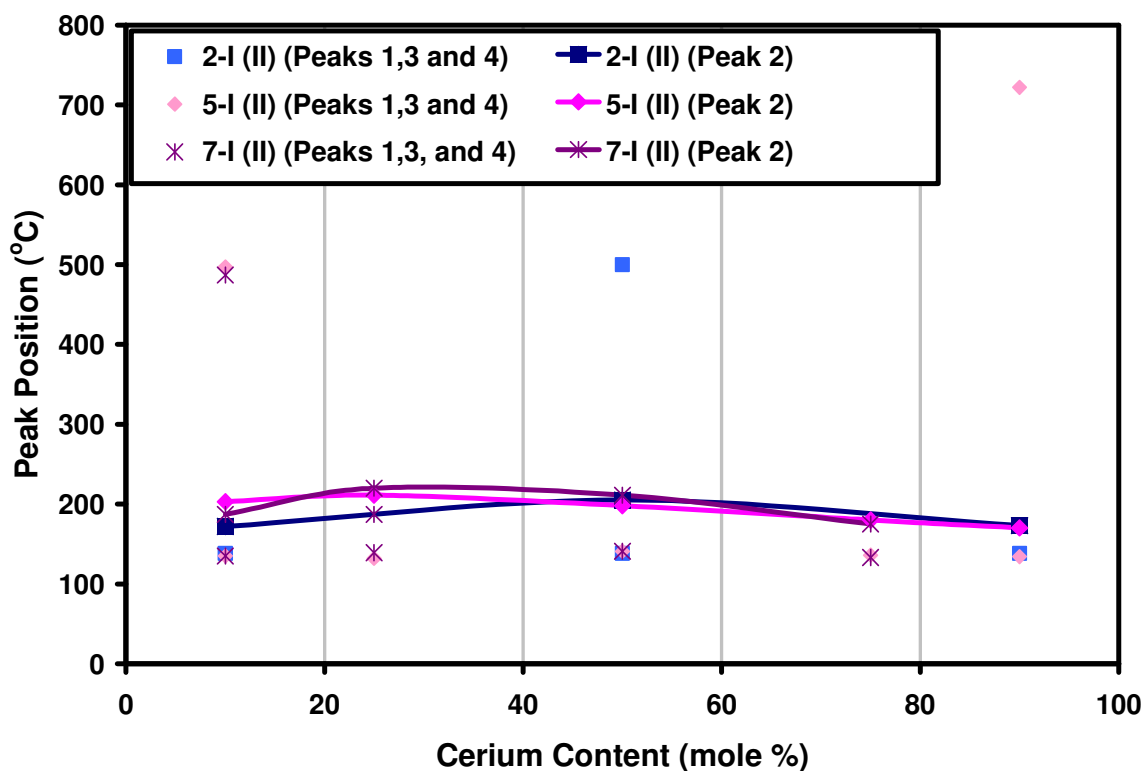


**Figure 5.21** TPR water traces for as-prepared (a) 5-10-I (II), (b) 5-25-I (II), (c) 5-50-I (II), (d) 5-75-I (II), (e) 5-90-I (II).



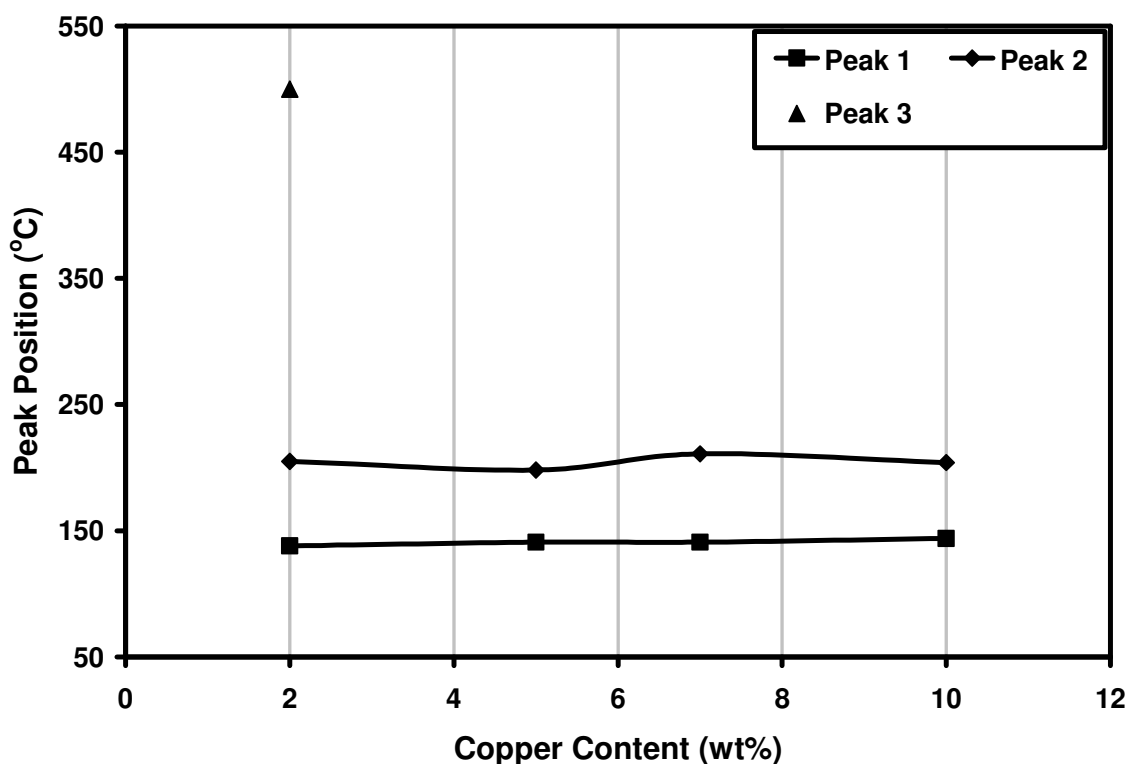
**Figure 5.22** TPR water traces for as-prepared (a) 7-10-I (II), (b) 7-25-I (II), (c) 7-50-I (II), (d) 7-75-I (II).

Figure 5.23 was prepared to graphically display the effect of the different copper loadings on the various oxides. It was apparent that the different copper loadings had only a small effect on the main reduction peak position (2) for all the oxide compositions. The low temperature reduction peak positions (1) were also very similar for all copper loadings and also for all the oxide compositions. The largest variation with regards to peak reduction temperature (2) was seen for the ZCe10, where the peak reduction temperature went from 172°C for 2-10-I (II), to 203°C for 5-10-I (II) only to then drop to 187°C for 7-10-I (II). As for the lower temperature reduction peak (1) all the as-prepared I samples were between 132°C (2-25-I (II)) and 144°C (10-50-I (II)). Also included in Figure 5.23 are the high temperature peaks (3 and 4), which fit loosely with the reduction peaks observed for the bare oxides.



**Figure 5.23** TPR reduction peak positions for as-prepared I samples for varying oxide compositions.

Figure 5.24 presents a plot of reduction peak position against Cu content as observed in the TPRs of the ZCe50-I samples. The temperature of the peak reduction of the samples varied by only 13°C from the highest of 211°C for 7-50-I (II), to the lowest 198°C for 5-50-I (II). The temperature of the initial reduction peak (1) was also consistent irrespective of copper loading.



**Figure 5.24** TPR reduction peak positions for as-prepared ZCe50-I samples as a function of copper loading.

#### 5.5.2.4 Effect of the Thermal Cycling Involved in TPD experiments

The water traces of the straight TPR experiments involving the 5 wt% Cu impregnated samples have already been discussed and were included in Figures 5.17 and 5.18. To demonstrate the effect on those materials of the TPD experiments, in which samples were heated to 800°C, the TPD/R water traces for these same materials are shown in Figures 5.25 and 5.26.

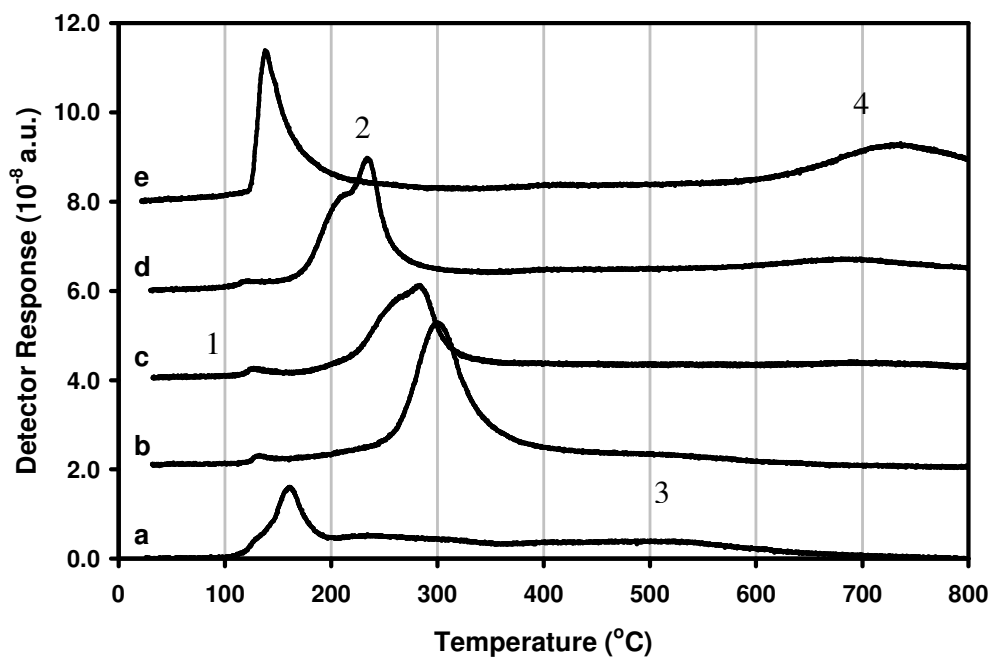


**Figure 5.25** Water traces from TPD/R of (a) 5-10-I, (b) 5-25-I, (c) 5-50-I, (d) 5-75-I, (e) 5-90-I.

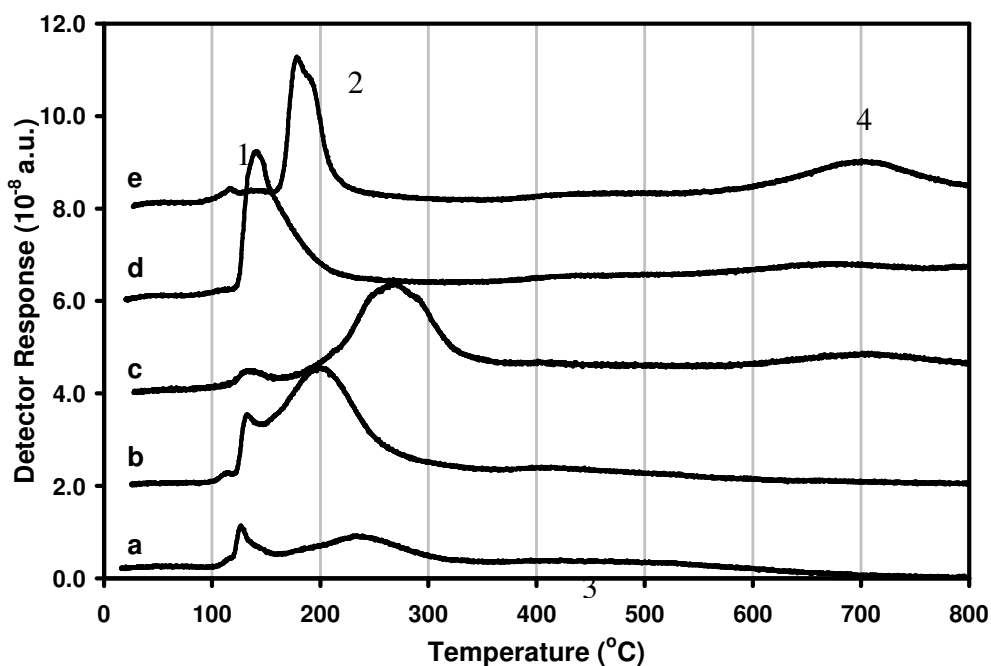


**Figure 5.26** Water traces from TPD/R of (a) 5-10-D, (b) 5-25-D, (c) 5-50-D, (d) 5-75-D, (e) 5-90-D.

Prior to the TPD experiments the main reduction peak (2) positions for the 5-D and the 5-I (II) samples were similar, regardless of oxide composition, varying by 33°C for 5-I (II) and by 44°C for the 5-D samples. In the TPD/R results, the differences in the main reduction

peak position (2) increased to 163°C for 5-I (II) and 141°C for 5-D samples. For the 5-I (II) samples, both of high and low ceria content, that is 5-10-I (II) and 5-90-I (II), there was a decrease in the temperature at which the materials were reduced (-41°C from 203 to 162°C for 5-10-I (II) and -33°C from 170 to 137°C for 5-90-I (II)). The effect of the TPDs was most pronounced on the samples with intermediate Ce/Zr ratios: 5-25, 5-50 and 5-75-I (II). All of these materials showed a marked increase in the temperature of the main reduction peak, 99°C for 5-25-I (II), 87°C for 5-50-I (II) and 55°C for 5-75-I (II). These changes are displayed in Figure 5.27 in which the peak reduction temperatures are shown for 5-I (II) and 5-D samples both for TPR and TPD/R experiments.

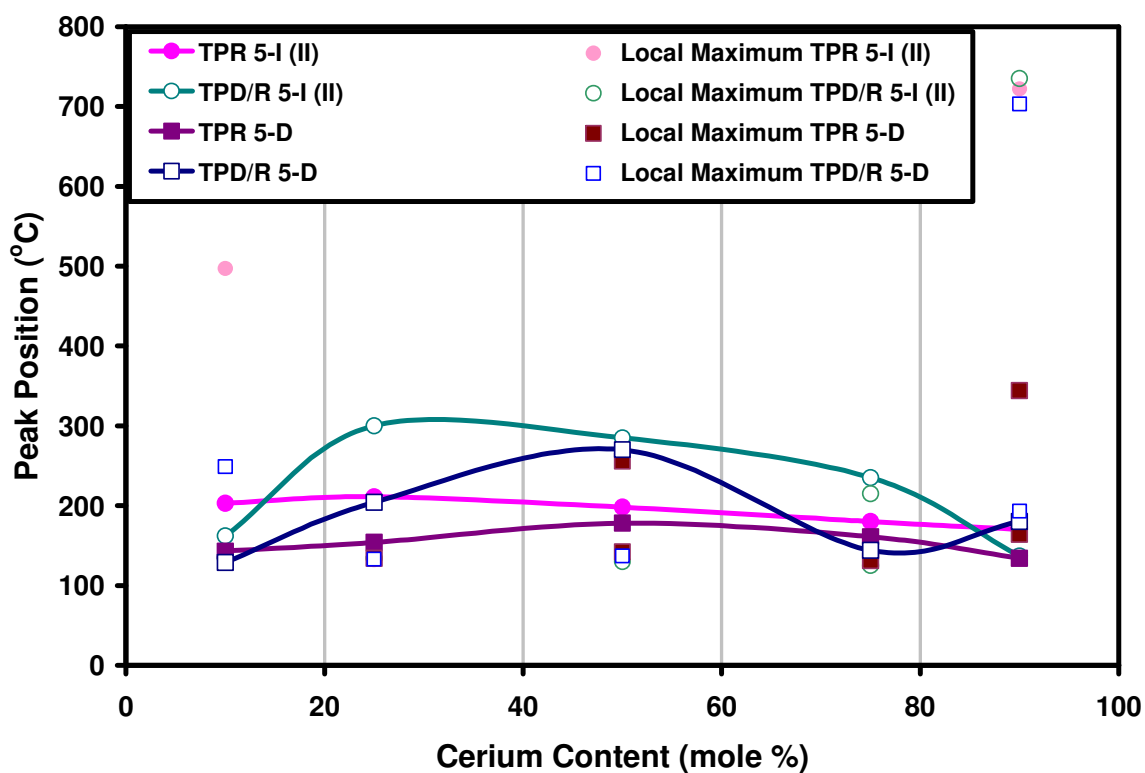


**Figure 5.27** TPR and TPD/R reduction peak temperatures for 5 wt% copper containing samples.

The 5-50-D sample showed the greatest change due to the TPD, with an increase of 92°C, which was in excess of the change displayed in the peak reduction temperature (2) of the 5-50-I (II) sample (which increased by 87°C). As with the 5-I samples, two samples displayed a decrease in the temperature of peak reduction in the TPD/Rs. These were the ZCe10 impregnated sample (-14°C for 5-10-D), again, and also the ZCe75 sample (-17°C for 5-75-D). Again the ZCe25 sample showed a large increase in peak reduction

temperature, though the increase was roughly half of that for the 5-25-I (II) sample (+50°C for 5-25-D compared to +99°C for 5-25-I (II)). In contrast to the 5-90-I (II) samples, which displayed a decrease in the temperature of the main reduction peak, for the TPD/Rs compared to the TPRs, 5-90-D displayed a large increase (+46°C).

A number of samples showed an increase in the area of the lower temperature reduction peak (1), or the area relative to the second reduction peak (2). This was true for 5-10-I (II), 5-90-I (II), 5-10-D, 5-25-D and 5-75-D. The TPD/Rs had the effect of practically eradicating these peaks for the remaining samples. For 5-25-I (II), 5-50-I (II), 5-75-I (II), 5-50-D and 5-90-D the low temperature reduction peaks (1) which were quite pronounced during the TPRs became insignificant in the TPD/Rs.

Figure 5.28 shows the amount of water evolved during the TPR and TPD/R experiments as a % of the theoretical maximum, that is assuming that all Ce present in the oxide was present as  $\text{Ce}^{4+}$  which was reduced to  $\text{Ce}^{3+}$  during the course of the TPR and all Cu was present as  $\text{CuO}$  and was reduced to  $\text{Cu}^0$ . The amount of oxygen that would be released and hence the amount of  $\text{H}_2\text{O}$  that would be produced was calculated. There are few consistent trends easily discernable for these data. The TPRs, as would be expected due to the evolution of any adsorbed water, do contain more water than the TPD/Rs for the 5-I (II) samples. For the 5-D samples the same is true, as expected. Higher copper loadings were expected to increase the amount of water evolved, due to the increase of  $\text{CuO}$  content in the material and this was the case for the majority of samples. The extent of reduction also increased with the copper content with the exception of 10-50-I (II). These results are summarised in Table 5.1. This table contains the moles of water evolved during TPRs and TPD/Rs, and what percentage of total theoretical sample reduction these values relate to. Also included are the moles of  $\text{O}_2$  released during TPD experiments. The amount of oxygen desorbed during TPDs was combined with the water released during the subsequent TPR (TPD/Rs) in order to establish the extent of reduction of the sample across both experiments.

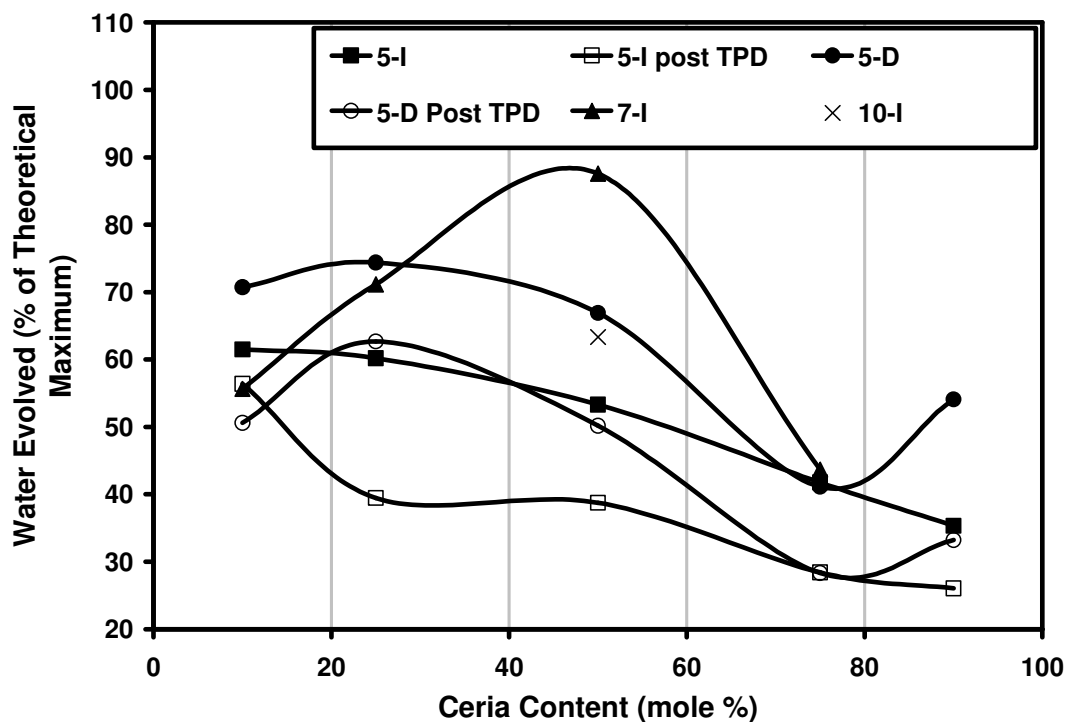


**Figure 5.28** The amount of water evolved during TPR and TPD/R experiments for all copper wt% and oxide composition samples.

There was significant desorption of  $O_2$  during the TPDs of nearly all the 5-D samples. This may have been the release of  $O_2$  from the more active surface sites which were responsible for the lower temperature reduction peaks observed in the TPRs of the as-prepared samples. As a result, the oxygen content of the samples would have been reduced before the TPD/Rs. This would explain the large decrease in the size of the low temperature reduction peaks observed in the TPD/Rs compared to TPRs. The 5-I samples displayed much less  $O_2$  desorption during the TPDs.

**Table 5.1** Water and O<sub>2</sub> released during the course of TPD, TPD/R and TPR experiments for impregnated samples and B) D impregnated samples.

Material	Cu (wt %)	Moles of Water (10 <sup>-5</sup> )	Theoretical Reduction (%)	O <sub>2</sub> Desorption (10 <sup>-5</sup> moles)	H <sub>2</sub> O+O <sub>2</sub> (% reduction)
10	2-I	7.96	229.5		
	5-I	3.54	61.5		61.5
	5-I TPD	3.25	56.4	0.27	61.1
	7-I	4.06	55.7		
25	5-I	4.97	60.2		60.2
	5-I TPD	3.26	39.5	0.41	44.5
	7-I	6.92	71.2		
50	2-I	3.57	36.4	0.90	45.6
	5-I	6.34	53.3		53.3
	5-I TPD	4.61	38.8	0.98	47.0
	7-I	11.60	87.6	2.52	106.6
	10-I	9.69	63.3		
	10-I TPD	5.43	35.5	1.70	46.6
75	5-I	6.22	41.7		41.7
	5-I TPD	4.23	28.4	0.99	35.1
	7-I	6.51	43.7		
90	5-I	5.83	35.3		35.3
	5-I TPD	4.30	26.0	0.86	31.2

**Table 5.2** Water and O<sub>2</sub> released during the course of TPD, TPD/R and TPR experiments for D impregnated samples.

Material	Cu (wt %)	Moles of Water (10 <sup>-5</sup> )	Theoretical Reduction (%)	O <sub>2</sub> Desorption (10 <sup>-5</sup> moles)	H <sub>2</sub> O+O <sub>2</sub> (% reduction)
10	5-D	4.07	70.7		70.7
	5-D TPD	2.91	50.6	1.21	71.6
25	5-D	6.14	74.4		74.4
	5-D TPD	5.18	62.7	1.08	75.7
50	5-D	7.96	66.9		66.9
	5-D TPD	5.97	50.2	1.50	62.8
75	5-D	6.13	41.1		41.1
	5-D TPD	4.22	28.3	1.13	35.9
90	5-D	8.92	54.1		54.1
	5-D TPD	5.48	33.2	1.04	39.5

### 5.5.3 Temperature Programmed Reaction

As was done for the bare oxides, a small number of copper containing samples were studied in TPRx experiments during which the as-prepared samples were heated to 800°C in a flow of 5% CH<sub>4</sub>/Ar. The samples chosen for investigation were 5-50-I (II), 5-50-D and 10-50-I (II). Their TPRx plots are given in Figures 5.29 and 5.30 (a), (b) and (c) respectively. It was felt that these samples would show any effects of the different impregnation techniques and the higher copper loading. Figure 5.29 shows the log plots of the TPRx experiments. The log plots, whilst displaying the majority of the traces clearly, made it difficult to discern any change in the CH<sub>4</sub> level. To better display the changes in the CH<sub>4</sub> partial pressure, the signal was reduced and plotted on a linear scale along with other species likely to change (Figure 5.30). As the CH<sub>4</sub> levels were much higher than the other species involved, adjusting the level so that it was comparable to the other species made it appear extremely noisy. Despite the CH<sub>4</sub> flow being left for 30 min to stabilise, there was still a slight increase in the background reading for all experiments. This was most pronounced for 5-50-D as shown in Figure 5.30(b) where there was a relatively sharp initial increase in the trace for CH<sub>4</sub>.

As was observed in the TPRs, the addition of copper had the effect of lowering the temperature at which the materials reacted. As with the bare oxides, there was initially complete oxidation of the CH<sub>4</sub>, demonstrated by the production of CO<sub>2</sub>. All the CO<sub>2</sub> traces displayed two roughly equivalent peaks (at 400 and 550°C for 5-50-I (II), 435 and 475°C for 5-50-D and 385 and 450°C for 10-50-I (II)). There was also an increase in the water signal corresponding to the CO<sub>2</sub>, confirming that complete oxidation was taking place. As the CO<sub>2</sub> levels dropped the partial pressure of CO increased, as the reaction tended towards the partial oxidation of CH<sub>4</sub>. There was a peak in the level of CO for all materials at around 840°C. The CH<sub>4</sub> level did not drop noticeably until around 15°C above this. For all materials the sharp decrease in CH<sub>4</sub> level was accompanied by a decrease in the level of C. This decrease in the amount of carbon species entering the QMS would suggest carbon deposition onto the catalyst. The CO trace increased and peaked before any noticeable decline in the CH<sub>4</sub> trace. This is explained by the relatively low levels of CO produced compared to the amount of CH<sub>4</sub> present. H<sub>2</sub> production initially corresponded with the increase in CO production. There was then a relatively sharp peak in H<sub>2</sub> production which

corresponded to the decrease in the trace for methane. It therefore appears that there were three reactions taking place during the TPRx experiments.

Firstly the total oxidation of methane which resulted in the release of CO<sub>2</sub> and water, followed by the partial oxidation of methane with the release of CO and H<sub>2</sub>. The methane trace contained too much noise to show any decrease when the CO<sub>2</sub> and CO was produced by these two reactions. The third reaction occurred when the partial oxidation stopped releasing CO and instead deposited carbon onto the sample. This third process appears to have occurred when all available oxygen from the samples had been consumed by the complete oxidation and then partial oxidation reactions. As a result there was no oxygen left to oxidise the methane. Instead the methane was broken down as is shown by the pronounced decrease in the m/q = 16 trace and the corresponding production of H<sub>2</sub>. The carbon from the methane was likely to have been deposited onto the catalyst. The most pronounced decreases in CH<sub>4</sub> was observed in Figures 5.30(a) and (c), for the I samples. The 5-50-D sample displayed a relatively minor reduction in methane level as well as continued CO production for the duration of the TPRx run. The impregnation technique seems to have had a much greater influence on the behaviour of the materials during the TPRx than the copper loading.

Figure 5.30(a) and (c) are directly comparable, there being only relatively minor differences in the plots despite the large difference in Cu loading (5 wt% vs 10 wt%). The 5-50-D sample does not appear to be as readily reduced, as is shown by the smaller CO and CO<sub>2</sub> traces (in Figure 5.30(b)). The relatively minor decrease in methane compared to that observed for the other copper containing samples does suggest that this sample may not be as prone to carbon deposition as the others, which were prepared by the I technique.

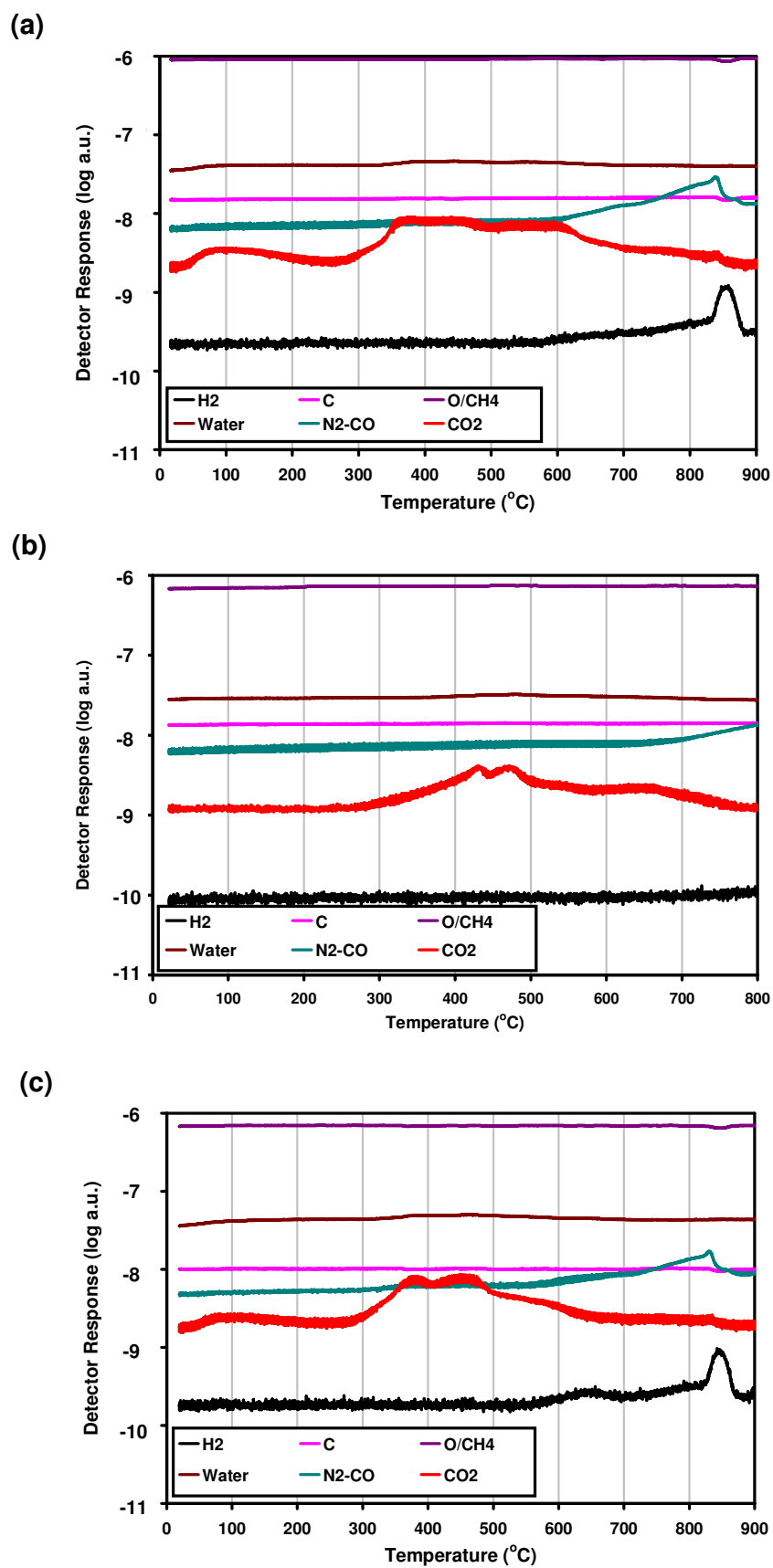


**Figure 5.29** Log TPRx traces for as-prepared a) 5-50-I (II), b) 5-50-D, c) 10-50-I (II).

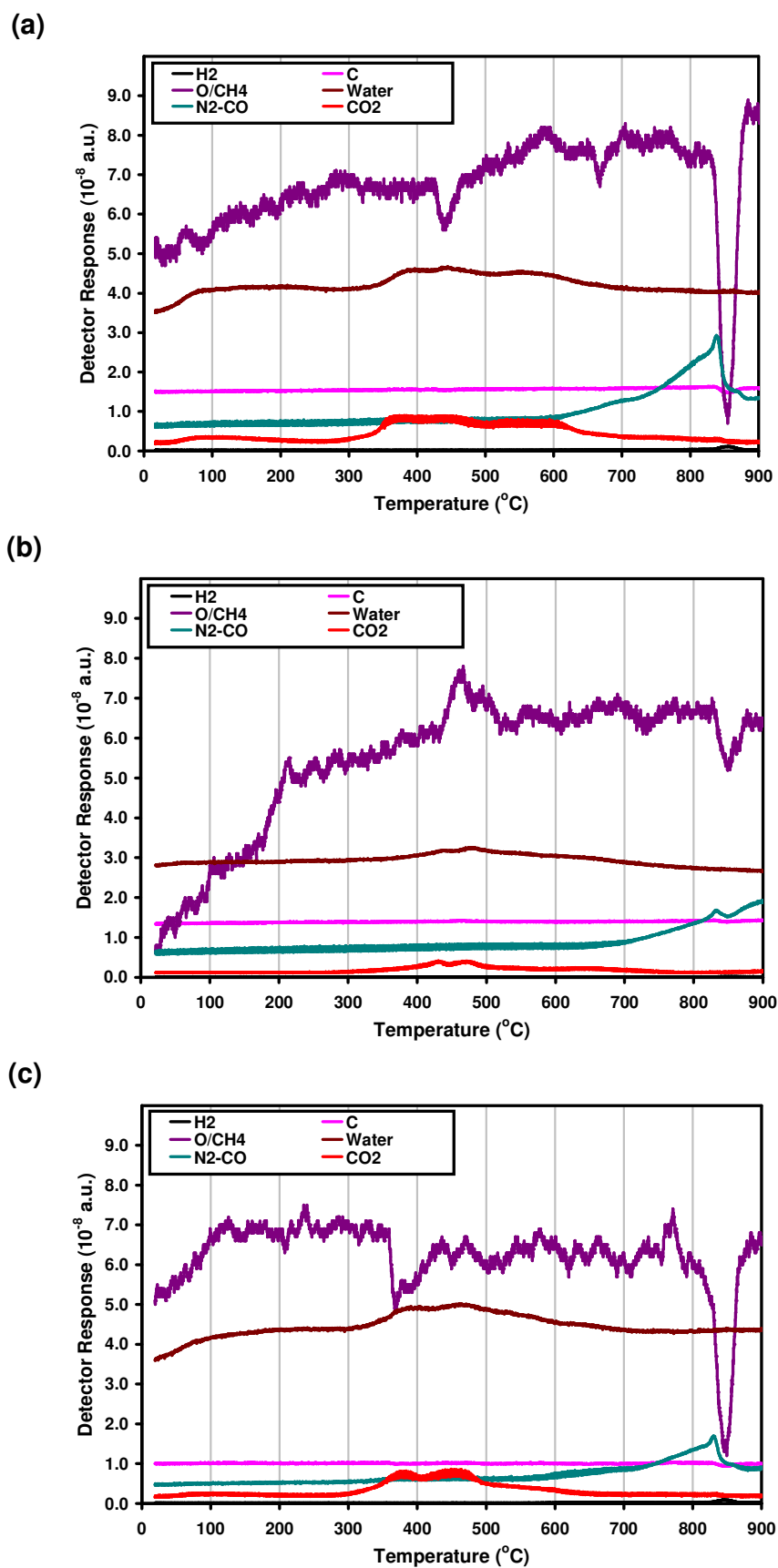


**Figure 5.30** Linear TPRx traces for as-prepared a) 5-50-I (II), b) 5-50-D, c) 10-50-I (II).

#### 5.5.4 Temperature Programmed Oxidation

In order to establish the extent of any carbon deposition onto the catalysts during the TPRx experiments, TPO experiments were performed on the samples and the resulting traces are presented in Figure 5.31. During the TPO, carbon deposited onto the catalyst would be oxidised, by a flow of 5% O<sub>2</sub>/Ar, and subsequently detected by the QMS as carbon oxides. The 5-50-D trace shown in Figure 5.31 (b) shows the initial evolution of a small amount of N<sub>2</sub>, this was most likely the result of a pulse of air which had been trapped in the equipment travelling to the QMS. As this pulse was at a low temperature and it was an oxidation reaction taken place it was felt that the effects of this air pulse on the overall experimental results would be negligible.

The three copper-containing samples all displayed pronounced evolution of carbon containing species (CO, CO<sub>2</sub> and m/q=30 which was thought to be either CH<sub>2</sub>O or C<sub>2</sub>H<sub>6</sub>) around 300°C as was observed for the bare ZCe50 oxide. For both of the wet impregnated samples there is a distinct shoulder at around 400°C, with both samples displaying subsequent CO<sub>2</sub> peaks around 620 and 690°C. A high temperature peak was also present at around 680°C in the TPO of 5-50-D, as was a large peak around 550°C which was not observed for the wet impregnated samples. 5-50-D did have a series of peaks related to carbon evolution around 400°C, but these were relatively small when compared with those for the I samples.

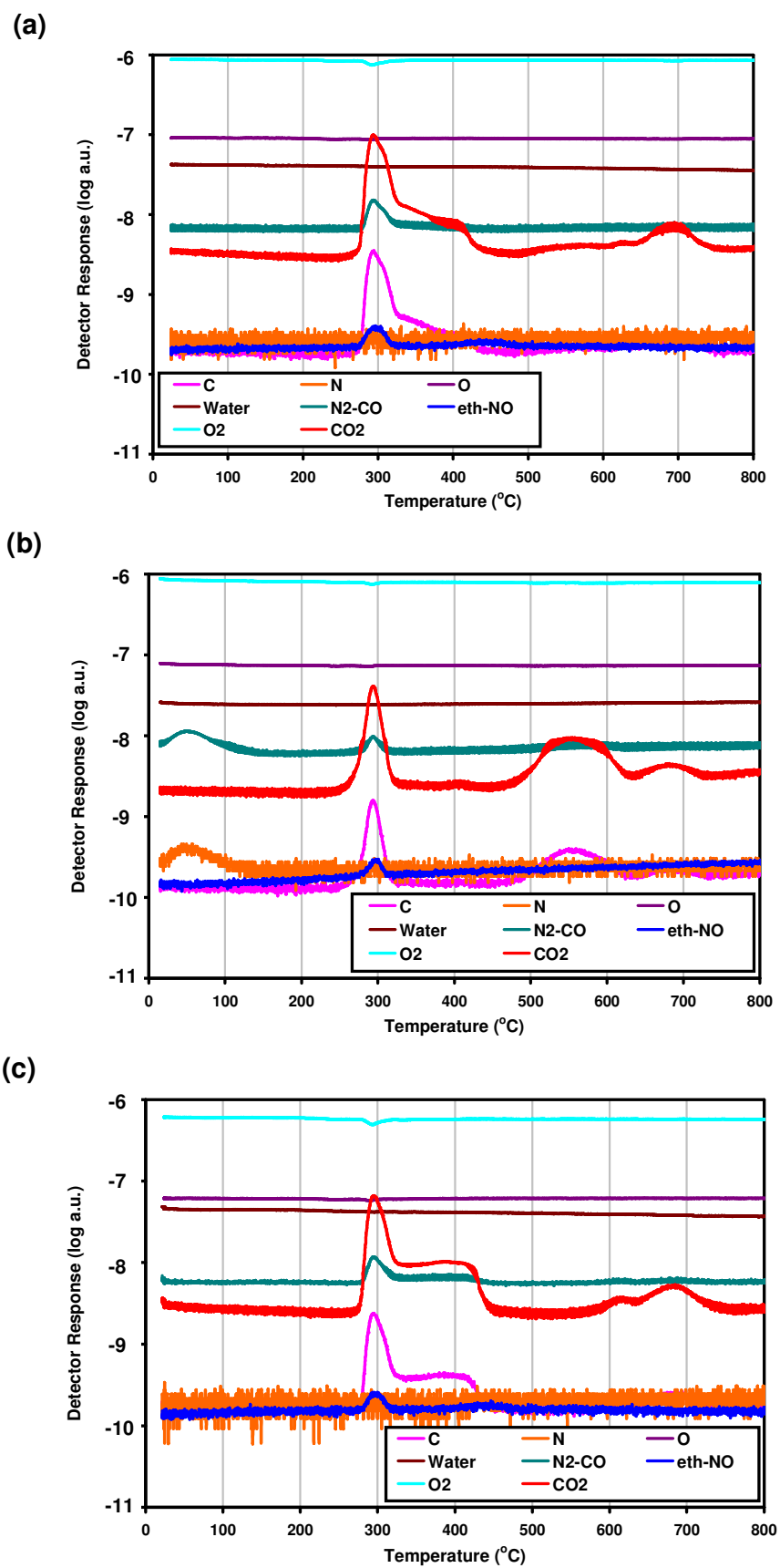


**Figure 5.31** Logarithmic TPO traces post TPRx for a) 5-50-I (II), b) 5-50-D, c) 10-50-I (II).

In order to show the extent of the carbon deposited during the TPRxs the CO<sub>2</sub> traces from the TPOs have been plotted in Figure 5.32. It was apparent that the assertion about the 5-50-D sample being the least prone to carbon deposition carries weight, as this sample evolved the least CO<sub>2</sub> during the TPO experiments (Figure 5.32(a)). Increasing the copper loading resulted in a decrease in the amount of carbon deposited onto the catalysts, as shown by the traces in Figure 5.32 (b) and (c).

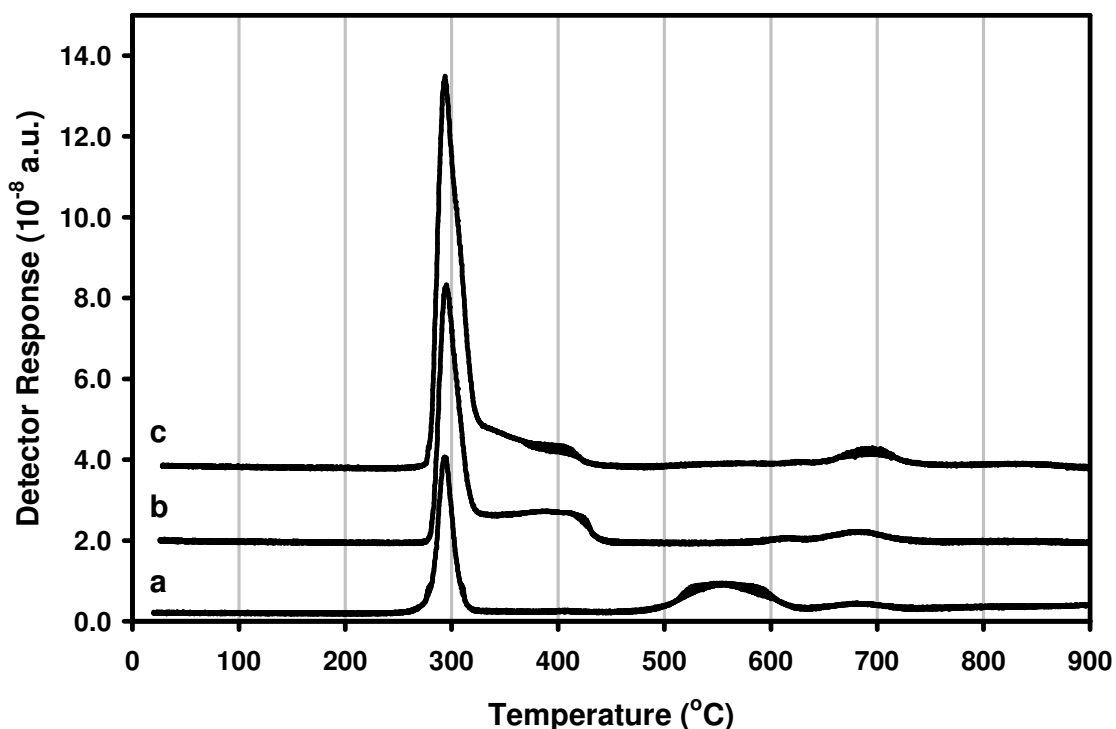


**Figure 5.32** CO<sub>2</sub> traces from the TPOs post TPRx for a) 5-50-D, b) 10-50-I (II), c) 5-50-I (II).

### 5.5.5 Lightoff Experiments

Lightoff experiments involved passing a stoichiometric gas mixture of CH<sub>4</sub> and O<sub>2</sub> over pre-reduced catalysts. An example is given in Figure 5.33. The remaining plots are included as Appendix 5 for completeness. The traces obtained from lightoff experiments involving copper containing samples were similar to those of the bare oxides included in Section 4.3.5. The partial pressures of the reactants at m/q = 14 (N/CH<sub>2</sub>), 15 (CH<sub>3</sub> and overlap with 16), 16 (O and CH<sub>4</sub>) and 32 (O<sub>2</sub>) start off flat before beginning to decrease at around 350°C. The traces continue to decrease at an approximately uniform rate until at

around 600°C they stabilise. The initial products are CO<sub>2</sub>, water and to a lesser extent CO. In the lightoff experiments the 5-D, 5-I (II), 10-50-I (II) and 10-50-D samples were all investigated. This range of materials should provide an overview on how the preparation techniques affected catalyst performance for the full range of oxide compositions. The higher copper (10 wt%) samples would also reveal if increasing the copper loading improves the catalytic performance of the catalysts. The lightoff point was taken to be the temperature at which 10% of the maximum conversion of the reactants was attained.

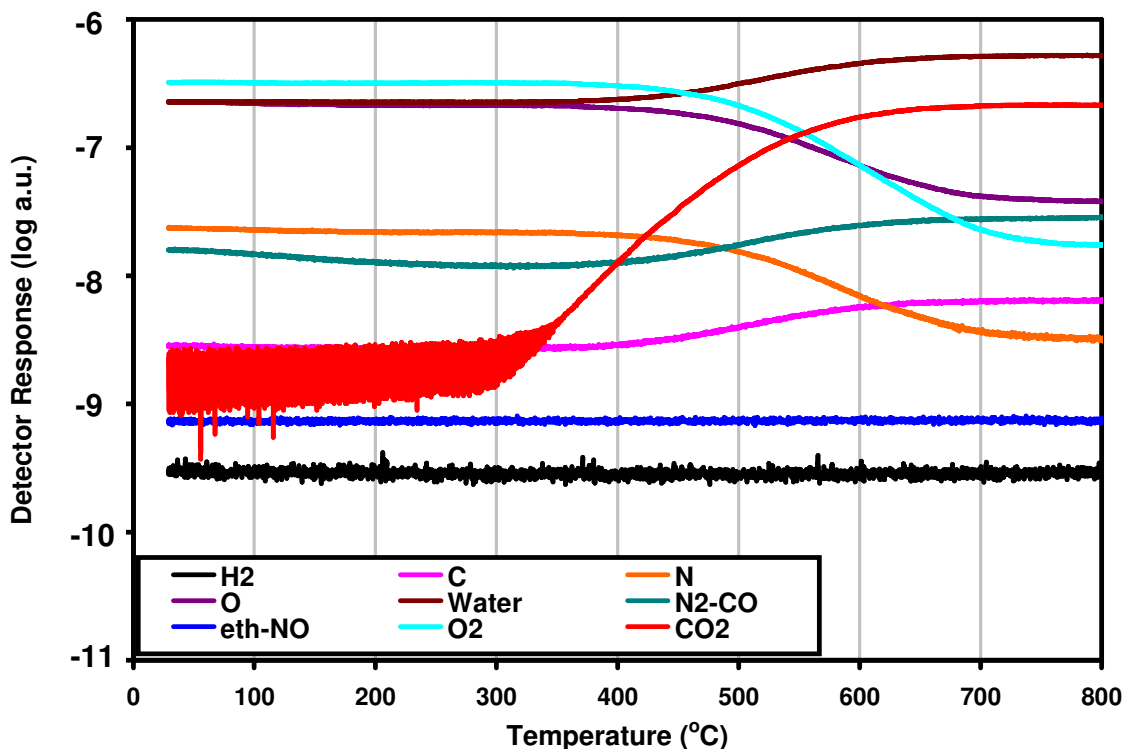


**Figure 5.33** Lightoff plot of 5-50-I (II) sample pre-reduced at 500°C.

### 5.5.5.1 Effect of Catalyst Reduction Temperature

The catalysts were pre-reduced before the lightoff experiments. In order to investigate the effect of the reduction temperature on the catalyst performance, an unreduced sample and samples reduced at a range of temperatures (250, 500 and 800°C) were used in lightoff experiments. Figure 5.34 shows plots of the partial pressures of the reactants and products during the lightoff experiments on 5-50-I (II) samples reduced at these temperatures. The first sample investigated was reduced at 800°C and the subsequent lightoff run also performed to 800°C. After analysing the results of the lightoff it was felt that the reaction had not reached completion and so subsequent lightoff experiments were run to 900°C.

The samples which were reduced at 250 and 500°C showed comparable activity. Increasing the reduction temperature to 800°C resulted in an increase in the temperature at which products were formed. The catalyst that was not reduced prior to the lightoff experiments initially proved to be as active as the pre-reduced samples.

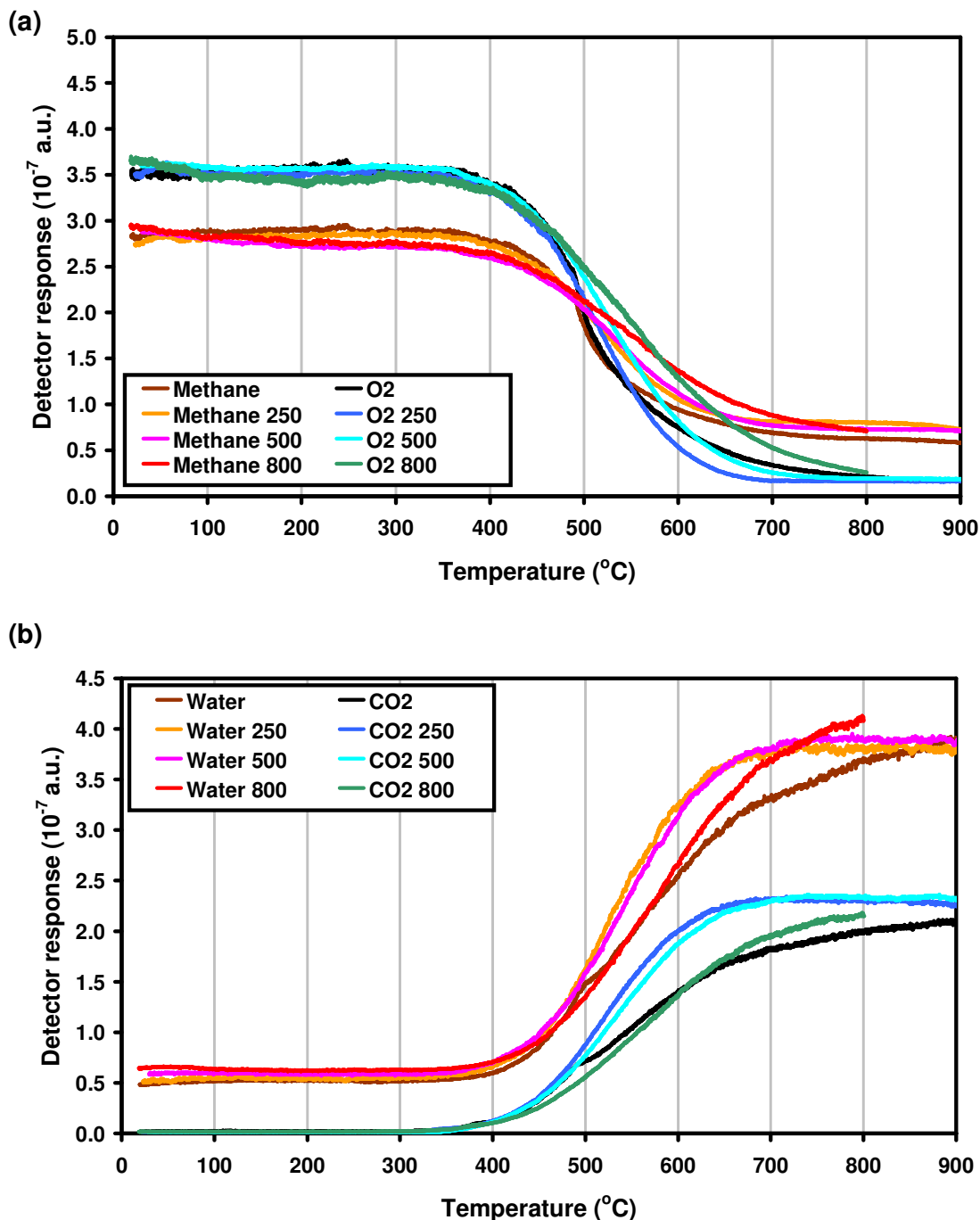


**Figure 5.34** Main reactants (a) and products (b) from lightoff experiments for 5-50-I (II) samples as-prepared and pre-reduced at 250, 500 and 800°C. Legends identify the reactants - H<sub>4</sub> (m/q = 16) and O<sub>2</sub> (m/q = 32); products: water (m/q = 18) and CO<sub>2</sub> (m/q = 44) - and the reduction temperature (°C).

Above roughly 500°C, the unreduced samples relative performance tailed off, becoming comparable with the sample reduced at 800°C. After consulting the results from the TPR experiments, it was concluded that 500°C was an adequate temperature to reduce the copper impregnated samples and it was not necessary to use a higher reduction temperature (800°C).

#### **5.5.5.2 Effect of Catalyst Composition and Impregnation Technique**

In total twelve different samples of varying copper loading (wt %), oxide composition and copper impregnation technique were studied in lightoff experiments. The samples chosen for investigation were all of the 5-I (II) and 5-D samples as well as 10-50 samples prepared using both copper impregnation techniques. This range of samples would show which oxide gave rise to the most active catalysts when provided with a copper active phase. Whilst it may be expected that the same oxide would be the most active for both the wet impregnated (I) samples and those prepared by the direct method (D), the TPR results suggested this may well not be the case.

A number of the main reactants and products of the combustion of methane were plotted (Figure 5.35-5.40), using the copper impregnation technique to divide the samples. The consumption of methane is displayed in Figure 5.35. The results for the wet-impregnated samples shown in Figure 5.35(a) displayed remarkably comparable activity across all samples for the majority of the experiments. The lowest temperature decline in methane levels was displayed by 5-25-I (II), very closely followed by 10-50-I (II) and 5-10-I (II). The samples containing higher ceria concentration did not perform quite as well, with 5-50-I (II), 5-75-I (II) and 5-90-I (II) showing methane consumption at slightly higher temperatures. These three samples showed comparable methane consumption until around 580°C when the performance of firstly 5-75-I (II) and then 5-50-I (II) tailed off compared to that of 5-90-I (II). Two samples displayed a second, sharp higher temperature drop in methane level. For both 5-75-I (II) (840°C) and 5-90-I (II) (860°C), the methane signal levelled off following the initial decrease before dropping sharply and then levelling off for a second time.

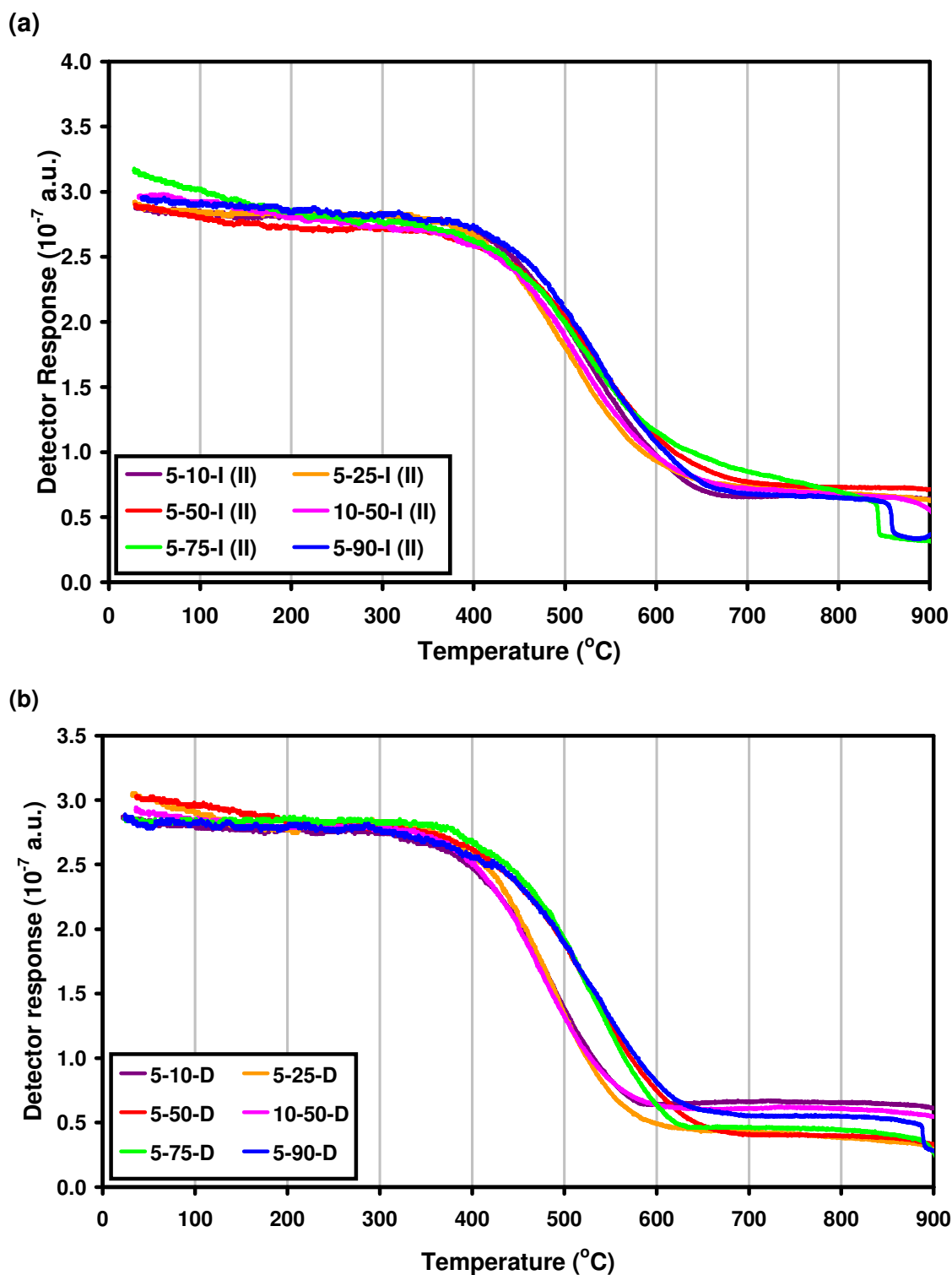


**Figure 5.35**  $\text{CH}_4$  traces from lightoff experiments on (a) I samples and (b) D samples. Both sets of samples were pre-reduced at  $500^{\circ}\text{C}$ .

The D samples did display a similar pattern in terms of activity (Figure 5.34(b)) to the I samples. Again 10-50, 5-10 and 5-25 samples are all comparable in terms of methane

consumption. The activity of the D samples was even harder to separate than for the I samples. There was then a distinct gap of around 50°C before the second group of samples, in terms of activity. The activities of all three of the samples of this second group were comparable with only slight differences apparent above 550°C where 5-75-D was the most active, ahead of 5-50-D and 5-90-D proving to be the slowest to reach its maximum level of methane consumption. There was also a repeat of the high temperature dip in the methane trace for 5-90-D, though the temperature at which this dip occurred was higher at around 880°C.

The consumption of O<sub>2</sub> shown in Figure 5.36, would be expected to mirror the consumption of CH<sub>4</sub>, since the primary mechanism for consumption of both methane and O<sub>2</sub> was the complete oxidation of methane. The activities of the materials for the consumption of O<sub>2</sub> were the same as those observed for the consumption of CH<sub>4</sub>. The wet impregnated samples were all comparable in terms of activity for the majority of the experiment with 5-75-I (II) again tailing off relatively. One distinct difference between the methane and O<sub>2</sub> traces was that for both sets of samples, once the O<sub>2</sub> levels stabilised there are no high temperature drops for any of the samples.

The CO<sub>2</sub> levels increased (Figure 5.37) with decreasing O<sub>2</sub> and CH<sub>4</sub> levels. The exception to this was for 5-75-I (II) above 840°C and 5-90-I (II) above 860°C, when the CO<sub>2</sub> levels decreased. This corresponds to the temperature at which CH<sub>4</sub> levels dipped. This pattern is also repeated for the water traces as shown in Figure 5.38. Carbon dioxide and water were still being produced, but the levels dip at higher temperature as it appears that the steam reforming of methane occurs for these samples. This is confirmed by Figures 5.39 and 5.40 which show the traces for CO and H<sub>2</sub>. The hydrogen trace was smoothed using a 10 point moving average. There was corresponding CO and H<sub>2</sub> production at the temperatures at which water and CO<sub>2</sub> levels decrease. There were also low temperature CO peaks, observed for all samples. As with the oxides these peaks can be attributed to the decomposition of CO<sub>2</sub> in the QMS.

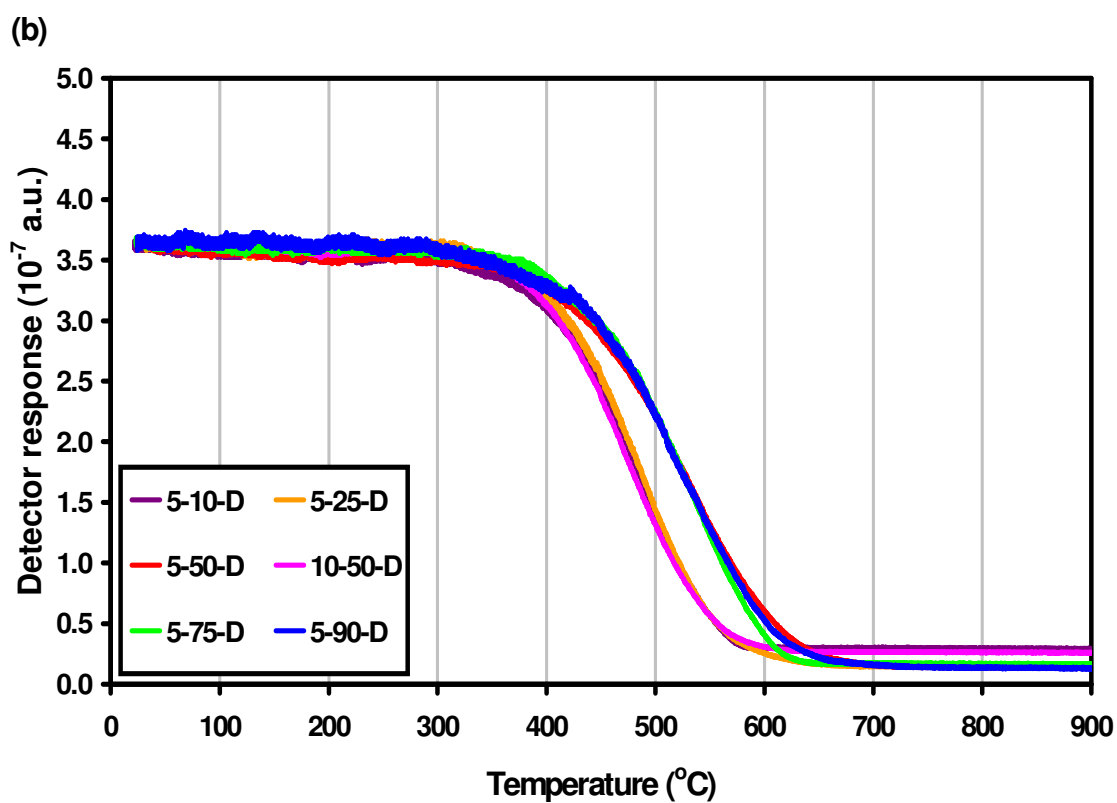
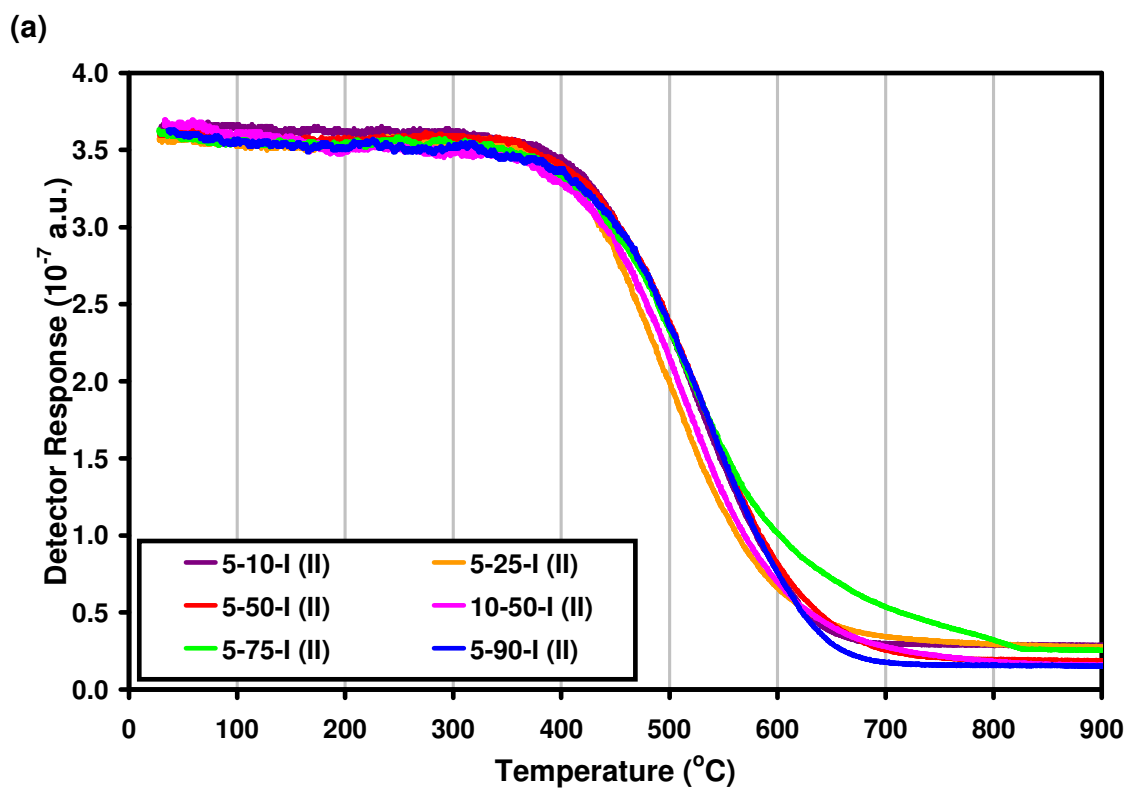


**Figure 5.36** O<sub>2</sub> traces from lightoff experiments on (a) I samples and (b) D samples. Both sets of samples were pre-reduced at 500°C.

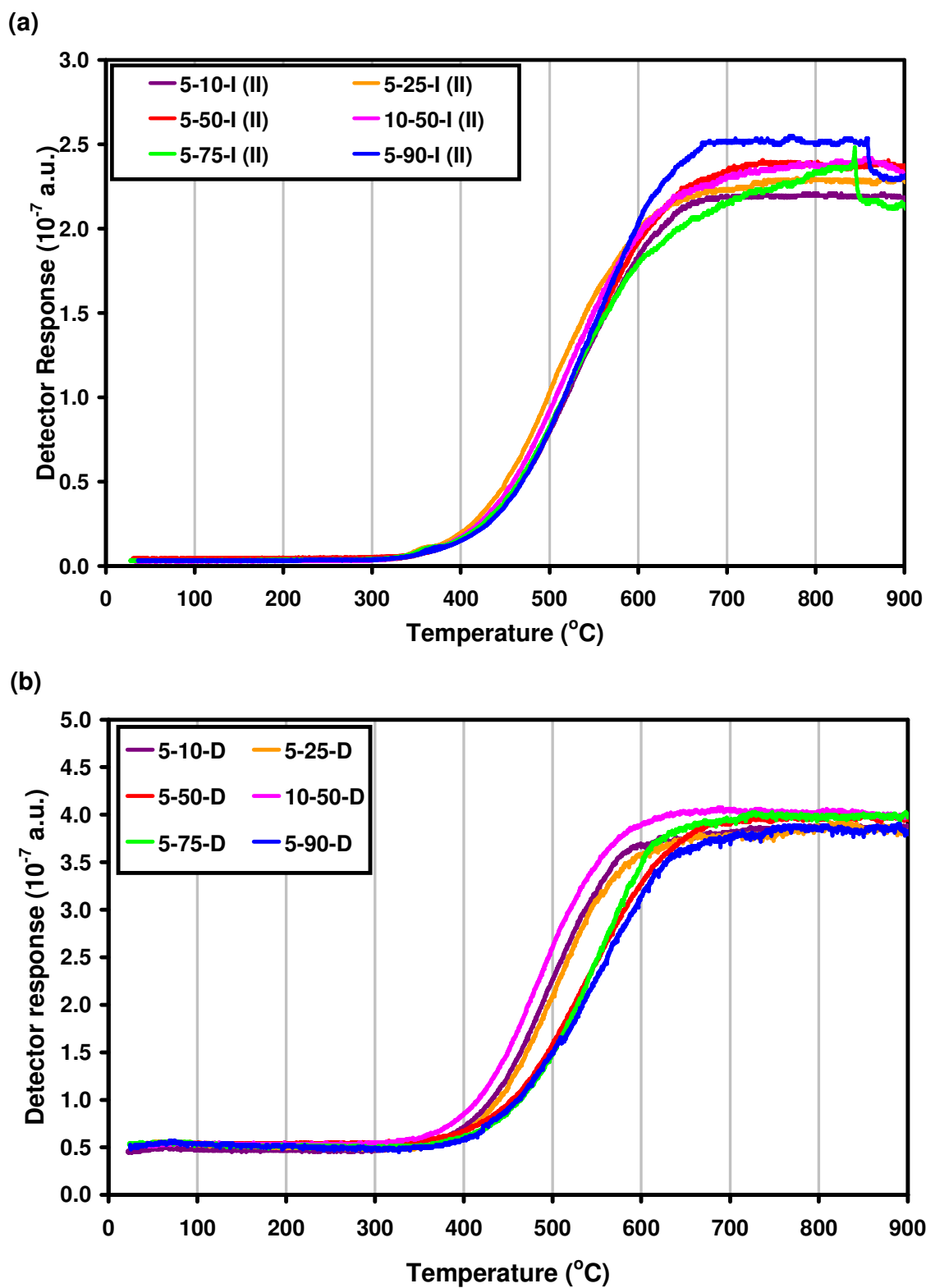


**Figure 5.37**  $\text{CO}_2$  traces from lightoff experiments on (a) I samples and (b) D samples. Both sets of samples were pre-reduced at  $500^{\circ}\text{C}$ .

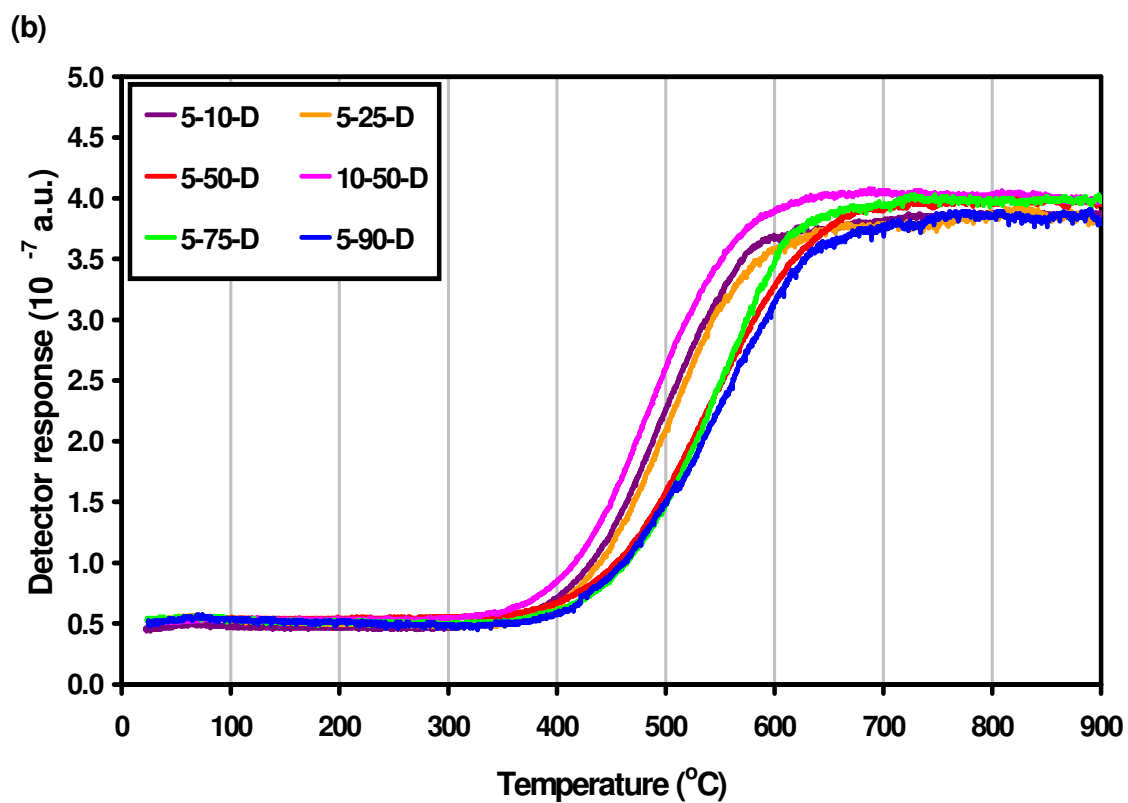
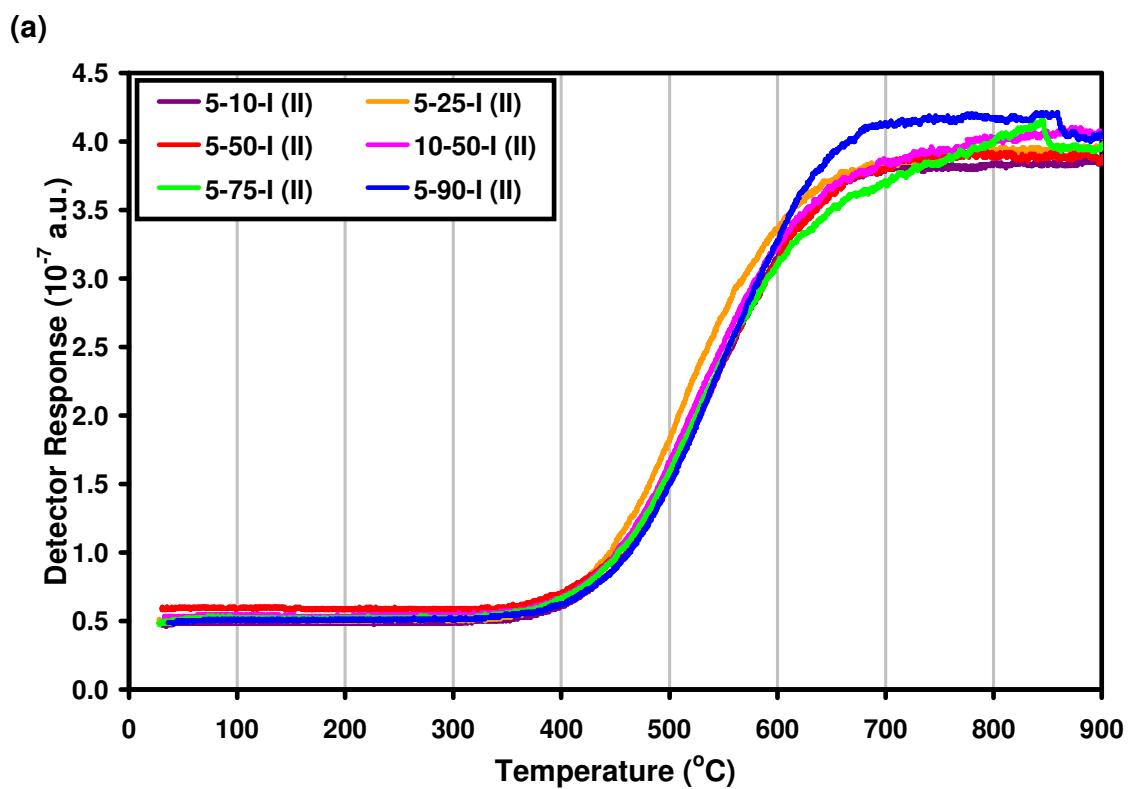


**Figure 5.38**  $\text{H}_2\text{O}$  traces from lightoff experiments on (a) I samples and (b) D samples. Both sets of samples were pre-reduced at  $500^{\circ}\text{C}$ .

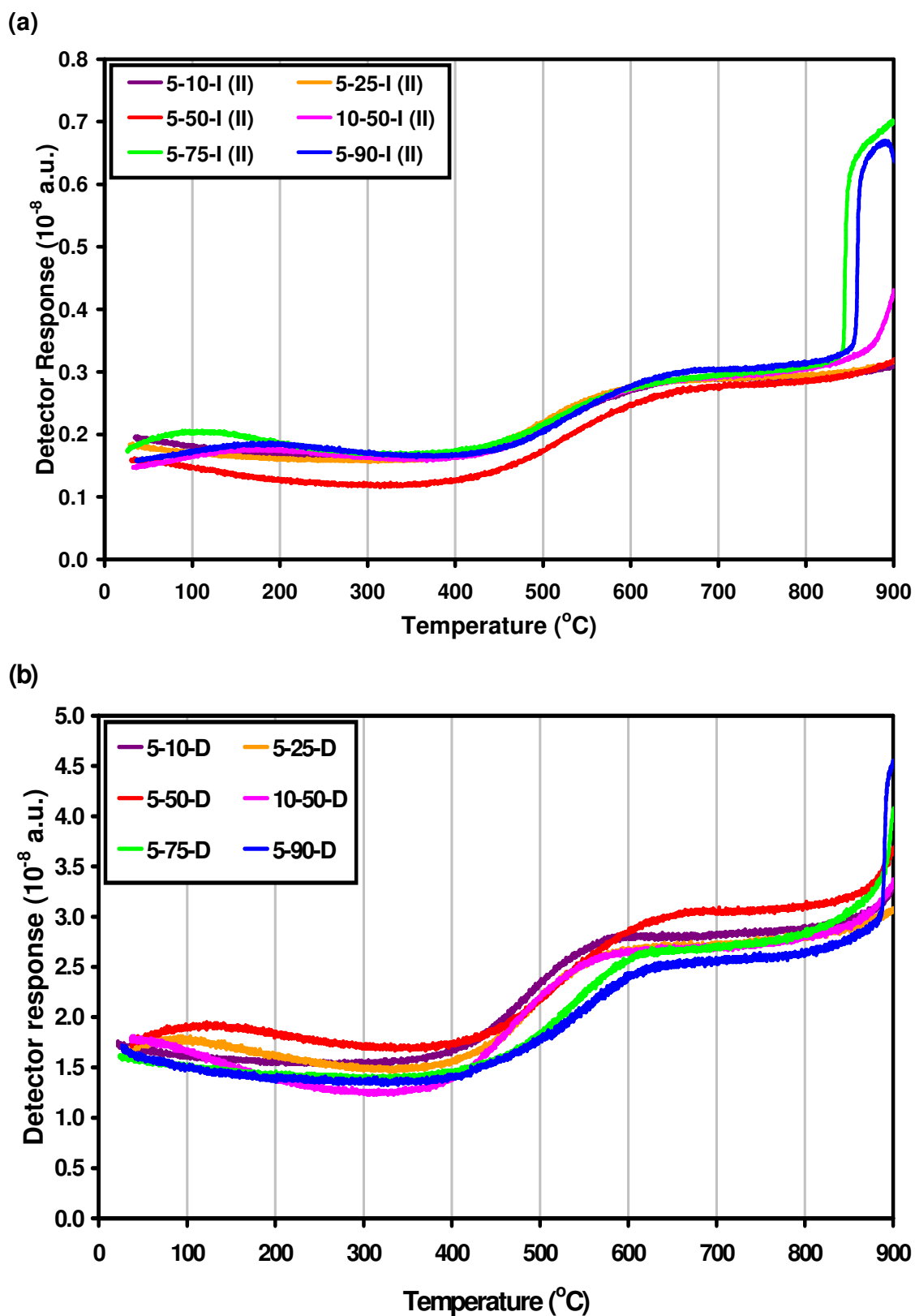


**Figure 5.39** CO traces from lightoff experiments on (a) I samples and (b) D samples. Both sets of samples were pre-reduced at 500°C.

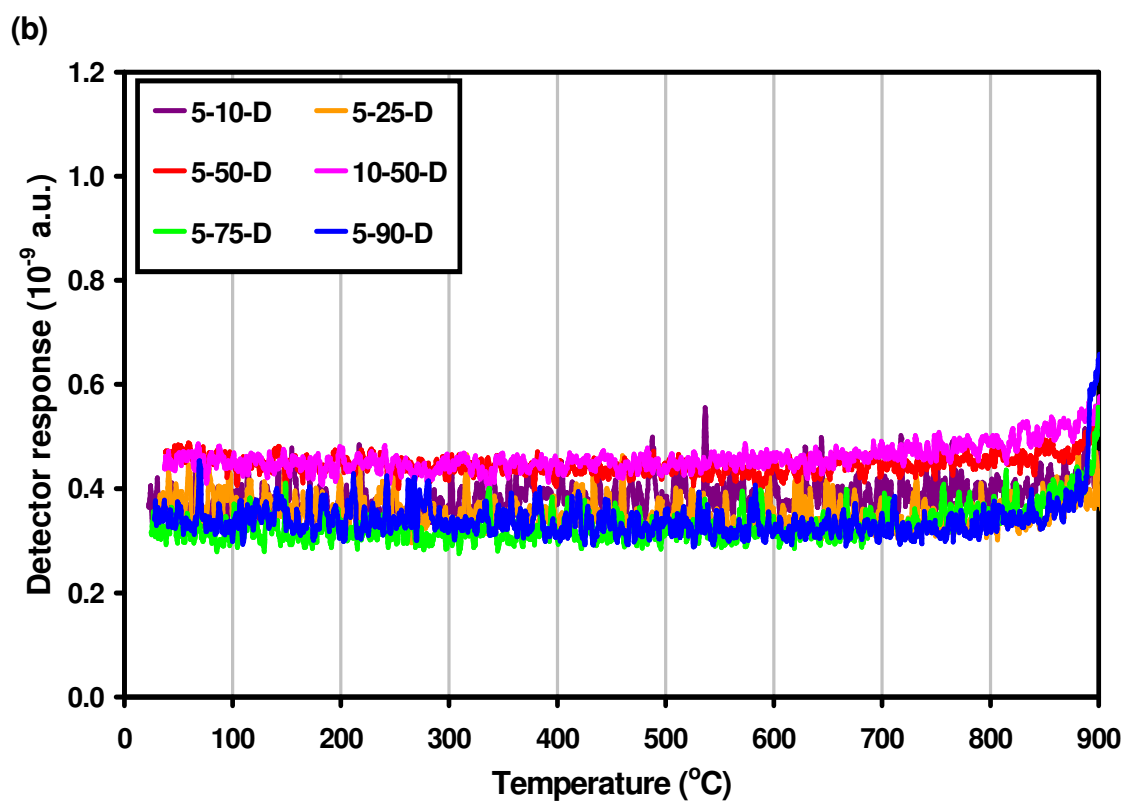
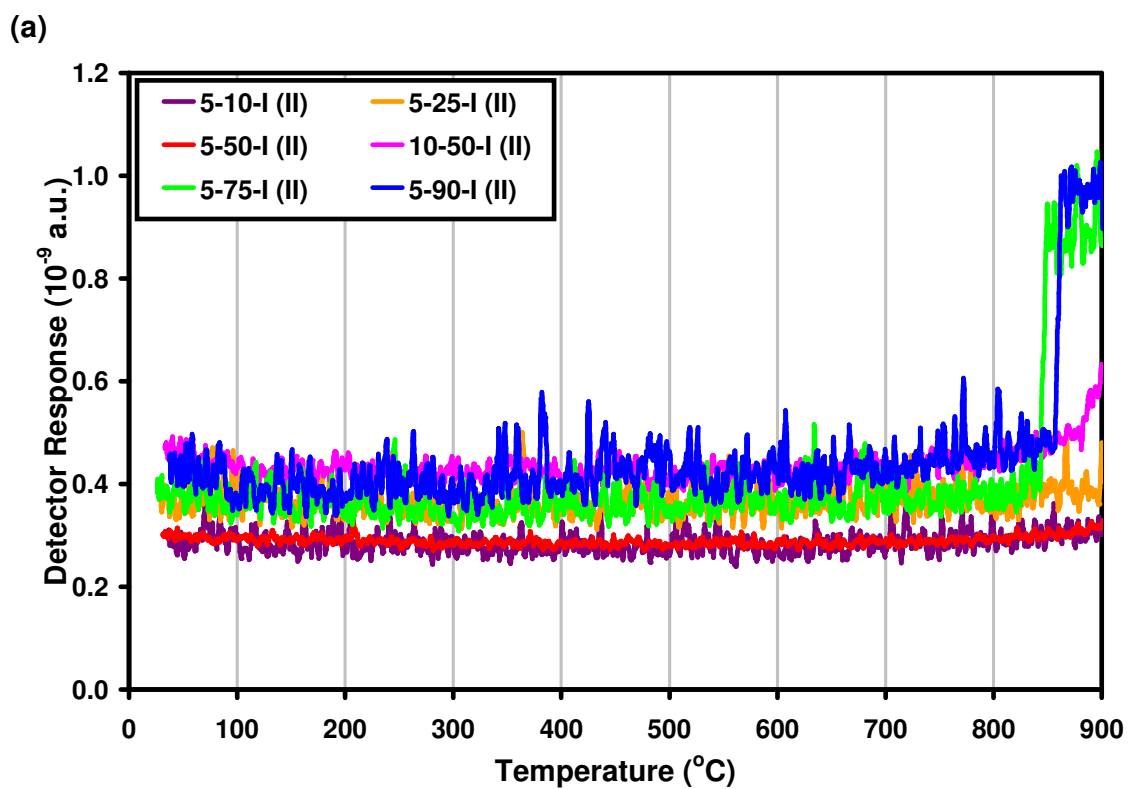


**Figure 5.40**  $\text{H}_2$  traces from lightoff experiments on (a) I samples and (b) D samples. Both sets of samples were pre-reduced at  $500^{\circ}\text{C}$ .

In order to show the effect of the copper impregnation on each of the oxide compositions, the oxygen traces from the lightoff experiments were plotted for each oxide composition, as shown in Figure 5.41. For all of the oxide samples the same behaviour is observed with the 5-D sample showing the lowest temperature decrease in  $O_2$  and also consistently being the first material to reach the maximum level of  $O_2$  consumption. The remaining copper impregnated sample, 5-I (II), was the next active, with the bare oxides being consistently the last material to catalyse the reaction of  $O_2$  and  $CH_4$ .

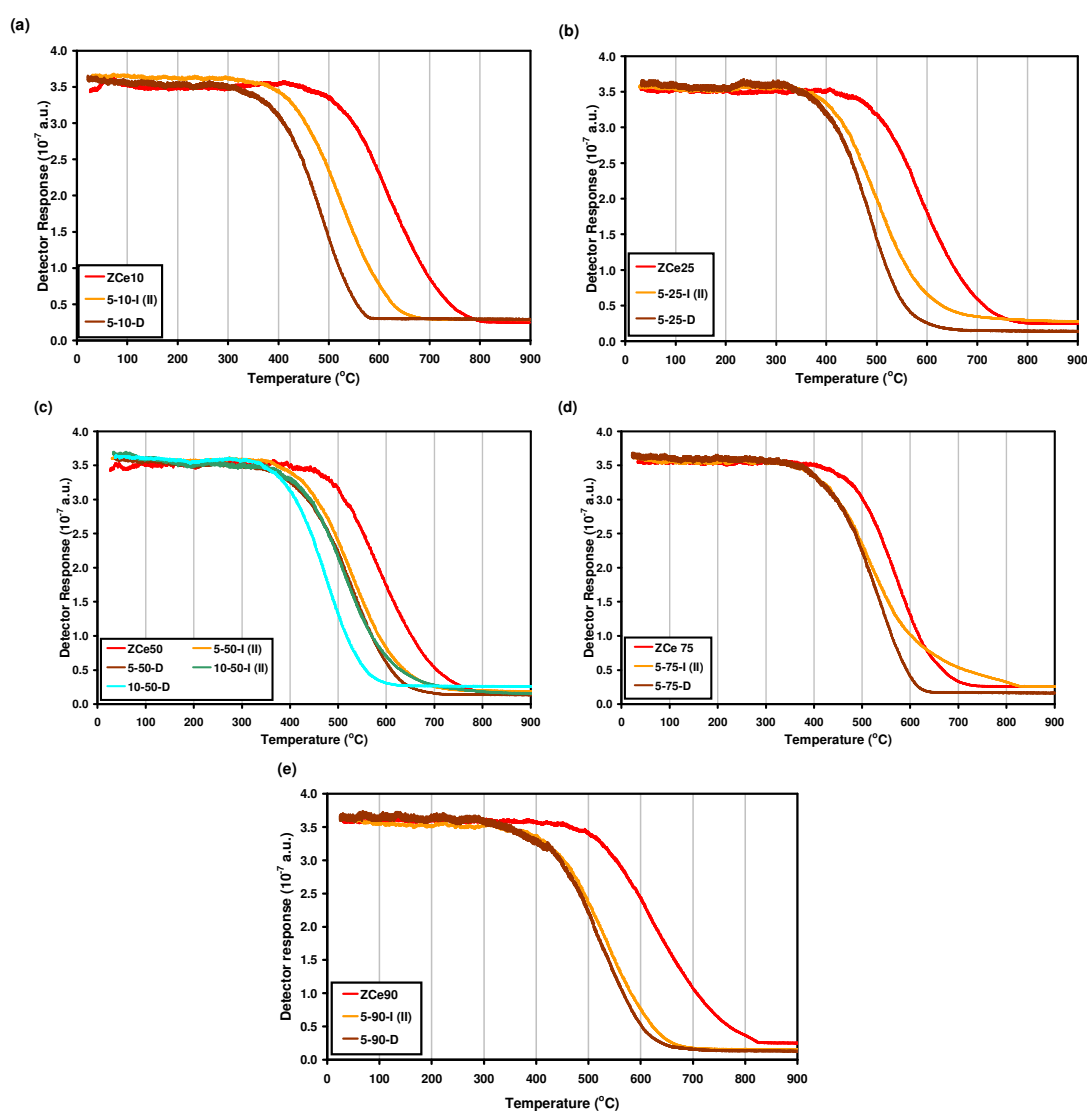


**Figure 5.41**  $O_2$  traces from lightoff experiments on bare oxides and copper impregnated samples of (a) ZCe10, (b) ZCe25, (c) ZCe50, (d) ZCe75 and (e) ZCe90.

The lightoff temperatures for all the materials which were used in the experiments are plotted in Figure 5.42. The samples prepared using wet impregnation display a similar

pattern of activity to those observed for the bare mixed oxides ( $Zr_{0.75}Ce_{0.25} > Zr_{0.5}Ce_{0.5} > Zr_{0.25}Ce_{0.75} > Zr_{0.1}Ce_{0.9}$ ). The addition of the copper using the I technique decreased the lightoff temperature most for mixed oxides at the extremes of the compositional range ( $154^{\circ}\text{C}$  for  $Zr_{0.1}Ce_{0.9}$  and  $123^{\circ}\text{C}$  for  $Zr_{0.9}Ce_{0.1}$ ). The effect of the copper loading was not as pronounced for the samples with intermediate Ce/Zr ratios ( $106^{\circ}\text{C}$  for  $Zr_{0.25}Ce_{0.75}$ ,  $94^{\circ}\text{C}$  for  $Zr_{0.5}Ce_{0.5}$  and  $81^{\circ}\text{C}$  for  $Zr_{0.75}Ce_{0.25}$ ). Doubling of the copper loading to 10 wt% further decreased the lightoff temperature observed for the  $Zr_{0.5}Ce_{0.5}$  sample (lightoff temperature decrease by  $13^{\circ}\text{C}$  for 10-50-I (II) compared to 5-50-I (II)).

The D samples showed a near linear increase in lightoff temperature with increasing ceria content. The effect of increasing the copper loading to 10% was less pronounced for the D sample, where the lightoff temperature was decreased by  $8^{\circ}\text{C}$  compared to  $13^{\circ}\text{C}$  for the I sample. The fact that the 5-50-D sample already had a lightoff temperature  $17^{\circ}\text{C}$  lower than that of 5-50-I (II) leads to a difference of  $12^{\circ}\text{C}$  between the two 10 wt% copper samples prepared by the different methods.

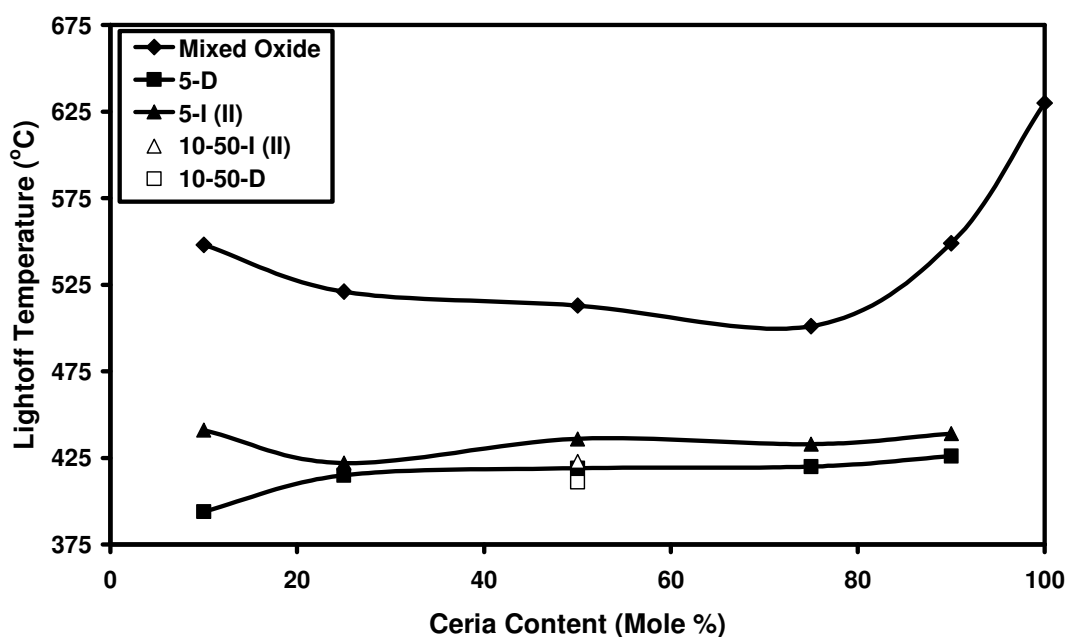


**Figure 5.42** Lightoff temperatures from  $\text{O}_2$  consumption for copper impregnated samples, bare Ce/Zr oxides and  $\text{CeO}_2$ . All samples were pre-reduced at  $500^{\circ}\text{C}$ .

The samples which were impregnated during preparation (D) had consistently lower lightoff temperatures across all ceria content samples. The 5-50-D sample had a lower

lightoff temperature than that observed for 10-50-I (II). As a result, it appears that, for the intermediate ceria containing samples, the copper impregnation technique had a greater effect on the lightoff temperature than doubling the copper loading to 10%.

For each set of samples - the oxides, the 5-I and the 5-D samples - a different oxide composition displayed the lowest lightoff temperature. For the bare oxides, ZCe75 had the lowest lightoff temperature. Both copper impregnation techniques had least effect on this sample, however, so what was the most active bare oxide produced some of the least active catalysts in terms of lightoff temperature. Conversely, the greatest decrease in lightoff temperature as a result of copper impregnation was observed for 5-10-D where a 136°C decrease from that for the oxide was recorded. This had the effect that the most active catalyst in terms of lightoff temperature was produced using one of the least active bare oxides.

The lightoff temperatures obtained for consumption of O<sub>2</sub> and CH<sub>4</sub> across all 5 wt% impregnated samples as shown in Figure 5.43. With the exception of 5-10-D where the lightoff temperature from O<sub>2</sub> is 11°C lower than that for CH<sub>4</sub>, all the other 5 wt% materials had comparable lightoff temperatures for O<sub>2</sub> and CH<sub>4</sub> consumption (+/- 5°C). The lightoff temperature for CO<sub>2</sub> production was between 1 and 10°C above the lightoff temperature based on CH<sub>4</sub> conversion. The lightoff temperature for water was the highest of the four values calculated for all materials.

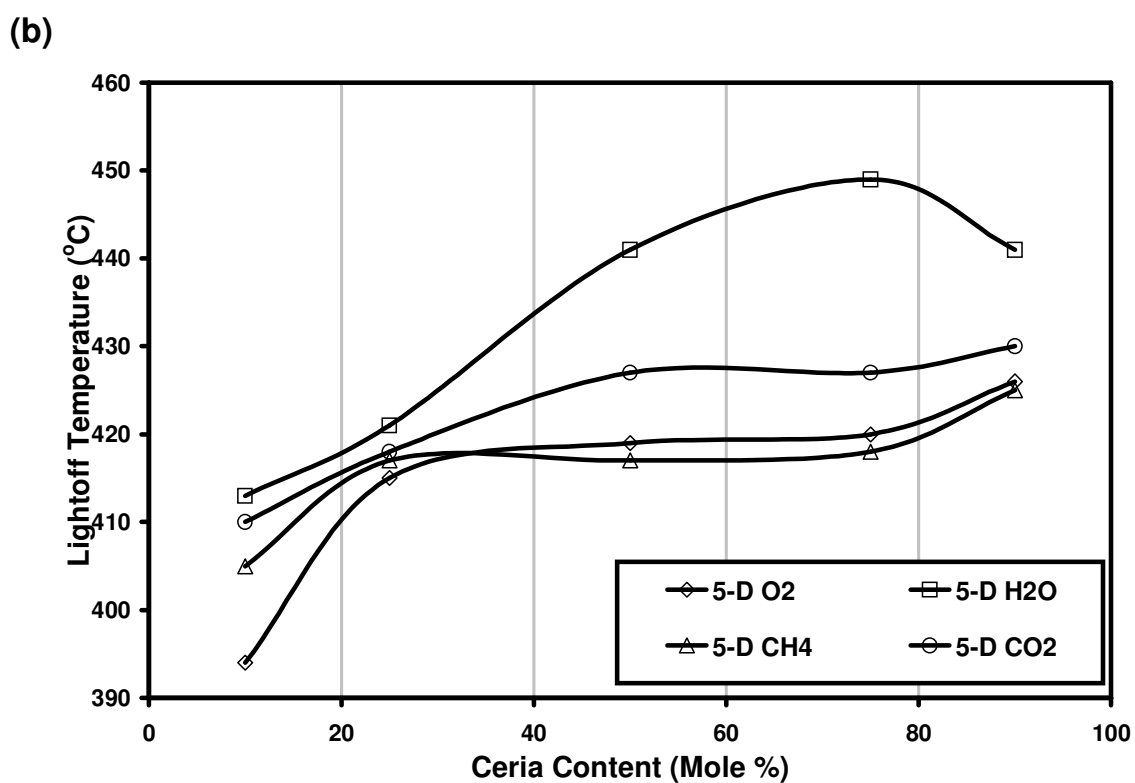
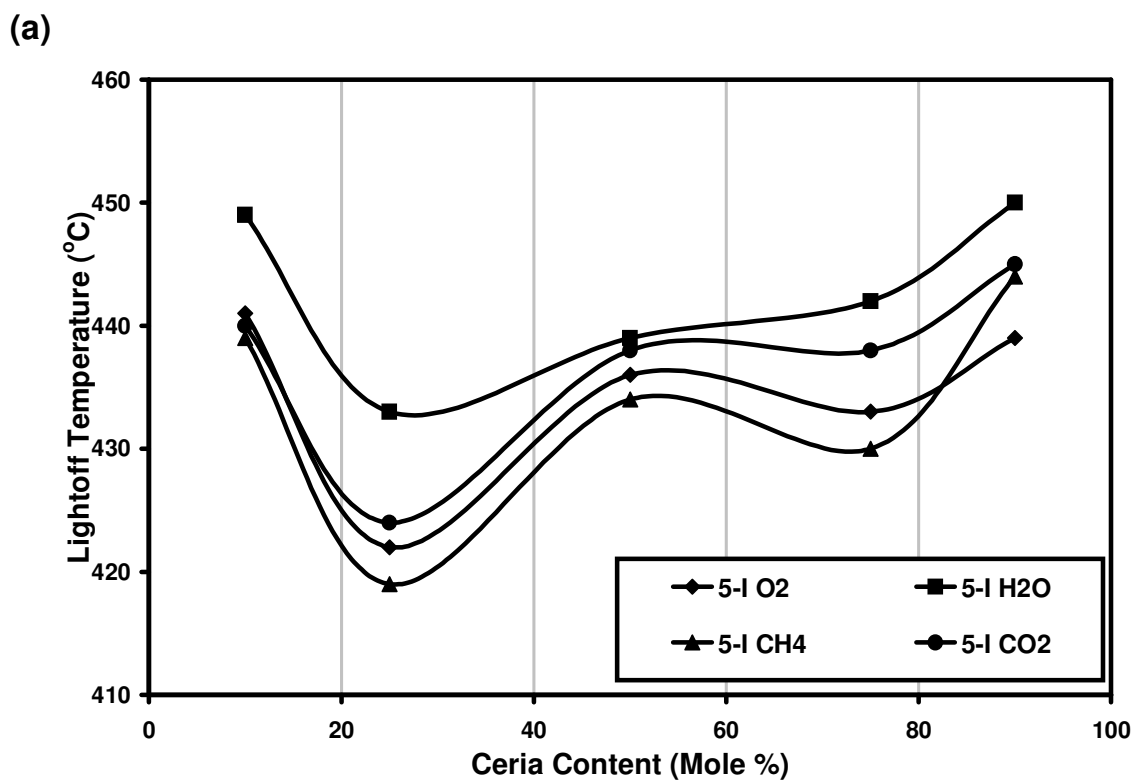


**Figure 5.43** Lightoff temperatures from O<sub>2</sub> and CH<sub>4</sub> consumption, as well as CO<sub>2</sub> and H<sub>2</sub>O production for 5 wt% copper impregnated samples. The lightoff temperatures are taken from (a) 5-I (II) and (b) 5-D impregnated samples. All samples were pre-reduced at 500°C.

## 5.6 Summary

The redox-behaviour and catalytic activity of a number of copper-containing, mixed Zr/Ce oxides was investigated using a series of temperature programmed experiments.

EDX of the as-prepared powders revealed that the I impregnation technique worked well for copper loadings of up to 5 wt%. At higher copper loadings however the copper was not evenly dispersed in the sample.

Incorporating the copper using the D technique gave rise to high, uniform copper dispersion and distribution for samples up to and including 10 wt % copper.

The addition of copper to the oxides using the I technique increased the specific surface area of all the oxide samples.

Impregnation using method D increased the specific surface area for the ZCe10, 25 and 50 samples, but actually decreased the specific surface area for the ZCe75 and ZCe90 samples.

Preliminary TPD experiments revealed that the first calcination temperature used, 250°C, was insufficient to fully decompose the copper nitrate used to incorporate the copper into the oxides. Therefore, samples were calcined at 500°C.

A number of copper samples desorbed oxygen during TPD experiments at high temperature, an effect that became more prominent with increasing copper loading.

Oxygen desorption during TPDs also varied with oxide composition. Low ceria samples, 5-10-D and 5-25-D, displayed almost equivalent peaks at roughly 725°C. The temperature of the desorption peak then rose to 760°C for 5-50-D and increased markedly in size. 5-50-D also displayed a small peak at around 660°C which was also observed for 5-90-D. The trace for 5-90-D corresponded closely to that of 5-50-D but the peaks observed at 660°C and 760°C were approximately half the area. The 5-75-D sample displayed the smallest O<sub>2</sub> desorption peak of all the materials tested, at around 680°C.

The amount of water desorbed during the TPDs of copper containing samples was much lower than that observed during the TPDs of the oxides.

The D materials consistently exhibited lower main reduction peak temperatures during both TPRs and TPD/Rs than the I materials.

The impregnation technique, copper loading and oxide composition had limited effect on the position of the lowest temperature reduction peak. The size of the low temperature peak did vary widely between samples of different compositions and between those made using the two impregnation techniques.

The TPD/R experiments generally contained much smaller low temperature reduction peaks when compared to the TPR runs. This was likely to be a result of the oxygen desorption that was observed in the prior TPDs.

Increasing the copper loading also had limited effect on the position of the reduction peaks observed.

Samples with higher copper loadings which were found to have poor copper dispersion displayed a number of reduction peaks. This was attributed to the variety of copper particle sizes within the samples resulting in a range of chemical environments in these samples.

TPRx experiments showed limited complete oxidation of the CH<sub>4</sub> followed by partial oxidation. There was then a decrease in the CH<sub>4</sub> signal and a corresponding H<sub>2</sub> peak as the CH<sub>4</sub> was broken down and carbon deposited on the sample. This sharp decrease in CH<sub>4</sub> level was most pronounced for the wet impregnated samples.

TPOs performed after the TPRx experiments revealed that the material investigated that was least prone to carbon deposition was 5-50-D. The two samples impregnated by incipient wetness showed more pronounced CO<sub>2</sub> production during the TPO.

Of the incipient wetness impregnated samples tested (5-50-I (II) and 10-50-I (II)), the one with the higher copper loading wt%, showed the lesser amount of carbon deposition.

Moderate reduction temperatures (250°C and 500°C) resulted in the lowest temperature lightoff peaks for the 5-50-I (II) sample. Increasing the reduction temperature resulted in decreased performance. When the sample was not pre-reduced, the reaction started at a rate comparable to that observed for the lower temperature reduced samples, before tailing off.

Copper addition to the bare oxide samples drastically reduced the lightoff temperature for all oxide compositions.

D materials had consistently lower lightoff temperatures than the I materials. This effect was most pronounced for the lower ceria containing samples (10, 25 and 50 mole% CeO<sub>2</sub>).

D materials also displayed a lower lightoff temperature than the I materials observed for the (10 wt%) ZCe50 samples with a higher copper loading.

## 5.7 References

- [1] R. O. Fuentes, R.T. Baker, *J. Phys. Chem. C*, 113, **2009**, 914
- [2] D.J. Burleson, W.L. Gladfelter, S.A. Campbell, J.T. Roberts, *J. Electrochem. Soc.*, 149, **2002**, F131

# **Chapter 6. Discussion**

## 6.1 Oxygen Evolution During TPDs

### 6.1.1 Low Temperature (<200°C) Oxygen Species

All of the samples which were subjected to TPD experiments displayed a small peak for O<sub>2</sub> at around 100°C. These peaks were sharpest in the bare oxides which all displayed a relatively sharp peak at roughly 110°C before levelling off for the remainder of the experiment. The copper-containing samples displayed much broader, low intensity O<sub>2</sub> peaks at lower temperature than the bare oxides. The adsorption of O<sub>2</sub> onto CeO<sub>2</sub> samples at room temperature has been established by Li et al. using FT-IR. [1] Li et al observed a marked decrease in the amount of O<sub>2</sub> (in the form of O<sub>2</sub><sup>-</sup>) adsorbed onto the CeO<sub>2</sub> as the temperature was raised from 27°C to 100°C. The authors suggested that the O<sub>2</sub><sup>-</sup> ions had adsorbed onto the co-ordinately unsaturated Ce<sup>4+</sup> site on the surface of the oxide. [1] The presence of these superoxide (O<sub>2</sub><sup>-</sup>) species would account for the initial O<sub>2</sub> desorption observed which peaked at around 100°C for all the samples tested during TPDs.

### 6.1.2 High Temperature Oxygen Species

No high temperature desorption of O<sub>2</sub> was observed for the bare oxide samples during TPD experiments. As a result of this the O<sub>2</sub> which was desorbed from the copper containing samples at high temperatures during TPD experiments can be attributed to the presence of the copper. The highly labile O<sub>2</sub> species released during the TPDs were thought to be evolved either through the decomposition of CuO particles, or the catalytic reduction of the Ce-Zr oxide by surface copper particles. In order to establish if one of these mechanisms was prevalent the reduction of the samples corresponding to the amount of O<sub>2</sub> desorbed during TPDs was calculated and compared to the theoretical maximum reduction of the Cu and of the whole Cu/Ce-Zr system as shown in Figure 6.1 and Table 6.1. If O<sub>2</sub> evolution was solely the result of copper oxide decomposition, then the desorption observed should vary little with oxide composition. In order to determine if this was the case the amount of O<sub>2</sub> desorbed was plotted against sample Ce content (Figure 6.2). If the desorbed oxygen species were due to the presence of copper in the samples, then the most important factor would be the dispersal and distribution of copper throughout the sample, whereas, if reduction of the oxide was being catalysed by the copper then the distribution and dispersal of the copper as well as the Ce content of the sample would be expected to affect the amount of O<sub>2</sub> desorbed.

**Table 6.1** Percentage of O<sub>2</sub> desorbed from 5 wt% copper containing samples during TPD experiments. Values given assume all copper was initially present as CuO and was reduced to Cu. The values in brackets include reduction of Ce also and assume all Ce was initially present as Ce<sup>4+</sup> and was reduced to Ce<sup>3+</sup>.

Material	5-I (%) Theoretical Reduction	5-D (%) Theoretical Reduction
ZCe10	6.92 (4.70)	30.82 (21.00)
ZCe25	10.49 (5.00)	27.38 (13.00)
ZCe50	24.80 (8.20)	38.23 (12.60)
ZCe75	25.27 (6.70)	28.77 (7.60)
ZCe90	21.81 (5.20)	26.35 (6.30)

The temperature at which peak O<sub>2</sub> desorption occurred varied slightly between materials depending on oxide composition, copper loading and copper incorporation technique. The reduction of CuO to Cu<sub>2</sub>O from a sample of copper sulphate was reported to occur at around 787°C during TPD by Kamruddin et al. [2] The temperature at which O<sub>2</sub> desorbed during the TPDs of the 5-I (II) samples was consistently around this temperature, ranging from 755°C for 5-75-I (II) to 785°C for 5-90-I (II). Peak O<sub>2</sub> desorption from the 5-D samples was consistently at lower temperatures than for the 5-I samples for all oxide compositions; between 710°C for 5-75-D and 760°C for 5-90-D. The slightly lower temperature observed for O<sub>2</sub> desorption in the TPDs for all 5-D samples compared to the 5-I (II) samples was likely a result of the fine dispersion of copper throughout the D samples. This fine dispersion of copper throughout the material would result in more of the copper being present at readily reducible surface sites. Similar behaviour has been reported by Chen et al. with copper reduction being promoted during TPR experiments when copper oxide was introduced into Ce/Zr systems. [3]

The D incorporated copper samples consistently evolved more O<sub>2</sub> at lower temperature than the 5-I (II) samples. The D samples were prepared in a single step which led to a better copper distribution and higher dispersion for all the samples as observed in the EDX and XRD results. This higher dispersion and integration into the oxide lattice appears to have led to the promotion of reduction of the copper contained within the samples.

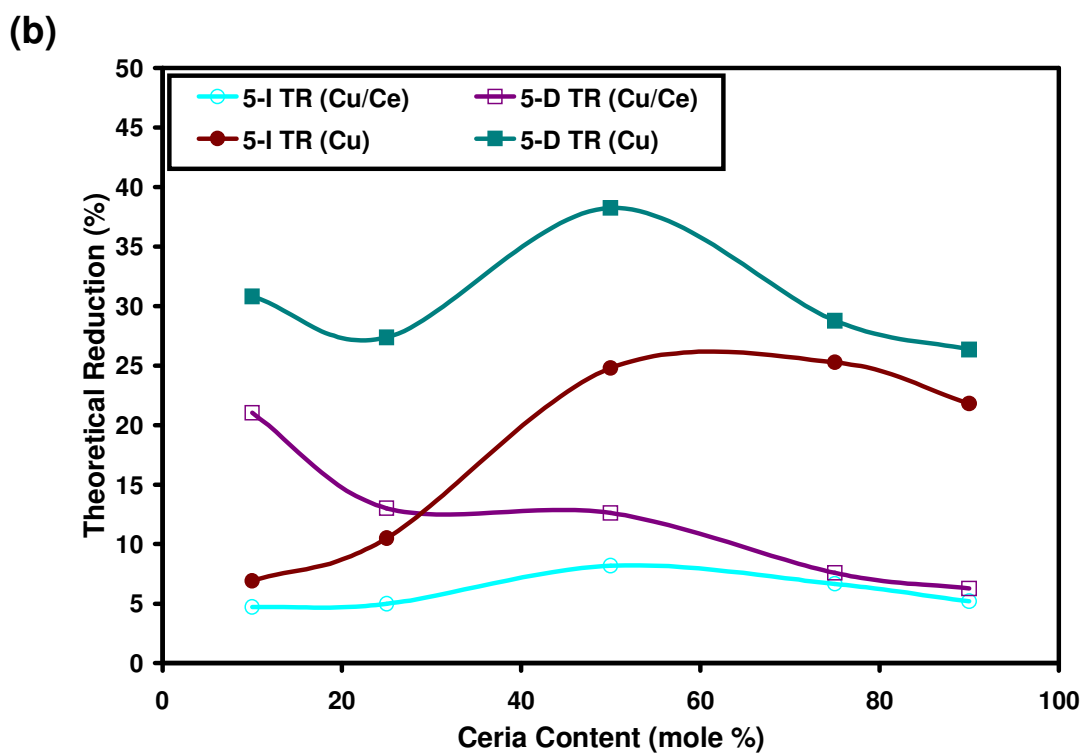
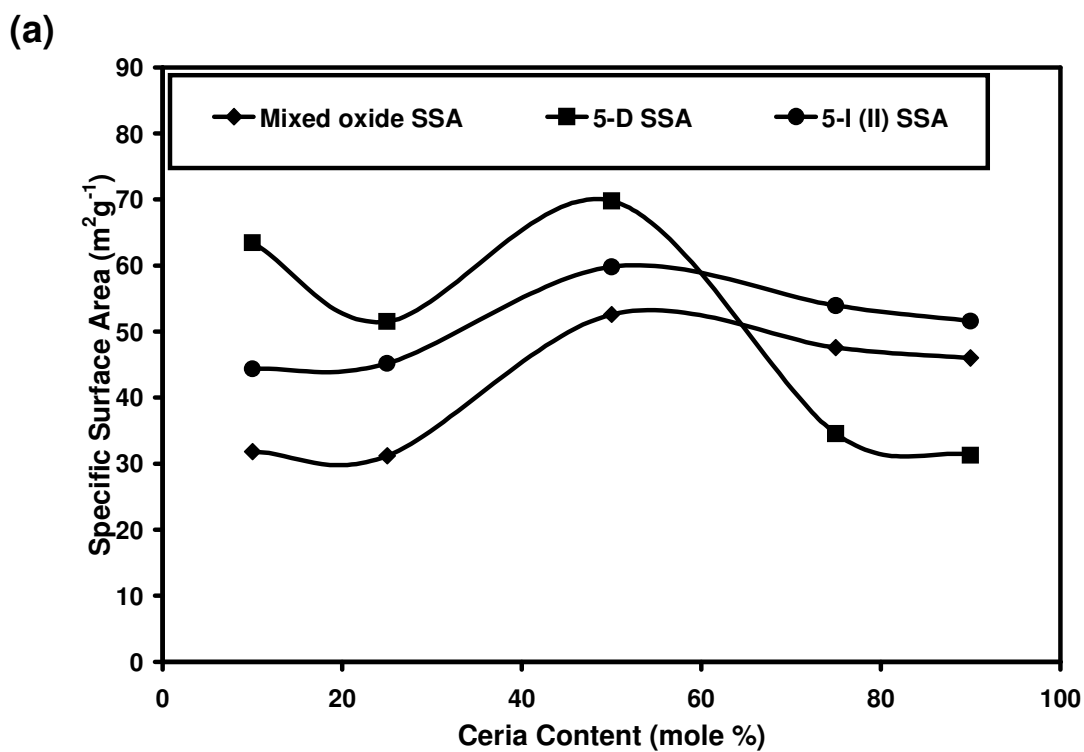


**Figure 6.1** a) SSA for 5-I and 5-D samples and the bare oxide materials and b) percentage theoretical reduction due to O<sub>2</sub> evolution during TPD experiments for 5-I and 5-D samples. The theoretical reduction was calculated for both the reduction of CuO and the reduction of Ce and CuO within the materials.

Figure 6.1 displays the SSA of the samples subjected to TPD experiments and the percentage of theoretical reduction (of both Cu and Ce/Cu) which corresponds to the amount of O<sub>2</sub> desorbed, plotted against ceria content of the samples. With regard to the 5-I (II) samples 5-10-I (II) and 5-25-I (II) both displayed smaller extents of reduction (clearly shown by the amount of O<sub>2</sub> desorbed in Figure 6.2) when the O<sub>2</sub> is assumed to be purely desorption from the copper contained in the sample. These were the two samples which displayed copper agglomerations in the EDX results. The poor dispersion of copper in these samples would be expected to result in a relative paucity of easily reduced surface copper species, which would explain these observations. For both I and D prepared materials, the 5-50 sample desorbed the highest amount of O<sub>2</sub> as well as having the highest surface area samples. The pattern for the SSA of materials does follow quite closely the level of sample reduction when it was assumed that only the copper was being reduced. This would seem to confirm the assignment of the oxygen desorption as being the result of highly dispersed and hence high SSA copper containing samples.

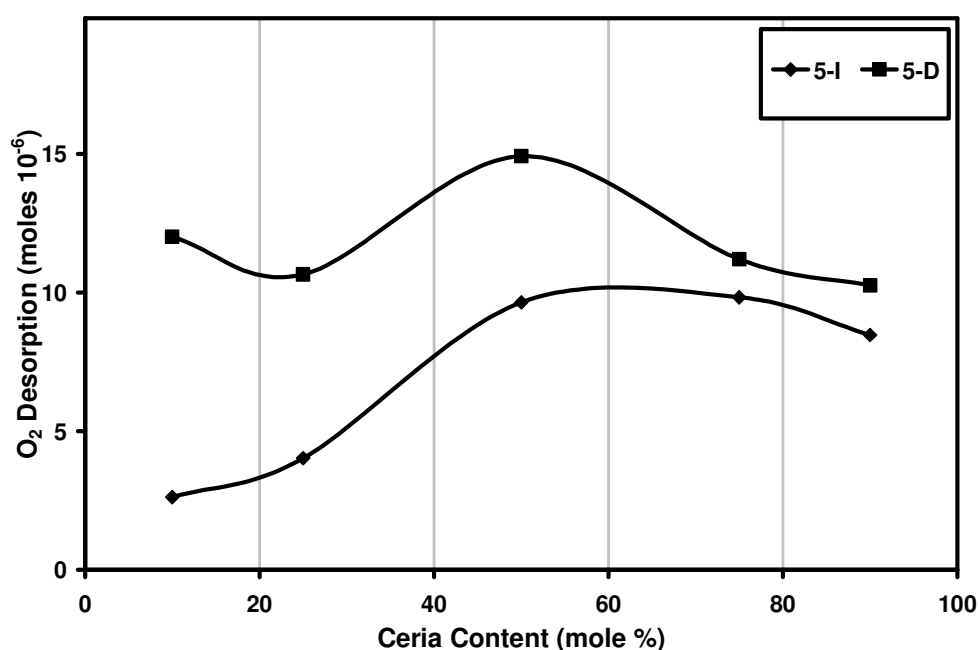


**Figure 6.2** Moles of O<sub>2</sub> desorbed during TPD experiments for all 5 wt% Cu impregnated samples.

The amount of oxygen desorbed during the TPDs increased with the copper loading for the 50-I (II) samples up to 7 wt% copper, before decreasing slightly for the 10 wt% sample (Figure 6.3). Copper agglomerations were observed in the EDX results for both the 7 wt% and 10 wt% copper samples. Increasing the copper loadings had the effect of increasing the

number of these agglomerations. This appears to have resulted in a lower dispersion of small Cu particles which are thought to be responsible for the labile oxygen species desorbed during the TPDs once the copper loading was increased beyond 7 wt%.

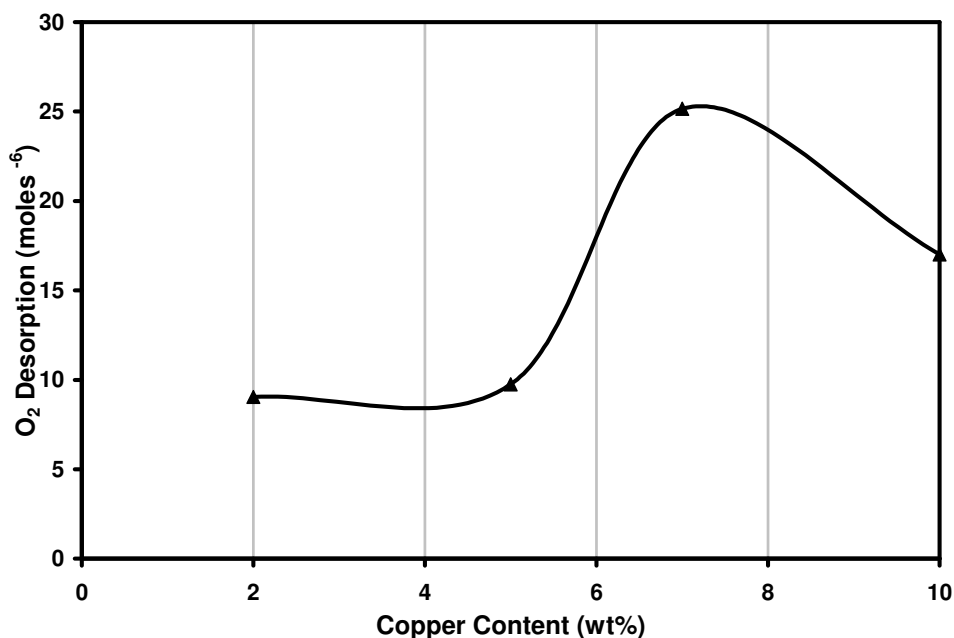


**Figure 6.3** Moles of O<sub>2</sub> desorbed during TPD experiments for ZCe50-I samples with a range of copper loadings.

In the opinion of the author, the temperature and extent of oxygen desorption across the range of samples subjected to TPD experiments suggest that surface copper sites were reduced at high temperature in the flow of Ar. The composition of the oxide does not appear to have had any noticeable effect on O<sub>2</sub> desorption during TPDs. The major influences on the amount of desorption appear to have been copper loading and dispersal, with the SSA of the material contributing to a lesser extent.

## 6.2 TPR Results

### 6.2.1 Assignment of TPR Peaks

The water traces from TPR experiments of the bare oxides generally contained one main reduction peak though there were also minor peaks observed for some samples (ZCe25 and ZCe90). The TPR profile of CeO<sub>2</sub> has been widely reported as containing two reduction peaks at around 500 and 800°C attributed to surface and bulk reduction, respectively. [3-5]

Blank et al. offered two explanations for the two reduction peaks present in the TPRs of  $\text{CeO}_2$ . [6] The first of these was the surface and bulk species mentioned. The second mechanism involved the reduction of different crystal sizes, with smaller crystals being more readily reduced. [6] The introduction of Zr into the  $\text{CeO}_2$  lattice has been consistently shown to promote the release of bulk oxygen. [7,8] This leads to an increase in the size of the first reduction peak in relation to the second reduction peak, as Zr content is increased up to 50 mole %. [3-5, 9] Following on from the assignment of the reduction peaks this suggests that the addition of Zr promotes the dispersion of Ce leading to more of the Ce being present in the more readily reduced surface sites. This corresponds with the results obtained for the TPRs of the direct oxide where ZCe90 was the only sample to have two pronounced high temperature reduction peaks. The presence of only one reduction peak for the majority of the Ce/Zr mixed oxides was taken to indicate the reduction of the bulk oxide. With either the difference between the temperature of surface and bulk reduction being so small that distinction was problematic, or the surface species being so sparse and so 'drowned out' by the bulk material reduction.

The addition of copper to the oxide materials led to a large decrease in the size of the high temperature peaks observed to the extent that they were impossible to detect for many samples. Figure 6.4 is the TPR water trace for the 2-50-I (II) sample. This trace contains four distinct reduction peaks assigned I to IV. The first reduction peak appears as a shoulder on the main low temperature reduction peak, positioned at around  $140^\circ\text{C}$ , assigned as I. The main low temperature reduction peak (II) was observed at around  $175^\circ\text{C}$ . These two low temperature reduction steps have previously been assigned to surface CuO species, and bulk CuO respectively. [10, 11] The two high temperature reduction peaks (III and IV) can be attributed to the low (surface) and high (bulk) temperature reduction of  $\text{Ce}^{\text{IV}}$  by comparison with literature results. [10]

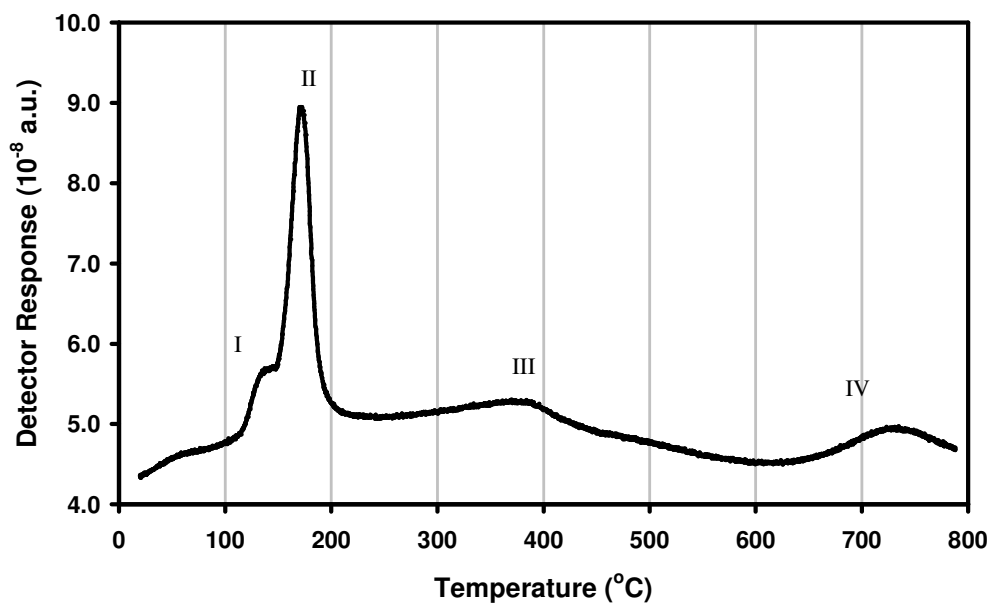


**Figure 6.4** TPR water trace for as-prepared 2-90-I (II) sample.

The decrease in the size of the high temperature reduction peaks with the addition of copper to the mixed oxides suggested the promotion of oxide reduction by the addition of the copper. In order to establish if the low temperature reduction peaks (<350°C) did include a contribution from reduction of the Ce/Zr oxide the amount of water produced was calculated and is shown in Figure 6.5. Oxygen released during TPD experiments was also included as this was attributed to desorption from the copper in the materials. The amount of water and oxygen produced was then expressed as a percentage of the total theoretical reduction of the copper present in the samples. The results shown in Figure 6.5 seem to echo the results reported by Manzoli et al. [14] The low temperature reduction peaks account for well over 100% reduction of the copper present in a number of materials. This combined with the relative absence of high temperature reduction peaks shows clearly that the low temperature reduction peaks are likely to contain a contribution from reduction of the oxide promoted by the copper.

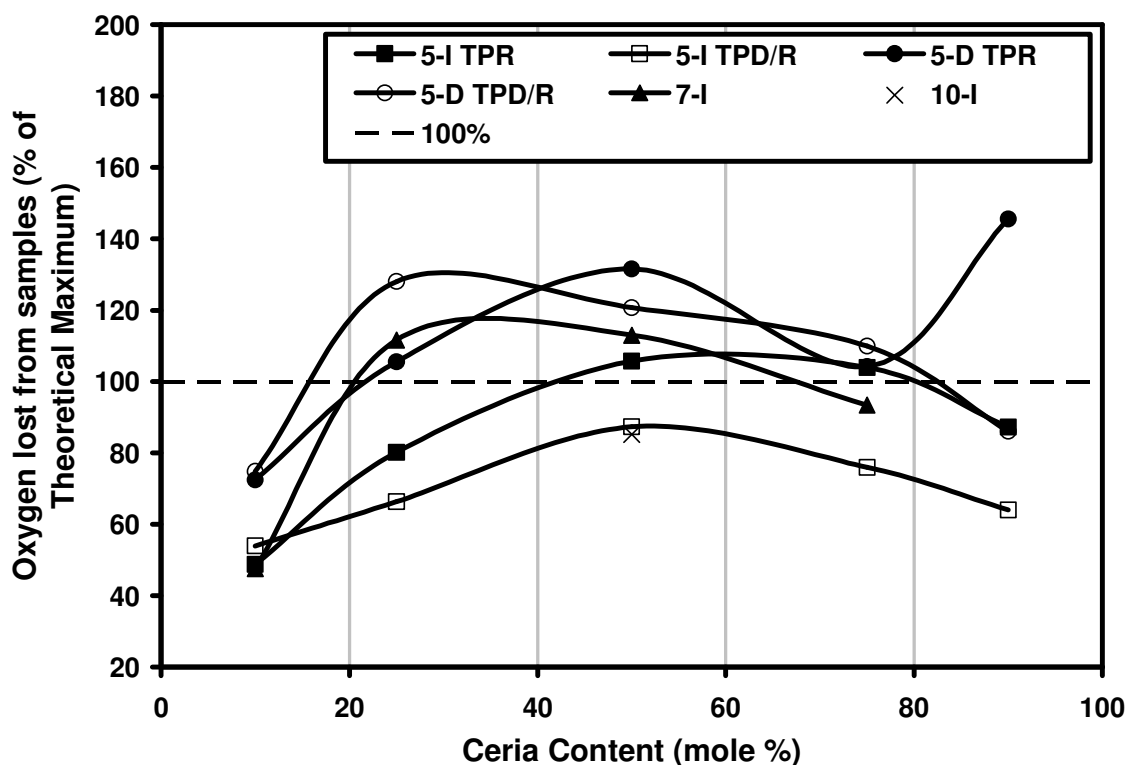


**Figure 6.5** Oxygen lost from samples as water (in TPRs, below 350°C) and O<sub>2</sub> (where applicable, in TPDs) and expressed as a percentage of total theoretical reduction of sample copper content. See text for details.

The water which desorbed from the samples during the TPRs would have led to slightly elevated calculation of the sample reduction. The level of water desorption observed for the copper samples was markedly lower than that of the bare oxides. This combined with the addition of copper raising the amount of oxygen present in the samples meant that the effect of desorbing water during TPRs was less of a concern for the TPRs of copper containing samples, than the TPRs of the bare oxides.

### 6.2.2 Effect of Impregnation Technique

The two methods of copper impregnation resulted in samples which produced markedly different TPR results. The D prepared samples all had significant I peaks, which in some cases (5-50-D and 5-90-D) were roughly equivalent in size to the II peak. As discussed in the previous section this suggests that the D impregnation technique was very effective in creating samples with highly dispersed copper which interacted strongly with CeO<sub>2</sub>, resulting in the large I peaks. [10, 11] Reduction peak II, which was attributed to reduction

of the bulk CuO, [10, 11] was, for the majority of the 5-D samples, at temperatures below that observed for the reduction of CuO nanopowder (Figure 5.14). The exception to this was 5-50-D, which had a slightly higher peak II (178°C compared to 165°C for CuO nanopowder). This suggests that in general the bulk CuO in the 5-D samples were more readily reduced than the CuO nanopowder (NanoArc 97.5%, S.A. 25-40 m<sup>2</sup>g<sup>-1</sup>, 23-37 nm).

There is the suggestion of high temperature reduction peaks in the 5-D samples, primarily for 5-90-D. The decrease in size of the high temperature reduction features has previously been described by Manzoli et al. [14] They suggested that the support was reduced at low temperature as part of the peaks attributed to copper (peak II). As a result the lack of distinct high temperature peaks suggests good copper distribution throughout the sample. The 5-I samples displayed the same low temperature TPR features as the 5-D samples. Peak I was much smaller than peak II for the 5-I samples than in the 5-D samples. Peak II was consistently at a higher temperature for the 5-I samples than for the 5-D samples. Two of the 5-I samples (5-90-I and 5-10-I) displayed distinct high temperature reduction peaks, suggesting poorer distribution of copper in these samples. The increase in the size of peak II with increasing ceria content appears to support the reasoning of Manzoli et al. that this peak includes reduction of the oxide support. [14]

The difference in the TPR results as a function of copper incorporation technique suggest that the D technique was more effective in terms of achieving both a high copper dispersion and good distribution. As a result, the catalysts produced by the D technique were more easily reduced.

### **6.2.3 Increased Copper Loading**

The 2 wt% Cu samples which were subjected to TPR experiments all displayed pronounced high temperature reduction peaks. These generally decreased as copper loading was increased. It appears that increasing the copper loading improved the copper distribution throughout the sample. This decreased the size and occurrence of high temperature reduction peaks which are attributed to reduction of the bare oxide. Increasing the copper loading to 7 wt% was shown in the EDX and XRD results to lead to the formation of copper agglomerations. These copper agglomerations led to a broadening of the second reduction peak (II) and also led to the formation of a number of shoulders on

the second reduction peak, particularly for 7-25-I (II) and 7-50-I (II). The larger copper oxide particles that would result from the agglomeration of copper oxide are likely to have led to the higher temperature shoulders observed for the 7 wt% copper samples. [9]

Increasing the copper loading did not noticeably increase the size of the first low temperature reduction peak. This corresponds with results reported by Águila et al., who noticed that increased copper loading for a ZrO<sub>2</sub> system did not increase the size of the initial reduction peak above a certain loading (3 wt%). [12] This was reported as being a result of saturation of the surface vacancies on which well dispersed copper was situated. [12] As a result increasing the copper loading beyond the saturation point of these surface vacancies results in the formation of copper agglomerations, decreasing the size of the initial reduction peak which was the result of surface copper oxide species, and shifting the second reduction peak to higher temperature. As the copper particles increase in size, the oxygen becomes less labile and as a result is released at higher temperature.

### **6.3 Effect of TPD on TPR Results**

During the TPDs of the copper impregnated samples, there was significant O<sub>2</sub> desorption. As a result there was a noticeable shift in the peak positions in the TPRs conducted post TPD. For the I prepared samples, all of the samples with intermediate Ce contents (5-25, 5-50 and 5-75-I) showed low temperature reduction peaks (peak II) which were shifted to higher temperature. This corresponded with a decrease in the size of the initial reduction peak (peak I). The oxygen desorption observed during the TPD experiments has been attributed to reduction of the surface layer of CuO particles, to which the I peaks in the TPRs were also assigned. The increase in the temperature of peak reduction was thought to be as a result of some sintering of the samples due to the high temperatures of the TPDs. This would reduce the surface area of the CuO particles in the catalysts [13] and result in them being reduced at higher temperature. The 5-10-I and 5-90-I TPD/Rs are harder to explain as the TPDs had the effect of decreasing the temperature at which the samples were reduced which appears to be counterintuitive. 5-10-I displayed poor copper dispersion in the EDX maps, it may therefore be that the thermal cycling of the TPDs resulted in re-dispersion of the copper within the samples.

The 5-D samples displayed similar behaviour to the 5-I samples with a noticeable decrease in the size of the initial reduction peak for those samples with the highest O<sub>2</sub> desorption at high temperature during the TPDs (5-50 and 5-90-D). The second low temperature reduction peak (II), for all the 5-D samples was shifted to a slightly higher temperature and became broader for the TPD/Rs compared to the TPRs. The exception to this was 5-75-D for which the main reduction peak was shifted to slightly lower temperature (144°C for TPD/R compared to 166°C in the TPR).

#### **6.4 Lightoff Mechanisms**

Oxidation of methane during the lightoff experiments appeared to take place through similar mechanisms for the bare oxide and copper containing materials. For the bare oxides CH<sub>4</sub> decreased and CO<sub>2</sub> increased at slightly lower temperature than O<sub>2</sub> decreased and water increased. If complete oxidation of the methane is assumed all of these changes would happen at the same temperature. The pre-reduction temperature was known to be insufficient to reduce the oxides. This accounts for the slight lag in O<sub>2</sub> consumption as oxygen from the oxides was consumed before the O<sub>2</sub> from the gas flow was taken up. The lag in the production of H<sub>2</sub>O may then have been the result of hydroxide ions forming on the oxide surface. These ions would then have been retained on the oxide surface until these they reached a critical level at which they reacted together to form water.

The copper containing samples displayed similar patterns for the lightoff temperatures of the various gasses. The exception to this was O<sub>2</sub> which for the copper containing samples was generally consumed within a few degrees of the methane and before CO<sub>2</sub> was produced. As these samples were well reduced before commencement of the lightoff experiments, the catalyst would use the O<sub>2</sub> to oxidise the CH<sub>4</sub> to CO<sub>2</sub> and as previously described OH ions formed on the surface before reacting to form water at slightly elevated temperature.

#### **6.5 Catalyst Performance**

The materials produced as part of this work are intended to act as catalysts for the oxidation of methane. It was felt that the most effective catalysts for methane oxidation would have high OSC, in order to increase the amount of oxygen present in the sample and

hence increase the number of sites where reduction could take place. This was investigated using the TPR experiments. High distribution and dispersion of the copper active phase was also expected to increase catalyst activity and was investigated using SEM/EDX. The lightoff experiments provided a means of directly assessing the catalysts performance for methane reduction. With the temperature of the lightoff point providing the most reliable data as to the most active of the catalysts.

With regard to the bare oxide materials it was the intermediate composition samples (ZCe25, ZCe50 and ZCe75) that proved to be the most active catalysts. The presence of higher levels of CeO<sub>2</sub> could be expected to lead to more active catalysts, as it will increase the OSC of the materials. It has previously been shown that the introduction of Zr<sup>4+</sup> into the CeO<sub>2</sub> lattice promotes the efficiency of the Ce<sup>4+</sup>-Ce<sup>3+</sup> redox couple. [15] It therefore appears that the intermediate oxide composition samples combine the increased OSC owing to the presence of CeO<sub>2</sub>, whilst benefitting from the promotional effects of Zr<sup>4+</sup>.

The addition of copper to the oxides greatly enhanced the oxidation of methane for all of the oxide compositions. The lightoff temperatures for the copper containing samples were noticeably lower than for the bare oxides with the largest decrease in lightoff temperature observed for the lower CeO<sub>2</sub> containing samples. The addition of copper to the samples may have had the largest impact on the lightoff temperatures observed for the lower CeO<sub>2</sub> content samples, owing to the fact these samples originally had the lowest OSC. So the effect of the extra OSC and activity that the addition of copper provided, was more pronounced in the low CeO<sub>2</sub> containing samples, as they previously had a relative paucity of available oxygen.

Samples prepared by the D technique were revealed, using SEM/EDX and XRD, to have greatly increased copper distribution and dispersion when compared to the I samples. It was felt that this improved distribution and dispersion of the Cu on the oxides was what led to the improved catalytic performance of the D samples when compared to I samples of the same composition.

Of the 5-D samples the most active catalysts were 5-10-D and 5-25-D. In the copper containing samples the OSC of the oxide appeared to have minimal effect on the materials catalytic performance. It may then be the case that the presence of the Zr which has

previously been identified as improving the thermal stability of Ce/Zr based systems [16-18] leads to the preparation of more thermally robust catalysts which maintained their activity and structure better during the TPR and lightoff experiments.

## 6.6 References

- [1] K. Maruya, T. Onishi, *Chem. Comm.*, 23, **1988**, 1541
- [2] M. Kamruddin, P.K. Ajikumar, S. Dash, A.K. Tyagi, B. Raj, *Bull. Mater. Sci.*, 26 (4), **2003**, 449
- [3] Y.-Z. Chen, B.-J. Liaw, H. -C. Chen, *International Journal of Hydrogen Energy*, 31, **2006**, 427
- [4] Y. Guo, G. Lu, Z. Zhang, S. Zhang, Y. Qi, Y. Liu, *Catalysis Today*, 126, **2007**, 296
- [5] D. Terribile, A. Trovarelli, C. de Leitenburg, A. Primavera, G. Dolcetti, *Catalysis Today*, 47, **1999**, 133
- [6] J.H. Blank, J. Beckers, P.F. Collingnon, G. Rothenberg, *Chem Phys Chem*, 8, **2007**, 2490
- [7] J.R. González-Velasco, M.A. Gutiérrez-Ortiz, J.-L. Marc, J.A. Botas, M.P. González-Marcos, G. Blanchard, *Applied Catalysis B: Environmental*, 22, **1999**, 167
- [8] A.B. Hungria, N.D. Browning, R.P. Erni, M. Fernández-Garcia, J.C. Conesa, J.A. Pérez-Omil, A. Martínez-Arias, *Journal of Catalysis*, 235, **2005**, 251
- [9] H. Vidal, J. Käspar, M. Pijolat, G. Colon, S. Bernal, A. Cordon, V. Perrichon, F. Fally, *Applied Catalysis B: Environmental*, 30, **2001**, 75
- [10] X. -C. Zheng, S. -P. Wang, S. -R. Wang, S. -M. Zhang, W. -P. Huang, S. -H. Wu, *Material Science and Engineering C*, 25, **2005**, 516
- [11] G. R. Rao , H. R. Sahu, B. G. Mishra, *Colloids and Surfaces A: Physicochem. Eng. Aspects*, 220, **2003**, 261
- [12] G. Águila, F. Gracia, J. Cortés, P. Araya, *Applied Catalysis B: Environmental*, 77, **2008**, 325
- [13] H. Vidal J. Käspar, M. Pijolat, G. Colon, S. Bernal, A Cordon, V. Perrichon, F. Fally, *Applied Catalysis B: Environmental*, 27, **2000**, 49
- [14] M. Manzoli, R. Di Monte, F. Boccuzzi, S. Coluccia, J. Käspar, *Applied Catalysis B: Environmental*, 61, **2005**, 192
- [15] D. Terribile, A. Trovarelli, C. de Leitenburg, A. Primavera, G. Dolcetti, *Catalysis Today*, 47, **1999**, 133

- [16] A.B. Hungria, N.D. Browning, R.P. Erni, M. Fernández-Garcia, J.C. Conesa, J.A. Pérez-Omil, A. Martinez-Arias, *Journal of Catalysis*, 235, **2005**, 251
- [17] S. Larrondo, M.A. Vidal, B. Irigoyen, A.F. Craievich, D.G. Lamas, I.O. Fabregas, G.E. Lascalea, N.E.W. de Reza, N. Amadeo, *Catalysis Today*, 107-108, **2005**, 53
- [18] L.M. Gomez-Sainero, R.T. Baker, I.S. Metcalfe, M. Sahibzada, P. Concepcion, J.M. Lopez Nieto, *Applied Catalysis A: General*, 294, **2005**, 177

# **Chapter 7. Conclusions**

## 7.1 Ce/Zr Mixed Oxides

1. The citrate complexation preparation technique established by Fuentes et al. [1] provides a simple way of preparing Ce/Zr mixed oxide nano-powders of any composition and in which all compositions providing an even distribution of Ce and Zr throughout the sample.

2. TPR (in H<sub>2</sub>) experiments showed the high Ce content samples (ZCe50, ZCe75 and ZCe90) to be the most easily reduced, with the low Ce samples (ZCe10 and ZCe25) being reduced at higher temperature.

3. The majority of the mixed oxides displayed a single high temperature reduction peak in the TPR experiments. This was taken as being a result of the reduction of the bulk of the oxide material. Some samples displayed two high temperature reduction peaks (ZCe25 trace contained a shoulder on the main peak and ZCe90 had two distinct peaks), the lower temperature of which was assigned as the result of surface oxygen species on the oxide material.

4. The low Ce content samples (ZCe10 and 25) and the highest Ce containing sample (ZCe90) displayed the greatest thermal stability, the TPDs having a minimal impact on the reduction peak temperatures for these samples in TPD/Rs compared to TPRs. The greatest change in peak reduction temperature for the TPD/Rs compared to the TPRs was for the intermediate compositions, ZCe50 and ZCe75. These two materials were shown to have the highest SSAs in the BET results and also had the lowest peak reduction temperatures in the TPRs. It seems that the intermediate composition samples were the most susceptible to thermal ageing.

5. The number of moles of water produced during the TPR experiments increased with increasing Ce content up to ZCe75, before decreasing slightly to ZCe90. As a result, ZCe75 produced the most water per unit mass in both the TPRs and the TPD/Rs. In terms of percentage of maximum theoretical sample reduction the TPD/R experiments were more accurate as they did not contain water desorbed from the oxide. In the TPD/Rs the percentage of maximum theoretical reduction of the oxides decreased in the order: ZCe10>ZCe75>ZCe90>ZCe25>ZCe50. Though ZCe10 was the material with the highest value, it produced less than a quarter of the amount of water of the ZCe75 and ZCe90 samples in absolute terms.

6. The TPRx and TPO experiments that were performed showed the intermediate composition ZCe50 to be more prone to carbon deposition than the high Ce ZCe90.

7. Lightoff experiments were used to investigate the catalytic activity of the oxides for the oxidation of methane. In order to establish if the addition of Zr did enhance the activity of these CeO<sub>2</sub>-based materials, pure CeO<sub>2</sub> was also subjected to a lightoff experiment. The results agreed with what is reported in the literature [2, 3] with CeO<sub>2</sub> being a much less active methane oxidation catalyst than all of the Ce/Zr mixed oxides examined.

8. The most active of the oxides for methane oxidation proved to be ZCe75, followed by the other intermediate composition materials ZCe25 and ZCe50. The high and low ceria samples proved to be the least effective methane oxidation catalysts.

9. The mechanism of methane oxidation initially involved the formation of CO<sub>2</sub> from oxygen contained in the oxides. The hydrogen from the methane was temporarily retained on the oxide surface as hydroxyl ions. As temperature increased, the hydroxyl ions on the oxide surfaces reacted with each other to form H<sub>2</sub>O.

## 7.2 Copper - Containing Ce/Zr Mixed Oxides

1. The EDX and XRD results for the copper samples prepared using the two copper incorporation techniques showed a higher dispersion and distribution of copper in samples prepared using the D technique. Samples impregnated using the I technique began to show copper agglomerations at 5 wt% loading. These agglomerations then increased in size and frequency as the copper loading increased. The samples in which the copper was incorporated using the D technique gave rise to an even, good distribution of copper for samples up to and including 10 wt % copper.

2. The addition of copper to the oxide resulted in the presence of highly labile oxygen, which desorbed during the TPD experiments. The amount of oxygen which was desorbed during the TPDs increased with increasing copper loading.

3. The TPR traces for the copper containing samples contained up to 4 reduction peaks. These were assigned as being the result of (from lowest to highest temperature); reduction of the copper oxide surface, bulk copper oxide (which also included a contribution from the oxide support) and the two high temperature peaks were the result of un-catalysed surface and bulk Ce/Zr oxide reduction.

4. The TPD experiments drastically reduced the size of the first reduction peak in subsequent TPRs for all copper-containing samples. The oxygen desorption observed during the TPD experiments was thought to remove the majority of the highly labile oxygen species which were responsible for the first reduction peak.

5. The D materials consistently exhibited lower main reduction peak (peak II) temperatures during both TPRs and TPD/Rs than the I samples. This was explained as being a result of the high copper dispersion which was shown in the EDX and XRD results.

6. Increasing the copper loading had minimal impact on the position of the low temperature reduction peaks. The major effect of increasing the copper loading on the TPR results was to increase the size and to a lesser extent the temperature of the second low temperature reduction peak (attributed to bulk copper reduction plus a contribution from reduction of the Ce/Ze support). This was as a result of more copper being present leading to the formation of larger copper particles. These larger particles contained more bulk copper and were less readily reduced.

7. The number of moles of water produced for the I materials during TPD/Rs was in the order 5-50-I > 5-90-I > 5-75-I > 5-25-I > 5-10-I. However the percentage of maximum theoretical reduction of the materials when O<sub>2</sub> desorption was also taken into account was 5-10-I > 5-50-I > 5-25-I > 5-75-I > 5-90-I. For the D materials a similar pattern for water production in TPD/Rs was observed: 5-50-D > 5-90-D > 5-25-D > 5-75-D > 5-10-D. When the TPD/R water production and TPD oxygen desorption were considered then in terms of total theoretical sample reduction, the order was: 5-25-D > 5-10-D > 5-50-D > 5-90-D > 5-75-D.

8. TPRx experiments showed limited complete oxidation of the CH<sub>4</sub>, followed by partial oxidation. There was then a decrease in the CH<sub>4</sub> signal and a corresponding H<sub>2</sub> peak as the CH<sub>4</sub> was broken down and carbon deposited on the sample. This sharp decrease in CH<sub>4</sub> level was most pronounced for the I prepared samples.

9. TPOs performed after the TPRx experiments revealed that of the samples investigated, the one that was least prone to carbon deposition was 5-50-D. The two I prepared samples showed more pronounced CO<sub>2</sub> production during the TPO, suggesting more carbon was deposited onto them during the TPRx.

10. Of the incipient wetness impregnated (I) samples tested (5-50-I (II) and 10-50-I (II)), the one with the higher copper loading, showed less carbon deposition. It appears that increased copper loading and using the D impregnation technique can minimise the extent of carbon deposition.

11. The addition of copper to the oxides greatly decreased the lightoff temperatures observed for all oxide samples. D materials had consistently lower lightoff temperatures than the I materials. This effect was most pronounced for the lower ceria containing

samples (10, 25 and 50 mole% CeO<sub>2</sub>). The 10-50-D material also displayed a lower lightoff temperature than the 10-50-I material.

### 7.3 References

- [1] R. O. Fuentes, R.T. Baker, *J. Phys. Chem. C*, 113, **2009**, 914
- [2] J. Kašpar, P. Fornasiero, G. Balducci, R. Di Monte, N. Hickey, V. Sergo, *Inorganica Chimica Acta*, 349, **2003**, 217
- [3] Y.-Z. Chen, B.-J. Liaw, H. -C. Chen, *International Journal of Hydrogen Energy*, 31, **2006**, 427

# **Chapter 8. Further Work**

## 8.1 Further Work

The addition of copper to the Ce/Zr mixed oxides produced by the citrate complexation technique has been shown to greatly enhance the catalytic activity of the materials for methane oxidation. The D materials where the copper was incorporated during the single preparation step have been shown to be more active in all the experiments conducted and related to this have the highest level of copper dispersion of the two preparation techniques. It would be interesting to establish at what copper loading the copper agglomerations formed for the D samples, as 10-D sample investigated showed no evidence of the copper agglomerations which were present in 5, 7 and 10 wt% copper I prepared samples.

An evolution of the lightoff experiment where by the catalysts were operated for prolonged periods in the O<sub>2</sub>/CH<sub>4</sub> gas mixture at elevated temperature would provide information about the thermal, physical and chemical stability of the materials in operating conditions.

The main concentration of further work should be directed towards taking the best performing materials from the lightoff experiments and using them as components in a test cell anode. All the experiments conducted in this work were done using powder samples, as a result it is necessary to know if the results obtained from these experiments are still applicable if these materials are turned into pellets and ran as anodes.